EYEC

MONOGRAPH

9TH EUROPEAN YOUNG ENGINEERS CONFERENCE

Faculty of Chemical and Process Engineering
WARSAW UNIVERSITY OF TECHNOLOGY

Warsaw University of Technology

FUNDACJA MŁODEJ NAUKI

MONOGRAPH

9th European Young Engineers Conference

Warsaw 2021

EYEC Monograph

This monograph has been issued for the ninth edition
of the European Young Engineers Conference, which
was held on 19–21 April 2021 at the Faculty of Chemical
and Process Engineering, Warsaw University of Technology

Warsaw 2021 · Seventh volume · Second revision
ISBN 978-83-936575-9-9

Contents

Introduction

Work on the 9th edition of the Conference started early, just by the end of last year's April. Unfortunately, it turned out that 2020 became the year marked by the COVID-19 pandemic. For the first time in the history of the European Young Engineers Conference, with great sadness, we had to cancel it. The most important thing was to minimise the spread of infection, and due to this, we had no choice but to call the event off.

Throughout this past year, we have been wondering how to start all over again. We asked whether the next edition should be held online just partially or if we should switch entirely. Due to the ever-increasing number of COVID-19 cases, we decided to go completely remote quite quickly. We have also agreed that this edition (like the cancelled edition in 2020) will be marked as the 9th.

This 9th edition of the European Young Engineers Conference has brought us many new challenges that we had never faced before. That included the choice of an online platform to conduct the Conference, the form of the plenary and poster presentations, and additional attractions for conference participants, which have always been very important to us and allowed the participants to integrate. Although this time we will not meet with you in person, we are highly grateful for your presence at the Conference, the large number of submitted abstracts and articles, and being with us despite the "lost year".

The friendly atmosphere has always been significant to us because, combined with the high level of knowledge, it is the best way to start and develop a scientific career. We hope this book will be the first step to an excellent career for all conference participants.

This event is the second attempt at organising the 9th edition of EYEC. As a result, with some extra months in-between, we have been able to implement some ideas that have been in our minds for a long time. Every year we try to provide you with something new: interesting speakers, additional workshops or accompanying competitions. Apart from the form of the Conference, the most significant changes have affected our monograph's appearance. In this book, you will find the most promising, important, peer-reviewed papers by young scientists from all over Europe. We felt that such content requires a new form that tries to come closer to the one that researchers can find in scientific journals. We hope that the book you are holding in your hands will meet your expectations.

Fortunately, this year we are again pleased to continue the section of our monograph entitled "From the Expert's Perspective". We encourage you to read Prof. Jörg Vienken's article as an excellent opportunity to familiarise yourself with a new field of study or to expand your knowledge on a well-known issue. We also present you a new section that will bring you closer to the main organisers of the European Young Engineers Conference.

Finally, we would like to thank our Special Guests, the Scientific Commission members, and all members of the Scientific Committee. Due to your hard work on ensuring the highest level of submitted papers, we can provide you with a monograph of the highest scientific standard. Your invaluable help and advice are greatly appreciated by all of us, young scientists.

We hope that we will meet face-to-face during the 10th edition of the European Young Engineers Conference and joyfully exchange memories of this special edition. We also strongly believe that you will find the papers in this book very intriguing and important, just as we do.

– Organising Committee
Editorial Team of EYEC Monograph

1 Special guests

1.1 Prof. Jörg Vienken – Honorary Guest

Institute for Bioengineering, Technical University of Applied Sciences Mittelhessen, Giessen, Germany

Jörg Vienken graduated in Chemical Engineering at the Technical University of Darmstadt and received a Doctoral Degree in Biophysics and Bioengineering from the Technical University of Aachen, both in Germany. He was then appointed the position of an Associate Professor at the Institute for Biotechnology of the University of Würzburg, Germany.

In 1985, he switched to the medical device industry and worked for 11 years at AKZO NOBEL Membrana in Wuppertal (today 3M) as Director for Clinical Research and Science Services, followed by a position as Vice President BioSciences in Fresenius Medical Care in Bad Homburg, Germany until 2013. Vienken retired as pensioner in July 2013 reaching the age limit of 65 years. He, then, joined Nephro-Solutions AG in Hamburg, as one of its Board members in October 2013 and hold this position until December 2015.

Since January 2016, JV works as a Freelance Consultant for the European Medical Device Industry. He serves as member of Technical Advisory Boards of German Research Institutions e.g. for the Karlsruhe Institute of Technology (KIT), the Helmholtz-Association and the Berlin-Brandenburg Centre for Regenerative Therapies (BCRT). As a member of the Supervisory Board of Zytoprotec GmbH in Vienna and as a cofounder of the start-up company Aquarray GmbH at KIT Karlsruhe, he supports product innovation and development in life sciences up to market entry.

Jörg Vienken is Past President of the International Federation of Artificial Organs (IFAO), the umbrella society of the continental societies from Europe (ESAO), the USA (ASAIO) and Japan (JASO). He is also Past President of the Association of German Biotech Companies (VBU-DECHEMA).

Although retired from his professional career, Jörg Vienken is still engaged in R&D of Life Sciences by both, teaching "Biomaterials" and "Artificial Organs" at several European Universities, and by serving as co-editor of journals dedicated to the realm of Artificial Organs. JV has published more than 350 scientific publications, book chapters and 8 books. He holds the position of a "Distinguished Fellow of EDTA-ERA" and was honoured by receiving several international awards, among them the "Emil-Bücherl Award for Lifetime Achievement" of the European Society for Artificial Organs (ESAO).

1.2 Prof. Bernhard Christian Seyfang

Department for Life Sciences and Engineering, TH Bingen, University of Applied Sciences, Bingen, Germany

Prof. Dr. Bernhard Seyfang received his Diploma from Universität Karlsruhe (TH), specialising in chemical reaction engineering and electrochemical engineering. He then joined Paul-Scherrer-Institut to work on the simplification on polymer electrolyte fuel cell and received his PhD from ETH Zürich. Ten years of industrial experience, in a start-up company and in an enterprise producing chemical and pharmaceutical products, resulted in several publications covering topics about process engineering in industrial applications.

Since April 2018 Bernhard Seyfang is professor for chemical reaction engineering at TH Bingen, a university of applied sciences cooperating with the whole range of chemical and pharmaceutical companies in the wider area around Frankfurt. His research and development interests cover process optimisation procedures, surface characterisation of additively manufactured devices for process engineering applications as well as extraction centrifuges.

Abstract: Process optimization – you can only improve what you understand

KEYWORDS: *process optimisation*, *retrofit*, *cost engineering*, *process intensification*.

Chemical or biotechnological processes and the units included within are often designed for one particular operation point. Earlier or later in service, processes or their units need to be adapted due to commercial, ecological, and/or technical reasons resulting in process optimization projects. In the framework of thorough process analysis, regulatory, technical possibilities, and cost aspects it is not an easy task to choose an approach fitting to the problem. The lecture will give valuable insights in this context.

The altercation of one parameter in a rather small unit operation may have ramifications in remote parts of the process, resulting in the central learning outcome is that there might be whole a range of process optima.

Hence the question arises what type of optimization strategies are available for the responsible process engineer, what kind of process understanding is required and what the tools are that can be utilized to reach the target:

- retrofit of the whole process,
- improvement of particular unit operations by process intensification using apparatus such as dividing wall columns or rotating devices,

- modularisations,
- rescheduling of particular steps, a valid approach especially in highly regulated environments.

Examples gained from industrial practice will be presented aiming towards solutions of multi-criterial and consequently complex questions, where simulation plays an important role.

The lecture will demonstrate these aspects from an academic and from an industrial perspective, in order to demonstrate to young chemical engineers and young process engineers a pathway towards process understanding.

1.3 Prof. Andrzej I. Stankiewicz

Process and Energy Department, Delft University of Technology, Delft, The Netherlands

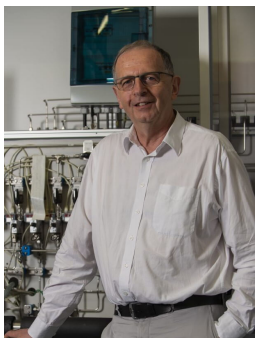

Emeritus Professor at Delft University of Technology, the Netherlands, and former Director of TU Delft Process Technology Institute. With more than 40 years of industrial and academic research experience he is an author of numerous scientific publications on process intensification, chemical reaction engineering and industrial catalysis.

Prof. Stankiewicz is one of the pioneers of process intensification. He is the principal author and co-editor of the world's first book on Process Intensification. The book was in 2012 translated to Chinese. Prof. Stankiewicz is also the author of the first full-size academic course on Process Intensification.

He is Editor of Chemical Engineering and Processing: Process Intensification (Elsevier) and Series Editor of the Green Chemistry Books Series (Royal Society of Chemistry). He was the founder and first Chairman of the Working Party on Process Intensification at the European Federation of Chemical Engineering. He currently chairs the Board of the European Process Intensification Centre (EUROPIC).

Current research interests of Prof. Stankiewicz focus on control of molecular interactions and intensification of chemical reactions using electricity-based energy fields (e.g. laser, microwave, UV). The research in that area has brought him prestigious Advanced Investigator Grant from the European Research Council.

More recently, Prof. Stankiewicz has initiated and coordinates the H2020 "ADREM" project on methane valorization using alternative forms of energy in modular catalytic reactors.

Abstract: Beyond electrolysis: old challenges and new concepts of electricity-driven chemical reactors

KEYWORDS: *energy transition*, *carbon footprint*, *alternative energy forms*, *process intensification*.

Decarbonization of the energy-intensive manufacturing industries presents one of the most urgent technological challenges of coming decennia. Among those industries, the chemical sector (including refineries) is by far the most significant energy consumer – according to the U.S. Energy Information Administration, in 2018, the bulk chemical and refining sectors were responsible for 46% of the entire energy consumption by the American industry. The transition scenarios to the low-carbon energy in the chemical process industries are commonly based on the so-called Power-to-X concept, which basically assumes using the low-carbon or renewable electricity to produce fuels and/or chemicals. However, in the vast majority of rich research literature related to those scenarios, the use of electricity is limited to the initial steps of electro(cata)lytic conversion of water, CO_2 and/or nitrogen, respectively to hydrogen, carbon monoxide, syngas, formic acid, methanol or ammonia. The subsequent reaction steps are usually assumed to be carried out in the conventional, thermochemical way.

While the electrocatalytic production of fuels from water, CO_2 or nitrogen is undoubtedly of fundamental importance for decarbonizing (or rather defossilizing) the chemical sector, it is equally important to address possible applications of electricity in the reactions further down the chain – the reactions that eventually lead to thousands of chemical products on the market today. With those reactions in mind, in the lecture I critically review the entire spectrum of relevant electricity-based chemical and catalytic reactors, focusing on the related challenges and the new concepts to address them.

1.4 Zoltán Kovács, PhD

Department of Food Process Engineering, Hungarian University of Agriculture and Life Sciences, Budapest, Hungary

Dr Kovács is currently a professor and head of Department of Food Process Engineering at the Hungarian University of Agriculture and Life Sciences, Hungary. He received his MSc degree on Food Engineering in 2003 from the Szent István University. In 2008, he obtained his PhD degree on Chemical Engineering from the Institute of Process Engineering at the Johannes Kepler Universitaet Linz, Austria. Prior to his current position, he had worked as a senior scientist for 5 years at the

Institute of Bioprocess Engineering and Pharmaceutical Technology of the University of Applied Sciences Mittelhessen, Giessen, Germany. In 2013, he obtained the Marie Curie Career Integration Grant that allow him – after 10 years of international experience in abroad – to return in his home country and to establish his own research group. During his career, he has received distinctions from the European Membrane Society, the Association of German Engineers, and recently awarded the Bolyai Research Fellowship by the Hungarian Academy of Sciences. He has participated to and is responsible for many out-of-campus projects with industrial partners on bioprocess design and membrane technology development.

Abstract: The production of galacto-oligosaccharides: state-of-the-art and challenges

Keywords: *galacto-oligosaccharides*, *process intensification*, *enzyme membrane reactor*, *selective fermentation*, *process analytical technology*.

Galacto-oligosaccharides (GOS) are carbohydrates composed of a terminal glucose linked to a chain of galactose units with a degree of polymerization between 2 and 10. They are recognized as prebiotic compounds with favorable nutritional and technological properties. At industrial scale, GOS are produced by the enzymatic conversion of lactose in stirred-tank reactors. The resulting raw GOS product consists of a mixture of carbohydrates including glucose and galactose as by-products as well as a considerable amount of non-reacting lactose. The yield of the bioconversion is low, typically limited to up to 55% GOS on total carbohydrate basis. In industrial practice, raw GOS is further purified by SMB chromatography. Recently, a number of competitive separation techniques has been developed to overcome the high processing costs associated with chromatography.

This talk provides an insight into the practice of the production of raw GOS and into the state of art technologies for manufacturing high-purity products. The possibilities for the intensification of GOS manufacturing processes will be discussed by highlighting the pros and contras that are associated with the novel competitive technologies. Moreover, the feasibility of the implementation of spectroscopic tools as in situ reaction-monitoring techniques in process analytical technology will be evaluated.

Acknowledgments

This research was supported by the New National Excellence Program of the Ministry of Human Capacities and by the European Union and co-financed by the European Social Fund (grant agreement no. EFOP-3.6.3-VEKOP-16-2017-00005).

1.5 Michał Wojasiński, PhD

Department of Chemical and Process Engineering, Warsaw University of Technology, Warsaw, Poland

Dr. Michał Wojasiński is a chemical engineer working in the intersection fields like biomedical engineering, tissue engineering, and nanotechnology, building interdisciplinary approaches to various research and engineering problems. He graduated in Chemical Engineering from the Faculty of Chemical and Process Engineering, Warsaw University of Technology (2011). In 2019, he obtained a PhD in the field of chemical engineering. He took up the position of assistant professor in the same Faculty. He teaches medical nanotechnology, implantable medical devices, and bioprocess in the laboratory.

His research interest covers nanostructures formation processes – polymer nanofibers and ceramic nanoparticles – for application in tissue engineering/regenerative medicine. He works on a description of a process of air blowing of polymer fibers, called solution blow spinning, as an extension of his research project granted from the National Science Centre and his PhD. Recent publications of his deal with the application of polydopamine coatings on the surface of polyurethane fibers for enhanced adhesion of cells in 3D culture, design of specific nanofibrous materials for microfluidic systems, and a continuous method for the production of hydroxyapatite nanoparticles. Now, Dr. Wojasiński works on incorporating his experience in nanofibers production and synthesis of hydroxyapatite nanoparticles into 3D printing of composite materials and advanced hybrid scaffolds for tissue engineering.

Abstract: Nanofibrous medical scaffolds from solution blow spinning

Keywords: *solution blow spinning*, *nanofibers*, *scaffolds*, *tissue engineering*.

The current medicine development pushed engineers to develop new materials and ways to process them into medical products. Since the ’80s of the last century, the field of tissue engineering and regenerative medicine continued such search leading to the application of nanofibrous materials as scaffolds for in vitro cultured tissues. Nanofibers structurally mimic the natural scaffold – an extracellular matrix – composed of collagen. Amongst several methods to process polymers into scaffolds to form a nanofibrous mat, electrospinning remains the most popular. However, a new process called solution blow spinning produces nanofibrous materials in various forms in a scalable and efficient way. Comparing to electrospinning, blowing of polymer solutions generates lower cost with the same level of control

over product properties and a more versatile choice of collectors. Choice of polymer/solvent system, with known rheological properties, with an adjustment of processing parameters and collectors, results in nanofibrous structures potentially applicable as scaffolds in regenerative medicine.

Medical scaffolds composed of polymeric nanofibers can be individually designed and produced for the desired purpose. This talk aims at describing three types of scaffolds we were working on 1) three-dimensional polystyrene scaffolds for macrophage phenotype modification; 2) composite nonwovens composed of poly-L-lactic acid and hydroxyapatite nanoparticles, and 3) cardiovascular scaffolds. The talk ending will show the direction for the design and build of bi-layered cylindrical conduits composed of nanofibers potentially applicable in medicine as vascular grafts.

The efficiency and reliability of solution blow spun nanofibrous materials generate enormous interest in such products. Now, we are developing the more advanced tissue-engineered vascular grafts, and we work on applying water-soluble polymers as a building material for nanofibrous wound dressing.

Acknowledgments

The research funding: Biomimetic vascular prostheses of small diameters, "Microsystem Lab-on-a-chip for biomimic and growth analysis of cardiac cells" (both the National Centre for Research and Development in the LIDER program), and research project no. DEC-2013/11/N/NZ1/02428 (by the National Science Centre, Poland).

2 Scientific Commission

2.1 Prof. Dr. Łukasz Madej

Department of Applied Computer Science and Modelling, AGH University of Science and Technology, Cracow, Poland

Łukasz Madej, in 2003, received an Engineering degree at the Department of Physics and Nuclear Techniques of the AGH University of Science and Technology in the field of Solid State Physics. In 2004 he defended his Master's thesis at the Faculty of Metallurgy and Materials Science in the field of Information Technology in Material Science. In 2007 he obtained a Ph.D. degree in the field of Applied Informatics. In 2011 he received a D.Sc. degree and a full professor title was granted by the President of Poland in 2019. Presently he is head of the Multiscale Modelling division at the Department of Industrial Computer Science and Modelling AGH University. He is also a vice-president of the Polish Forging Association, executive board member of the Euroforge, a member of the board of directors of Esafom and an associate member of the CIRP, The International Academy for Production Engineering. During his research carrier, he was a visiting academic or visiting professor at renowned academic centers around the world.

His expertise lies in computer-aided technology development solutions, material science, process digitalization, production process monitoring tools within the concept of Industry 4.0, and multiscale modelling techniques.

2.2 Magda Barecka, PhD

Lodz University of Technology/TU Dortmund University, Poland/Germany

Dr. Magda H. Barecka is a chemical engineer with both academic and industrial expertise in process intensification, process retrofitting and design. She received the PhD title from TU Dortmund University and Lodz University of Technology as a joint Diploma.

She is an author of a systematic methodology supporting implementation of intensified technologies in the chemical industry, which has been successfully transfer into industrially applicable tools. Currently, Dr. Barecka is working at an overseas department of University of Cambridge (Cambridge CARES) in Singapore, focusing on application of novel intensified operations in the field of carbon dioxide conversion.

Apart from research related to process simulations, modelling and photochemistry, she actively contributed in several European grants in the field of energy efficiency, sustainability and environmental impact assessment (LCA).

2.3 Jozsef Kupai, PhD

Department of Organic Chemistry and Technology, Budapest University of Technology, Budapest, Hungary

Jozsef Kupai from the Faculty of Chemical and Bioengineering, Budapest University of Technology and Economics defended his PhD thesis "Synthesis and application of chiral 18-crown-6 ethers containing a pyridine subunit" in 2012 at the Faculty of Chemical and Bioengineering, Budapest University of Technology and Economics (BME). Since January 2021 he is employed as an Associate Professor at Department of Organic Chemistry and Technology. He is the head of Organocatalysis Research Group (*www.kupaigroup.com*), and member of Faculty Council from 2016, and recently (at the end of 2020) he became the vice-head of the Institute for Organic Chemistry Group.

He was a principal investigator (2013–2017) of the "Synthesis and application of new thiourea, amide and sulfonamide type organocatalysts containing heterocycle subunits" National Research, Development and Innovation Office project financed by the Hungarian Academy of Sciences. This grant was received excellent (10/10) qualifications by the reviewers. Since then he is focused on the synthesis, application, and recovery of cinchona-based organocatalysts.

In 2016 Dr. Kupai worked as a visiting academic in School of Chemical Engineering and Analytical Science at The University of Manchester, UK in the laboratory of Professor Gyorgy Szekely.

Jozsef Kupai is the co-author of 34 publications in peer-reviewed international journals (in 9 of them as a corresponding author), his articles have 381 independent citations, his Hirsch index is 13, and in 2018 he has been awarded the Bolyai Research Fellowship by the Hungarian Academy of Sciences (H.A.S), and recently (2020) the Gyozo Bruckner Prize by H.A.S. He is a supervisor of 1 postdoc, 2 Ph.D. students, 1 MSc, and 6 BSc students, and takes the Organic chemistry I and II lectures, practicals, and laboratory for international and Hungarian students at the university. He won the prize "Excellent Lecturer of BME" as the second-best lecturer among all the professors at the university according to the votes of students in 2016. At the end of 2020, two of his Ph.D. students suc-

cessfully defended their Ph.D. theses (entitled "Synthesis, application, and membrane-assisted recovery of homogeneous organocatalysts" and "Synthesis, application, and recycling of new asymmetric organocatalysts containing cinchona skeleton").

Dr. Kupai is a Guest Editor of a Special Issue entitled "Advances in Organocatalysts: Synthesis and Applications" at the MDPI journal Materials, and Review Editor of the Separation Processes section of the journal Frontiers in Chemical Engineering.

In 2020 he won the prize for the best article in Hungary in the chemical field (the so-called Kisfaludy Prize) with his paper published in ACS Catalysis (IF = 12.2).

2.4 Maria Kurańska, PhD

Cracow University of Technology, Cracow, Poland

Maria Kurańska has been working at Cracow University of Technology since 2014. A substantial part of her works is aimed at evaluating a possibility to apply selected renewable materials in the form of biopolyols and natural fillers as well as flammability-reducing substances in the synthesis of thermal insulation rigid foams with a low apparent density. She has participated in research projects (EranNet Matera BBPM, BIOPURFIL PIRSES, EPURNAT). Currently, she is project coordinator of the project no. LIDER/28/0167/L-8/16/NCBR/2017 financed by the National Centre for Research and Development in Poland. The main goal of her research is to develop a technology of waste vegetable cooking oil recycling following the methods of chemical synthesis through epoxidation and oxirane ring opening and transesterification.The studies fit in the circular economy model.

She is an author of numerous scientific publications with the Total Impact Factor exceeding 130. She has been honoured by the magazine Wysokie Obcasy and listed among "50 Bold Women of 2018" whose work changes the world for the better. The technology she has developed has been distinguished by the Polish Women Scientists Network in the contest "Innovation Is a Woman". For her research activity, she has also received a Polish Intelligent Development Award 2019 in the category "Scientist of the Future".

2.5 Agata Przekora-Kuśmierz, PhD

Department of Biochemistry and Biotechnology Faculty of Pharmacy, Medical University of Lublin, Lublin, Poland

Research Professor (scientific post) at the Department of Biochemistry and Biotechnology of Medical University of Lublin (Poland). She obtained her master's degree (2009) as Biotechnologist from Maria Curie-Skłodowska University in Lublin (Poland) and PhD (2014) as well as habilitation degree (2018) in Pharmaceutical Sciences from Medical University of Lublin.

An expert in the field of engineering of biomaterials and tissue engineering. Her scientific background includes fabrication of polymeric drug carriers and biomaterials for bone, cartilage, and skin regeneration. Specialist within the isolation of stem cells from adipose tissue for regenerative medicine applications as well as within the use of in vitro cellular models in preclinical studies, including preliminary evaluation of biocompatibility of novel biomaterials.

Since 2018 an expert of European Commission for evaluation of R&D projects within Horizon 2020 Programme. An author/co-author of 8 patents, 4 patent applications, and 62 scientific articles (IF = 195.665) in the field of tissue engineering, materials science, and drug discovery. Main or Principal Investigator in 11 research projects related to engineering of biomaterials and tissue engineering. Her current research projects is: OPUS (NCN) "Comprehensive evaluation of biomedical potential of novel macroporous cryogel-based biomaterials produced by freeze-drying technique combined with foaming agent".

2.6 Lena Ruzik, PhD

Department of Analytical Chemistry, Warsaw University of Technology, Warsaw, Poland

Lena Ruzik studied chemistry at the Warsaw University of Technology and received her PhD there in 2007. She was employed as Assistant Professor at the Faculty of Chemistry from 2007 to 2020, did her habilitation at the Warsaw University of Technology in 2019, and since 2020 has been employed as Associate Professor. Her research focuses on the bioavailability investigation of element species and analytical methods to characterize their behaviour in presence of biomolecules. Her research centres around speciation analysis of trace elements, metals, and metalloids in food using hyphenated techniques. She has also been involved in the investigation of metal-based nanoparticles metabolism in edible plants. She has published more than 30 original papers and reviews. She is a member of Food Analysis Group in the frame of the Committee on Analytical Chemistry, Polish Academy of Sciences.

3 Scientific Committee

Alessandro Benedetti, PhD – Institute of Condensed Matter Chemistry and Technologies for Energy, Italy
Marta Bojarska, PhD – GVS, Italy
Robert Cherbański, PhD – WUT, Poland
Prof. Marek Henczka, PhD – WUT, Poland
Oleksandr Ivashchuk, PhD – Lviv Polytechnic National University, Ukraine
Magdalena Jasińska, PhD – WUT, Poland
Zoltan Kovacs, PhD – Szent István University, Hungary
Andrzej Krasiński, PhD – WUT, Poland
Jan Krzysztoforski, PhD – WUT, Poland
Prof. Łukasz Makowski, PhD – WUT, Poland
Artur Małolepszy, PhD – WUT, Poland
Marta Mazurkiewicz-Pawlicka, PhD – WUT, Poland
Prof. Eugeniusz Molga, PhD – WUT, Poland
Prof. Arkadiusz Moskal, PhD – WUT, Poland
Marc Müller, PhD – Leibniz University Hannover, Germany
Marcin Odziomek, PhD – WUT, Poland
Wojciech Orciuch, PhD – WUT, Poland
Agata Penconek, PhD – WUT, Poland
Mariusz Pietrzak, PhD – WUT, Poland
Maciej Pilarek, PhD – WUT, Poland
Rafał Przekop, PhD – WUT, Poland
Prof. Tomasz Sosnowski, PhD – WUT, Poland
Prof. Ilya Vorotyntsev, – NNTU, Russia
Michał Wojasiński, PhD – WUT, Poland
Anna Zagórska-Jackiewicz, PhD – WUT, Poland

4 Organising Committee

The ninth edition of the European Young Engineers Conference has been organized by the following members of the Scientific Club of Chemical and Process Engineering, students and researchers of the Faculty of Chemical and Process Engineering:

Dominika Kasprzak – Main Coordinator

Mateusz Bartczak, MSc
Jan Bartha, BSc
Weronika Berent
Grzegorz Bernacki
Monika Binkiewicz
Mieszko Boczkowski, BSc
Zuzanna Bojarska, MSc
Nina Borzęcka, MSc
Piotr Cendrowski, MSc
Nikodem Dąbrowski
Katarzyna Dobrowolska, MSc
Aleksandra Jurkiewicz, BSc
Monika Klimek
Radosław Krzosa, MSc
Magdalena Majchrzyk
Sandra Mochtak
Hanna Nurczyńska, BSc
Grzegorz Pawełkiewicz, BSc
Olga Przybył, BSc
Izabela Słomska
Marek Sutkowski
Justyna Szczepańska, BSc
Maria Ziąbska, BSc

4 Coordinators of the 9th EYEC

4.1 Dominika Kasprzak, BSc

Main Coordinator, Board member of the Scientific Club of Chemical and Process Engineering

Dominika Kasprzak is the head coordinator of EYEC. She has to ensure that each section fulfils its obligations and knows what is to be accomplished. As a head coordinator, she represents all organizers of the conference.

Dominika started her studies at the Faculty of Chemical and Process Engineering at the Warsaw University of Technology in 2017 and became an engineer in 2021 with her engineering thesis "Experimental studies of MoS_2 nanoparticles production in tank reactors".

She joined the Scientific Club of Chemical and Process Engineering in 2018, and since then, she has taken part in scientific festivals and projects. She helped in Logistics Section in the 8th edition and was the coordinator of Logistics in 2020. Now, she is studying for a master's degree at the same faculty and is a member of the Scientific Club council. She also works in a planning and design company as a technologist.

4.2 Sandra Mochtak

Coordinator of the Sponsorship Section, Member of the Scientific Club of Chemical and Process Engineering

Sandra Mochtak is the coordinator of the sponsorship section. She is a third-year student of Chemical and Process Engineering at the Warsaw University of Technology. She has been a member of the Scientific Club of Chemical and Process Engineering for two years. Sandra joined the science club due to the desire to develop and meet new people. She likes to get involved in new activities such as the organisation of job fairs, conferences or scientific projects, and in her free time likes to play board games and watch psychological films.

Sandra has been taking part in the preparations for the EYEC conference for two years – in the last year in the group of logistics and sponsorship. In the current edition, she is a coordinator of the sponsorship section.

Her main task is to look for sponsors and media patrons who help us reach a larger audience. Next, she controlled the sharing of our materials and the materials of our patrons. Thanks to participation in the organisation, she gained a lot of soft skills.

4.3 Maria Ziąbska, BSc

Coordinator of the Monograph Section, Member of the Scientific Club of Chemical and Process Engineering

Maria Ziąbska, for the first time, got involved in the EYEC conference during the 7th edition. She started by performing small tasks in the logistics group. During the 8th edition, she joined the monograph group and has now become its leader. Her most important job is to do an editorial check of articles and abstracts verified by reviewers and assemble them into one book.

She started her studies at the Faculty of Chemical and Process Engineering in the Warsaw University of Technology in 2016. However, she joined the Scientific Club only a year later in 2017. She obtained the title of engineer in 2020, the subject of her engineering thesis was "Development and production of catalysts for the hydrogen evolution based on MoS_2 nanoparticles".

After graduating, she decided to continue her studies and currently, she is in the 2nd semester of M.Eng. course, specialising in Industrial Process Engineering. Daily, she lives in Lublin and works in one of the Polish natural gas mines.

4.4 Weronika Berent

Coordinator of the Logistics Section, Member of the Scientific Club of Chemical and Process Engineering

Weronika Berent is the coordinator of the logistics section. In 2018 she started studying at Warsaw University of Technology. After one year, Weronika decided to join the Scientific Club of Chemical and Process Engineering. She supported organising EYEC in 2020, but unfortunately, that event could not take place because of the pandemic. Through that, she has an extra motivation to do her best for Conference. Her primary goal in life now is obtaining an engineer's degree.

In this year's edition Weronika was responsible for planning budget and financial matters. She chose and ordered awards for participants. She also supported the Monograph Team by contact with the printing house. Logistics Team often solves troubleshoots – thanks to this fact work in logistic is very lively and full of effects.

She hopes that every attendee enjoys European Young Engineers Conference just like her. She can't wait for this and all the upcoming editions of EYEC.

4.5 Monika Klimek

Coordinator of the Graphics Section

This edition of EYEC is the first in which Monika has been involved. Interestingly, she is the first-ever graphic section coordinator. Monika is responsible for the entire graphic design of the European Young Engineers Conference, including all of the posters and logos. One of the tasks she had was to create the cover of this monograph – both for the printed and the digital version.

Monika started her studies at the Faculty of Chemical and Process Engineering at the Warsaw University of Technology in 2019. As of today, Monika is not a member of the scientific club.

4.6 Marek Sutkowski

Coordinator of the Promotion Section, Member of the Scientific Club of Chemical and Process Engineering

Marek was originally tasked with coordinating the Conference's budget. Due to the remote form of the event, he had to help with the social media. Among other things, he ran an Instagram account. Internauts could find more information about the Conference, special guests, meet coordinators and see the event from backstage. He also created surveys, participated in promotions, helped with the website and supported other coordinators of the Conference.

Marek started his studies in 2019. As a young student, he was curious about student life and joined the faculty's research club on the very first day. Marek participated in smaller projects and tasks, and at the beginning of 2020, became an assistant to the former EYEC budget coordinator Rafał Pakuła. Although the last Conference did not take place, he decided to become one of the coordinators the following year. In the meantime, Marek managed to become the Mister of Internauts at the Warsaw University of Technology. Daily, he is an enthusiast of physical experiments and all areas of sport. He devotes his free time to callisthenics training and playing video games with his friends on the Internet.

4.7 Izabela Słomska

Coordinator of the Media Section, Vice-chairman of the Scientific Club of Chemical and Process Engineering

Izabela is currently a student of Chemical and Process Engineering, Warsaw University of Technology. She started her studies in 2018. From the beginning of her university life, she was involved in the Scientific Club of Chemical and Process Engineering. Her incentive to join the Scientific Club was matters covered by the projects in the Club and the organization of such a big event as the European Young Engineers Conference.

She has been committed to the organization of EYEC for three editions, for two as a coordinator of the media section. In her opinion, the most rewarding thing after the Conference is the contentment of the participants and guests.

4.8 Jan Bartha, BSc

Coordinator of the Contact Section, Member of the Scientific Club of Chemical and Process Engineering

Jan Bartha works on every EYEC since 5th edition. As a Communication Chief, his job was to speak with the participants, Special Guests and Scientific Commission members. He was responsible for email communication: informing about technical aspects of the Conference and replying to peoples' questions and requests.

Additionally, his role was to find perfect candidates for Scientific Commission and convince them how great for young scientists EYEC is, so they would agree to participate.

Last, but not least, he oversaw the Conference schedule to accommodate every person into a specific timeframe.

5 From expert's perspective

5.1 Polymer properties to comply with requirements for medical devices

Jörg Vienken [*,1]

1 Technische Hochschule Mittelhessen (THM), Giessen, Germany

Keywords: *polymer selection*, *CFD*, *blood compatibility*, *biostability*, *extractables*.

Abstract

Polymer selection for their use in medical devices is one of the most prominent tasks of a bioengineer. As a major constituent of such devices their composition can be made responsible for device failure and patient's adverse clinical events. Polymers have to be adapted to their prescribed use, i.e., to a specific device and related to a specific disease. Market and patient analyses thus determine needs and prerequisites. Polymer characteristics also determine the mode of sterilisation for the final device its biocompatibility and biostability. Depending on the quality of the chemical polymerisation process and whether a plastic material is applied as a blend, leachables from this material play a significant role, given that they can reach the patients blood stream. Among those are plasticizers and bis-phenols due to their action as endocrine disruptors.

Introduction

"The hottest job of the decade is the job of the bioengineer!" This often-repeated statement motivates students from many scientific disciplines to specialize from chemistry, physics and biology to bioengineering. Indeed, the bioengineer explores and analyses physiological and biochemical conditions of tissue and organ malfunction and profits from experiences gained here to develop sophisticated medical devices. As a result, therapeutic options for either treating diseases or ameliorating lifestyle conditions are achieved. A special and ultimate goal is to construct systems, such as artificial organs for people with organ failure. These devices represent the *Champions League* of medical device technology and require knowledge of both physiology and bioengineering. They must be planned and prepared in detail from the very beginning of development in order to guarantee their desired function, to minimize the risk of failure and/or avoid unintended clinical consequences. Developing such biosystems from concept to a marketable device requires the precise knowledge of all components and their properties, especially of device constituting polymers. In other words, bioengineering does not exclusively begin with device concepts and the outline of a design. In the early conceptual phase properties and performance profiles of polymers and plastics designated to be used must be explored and checked for their suitability for their later clinical application. This paper will address some of the main challenges related to polymer selection for medical devices.

I. Challenges for polymer application related to current and future target groups

Properties and performance of medical devices and their constituting polymers must be adapted to their intended target groups, such as patients from different continents, different gender and age. It's current knowledge, that global populations show an advanced ageing. For instance, already on October 28, 2010 the French daily newspaper *Le Monde* predicted, that among the 73,6 million population in 2060, France will register a number of 200.000 centenarians in this year. Current actual analyses show that this figure will already become true even earlier than 2060. The French example represents a trend which can also be observed in other countries of the Western hemisphere. Aged people suffer from a higher incidence for diseases and require more medical devices than the younger generation. However, simultaneously occurring changes in body physiology and comorbidities may exacerbate an easy approach to medical device design and polymer selection for these varying target groups.

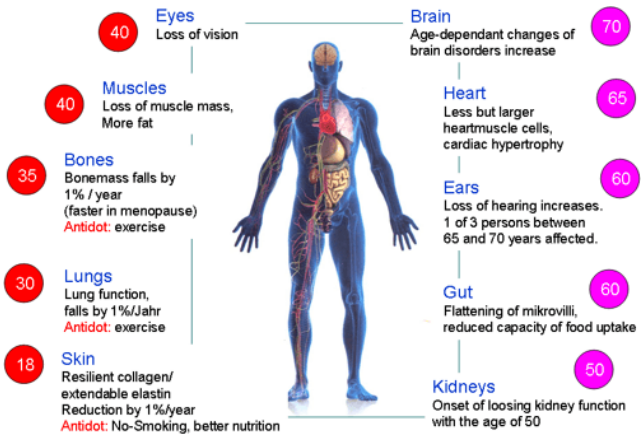

Figure 5.1.1: The ageing human body undergoes significant changes in its organ performance. Future medical devices need to be designed in such a way, that the involved polymers perform under the specific conditions of different organs accordingly and satisfactorily. Numbers in the circles refer to the onset of human failures in terms of life years.

Bioengineers, who plan and design medical devices, must anticipate those changing patient figures and should not neglect additional conditions, such as country- or continent-specific bystander diseases, local habits of administered drugs and patient compliance. Apart from pure engineering aspects, medical device performance in the final clinical application cannot be separated from polymer properties and the above- mentioned bystander conditions. This will be discussed in more detail below. Fig. 5.1.1 describes changes in organ perfor-mance related to ageing and the subsequent need for medical devices.

* Corresponding author, e-mail: *Vienken.usingen@gmail.com*

Table 5.1.1: Stability and reliability for performance of polymers during sterilisation processes.

Polymer	Steam ~134 °C	Plasma	Hot air ~180 °C	Formaldehyde	Ethylene oxide	Irradiation
PEEK	++	+	++	+	+	++
PTFE	++	+	++	+	+	+
PPS	++	+	++	+	+	++
PPSU	++	+	+	+	+	+
PES	+	+	+	+	+	+
PEI	+	+	+	+	+	+
PSu	+	+	o	+	+	+
PVDF	+	+	–	+	+	(+)
POM	(+)	+	–	+	+	o
PP	(+)	+	–	+	+	(+)
PET	o	+	–	+	+	+
PC	o	+	–	+	+	–
PMMA	+	+	+	–	–	+
Legend:	++ excellent	+ good	o limited usability		– not suitable	

Abbreviations: PEEK – Polyether ether ketone; PTFE – Polytetrafluorethylene; PPS – Polyphenylene sulfide; PPSU – Polyphenylsulfone; PES – Polyethersulfone; PEI – Polyetherimine; PSu – Polysufone; PVDF – Polyvinylidene difluoride; POM – Polyoxymethylene; PP – Polypropylene; PET – Polyethylene terephthalate; PC – Polycarbonate.

II. Physico-chemical and biological requirements

Today, an estimated 50% of all materials for medical devices consist of plastics. They have to undergo global regulatory requirements and are specifically engineered for medical use. However, when it comes to the right polymer choice for a specific medical application, problems arise due to a lack of a universally accepted definition of medical grade polymers. This becomes important when considering polymer purity, not in relation to their chemical composition but also in relation to leachable substances. Medical grade polymers are still at the discretion of the manufacturer. However, everybody selling polymers can have his own definition of what medical grade is. When choosing the material for application in medical devices, manufacturers rely on compliance with applicable standards, such as the US-American USP, Class VI, or the ISO 10993 with a mostly exclusive regard to biocompatibility of the latter. This implies in reality, that manufacturers refer to their own in-house analyses in their accompanying leaflets.

In May 2020, the new Medical Device Regulation from 2017 (MDR) will be mandatory. In addition to prescribed biocompatibility tests to be performed, this European law places a strong emphasis on risk management and safety related to polymer selection. In Annex I of the MDR it is stipulated that special attention should be paid to the choice of materials being used and their related properties. This holds especially true for their toxicity and mutual compatibility with tissues, cells, body liquids as well as with other simultaneously used plastics. It's important to note, that in all cases the intended final use of the medical device must always be considered in this process.

Summarising, there is no standardized accepted definition of medical grade plastics currently available. Manufacturers refer their qualification mostly to their own test results on possible polymer toxicity and biocompatibility, but exclude leachables. New European regulations however, require additional risk and safety analyses.

Apart from biocompatibility and toxicity pattern of polymers and plastics, their mechanical and stability properties have to be assessed either. Given that the bioengineer has a preference or a priority for a specific plastic material, this assessment has to be performed already during the early conceptual phases of device development. Polymer stability refers to both, resistances against sol-vents, acids and bases and stability during the necessary sterilization processes (e.g., Tab. 5.1.1). In case of a preference for a specific device sterilisation method, e.g., for steam, the glass transition temperature of a plastic material will play a significant role.

Polymer biostability, e.g., for implantable devices such as pacemakers, must be proven under aspects of their future clinical use. Given that polymers and devices are exposed to biologically highly active body liquids, such as blood or plasma (see below) or tissue fluids, they may suffer from a long-term and highly corrosive environment of the body. Parameters to be assessed in this regard, both for biocompatibility and biostability are outlined in a set of norms and standards published by the International Standard Organization under ISO 10993 [1,2]. Referring to Fig. 5.1.1, it is obvious, that such assessments cannot be generalized on behalf of all polymers and plastics due to their application in rather heterogeneous medical therapies [3].

Analyses for the characterisation of polymers in the early conceptual phase of a device have to involve tests on biocompatibility and biostability. Parameters for biocompatibility can be listed under aspects of protein adsorption, thrombo-genicity, stimulated immune reactions, endothelial cell and leukocyte activation and vasoactive events. They have to be assessed under the specific conditions of their intended later application. Reasoning that their blood compatibility may vary due to

differences in the manufacturing process of devices, it has become obvious, that polymers with the same name but processed by a variety of manufacturers behave differently in this respect [4].

Prominent and generally accepted definitions of the two terms are provided by the European Society of Biomaterials, such as:

1. **Biocompatibility** is the ability of a material to perform with an appropriate host response in a specific application

2. **Biostability** is the property of a substance to remain unchanged in a given biological environment.

Please allow the author to repeat: At the early conceptual phase of device development, polymer testing must be assessed under conditions of their final specific clinical application. This might even include biomaterial testing with the blood of sick patients instead of blood from healthy donors, because differences between these two test solutions have been shown [3].

Finally, safety and risk management aspects and subsequent interventions must contribute to the early assessment of polymers and plastics as a predictive tool for their selection. The new European Medical Device Regulation from 2017 [5] has set priorities on such evaluations in order to guarantee patient safety during clinical therapies.

Properties, such as mechanical and thermal stability, radiation and chemical resistance, as well as transparency (for analyses with NMR, microwaves, at high frequencies, or with γ- and X-rays) belong to the wish list of subsequent users. Last but not least, device sterilisation with ethylene oxide, steam, γ-rays and e-beam must be considered already in the early phase of polymer selection in order to prove polymer stability under sterilisation conditions. Problems may arise here given that polymers under investigation have been produced with modified biologically active surfaces, bearing e.g., immobilized antibodies, enzymes or proteins.

III. Biocompatibility and leachables from medical devices

Biocompatibility of polymers and medical devices depends on the specific application and circumstances of the material in question [3, 4]. A material may be biocompatible in one particular usage but may not be in another. In general, a material may be considered biocompatible, if it causes no harm to the host. This is distinct, however, from causing no side effects or other consequences.

Leachables from polymers or medical devices and their clinical adverse effects in patients have been neglected for a long time. In order to better understand the phenomenon of extractable material, a close look on the properties of body liquids is needed.

"Blood is a highly peculiar liquid!" stated Mephisto to Faust in the famous tragedy of J.W. Goethe written in 1775 [6]. Indeed, this also holds true for the liquid blood (plasma or serum) or other body liquids, when they come in contact with polymers or plastics. These liquids contain water, fat, electrolytes, carbohydrates, proteins, enzymes, antibodies and hormones. Consequently, liquids such as blood are capable to wet all polymer surfaces independent of their surface characteristics. In other words, artificial polymer surfaces are wet by body liquids whatever the composition of their surface is, whether it's hydrophilic, hydrophobic or showing both characteristics at a time, such as domain structures.

Wetting of polymer surfaces allows the extraction of loosely bound or not covalently-bound molecules from plastic materials. It's common knowledge, that

1. The molecular weight distribution of most polymers resembles a bell-shaped curve, i.e., that a polymer may contain both, oligomers and larger molecular weight entities surrounding a medium molecular weight.

2. During an inaccurate stoichiometric processing of polymers, redundant compounds form one or the other monomer may be present that can leach out.

This leads us to the generally accepted definition of leachables: "Chemicals that migrate spontaneously from a container-closure system, from packaging components and/or processing equipment under recommended or routine conditions of use and storage."

For many bioengineers, it's hard to believe that extractables from the polymers, from the tubes and tips they use every day could impact and even skew their experimental results. Recent reports show that chemicals used to formulate plastic materials can leach into liquid solutions with profound consequences for both, biological test assays and clinical adverse events in patents (see e.g., [7]). ISO 10993-9 describes the framework for identification and quantification of potential degradation products originating from polymers for medical application [8].

Famous examples for extractables from polymers with clinical consequences are plasticizers leaching out of PVC. Given that e.g., bags for blood transfusion are currently stored for up to 42 days, plasticizers, such as DEHP, may leach out. During that time, they may accumulate in the stored blood and may later be directly administered to the patient. Most recently it was shown that such extractables from specific polymers may act as endocrine disruptors. Because they show endocrine activity without being hormones, they are also called "exogenous hormones". Apart from the plasticizer DEHP, among those leachables are known as bis-phenols. They constitute polycarbonate (PC), polysulfone (PSu), epoxides and other polymers. Their biochemical mode of action is the interaction with receptors for sexual hormones located at the surface of cell- or nuclear membranes.

These receptors are specific for estrogen or testosterone. A binding of the hormone – or of the exogenous hormone - to the receptor exerts signals within the biological cell, such as stimulating mRNA activity or others (Fig. 5.1.2, [9]).

In order to avoid such interactions, the 3D-configuration of these molecules needs to be modified. Three approaches to avoid receptor binding have recently been realized by manufacturers of plasticizers for PVC.

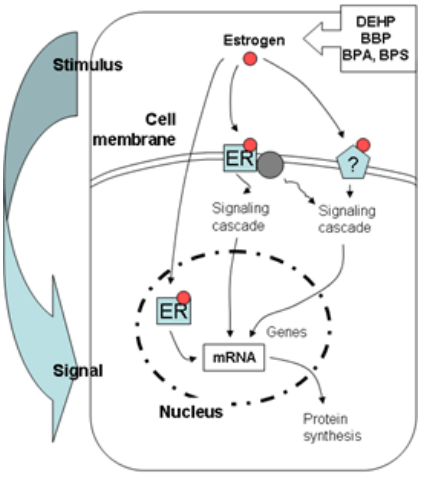

Figure 5.1.2: Artists view of a biological cell showing the mode of action of exogenous hormones. Plasticizers and Bis-phenols (e.g., DEHP, BBP and BPA, BPS) are considered to act as endocrine disruptors or exogenous hormones. They are able to interact with the respective receptors for sexual hormones and thus, stimulate uncontrollable signal cascades across the cell and nuclear membranes comparable with sexual hormones. *Abbreviations:* ER – estrogen-receptor, BBP – Benzyl butyl phthalate; DEHP: – Diethylhexyl phthalate, BPA – Bis-phenol A, BPS – Bis-phenol S (modified according to [9]).

1. The molecular weight and thus the structure of Di-ethylhexyl phthalates (DEHP, DOP) was increased by lengthening the ester moiety, from C6 (DEHP) to C9–12, achieving the nonyl- or dodecyl-ester compound. This molecule will not interact with the receptor simply due to its larger molecular weight and can be used as a plasticizer.

2. The molecular weight of Di-ethyl-hexyl-phthalates (DEHP, DOP) and by this means its molecular geometry could be further modified by a adding a third ester-group to the benzene ring of the phthalate molecule. The result is a tri-octyl-mellitate (TOTM). This molecule will not interact with the receptor either due to its larger molecular weight and change in geometry.

3. The hydration of the benzene ring in the phthalate molecule leads to a cyclohexane representing a molecule with a hook (DINCH: Di-iso-nonyl-cyclohexane). Extraction from the bulk PVC polymer is blocked and the plasticizers are unable to leach out.

Apart from specific plasticizers (DEHP, BBP), bis-phenols, such as Bis-phenol A, Bis-phenol S and others (Fig. 5.1.3) behave similarly and exert hormone-like activities. Their presence in polymers for medical devices must therefore, carefully assessed and followed by methods for their removal.

In addition to their endocrine disruptor properties, a series of recent publications have reported other related adverse effects in humans. They range from coronary artery stenosis [10], endometriosis [11], diabetes and obesity to autism (among others [10–12]). Not only Bis-phenol A must be considered to stimulate adverse events. Other

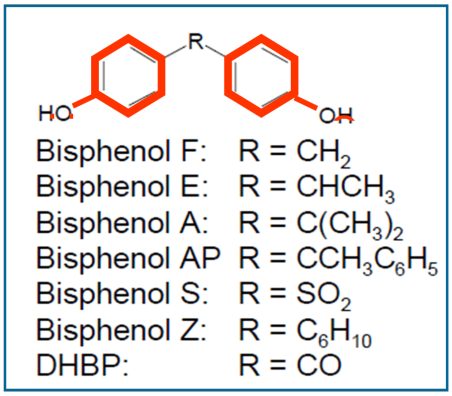

Figure 5.1.3: Bis-phenols (BPs) consist of two phenol entities brigded with a functional group. The type of the functional group determines the name of the bis-phenol. The most prominent culprit molecules are BPA and BPS, bearing a either a $-C(CH_3)_2-$ or a SO_2- group.

members of the bis-phenol family, such as BP-AF, BP-F and BP-S, are no safe alternatives for BPA [11,13]. Several legal authorities have, therefore taken action to stop their use, among them France [14] and Canada.

Summary

Bioengineers in charge of polymer selection for medical devices need to be familiar with market analyses and related changing patient profiles. When selecting a polymer for medical devices in contact with body liquids, priority should be given to their mechanical stability, biocompatibility and biostability.

Bioengineers must further anticipate and assess polymer constituents that may leach out of bulk material and originate from either non-stoichiometric polymerisation or from polymer blends. Related possible adverse events have to avoided by finding ways to minimize the amount of leachables.

References

[1] International Standard ISO 10993-1: Biological evaluation of medical devices – Part 1: Evaluation and testing within a risk management process 2009.

[2] International Standard ISO 10993-4: Biological evaluation of medical devices – Part 4: Selection of tests for interactions with blood, 2002.

[3] Braune S., Groß M., Walter M., Zhou S., Dietze S., Rutschow S., Lendlein A., Tschöpe C., Jung F.: Adhesion and activation of platelets from subjects with coronary artery disease and apparently healthy individuals on biomaterials. *J Biomed Mater Res Part B 2016*, 104:210–217.

[4] Koga Y, Fujieda H, Meguro H, Ueno Y, Aoki T, Miwa K, Kainoh M: Biocompatibility of polysulfone hemodialysis membranes and its mechanisms: Involvement of fibrinogen and its integrin receptors in activation of platelets and neutrophils, *Artif Organs*, 2018, 42:E246–258.

[5] Regulation (EU) 2017/745 of the European Parliament and of the Council of 5th April 2017 on medical devices. *Official J European Union*, 2017; L117–175.

[6] Goethe JW: Faust, the second part of the tragedy; 1775.

[7] Gerstel GmbH: Extractables and leachables analysis of IV-bag systems based on thermal extraction of materials and stir-bar sorptive extraction of aqueous solutions using GC–MS and GC–TOF-MS: Adv Pharmaceutic Anal – Oct 2018, p. 14–15.

[8] International Standard ISO 10993-9: Biological evaluation of medical devices- Part 9: Framework for identification and quantification of potential degradation products, 2009.

[9] Hewitt S, Deroo B, Korach K: A new mediator for an old hormone? *Science*, 2005; 307: 1572–1573.

[10] Shankar A, Teppala S, Sabanayagam C: Bisphenol A and peripheral arterial disease: Results from the NHANES. *Environ Health Perspect*, 2012,120:1297–1300.

[11] Jones R, Lang S, Kendziorski J, Greene A, Burns K: Use of a mouse model of experimentally induced endometriosis to evaluate and compare the effects of Bisphenol A and Bisphenol AF exposure. *Environ Health Perspect*, 2018, 26:170004.

[12] Gong H, Zhang X, Cheng B, Sun Y, Li C, Li T, Zheng L, Huang K: Bisphenol A accelerates toxic amyloid formation of human islet amyloid polypeptide: A possible link between Bisphenol A exposure and type 2 diabetes. *PLoS ONE*, 2013, 8: e54198.

[13] Eladak S, Grisin T, Moison D, Guerquin MJ, N'Tumba-Byn T, Pozzi, Gaudin S, Benachi A, Livera G, Rouiller-Fabre V, Habert R: A new chapter in the bisphenol A story: bisphenol S and bisphenol F are not safe alternatives to this compound. *Fertil Steril*, 2015, 103:11–21.

[14] ANSES (Agence Nationale de Sécurité Sanitaire, de l'Alimentation, de l'Environnement et du Travail), France: Evaluation des risques du bisphénol A (BPA) pour la santé humaine, 2012.

6 Monographic articles

6.1 Biological role of citric acid and its derivatives and their applications in medicine

Aleksandra Bandzerewicz*,[1], Anna Kołakowska[1], Agnieszka Gadomska-Gajadhur[1]

1 Faculty of Chemistry, Warsaw University of Technology, Warsaw, Poland

Keywords: *citric acid*, *metabolic regulation*, *biomaterial*, *citrate-based therapy*, *citrate biology*.

Abstract

Citric acid is one of the most important organic compounds, manufactured in great amounts every year. It is widely used in food and pharmaceutical industry alike. Still, citric acid is a fundamental metabolite first and foremost. As a intermediate in Krebs cycle citrate is present in every cell of any aerobic organism, including human. Considering the multifunctional nature of citrate chemistry and its versatile role in various tissues, it is no surprise that citrate-based therapies and biomaterials are essential part of modern medicine. Most important features of citrate biological function and medical application are outlined in this review.

Introduction

Citric acid is produced worldwide in million tons every year and is commonly known for its important role in the food industry (acidity regulator, flavouring agent). It occurs naturally in various fruits and vegetables, especially citrus fruits such as lemon, grapefruit and orange – and from lemon juice it was first isolated and crystallized. This was achieved by the Swedish chemist Carl Wilhelm Scheele in 1784. Since mid-1800s industrial-scale production was based on traditional extraction from the juice of limes and lemons. Nowadays, citric acid is mostly produced by microbial fermentation using *Aspergillus niger* [1].

For all its importance in food industry, citric acid is first and foremost a substantial part of every aerobic organism, although predominantly present in the form of a trivalent anion as citrate is an intermediate in Krebs cycle, a stage of cellular respiration [2]. Krebs cycle, also known as citric acid cycle or tricarboxylic acid (TCA) cycle, is a series of enzyme catalyzed reactions, the final common pathway connecting carbohydrate, lipid and protein metabolism. TCA cycle is the source of approximately 2/3 of total ATP (energy-carrying molecule) production in cells. It occurs in the matrix of the mitochondrion (Fig. 6.1.1) [3,4].

Several intermediates of TCA cycle serve as precursors for biosynthetic processes and/or are compounds of great physiological significance themselves, including citrate. Versatile biological functions of citrate are represented by its role in mineralization regulation, modulating neuronal excitability, anticoagulant effect etc. Citrate chemistry and biology is an important part of regenerative medicine and biomaterials engineering [4,5].

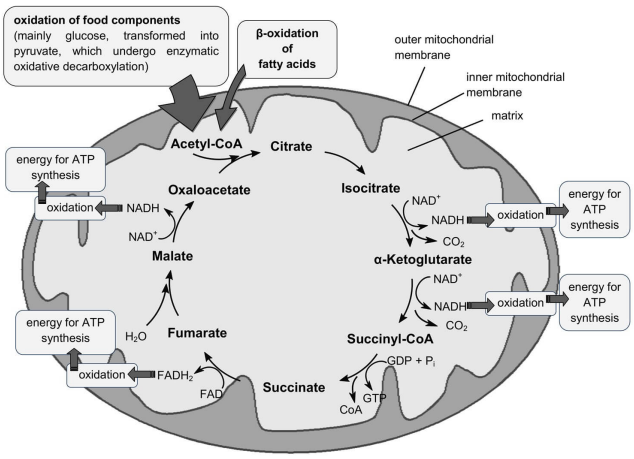

Figure 6.1.1: Krebs cycle.

Citrate and bone tissue

The importance of the relationship between citrate and bone structure

First reports of high level of citrate content of animal bones date back to 1941 [6]. Since then, amount of data regarding the relationship between citrate and bone physiology has increased abundantly, yet many questions about the basics of such a connection remain unanswered. However, it is known that citrate comprises approximately 1.6% of the bone content and represents up to 5% of its organic component. What is even more crucial, about 80% of total body citrate resides in bone. These findings clearly indicate that citrate must exhibit some essential properties necessary for development and maintenance of normal bone [7,8].

The results of recent studies confirmed that citrate is incorporated in the structure of the apatite nanocrystal/collagen complex, an organic-inorganic composite bone-building material [8–10]. The influence of citrate molecules is crucial to understand the mechanism of bone tissue development. Such a statement is based on the knowledge that approximately 1/6 of the available apatite surface area in bone is covered by citrate molecules. Due to the particular interaction with apatite nanocrystals, the citrate methylene groups are turned outward and cause the decrease in hydrophilic character of the surface, improving its compatibility with nonpolar components of collagen matrix. This may be the reason behind formation of layer-by-layer bone structure and promotion of oriented self-assembly and longitudinal growth of the nanocrystals [11]. By such interference, citrate affects bone stability, strength and resistance to fracture [8].

Still, there is a question of the source of citrate in bone and it remains unsolved. Contrary to the previous view that it is somehow derived from blood, there are reported

* Corresponding author, e-mail: *aleksandra.bandzerewicz.stud@pw.edu.pl*

evidences implying that citrate is in fact produced by osteoblasts, bone forming cells. This is possible due to the unique metabolic alteration and can be achieved by preventing citrate oxidation via Krebs cycle, as a result of limiting m-aconitase activity. This mechanism may be explained by similar inhibition of citrate oxidation demonstrated by prostate cells, based on suppressing the enzyme activity by the accumulation of zinc [6,8,12].

Citrate treatment of osteoporosis

It is a common knowledge that supplements based on combination of calcium and vitamin D3 form the basis of osteoporosis treatment and prevention – adequate intake is essential for maintaining optimal bone mass throughout life [13]. Several forms of calcium salts are available. It is necessary that the supplement must be characterised by it safety and proper tolerability. Yet it is possible that calcium supplements may increase the risk of the formation of calcium oxalate stones, although they also reduce the absorption of intestinal oxalate by binding it to calcium. Supplementing calcium with calcium citrate results in lower saturation of calcium oxalate than with calcium carbonate [14].

It was reported that taking calcium citrate between meals can lower the unfavourable effects of competition between its own absorption and that of other nutrients [14]. The solubility of calcium citrate and carbonate improve with decreasing pH value and their absorption is simplified in the presence of glucose polymers. However, a higher dependency on gastric acid secretion is reported regarding calcium carbonate than calcium citrate supplementing [15]. Some studies confirm that combining supplementation of calcium citrate with potassium citrate can reduce bone resorption in postmenopausal osteopenic women [16]. In general, using citrate-based supplements can restore mineralisation capability that has been weakened.

Citrate-based biomaterials for bone regeneration

Combination of biomaterials design, cells biology development and suitable biochemical factor forms the basis of tissue engineering, a fast-expanding field of regenerative medicine. Its main purpose is to improve, maintain or restore damaged biological tissues.

For the regeneration to be effective, it is necessary that the cells are seeded into scaffolds and thus provided means of proper cellular interactions, allowing for the formation of three-dimensional tissue structure. For obvious reasons scaffolds cannot be made from any material, but a very particular kind known as biomaterials, characterized by their good biocompatibility, specific mechanical properties and biodegradability. The last feature is demanded due to the fact that scaffold is expected to decompose after fulfilling its role in enhancing cells differentiation and growth. Therefore there is no need for a patient to undergo a surgery to remove the scaffold [17].

A variety of biodegradable polymers have been evaluated and acknowledged as new biomaterials for scaffolds development and many of them are polyesters. Citric acid-based biomaterial design dates back to 2004 and synthesis of poly(1,8-ocatanediol-co-citric acid), a biodegradable elastomer with potential for application in small-diameter blood vessels engineering [18]. However, mechanical properties of materials can be modified and tailored to imitate the structure and function of certain tissues. Bone replacements are mostly based on composites consisting of biodegradable polymers and ceramic particles. Such materials can – to some extent – mimic the real bone, as it is naturally composed of inorganic and organic compounds [19,20].

When designing a biodegradable elastomer, it is important to look for at least one multifunctional monomer. Therefore, it is possible to create a cross-linked three-dimensional structure. The concept of fabricating cross-linked polymers has been a major improvement in the biomaterial engineering, as cross-linking process can be used to modulate mechanical properties and a degradation rate of biomaterial. Thus, biodegradable elastomers can be tuned to fulfill the requirements of a specific tissue [21]. Citric acid, having three carboxyl groups and one hydroxyl group (Fig. 6.1.2), can be used as such multifunctional monomer.

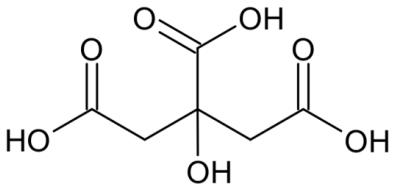

Figure 6.1.2: Citric acid.

Citrate-based polyester can be obtained by carrying out a non-solvent catalyst-free polycondensation of citric acid and diol monomers. It is a simple and cost-effective reaction, enabling ester bond formation. Polyesters undergo a biodegradation via hydrolysis. Degradation can be actively initiated by enzyme-catalyzed hydrolysis [21,22]. There is, however, a major flaw in the biodegradation process of polyesters, which is the acidic by-products. They may cause an inflammation, the response of immune system to harmful stimuli. The solution to that problem is minimizing the decrease in pH, achieved by incorporating basic salts into polyester structure [22].

Properties of citrate-based biomaterials are highly dependent on the choice of the diol component of the polyester. It was reported that material stiffness decreases (along with increasing elasticity) with increasing the length of the aliphatic diol chain (C4–C12). Materials based on longer and more hydrophobic diols display slower degradation [23]. If the diol length is further increased (C12–C16) it is possible to obtain materials capable of shape memory [5]. To synthesize polyesters characterized by increased mechanical properties and faster degradation rate simultaneously, nitrogen-containing diols (like N-methyldiethanolamine) can be used [21].

Bearing in mind that bone tissue is a natural composite of hydroxyapatite crystals and collagen matrix, the reasonable strategy of developing a biomaterial specifically for bone regeneration is to incorporate such crystals into a polymer matrix phase. It is possible to produce a composite consisting of bioceramic and polymer (poly(1,8-octanediol-co-citrate)), displaying hydroxyapatite content similar to that of the bone, which should improve osteointegration

[24]. The degradation rate can be modulated by changing the monomer ratio and adjusting the cross-linking temperature and time [18]. This is an alternative method to previously designed implants based on different polymers, such as poly-L-lacide, which were not osteoconductive [24]. Some studies confirm the long-term in vivo biocompatibility of poly(1,8-octanediol-co-citrate)/hydroxyapatite composite biomaterial. Such scaffolds are reported to support subchondral bone growth. Those are promising results indicating the possibility of the common usage of such materials as bone substitutes in the future [20].

An interesting turn in citrate-based scaffolds fabrication is developing clickable elastomers to meet the biomimetic structural requirements for bone regeneration. Using azide-alkyne cycloaddition (clickable moieties) as an auxiliary cross-linking procedure is a way of improving mechanical strength of the material while preserving pendant carboxyl groups for hydroxyapatite binding [25].

Hydroxyapatite, although the most commonly used, is not the only bioceramic suitable for a biocompatibile and biodegradable composite development. Some studies report successful fabrication of material composed of β-calcium silicate and poly(1,8-octanediol citrate). Cell proliferation tested on human osteoblasts was confirmed to be improving with increasing ceramic content. One significant feature of β-calcium silicate is its ability to cause the formation of a layer of hydroxyapatite on its surface. It was suggested that poly(1,8-octanediol citrate)/β-calcium silicate composites display potential for application in bone repairing devices [26].

Citrate biology in blood

Plasma citrate homeostasis

Many physiological activities require the homeostatic maintenance of a normal plasma citrate concentration, which means adjusting the level of the concentration to the steady optimal value. Normal human plasma citrate concentration falls within the range between 100 and 150 μM. Any disruption of the equilibrium may lead to pathophysiological status (hypocitricemia or hypercitricemia) [27].

The maintenance of the concentration of plasma citrate is a result of balancing the amount of citrate entering and being removed from the circulation. However, it is not an entirely known and understood mechanism. According to prevailing views, the source of citrate is food – it is absorbed from digestive tract. The endogenous source is cellular metabolism. The removal process consist of citrate urinary excretion and its uptake by various tissues. Nevertheless, it was reported that dietary citrate – although important when available – is not necessary to maintain optimal plasma citrate concentration. This indicates that in case of exogenous citrate source being insufficient, another sources must exist. As cellular metabolism of soft tissues does not provide plasma with an adequate amount of citrate, its major source must be bone (via bone resorption). The major factor for the removal of citrate from plasma is believed to be the renal clearance, which consists of citrate urinary excretion and reabsorption of citrate in the proximal tubule, a segment of a nephron (functional unit of the kidney). Citrate is later metabolized [5,27,28]. Some studies suggest that the plasma citrate concentration may be regulated by hormones – Parathyroid Hormone and Calcitonin – a hypercitricemic and hypocitricemic hormone respectively. However, mechanism of this regulation is yet to be established [27,29,30].

Citrate as an anticoagulant

A disturbance of the plasma citrate concentration equilibrium most likely should result in pathophysiological and clinical consequences, although still not clearly acknowledged. What is confirmed is that the connection between plasma citrate and plasma calcium exists. Blood clotting (coagulation), cardiac activity, neuromuscular irritability etc. are effected by total plasma calcium concentration and concentration of Ca^{2+} or various forms of calcium complexes. These have dependency on the amount of citrate in plasma, due to citrate calcium-chelating properties, which are the reason behind its common usage in hospitals as a anticoagulant. Therefore, the clotting cascade is inhibited [5,27].

Effective anticoagulation is essential to prevent clotting and counteract delivery failure in the extracorporeal circuit, which is the path that the hemodialysis patient's blood takes outside of their body. For example, such procedure is required during continuous renal replacement therapy (CRRT). Heparin is still the most commonly and widely used anticoagulant. Although considered effective and instantaneous in its anticoagulation, heparin is not free of its disadvantages. The major complication is increasing the risk of bleeding, in critically ill patients in particular [31,32]. Furthermore, anticoagulation with heparin may result in development of heparin-induced thrombocytopenia (condition characterized by lower than normal blood platelet count; platelets, also known as thrombocytes, are the cells that help blood clot). There is a possibility of heparin inducing an unpredictable and potentially harmful pro- and antiflammatory pathways interference [33].

Recently, as a possibly successful alternative, regional citrate anticoagulation (RCA) has been put into clinical practice, although it is not standard care yet. General acceptance of RCA is still low worldwide, but used in several countries nonetheless. RCA technique is deemed complex, difficult to steer and having high additional costs, but at the same time has a number of undeniable advantages. Comparing to heparin-based anticoagulation in CRRT, RCA prolongs circuit running time, decreases risk of bleeding complications and therefore can be the recommended choice for critically ill patients particularly [31,34].

Infusing citrate into the extracorporeal circuit is the basic principle of the RCA technique. Various citrate solutions can be used: trisodium citrate, acid-citrate-dextrose solution, isotonic citrate saline with or without citric acid. They all have different metabolic consequences, but none of them was reported to be superior for clinical practice. Chelating Ca^{2+} reduces its concentration in the extracorporeal circuit. Citrate is partially removed by dialysis or filtration [31,33].

There are, however, some limitations of using citrate as a anticoagulant agent, the main being unintended infusion of substantial quantities of citrate into the patient's blood circulatory system. The outcome of the intoxication is usually

severe hypocalcemia (low blood calcium level) and hypotension (low blood pressure), eventually leading to cardiac arrest. Another limitation is citrate accumulation as a consequence of reduction of its mitochondrial metabolism. This risk concerns especially patients with chronic liver disease whose metabolism of citrate is diminished. Even though citrate itself is not toxic, its accumulation is the cause of hypocalcemia and acidosis. Therefore, it is necessary to control calcium ion concentration in the patient's blood [33].

Citrate metabolism complications in blood transfusions

Contrary to the general conviction that transfusion of blood is safe and hardly hazardous procedure, some of its risks has been lately recognized, hence the enhancement in the guidelines strictness. One of the frequent complications after massive blood transfusion is citrate intoxication, which common symptom is metabolic alkalosis, a condition when the pH value of a tissue is elevated above the normal range (7.35–7.45). This is, again, the possible side effect of applying citrate as an anticoagulant in blood bags [35,36].

Citrate is deemed a safe anticoagulant agent, because it is under normal circumstances immediately utilized. However, considering massive amounts of blood that are currently used, the risk of citrate concentration rising to a toxic level must be administered. The citrate concentration in the patient's body results in a toxicity, when citrate turns to bind calcium ions. Still, it is not likely to occur, should the rate of transfusion be acceptable. Regarding metabolic alkalosis, it is reported to resolve after restoring normal perfusion. In general, acid-base equilibrium disturbances should be possible to handle, but the protocol of the procedure must be always strictly followed [36,37].

Citrate application in ophthalmology

Plasma citrate as a potential biomarker for glaucoma

Glaucoma is a chronic progressive disease, which results in optic nerve damage and cause vision loss. It is principally developed from an excessive intraocular pressure. In early glaucoma the diagnosis is often difficult and uncertain due to anatomical variations in optic nerve head appearance. Patients with suspected glaucoma can be monitored at appropriate frequency to eventually confirm the diagnosis. However, if some biomarkers (measurable objective indicators of normal biological processes or pathogenic processes) for glaucoma could be used, it would be great help in clinical examination and making decision of starting a treatment [38,39].

The vast majority of the molecular mechanisms contributing to the development of glaucoma still remains mostly unknown. Even so, association between the disease and certain genetic factors has been identified. Several biomarkers for glaucoma has been evaluated and reported in literature and one of them is plasma citrate level [40,41].

Studies in adult and children population report that plasma citrate concentration is significantly lower in the glaucoma-diagnosed patients compared to the normal optimal level, while there is no difference in urine citrate amount. It is generally accepted that impaired mitochondrial function is a probable indicator of glaucoma and may be contributing to its pathogenesis. Decreasing mitochondrial activity may lead to reducing citrate production, and therefore result in lower plasma citrate concentration. Krebs cycle, taking place in the matrix of the mitochondrion, is a major source of ATP production, which is essential for proper functioning of all tissues, nerves – including optic nerve – among them [38,40,42].

Other features of citrate biology

High concentration of citrate was detected in the cerebrospinal fluid of the central nervous system and is believed to be maintained by cerebella astrocytes (characteristic star-shaped brain cells) [5,43]. It is reported that astrocytes are responsible for maintaining citrate-rich equilibrium in cerebrospinal fluid, which is believed to be supporting neuron function in central nervous system. There is a possibility that neurons use extracellular citrate for energy production or glutamate synthesis, but direct evidence is lacking. However, significant amounts of citrate may be a strong indicator of a potential application of citrate-based biomaterials in spinal cord repairs [5].

Chelating properties of citrate are important in renal system – binding intestinal and urine Ca^{2+} ions prevents their precipitation and reduce calcium salts supersaturation. Citrate increase the activity of Tamm-Horsfall protein, the most abundant protein in ordinary human urine and one of the glycoproteins inhibiting formation of renal stones [5,44].

Finally, there are some evidences that citrate may be suppressing tumor growth (several tumor types, for example breast and lung) mainly by inhibiting glycolysis. It is suggested that citrate can promote a striking increase across a wide range of cytokines, resembling cytokine storm. Such results implicate some possibility of citrate-based cancer treatment [45].

Conclusions

Citrate homeostasis is crucial for a normal physiological activity of the human body. Any dysregulation may result even in clinical consequences. Many functional properties of citrate and mechanisms of its metabolic regulation are yet to be established. Multifunctional nature of citrate indicates its vast potential for medical applications, still not fully discovered. Nonetheless, continuation of research regarding citrate chemistry is expected to inspire and allow for design of new materials and implicate possible new medical treatment procedures.

Acknowledgements

The authors would like to thank the Faculty of Chemistry of the Warsaw University of Technology for providing laboratory equipment.

This scientific research was financed from the National Science Centre as a research project "Miniatura 3" (2019/03/X/ST5/01208) titled "Preparation and testing of the properties of cell scaffolds from poly(glycerol citrate)".

References

[1] Akram M., Citric Acid Cycle and Role of its Intermediates in Metabolism, *Cell Biochemistry and Biophysics*, 2014, 68, 475–478, doi:10.1007/s12013-013-9750-1.

[2] Enderle J.D., in:, *Introd. to Biomed. Eng.*, Elsevier Inc., 2011, pp. 447–508.

[3] Nazaret C., Heiske M., Thurley K., Mazat J.P., Mitochondrial energetic metabolism: A simplified model of TCA cycle with ATP production, *Journal of Theoretical Biology*, 2009, 258, 455–464, doi:10.1016/j.jtbi.2008.09.037.

[4] Akram M., Citric Acid Cycle and Role of its Intermediates in Metabolism, *Cell Biochemistry and Biophysics*, 2014, 68, 475–478, doi:10.1007/s12013-013-9750-1.

[5] Ma C., Gerhard E., Lu D., Yang J., Citrate chemistry and biology for biomaterials design, *Biomaterials*, 2018, 178, 383–400, doi:10.1016/j.biomaterials.2018.05.003.

[6] Dickens F., The citric acid content of animal tissues, with reference to its occurrence in bone and tumour, *Biochemical Journal*, 1941, 35, 1011–1023, doi:10.1042/bj0351011.

[7] Granchi D., Baldini N., Ulivieri F.M., Caudarella R., Role of citrate in pathophysiology and medical management of bone diseases, *Nutrients*, 2019, 11, doi:10.3390/nu11112576.

[8] Franklin R.B., Chellaiah M., Zou J., Reynolds M.A., Costello L.C., Evidence that osteoblasts are specialized citrate-producing cells that provide the citrate for incorporation into the structure of bone, *Open Bone Journal*, 2014, 6, 1–7, doi:10.2174/1876525401406010001.

[9] Costello L.C., Chellaiah M., Zou J., Franklin R.B., Reynolds M.A., The status of citrate in the hydroxyapatite/collagen complex of bone; and Its role in bone formation, *Journal of Regenerative Medicine and Tissue Engineering*, 2014, 3, 4, doi:10.7243/2050-1218-3-4.

[10] Hu Y.Y., Liu X.P., Ma X., Rawal A., et al., Biomimetic self-assembling copolymer-hydroxyapatite nanocomposites with the nanocrystal size controlled by citrate, *Chemistry of Materials*, 2011, 23, 2481–2490, doi:10.1021/cm200355n.

[11] Xie B., Nancollas G.H., How to control the size and morphology of apatite nanocrystals in bone, *Proceedings of the National Academy of Sciences of the United States of America*, 2010, 107, 22369–22370, doi:10.1073/pnas.1017493108.

[12] Costello L.C., Franklin R.B., Reynolds M.A., Chellaiah M., The important role of osteoblasts and citrate production in bone formation: "Osteoblast Citration" as a new concept for an old relationship, *Open Bone Journal*, 2012, 4, 27–34, doi:10.2174/1876525401204010027.

[13] Klibanski A., Adams-Campbell L., Bassford T., Blair S.N., et al., in:, *J. Am. Med. Assoc.*, vol. 285, American Medical Association, 2001, pp. 785–795.

[14] Gómez J.M.Q., Rubió J.B., Curiel M.D., Pérez A.D., Calcium Citrate and Vitamin D in the Treatment of Osteoporosis, *Clinical Drug Investigation*, 2011, 31, 285–298, doi:10.1007/bf03256927.

[15] Palermo A., Naciu A.M., Tabacco G., Manfrini S., et al., Calcium citrate: from biochemistry and physiology to clinical applications, *Reviews in Endocrine and Metabolic Disorders*, 2019, 20, 353–364, doi:10.1007/s11154-019-09520-0.

[16] Gregory N.S., Kumar R., Stein E.M., Alexander E., et al., Potassium citrate decreases bone resorption in postmenopausal women with osteopenia: A randomized, double-blind clinical trial, *Endocrine Practice*, 2015, 21, 1380–1386, doi:10.4158/EP15738.OR.

[17] Ma P.X., Scaffolds for tissue fabrication, *Materials Today*, 2004, 7, 30–40, doi:10.1016/S1369-7021(04)00233-0.

[18] Yang J., Webb A.R., Ameer G.A., Novel Citric Acid-Based Biodegradable Elastomers for Tissue Engineering, *Advanced Materials*, 2004, 16, 511–516, doi:10.1002/adma.200306264.

[19] Wei G., Ma P.X., Structure and properties of nano-hydroxyapatite/polymer composite scaffolds for bone tissue engineering, *Biomaterials*, 2004, 25, 4749–4757, doi:10.1016/j.biomaterials.2003.12.005.

[20] Chung E.J., Kodali P., Laskin W., Koh J.L., Ameer G.A., Long-term in vivo response to citric acid-based nanocomposites for orthopaedic tissue engineering, *Journal of Materials Science: Materials in Medicine*, 2011, 22, 2131–2138, doi:10.1007/s10856-011-4393-5.

[21] Tran R.T., Yang J., Ameer G.A., Citrate-Based Biomaterials and Their Applications in Regenerative Engineering, *Annual Review of Materials Research*, 2015, 45, 277–310, doi:10.1146/annurev-matsci-070214-020815.

[22] Woodard L.N., Grunlan M.A., Hydrolytic Degradation and Erosion of Polyester Biomaterials, *ACS Macro Letters*, 2018, 7, 976–982, doi:10.1021/acsmacrolett.8b00424.

[23] Yang J., Webb A.R., Pickerill S.J., Hageman G., Ameer G.A., Synthesis and evaluation of poly(diol citrate) biodegradable elastomers, *Biomaterials*, 2006, 27, 1889–1898, doi:10.1016/j.biomaterials.2005.05.106.

[24] Qiu H., Yang J., Kodali P., Koh J., Ameer G.A., A citric acid-based hydroxyapatite composite for orthopedic implants, *Biomaterials*, 2006, 27, 5845–5854, doi:10.1016/j.biomaterials.2006.07.042.

[25] Guo Y., Tran R.T., Xie D., Wang Y., et al., Citrate-based biphasic scaffolds for the repair of large segmental bone defects, *Journal of Biomedical Materials Research - Part A*, 2015, 103, 772–781, doi:10.1002/jbm.a.35228.

[26] Shirazi F.S., Moghaddam E., Mehrali M., Oshkour A.A., et al., In vitro characterization and mechanical properties of b-calcium silicate/POC composite as a bone fixation device, *Journal of Biomedical Materials Research - Part A*, 2014, 102, 3973–3985, doi:10.1002/jbm.a.35074.

[27] C Costello L., Plasma Citrate Homeostasis: How It Is Regulated; And Its Physiological and Clinical Implications. An Important, But Neglected, Relationship in Medicine, *Human Endocrinology*, 2016, 1, 1–8, doi:10.24966/he-9640/100005.

[28] Hamm L.L., in:, Kidney Int., vol. 38, Elsevier, 1990, pp. 728–735.

[29] Franklin R., Costello L.C., Stacey R., Stephens R., Calcitonin effects on plasma and urinary citrate levels in rats, *American Journal of Physiology*, 1973, 225, 1178–1180, doi:10.1152/ajplegacy.1973.225.5.1178.

[30] Wong G.L., Kent G.N., Ku K.Y., Cohn D. V., The Interaction of Parathormone and Calcium on the Hormone-Regulated Synthesis of Hyaluronic Acid and Citrate Decarboxylation in Isolated Bone Cells, *Endocrinology*, 1978, 103, 2274–2282, doi:10.1210/endo-103-6-2274.

[31] Kindgen-Milles D., Brandenburger T., Dimski T., Regional citrate anticoagulation for continuous renal replacement therapy, *Current opinion in critical care*, 2018, 24, 450–454, doi:10.1097/MCC.0000000000000547.

[32] Van De Wetering J., Westendorp R.G.J., Van Der Hoeven J.G., Stolk B., et al., *Heparin Use in Continuous Renal Replacement Procedures: The Struggle Between Filter Coagulation and Patient Hemorrhage*, 1996.

[33] Oudemans-van Straaten H.M., Ostermann M., Bench-to-bedside review: Citrate for continuous renal replacement therapy, from science to practice, *Critical Care*, 2012, 16, doi:10.1186/cc11645.

[34] Morgera S., Schneider M., Slowinski T., Vargas-Hein O., et al., A safe citrate anticoagulation protocol with variable treatment efficacy and excellent control of the acid-base status, *Critical Care Medicine*, 2009, 37, 2018–2024, doi:10.1097/CCM.0b013e3181a00a92.

[35] Pochet J.M., Laterre P.F., Jadoul M., Devuyst O., Metabolic alkalosis in the intensive care unit, *Acta Clinica Belgica*, 2001, 56, 2–9, doi:10.1179/acb.2001.002.

[36] Li K., Xu Y., Citrate metabolism in blood transfusions and its relationship due to metabolic alkalosis and respiratory acidosis, *International Journal of Clinical and Experimental Medicine*, 2015, 8, 6578–6584.

[37] Lima S.K., Begum M., Gupta A.K., Aziz L., Mitra S., Management of Massive Blood Transfusion-a case study, *Pulse*, 2014, 5, 39–43, doi:10.3329/pulse.v5i1.20189.

[38] Fraenkl S.A., Muser J., Groell R., Reinhard G., et al., Plasma citrate levels as a potential biomarker for glaucoma, *Journal of Ocular Pharmacology and Therapeutics*, 2011, 27, 577–580, doi:10.1089/jop.2011.0062.

[39] Garway-Heath D.F., Early diagnosis in glaucoma, *Progress in Brain Research*, 2008, 173, 47–57, doi:10.1016/S0079-6123(08)01105-9.

[40] Michalczuk M., Tadeusz P., Urban B., Anna W., Bakunowicz-Łazarczyk A., Plasma citrate concentration: A possible biomarker for glaucoma in children, *BMJ Paediatrics Open*, 2017, 1, doi:10.1136/bmjpo-2017-000023.

[41] Colligris B., Crooke A., Gasull X., Escribano J., et al., Recent Patents and Developments in Glaucoma Biomarkers, Recent Patents on Endocrine, *Metabolic & Immune Drug Discovery*, 2012, 6, 224–234, doi:10.2174/187221412802481739.

[42] Michalczuk M., Urban B., Porowski T., Wasilewska A., Bakunowicz-Łazarczyk A., Citrate usage in the leading causes of blindness: new possibilities for the old metabolite, *Metabolomics*, 2018, 14, doi:10.1007/s11306-018-1377-1.

[43] Sonnewald U., Westergaard N., Krane J., Unsgård G., et al., First direct demonstration of preferential release of citrate from astrocytes using [13C]NMR spectroscopy of cultured neurons and astrocytes, *Neuroscience Letters*, 1991, 128, 235–239, doi:10.1016/0304-3940(91)90268-X.

[44] Krieger N.S., Asplin J.R., Frick K.K., Granja I., et al., Effect of potassium citrate on calcium phosphate stones in a model of hypercalciuria, *Journal of the American Society of Nephrology*, 2015, 26, 3001–3008, doi:10.1681/ASN.2014121223.

[45] Ren J.G., Seth P., Ye H., Guo K., et al., Citrate Suppresses Tumor Growth in Multiple Models through Inhibition of Glycolysis, the Tricarboxylic Acid Cycle and the IGF-1R Pathway, *Scientific Reports*, 2017, 7, 1–13, doi:10.1038/s41598-017-04626-4.

6.2 Emulsions as vehicles for the controlled release of astaxanthin in topical application

Michał Dymek*,1, Elżbieta Sikora[1]

1 Faculty of Chemical Engineering and Technology, Cracow University of Technology, Cracow, Poland

Keywords: *astaxanthin*, *release kinetics*, *skin delivery systems*, *emulsions*, *antioxidant activity*.

Abstract

In the work, the antioxidant activity of astaxanthin (AST) and the influence of the base formulation on the kinetics of AST release were studied. Three stable O/W AST-loaded emulsions, differing in the internal phase droplet size (12.7 µm (E1), 3.8 µm (E2), 3.2 µm (E3)) and a nanoemulsion (0.13 µm, NE) were prepared. The results confirmed very strong antioxidant activity of AST. The emulsion internal phase droplet size did not significantly affect the AST release. The amount of released AST was respectively: 13.60% (E1), 11.42% (E2), 9.45% (E3), 9.71% (NE). The best fit to experimental data was obtained using the Higuchi model for emulsions and the Korsmeyer-Peppas model for NE. The results show that the AST release process is limited by the diffusion through carriers and the prepared O/W emulsions can be used as vehicles for the controlled delivery of AST to the skin.

Introduction

Modern cosmetics serve a comprehensive care for the skin due to the content of different active ingredients. Among others they show moisturizing, anti-wrinkle, anti-oxidant and anti-aging properties or protect skin against UV radiation. One such ingredient that is gaining popularity is astaxanthin (AST). AST is a hydrophobic, dark red substance, belonging to the xanthophyll group, found in nature in aquatic organisms, such as microalgae, shrimps, crabs and salmon, both in free and esterified form [1–3]. On an industrial scale, it is obtained from *Haematococcus pluvialis* microalgae, which is contains up to 3–5% of astaxanthin in dry matter [4]. AST is obtained using supercritical CO_2 extraction of algae or from food industry waste materials, such as shrimp residues, which allows obtaining AST without the risk of its decomposition [5,6]. The most important properties of astaxanthin, from cosmetics point of view, are its strong free radical scavenging abilities related to the presence of conjugated double bonds in its molecule [1]. Its antioxidant activity are similar to butylhydroxyanisole, a synthetic cosmetic antioxidant ingredient [7]. Compared to other carotenoids, such as canthaxanthin or β-carotene, AST has a stronger antiradical activity, that is why it is popularly called the "queen of carotenoids" [8]. Used as a cosmetic ingredient, astaxanthin protects skin against harmful UVA radiation, reducing transepidermal water loss (TEWL) and reducing wrinkles [9]. Also taken orally, AST reduces wrinkles ("crow's feet") and hyperpigmentation changes, increasing skin elasticity [10]. Its protective effect against oxidative stress [11] and inflammation are also observed [12]. Additionally, AST accelerates wound healing and prevents scab formation [13], and also protects against the development of burn wounds [14].

It is commonly known, that the efficiency of cosmetics is related to the effective delivery of the active substance from the cosmetic to the skin [15]. There are several reports in the literature studying the influence of the carrier (base formulation) on AST release. Lee et al. studied release of astaxanthin from nanoporous silicified-phospholipids assembled boron nitride complex [16]. Effect of particle size on astaxanthin release from ethyl cellulose carriers were analyzed by Tirado et al. [17]. Shanmugapriya and co-authors tested combined O/W nanoemulsions, prepared by spontaneous or ultrasonic emulsification, as carriers of AST [18]. Stable over a wide temperature range complexes of AST with cyclodextrins are also described [19].

Still there is not sufficient number of studies dealing with influence of carriers on the release of AST from different dermal delivery systems. The aim of this study was to investigate the effect of the emulsion droplets size on the kinetics of AST release.

Materials and Methods

Materials

The supercritical CO_2 *Haematococcus pluvialis* microalgae extract containing astaxanthin (Algalif Astaxanthin 5%) was kindly supplied by Algalif (Iceland). HPLC grade astaxanthin standard was purchased from Sigma-Aldrich. The emulsion ingredients were of cosmetic grade. Crodamol GTCC, Natragem EW-FL, Tween 20, Tween 80 and Arlacel 2121 were kindly supplied from Croda Poland. Borage and black cumin oil were purchased from Olvita sp. z o.o. Vitamin E was provided by DSM Nutritional Products. All other chemicals aspotassium dihydrogen phosphate (POCh), sodium hydrogen phosphate (POCh), sodium persulfate (POCh) were of analytical grade. Deionised water, filtered through a Milli-Q system, was used for the aqueous phase of the emulsion.

Radical scavenging capacity assay

In order to determine the antioxidant properties, a modified ABTS (2,2′-azino-bis(3-ethylbenzothiazoline-6-sulfonic acid)) radical scavenging capacity assay [20] was used. |SI7.4mM aqueous solution of ABTS and 2.6 mM aqueous solution of $Na_2S_2O_8$ were mixed in a 1:1 volume ratio and stored at 8 °C for 12 hours in the dark. Next, 5.5 cm^3 of the solution was taken out and mixed with 60 cm^3 of ethanol. The antioxidant properties assays were carried out for AST standard (chemically pure), for the AST containing extract (Algalif) and for vitamin E. An appropriate amount of each sample: AST standard and algae extract, containing approximately 0.001 g of AST, was mixed with 5 cm^3 of ethanol and then shaken (Vortex) for 15 minutes. Additionally, the mixture of ethanol and 0.001 g of vitamin E was prepared in order to

* Corresponding author, e-mail: *michal.dymek@doktorant.pk.edu.pl*

Table 6.2.1: Composition of prepared formulations.

Name of ingredients	INCI name of ingredients	Content (% wt.)			
		E1, E2	E3	NE	O1
Water	Aqua	76	76	80	–
Crodamol GTCC	Caprylic/Capric Triglyceride	15	–	2	98
Natragem EW–FL	Glyceryl Stearate (and) Polyglyceryl-6 Palmitate /Succinate (and) Cetearyl Alcohol	4.5	4.5	–	–
Arlacel 2121	Sorbitan Stearate (and) Sucrose Cocoate	2.5	2.5	–	–
Algalif Astaxanthin 5%	Helianthus Annuus Seed Oil (and) Astaxanthin	2	2	2	2
Borage oil	Borago Officinalis Seed Oil	–	7.5	–	–
Black cumin oil	Nigella Sativa Seed Oil	–	7.5	–	–
Tween 80	Polysorbate 80	–	–	16	–

compare its antioxidant properties with the AST sample. Afterwards, 2.85 cm^3 of ABTS solution was mixed with 0.15 cm^3 of each of the test samples (ethanolic solutions containing AST or vitamin E) or 0.150 cm^3 of ethanol (as a reference sample). After 2 hours from the initiation of the reaction with the radical for each of the mixtures the absorbance measurements were performed using NANOCOLOR UV-VIS spectrophotometer (Macherey-Nagel), at a wavelength of 734 nm. The degree of ABTS radical inhibition (ABTS scavenging ability) was calculated using the formula (6.2.1):

$$I_{\%} = \frac{(A_k - A_p)}{A_k} \cdot 100\% \qquad (6.2.1)$$

where: A_k – absorbance of the reference sample, A_p – absorbance of the test sample.

Study of the surface tension of oils

For capric-caprylic triglycerides (O1) and a mixture (1:1, w/w) of borage and black cumin oils (O2), to estimate the oils polarity, the surface tension was measured by a tensiometric method. Measurements were carried out at a constant temperature of 25 °C, using a STA-1 Sinterface Technologies tensiometer equipped with Du Nouy platinum ring system. The result was the average of 10 measurements.

Preparation of emulsions

As the cosmetic bases (astaxanthin carriers containing 0.1 %wt of AST) O/W emulsions differing in droplet sizes (E1, E2) or in applied oils (E3) as well as a nanoemulsion system (NE) were prepared. Additionally, as a reference sample (O1), Crodamol GTCC was used. The composition of the obtained formulations are presented in Tab. 6.2.1.

In order to prepare the formulations, the appropriate amount of water and emulsifier (Arlacel 2121) was placed into a beaker and dispersed using a magnetic stirrer (IKA C-MAG HS 7), at temperature $T = 65$ °C.

Next, the ingredients of the oil phase: Natragem EW-FL, Algalif Astaxanthin 5% extract and, depending on the type of sample, Crodamol GTCC or a mixture of naturals oils (black cumin and borage oils) were weighed in a separate beaker and mixed at the same, as the water phase, temperature. In the next stage, both phases were mixed using a high shear homogenizer (CAT Unidrive X 1000) by pouring the water phase into the oil phase and homogenizing the mixture for 6 minutes. The E1 emulsion was homogenized at 3500 rpm, the E2 and E3 emulsions were homogenized at 11 000 rpm. After preparing, all samples were stored at room temperature. NE was obtained by the phase inversion composition (PIC) method [21]. First the active was dissolved in the oil/surfactant mixture. The appropriate amount of polysorbate 80, Crodamol GTCC and Algalif Astaxanthin 5% was weighed and shaken using Vortex shaker (IKA) for 15 minutes until a homogeneous mixture was obtained. Water was then added dropwise to the oil/surfactant/AST mixture while shaking continuously, until a clear/transparent formulation was obtained. O1 was prepared by dissolving suitable amount of the algae extract in Crodamol GTCC, at 65 °C.

Particle size measurements and stability study

The average size of oil droplets in the emulsions (E1, E2, E3) were measured by an optical microscope, Motic B1, equipped with digital camera and connected to a digital image processing software. One drop of each formulation was applied to a microscope slide, then covered with a coverslip to form a thin layer of the samples. The emulsions droplets were observed through an objective lens of 40X magnification. In case of the nanoemulsion, the average size and size distribution of droplets were measured by means of dynamic light scattering method (DLS), using a particle size analyzer Malvern Zetasizer Nano-Z/S, at $T = 25$ °C. For each sample, three replicates were performed. The stability of the formulations was studied by the centrifugal method and freeze/thaw stability (FTS) study [22]. Samples of the emulsions and nanoemulsion were placed in a heat dish of a centrifuge and spun at 3500 rpm for 10 minutes. Next, the formulations were visually inspected for any changes in their texture. During FTS test the emulsions and nanoemulsion were placed for 24 hours, at minus temperature ($T < -10$ °C) followed by $T = 40$ °C to determine the

effect that freezing and subsequent thawing has upon the stability of the formulations. The studies were conducted with three cycles.

Study of rheological properties

The rheological measurements were carried out using Brookfield Model R/S Plus rheometer equipped with the plate-cone system (C-25-2). Measurements were carried out three times for each formulation, in the shear rate range of 1–500 s^{-1}, at 25 °C, during 50 seconds. Each time a 2 cm^3 sample of the formulation was placed on the measuring plate.

Release studies

AST release kinetics studies were carried out using Spectra/Por RC dialysis bags, at the temperature of 32 °C. Three repetitions were made for each of the samples. The dialysis bags were filled with about 3 g of the prepared formulations and placed in a thermostatic chamber filled with a solution (99.5 / 0.5; w/w) of phosphate buffer (PBS) of pH = 7.40 and polysorbate 20 – in order to increase the solubility of astaxanthin in hydrophilic acceptor solution [23]. The concentration of released AST was determined by use of Macherey-Nagel UV-vis spectrophotometer, at $\lambda = 480$ nm, on the basis of the previously prepared calibration curve of absorbance, A, as a function of AST concentration, C_{AST} ($A = 0.0086 \cdot C_{AST} - 0.0015$; $R^2 > 0,999$). The analysis of the obtained results was made by linear regression for four models: zero and first order [24], Higuchi [25–28] and Korsmeyer-Peppas [25,29].

Results and discussion

Radical scavenging capacity assay

The results of ABTS radical scavenging capacity assay are presented in Tab. 6.2.2.

Table 6.2.2: ABTS radical scavenging capacity assay results.

Sample	ABTS scavenging ability (%)
AST standard	34.49
AST extract (Algalif)	99.74
Vitamin E	89.16

The data presented in Tab. 6.2.2. proved that SC-CO_2 *Haematococcus pluvialis* extract containing 5% of astaxanthin is characterized by very good antioxidant properties, stronger than vitamin E (89.16% of ABTS inhibition), deactivating the ABTS radical almost in 100%. Pure AST standard (Sigma-Aldrich) showed much weaker antioxidant properties. The clearly stronger radical scavenging effect of the AST containing extract than chemically pure substance may result from the synergistic effect of the astaxanthin and the other carotenoid esters present in the algae extract. The mixture of the actives eliminate free radicals more effectively [30].

Emulsions and oils characterization and stability

Three stable O/W AST-loaded emulsions and a nanoemulsion (Tab. 6.2.1) were prepared using different process parameters, as described in the experimental part, in order to obtain emulsions differing in droplet size of the internal phase (Tab. 6.2.4). The emulsions E1 and E2 have this same composition, in the case of the E3 the oil phase consisted of natural oils (borage and black cumin oils). In the case of the nanoemulsion (NE) and the E1 and E2 emulsions, caprylic/capric triglycerides (Crodamol GTCC) were used. As a reference sample, astaxanthin dissolved in capric/caprylic triglycerides was prepared. The oils surface tension measurement results are shown in Tab. 6.2.3.

Table 6.2.3: Surface tension of O1 and O2 oil phases.

Oil mixture	Surface tension ± SD ($n = 10$) (mN/m)
O1	23.96 ± 0.01
O2	29.27 ± 0.06

As the polarity of oils has a direct influence on their interfacial tension (the higher the interfacial tension, the lower the oil polarity) [31], caprylic/capric triglycerides (O1) are more polar than the mixture of borage and black cumin oils (O2).

Optical micrographs of the emulsions (Fig. 6.2.1) revealed, as expected, that E2 emulsion, prepared with high-shear homogenization (11000 rpm), was a dispersion with droplets considerably smaller than those of E1 emulsion, which was obtained by lower-shear homogenization (3900 rpm). In the case of the emulsion E1, the low-shear homogenization process effect on the irregular shape of the droplets. The mean droplet size of E1, E2 and E3, calculated from a population of 600 droplets, was 12.7, 3.8 and 3.2 µm respectively. The average droplet size of the nanoemulsion was determined by dynamic light scattering (DLS, Tab. 6.2.4).

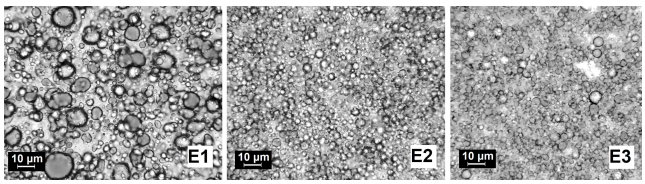

Figure 6.2.1: Microscopic photos of E1, E2, E3 emulsions.

The data presented in Tab. 6.2.4. revealed that the use of higher homogenizer rotation frequencies resulted in a decrease in the mean diameter of the droplets of the emulsions internal phase. Consequently, it is possible to obtain formulations with more uniform droplet sizes (lower SD), which may additionally increase their stability [32]. No significant difference was observed between the average droplet diameter of the emulsions containing oil phases of different polarity. DLS studies confirmed that the NE complies with the requirements for nanometric scale cosmetic products ($d = 0.130$ µm) [33], and was also characterized by a low value of the polydispersity index (PDI = 0.276).

To sum up, the values of droplet size were considered sufficiently different to detect a possible effect of droplet size on AST release. Concerning stability, the formulations

Table 6.2.4: Droplet sizes of the prepared formulations.

Formulation	Homogenizer rotational speed (rpm)	Mean diameter ± SD (n = 600) (μm)
E1	3900	12.7 ± 3.1
E2	11000	3.8 ± 1.0
E3	11000	3.2 ± 1.0
NE	–	0.130 (PDI = 0.276)

remained practically unchanged after the centrifugal tests and FTS study. The obtained results indicate that the formulations and the procedure used to prepare them were appropriate for the skin permeation studies. In the next stage of the research the rheological properties were established for the prepared AST-loaded formulations (Fig. 6.2.2).

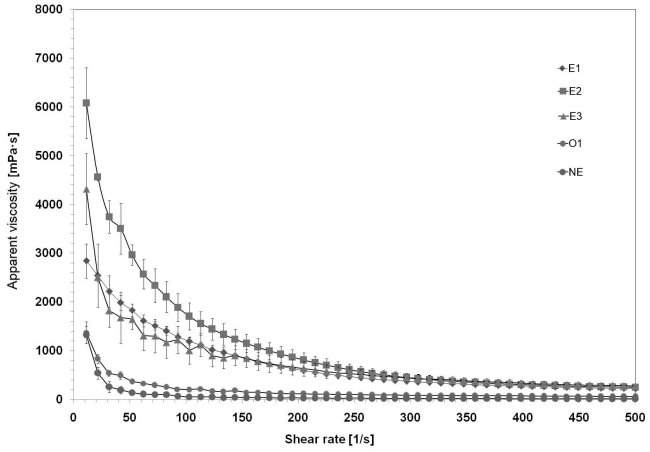

Figure 6.2.2: Viscosity curves of the prepared formulations (T = 25 °C). Values are expressed as mean ± SD (n = 3).

All of the prepared formulations were non-Newtonian, shear thinning fluids. Parameters of the homogenization process influence on the samples viscosity, with an increase of rotation frequencies the products viscosity also increases. For example, at the shear rate of 100 s^{-1}, the viscosity of E_1 emulsion was 1100 mPa s while in the case of E_2 – 1700 mPa s.

AST release studies

The in vitro release profiles of astaxanthin from the prepared emulsions (E1, E2, E3), nanoemulsion (NE) and the oil phase (O1) as the control sample are shown at Fig. 6.2.3. The amount of the active in all studied carriers was 0.1% wt. As it can be observed, the obtained profiles were similar and no significant differences in the percentage of the actives release at 24h were detected between formulations (13.60 ± 0.95%, 11.42 ± 0.75%, 9.46 ± 0.36%, 9.80 ± 0.13%, 7.68 ± 0.15% for E1, E2, E3, NE, O1, respectively). These differences are not significant from the cosmetic point of view.

The obtained results indicate that the droplet size of the emulsions does not influence the astaxanthin release from the carriers. This is confirmed even in the case of NE, despite the lowest droplet size of the internal phase (0.130 μm), after 24 hours released amount of AST was only slightly smaller than in the case of emulsions (d_{E1} = 12.7 μm ± 3.1 μm, d_{E2} = 3.8 μm ± 1.0 μm, d_{E3} = 3.2 μm ± 1.0 μm). On the other hand, comparing the amount of astaxanthin released from the E2 and E3 emulsions, similar in internal droplets size but differing in polarity of oil phase (23.96 ± 0.01 and 29.27 ± 0.06 mN/m for O1 and O2 respectively), we can conclude that the higher release rate of AST is related to the higher polarity of hydrophobic substances [34], as the oil phase of E2 (caprylic/capric triglycerides, O1) is more polar than the oil phase of E3 emulsion (the mixture of borage and black cumin oils, O2). The lowest amount of AST (7.68% ± 0.15 %wt) was released from the oil (O1). In the case of the reference sample we can explain it by a much higher affinity of AST to capric-caprylic triglycerides. However, the absence of significant differences observed between astaxanthin release from the prepared formulations could be explained by a residence of the actives at the lipid phase and/or at the lipid-rich interface [34,35].

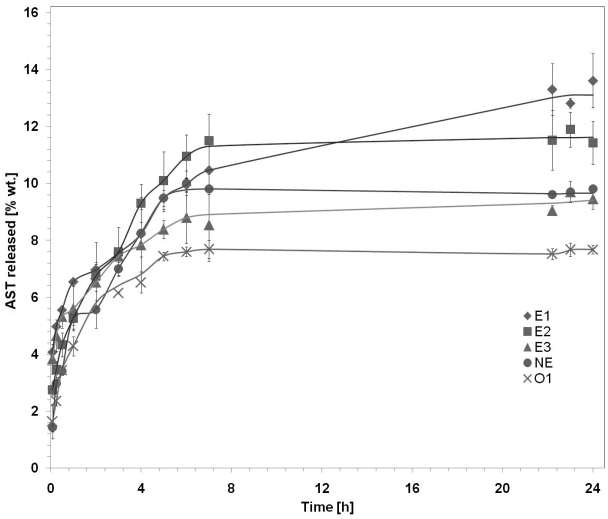

Figure 6.2.3: Release profiles of astaxanthin from the nanoemulsion (NE), O/W emulsions (E1, E2, E3) and oil solution (O1). Values are expressed as mean ± SD (n = 3).

In order to better understand the mechanism of AST release from the prepared carriers, a mathematical analysis was performed by fitting the most appropriate kinetic model. As in consumer conditions it is rare to keep an applied cosmetic for 24 hours on the surface of the skin, the calculations were made for the first 7 hours of the experiment, which was considered optimal. Among many mathematical models, the zero (equation 6.2.2) and first order (equation 6.2.3), Higuchi (equation 6.2.4) and Korsmeyer-Peppas (equation 6.2.5) models were selected to describe the release process. Systems with a constant mass exchange surface with an acceptor solution, for substances that are poorly soluble in water and penetrate not very quickly, usually show a good fit with the zero-order model. Moreover, it proves that the concentration of the active ingredient

Table 6.2.5: The kinetic model parameters for the release results.

Kinetic model	Parameter	Formulation				
		E1	E2	E3	NE	O1
Zero-order	R^2	0.9541	0.9663	0.8995	0.9173	0.7957
	$K \cdot 10^3$ (h^{-1})	8.40	1.24	6.60	1.15	8.10
First-order	R^2	0.8903	0.8772	0.8381	0.7355	0.7957
	$K \cdot 10^1$ (h^{-1})	1.17	1.88	1.04	2.23	1.80
Higuchi	R^2	0.9798	0.9960	0.9782	0.9833	0.9164
	$K \cdot 10^2$ ($h^{-0.5}$)	2.55	3.77	2.07	3.55	2.58
Korsmeyer-Peppas	R^2	0.9710	0.9839	0.9854	0.9848	0.9698
	$K \cdot 10^2$ (h^{-n})	6.49	5.68	6.00	4.45	4.17
	n	0.210	0.334	0.190	0.433	0.360

is kept constant, in contrast to the first-order model [24]. Higuchi's model is based on Fick's first law and is used in the description of the kinetics of release from emulsions and ointments, where the process is limited by the diffusion of the substance through the carrier, and the release itself is rather fast [25–28]. The Korsmeyer-Peppas model is an exponential model of release kinetics, used mainly to describe the behaviour of pharmaceutical systems, in which the physical interpretation of the mechanism is related to the value of the n parameter appearing in the equation [25,29].

$$\frac{M}{M_0} = K_0 \cdot t \tag{6.2.2}$$

$$\ln \frac{M}{M_0} = K_1 \cdot \mathrm{t} \tag{6.2.3}$$

$$\frac{M}{M_0} = K_H \cdot t^{0.5} \tag{6.2.4}$$

$$\frac{M}{M_0} = K_{KP} \cdot t^n \tag{6.2.5}$$

where: M – mass of released AST; M_0 – initial AST mass in the support; t – time; n – exponent characteristic for specific diffusion mechanisms; K_0 – constant for the zero-order kinetics model; K_1 – constant for the first order kinetics model; K_H – constant for the Higuchi model; K_{KP} – constant for the Korsmeyer-Peppas model.

The kinetic model parameters for the release results are shown in Tab. 6.2.5.

According to the results presented in the Tab. 6.2.5, it can be observed that the best fit of AST release from E1, E2, E3 emulsions and the O1 oil phase of the emulsion was obtained for the Higuchi model. Although for the E3 and O1 formulations a slightly better fit was achieved by the Korsmeyer-Peppas model, the values of the characteristic exponent n are much lower than the value of 0.45 (0.190 and 0.360, respectively). Due to this fact they do not fit into the original assumptions of this model [36] and therefore the description of the release mechanism from E3 and O1 carriers by Korsmeyer-Peppas model was abandoned. A good fit with the Higuchi model for emulsion formulations ($R^2 > 0.978$) proves that the AST release process is controlled by diffusion through the carrier. This relationship may also explain the lack of correlation between the greater dispersion of the internal phase of the emulsion and the greater degree of AST release. The lower viscosity of E1 (1189 mPa s) than E2 (1703 mPa s) seems to have a major influence on the transport of the active ingredient. Smaller droplets provide a larger mass exchange surface (E2, E3), but the higher rotational frequencies of the homogenizer needed to achieve desirable droplet sizes also increase the matrix viscosity, which makes it difficult for them to migrate to the mass transfer boundary layer, which is the cellulose membrane. It can therefore be assumed that in this case the matrix – acceptor solution penetration is fast, and the whole process is controlled by diffusion through the carrier, so the formulations with lower viscosities and larger droplet sizes (E1) achieve higher AST release rates.

NE can best be described using the Korsmeyer-Peppas model ($R^2 > 0.98$). The obtained value of the n parameter ($n = 0.433$) for it is close to the characteristic value of 0.45 in this model [36], which proves that the mechanism of AST release from NE is related to the classic Fick diffusion. At the same time, the good fit with the zero-order model for O/W emulsions ($R^2 > 0.95$) indicates that it was possible to obtain carriers providing a constant concentration of the active ingredient in the skin and the possibility of controlled release of AST. The results are consistent with the data provided by H.S. Lee et al. [16] for AST encapsulated in tetraethyl orthosilicate modified liposomes, where the release process was controlled by its diffusion through the carrier and fits the zero-order model.

Conclusions

During the study, stable O/W emulsion systems were obtained, showing the behaviour of non-Newtonian fluids, a O/W nanoemulsion and an oil formulation - containing AST at a concentration of 0.1 %w/w. The astaxanthin extracted from the SC-CO_2 *Haematococcus pluvialis* microalgae used in this study was characterized by very good antioxidant properties, inactivating the ABTS radical in almost 100%. The emulsion internal phase droplet size did not significantly affect the amount of released AST, which for the prepared formulations was respectively: 13.60% (E1), 11.42% (E2), 9.45% (E3), 9.71% (NE) and 7.68% (O1). Release kinetics studies, supported by calculations for four popular mathematical models, showed that the process of AST

release from the O/W emulsions is limited by diffusion through the carrier, which is probably directly related to the viscosity of the medium. For the emulsion, the best fit was achieved for the Higuchi model, and for the nanoemulsion – the Korsmeyer-Peppas model. For each cosmetic matrix prepared, the amount of released AST was greater than that of the base oil. Research shows that the emulsion bases used are very good carriers for the controlled release of astaxanthin, which, combined with its excellent ability to scavenge free radicals, can be used in modern deeply caring and anti-aging cosmetics.

Acknowledgments

Special acknowledgements to Dr. Haraldur Gardarsson and Algalif Iceland ehf. for providing free samples of the astaxanthin extract, without which the presented research would not have been possible.

References

[1] Guerin M., Huntley M. E., Olaizola M., Haematococcus astaxanthin: applications for human health and nutrition, *Trends in Biotechnology*, 2003, 21, 5, 210-216, doi:10.1016/S0167-7799(03)00078-7

[2] Lorenz R.T., Cysewski G.R., Commercial potential for Haematococcus microalgae as a natural source of astaxanthin, *Trends in Biotechnology*, 2000, 18, 4, 160–167, doi:10.1016/s0167-7799(00)01433-5

[3] Higuera-Ciapara I., Félix-Valenzuela L., Goycoolea F.M., Astaxanthin: A Review of its Chemistry and Applications, *Critical Reviews in Food Science and Nutrition*, 2006, 46, 2, 185–1965, doi:10.1080/10408690590957188

[4] Chekanov K. , Lobakova E., Selyakh I., Semenova L., Sidorov R., Solovchenko A., Accumulation of astaxanthin by a new Haematococcus pluvialis strain BM1 from the white sea coastal rocks (Russia), *Marine Drugs*, 2014, 12, 8, 4504-4520, doi:10.3390/md12084504

[5] ReyesF.A., Mendiola J.A., Ibañez E., del Valle J.M., Astaxanthin extraction from Haematococcus pluvialis using CO2 - expanded ethanol, *The Journal of Supercritical Fluids*, 2014, 92, 75-83, doi:10.1016/j.supflu.2014.05.013

[6] Radzali S.A., Baharin B.S., Othman R., Markom M., Rahman R.A., Co-solvent Selection for Supercritical Fluid Extraction of Astaxanthin and Other Carotenoids from Penaeus monodon Waste, *Journal of Oleo Science*, 2014, 63, 8, 769-777, doi:10.5650/jos.ess13184

[7] Sila A., Ayed-Ajmi Y., Sayari N., Nasri M., Martinez-Alvarez O., Bougatef A., Antioxidant and Antiproliferative Activities of Astaxanthin Extracted from the Shell Waste of Deep-water Pink Shrimp Parapenaeus longirostris, *The Natural Products Journal*, 2013, 3, 2, 82-89, doi:10.2174/2210315511303020002

[8] Chang C-S., Chang C-L., Lai G-H., Reactive oxygen species scavenging activities in a chemiluminescence model and neuroprotection in rat pheochromocytoma cells by astaxanthin, beta-carotene and canthaxanthin, *Kaohsiung Journal of Medical Sciences*, 2013, 29, 8, 412-421, doi:10.1016/j.kjms.2012.12.002

[9] Komatsu T., Sasaki S., Manabe Y., Hirata T., Sugawara T., Preventive effect of dietary astaxanthin on UVA-induced skin photoaging in hairless mice, *PLoS ONE*, 2017, 12, 2, doi:10.1371/journal.pone.0171178

[10] Tominaga K., Hongo N., Karato M., Yamashita E., Cosmetic benefits of astaxanthin on humans subjects, *Acta Biochimica Polonica*, 2012, 59, 1, 43-47, doi:10.18388/abp.2012_2168

[11] Al-Bulish M.S.M., Xue C., Waly M.I., Xu J., Wang Y., Tang Q-J., The Defensive Role of Antioxidants Astaxanthin against Oxidative Damage in Diabetic Rats Injected with Streptozotocin, *Journal of Food and Nutrition Research*, 2017, 5, 3, 191-196, doi:10.12691/jfnr-5-3-9

[12] Chew W., Mathison B., Kimble L., Mixter P.F., Chew B.P., Astaxanthin Decreases Inflammatory Biomarkers Associated with Cardiovascular Disease in Human Umbilical Vein Endothelial Cells, *American Journal of Advanced Food Science and Technology*, 2013, 1, 1-17, doi:10.7726/ajafst.2013.1001

[13] Meephansan J., Rungjang A., Yingmema W., Deenonpoe R., Ponnikorn S., Effect of astaxanthin on cutaneous wound healing, Clinical, *Cosmetic and Investigational Dermatology*, 2017, 10, 259–265,doi:10.2147/CCID.S142795

[14] Fang Q, Guo S, Zhou H, Han R, Wu P, Han C., Astaxanthin protects against early burn-wound progression in rats by attenuating oxidative stress-induced inflammation and mitochondria-related apoptosis, *Scientific Reports*, 2017, 7, doi:10.1038/srep41440

[15] Sikora E., Miastkowska M., Lasoń E., Chapter in a book: *Sub-micron vehicles of biologically active substances*, Selected skin delivery systems, Wydawnictwo PK, 2020

[16] Lee H.S., Sung D.K., Kim S.H., Choi W.I., Hwang E.T., Choi D.J., Chang J.H., Controlled release of astaxanthin from nanoporous silicified-phospholipids assembled boron nitride complex for cosmetic applications, *Applied Surface Science*, 2017, 424, 1, 15–19, doi:10.1016/j.apsusc.2017.03.036

[17] Tirado D.F., Palazzo I., Scognamiglio M., Calvo L., Porta G.D., Reverchon E., Astaxanthin encapsulation in ethyl cellulose carriers by continuous supercritical emulsions extraction: A study on particle size, encapsulation efficiency, release profile and antioxidant activity, *The Journal of Supercritical Fluids*, 2019, 150, 128-136, doi:10.1016/J.SUPFLU.2019.04.017

[18] Shanmugapriya K., Kim H., Saravana P. S., Chun B. S., Kang H. W., Astaxanthin-alpha tocopherol nanoemulsion formulation by emulsification methods: Investigation on anticancer, wound healing, and antibacterial

effects, *Colloids and Surfaces B: Biointerfaces*, 2018, 172, 1, 170–179, doi:10.1016/j.colsurfb.2018.08.042

[19] Yuan C., Du L., Jin Z., Xu X., Storage stability and antioxidant activity of complex of astaxanthin with hydroxypropyl-beta-cyclodextrin, *Carbohydrate Polymers*, 2013, 91, 1, 385–389, doi:10.1016/j.carbpol.2012.08.059

[20] Re R., Pellegrini N., Proteggente A., Pannala A., Yang M., Rice-Evans C., Antioxidant activity applying an improved ABTS radical cation decolorization assay, *Free Radical Biology and Medicine*, 1999, 26, 9–10, 1231-1237, doi:10.1016/s0891-5849(98)00315-3

[21] Jaworska M., Sikora E., Zielina M., Ogonowski J., Studies on the formation of O/W nano-emulsions, by low-energy emulsification method, suitable for cosmeceutical applications, *Acta Biochimica Polonica*, 2013, 60, 4, 779-782

[22] Sikora E., Chapter in a book: Stability study of cosmetic emulsions, *Cosmetic emulsions*, Wydawnictwo PK, 2019

[23] Chen Z., Li W., Shi L., Jiang L., Li M., Zhang C., Peng H., Kidney-targeted astaxanthin natural antioxidant nanosystem for diabetic nephropathy therapy, *European Journal of Pharmaceutics and Biopharmaceutics*, 2020, 156, 143-154,doi:10.1016/j.ejpb.2020.09.005

[24] Costa P., Sousa Lobo J.M., Modeling and comparison of dissolution profiles, *European Journal of Pharmaceutical Sciences*, 2001, 13, 2, 123–133, doi:10.1016/s0928-0987(01)00095-1

[25] Dash S., Murthy P.N., Nath L., Chowdhury P., Kinetic modeling on drug release from controlled drug delivery systems, *Acta Poloniae Pharmaceutica – Drug Research*, 2010, 67, 3, 217-223.

[26] Higuchi T., Rate of Release of Medicaments from Ointment Bases Containing Drugs in Suspension, Journal of Pharmaceutical Sciences, 1961, 50, 10, 874-875, doi:10.1002/jps.2600501018

[27] Higuchi T., Mechanism of Sustained- Action Medication Theoretical Analysis of Rate of Release of Solid Drugs Dispersed in Solid Matrices, *Journal of Pharmaceutical Sciences*, 1963, 52, 12, 1145-1149, doi:10.1002/jps.2600521210

[28] Petropoulos J.H., Papadokostaki K.G., Sanopoulou M., Higuchi's equation and beyond: Overview of the formulation and application of a generalized model of drug release from polymeric matrices, *International Journal of Pharmaceutics*, 2012, 437, 1-2,178–191, doi:10.1016/j.ijpharm.2012.08.012

[29] Peppas N. A.,Sahlin J.J., A simple equation for the description of solute release. III. Coupling of diffusion and relaxation, *International Journal of Pharmaceutics*, 1989, 57, 2, 169-172, doi:10.1016/0378-5173(89)90306-2

[30] Régnier P., Bastias J., Rodriguez-Ruiz V., Caballero-Casero N., Caballo C., Sicilia D., Fuentes A., Maire M., Crepin M., Letourneur D., Gueguen V., Rubio S., Pavon-Djavid G., Astaxanthin from Haematococcus pluvialis Prevents Oxidative Stress on Human Endothelial Cells without Toxicity, *Marine Drugs*, 2015, 13, 5, 2857-2874, doi:10.3390/md13052857

[31] El-Mahrab-Robert M., Rosilio V., Bolzinger M. A., Chaminade P., Grossiord J. L., Assessment of oil polarity: Comparison of evaluation methods, *International Journal of Pharmaceutics*, 2008, 348, 1-2, 89–94, doi:10.1016/j.ijpharm.2007.07.027

[32] Okonogi S.,Riangjanapatee P., Physicochemical characterization of lycopene-loaded nanostructured lipid carrier formulations for topical administration, *International Journal of Pharmaceutics*, 2015, 478, 2, 726-735, doi:10.1016/j.ijpharm.2014.12.002

[33] Aboofazeli R., Nanometric-Scaled Emulsions (Nanoemulsions), *Iranian Journal of Pharmaceutical Research*, 2010, 9, 4, 325–326

[34] Sikora E., Llinas M., Garcia-Celma M. J., Escribano E., Solans C., Transdermal delivery of forskolin from emulsions differing in droplet size, *Colloids and Surfaces B: Biointerfaces*, 2015, 126, 541–545, doi:10.1016/j.colsurfb.2015.01.008

[35] Izquierdo P., Wiechers J. W., Escribano E., García-Celma M. J., Tadros T. F., Esquena J., Dederen J. C., Solans C., A Study on the Influence of Emulsion Droplet Size on the Skin Penetration of Tetracaine, *Skin Pharmacology and Physiology*, 2007, 20, 5, 263–270, doi:10.1159/000106076

[36] Ritger P.L., Peppas N.,A simple equation for description of solute release I. Fickian and non-fickian release from non-swellable devices in the form of slabs, spheres, cylinders or disco, *Journal of Controlled Release*, 1987, 5, 1, 23-36, doi:10.1016/0168-3659(87)90034-4

6.3 Inulin and inulin acetate: obtaining, properties and applications – a basic review

Anna Kołakowska*,1, Aleksandra Bandzerewicz[1], Paweł Ruśkowski[1]

1 Faculty of Chemistry, Warsaw University of Technology, Warsaw, Poland

Keywords: *inulin*, *inulin acetate*, *inulin ester*.

Abstract

Inulin is described in this work: its structure, sources, process in which the saccharide is obtained, physical and chemical properties and inulin's applications in food industry, medicine, cosmetics and technology. Inulin acetate, one of inulin's esters, is described: syntheses proposed in literature (with conditions such as solvents, catalysts, temperature, duration). Ester physicochemical properties and applications in medicine and technology are reviewed. Potential applications in cosmetics and food industry are also mentioned.

Introduction

Saccharides are a group of organic compounds necessary for the proper functioning of living organisms. They are used as a spare material, often also building blocks, of basic structural and functional units of organisms – cells. More than 200 years ago, a substance known today as inulin was discovered in water left over from the boiling of elecampane (*Inula helenium*). Inulin is a polysaccharide of plant origin, that stands out from other commonly used polysaccharides, such as cellulose or starch, due to unusual structure. Structure also influences the properties of its derivatives, including esters. Inulin esters, a large group of compounds with various properties and a huge number of potential applications, is not yet widely described. The aim of the study is to introduce basic information about inulin and, more importantly, inulin acetate: means of obtaining, properties, industrial applications. As far as we know inulin acetate is not yet widely studied, but due to its properties it could become a valued and commonly used compound for example in medicine or cosmetics.

1. Inulin

Inulin is a linear polysaccharide consisting of up to 60 rings of fructofuranose [1] connected by β-1,2-glycosidic bonds [2]. The number of units forming a sugar chain depends on the plant of origin and the way it is obtained and purified. Inulin ends with either glucopyranose (GF) or fructose (F) unit (Fig. 6.3.1) [3].

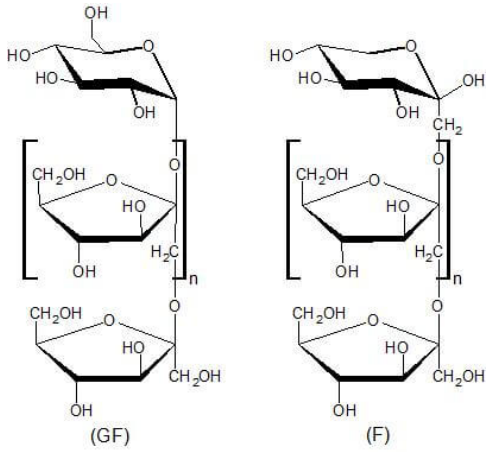

Figure 6.3.1: Inulin's structure.

1.1 Source and extraction

Inulin was discovered in 1804 by a German scientist Valentin Rose [4]. In 1817 Thomas Thomson named the saccharide and described its basic physicochemical properties [5]. Nowadays inulin is mainly obtained from chicory roots (*Cichorium intybus*) and sunflower tubers (*Helianthus tuberosus*) [6], but can be found in many other plants, for example the Jerusalem artichoke, dahlia, garlic, leeks, or bananas [7]. The process of industrial obtaining of inulin is similar to that of sugar beet in sugar production (Fig. 6.3.2). Firstly, roots or tubers are cleaned with water and sliced. Plants cannot be heated because inulin hydrolyses partially as a result of drying. The next step is hot water extraction at 60–90 °C. An industrially used extractant, i.e. water, is cheap and is not detrimental to the environment. The elevated temperature increases the solubility of saccharide. The plant pulp remaining after extraction is dried out and used as an additive to animal feed or as crop fertilizer. Filtration and purification of the extract is conducted in order to remove proteins, pectin and other plant components. To purify the extract, liming and carbonization are carried out in a high pH environment (to prevent inulin acidic hydrolysis). This way raw inulin is obtained, which can undergo fractionation to a short- and long-chain inulin if required. To purify raw inulin calcium and magnesium compounds are added, alternatively activated carbon can be used. Demineralization is carried out using cationic and anionic ion exchangers. The solution is carefully filtered, then concentrated and spray-dried [8–10].

Alternatively, inulin can be obtained in enzymatic synthesis. Bacterial enzyme fructosyltransferase can be used to obtain fructates from sucrose, this enzyme is present in some Gram-positive bacteria species, e.g: *Streptococcus mutans*, *Leuconostoc citreum* or *Lactobacillus reuteri*. These enzymes catalyze two types of reactions: transglycosylation (the elongation of saccharide chains) and sucrose hydrolysis. For industrial production of enzymatic inulin, enzymes of *Bacillus* sp.217C-11 bacteria can be used. The resulting saccharide is characterized by the presence of shorter chains (up to 30 monomers), better solubility in water, lower viscosity than the one obtained from plants [11,12].

* Corresponding author, e-mail: *01123540@pw.edu.pl*

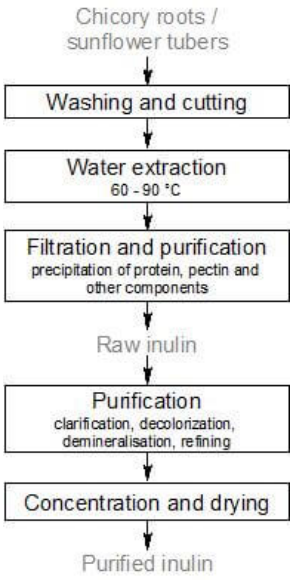

Figure 6.3.2: Process of obtaining inulin from chicory roots or sunflower tubers.

1.2 Properties

Inulin of plant origin is a white odorless powder, characterized by a faint, sweet taste. It is non-toxic. Melting temperature of inulin is 165–183 °C, it degrades above 200 °C. Water solubility of sugar depends on the degree of polymerization (DP), which is different for different plants of origin. At room temperature solutions up to 10% can be obtained, at higher temperatures inulin solubility increases. Inulin dissolves in DMSO, is almost insoluble in isopropanol and is not dissolved in ethanol, which is used to precipitate this saccharide [1,8,13].

Flexibility of inulin is higher than that of other polysaccharides because of β-1,2-glycosidic bonds – only one of carbon atoms forming this bond belongs to the furanose ring, which reduces the skeleton stiffness. Saccharide can end either with glucopyranose (GF inulin) or fructose (F inulin). Inulin F has reducing properties. A hexagonal ring chain ending reduces the chemical activity of the compound [14]. Hydrolysis of β-1,2-glycosidic bonds can occur at low pH at room temperature or at slightly acidic pH at elevated temperature. As a result of decomposition sugars are formed, mainly fructose, glucose and sucrose [15].

Due to hydroxyl groups of hydrophilic nature and a non–rigid, hydrophobic skeleton, inulin has surfactant properties. In aqueous solutions with high concentration (>25% standard inulin or >15% long chain inulin), it can form stable gels [8,14].

Inulin solutions are characterized by low viscosity at room temperature. This property may be affected by several variables. Viscosity increases with temperature or saccharide molecular weight and decreases with salt concentration in a solution [1].

Inulin has a low calorific value. It cannot be hydrolyzed by the human body because no inulinase enzymes are produced. This means that the saccharide passes through most of the digestive system almost unchanged. It is only in the large intestine, which contains *Bifidobacterium* sp., that the sugar is broken down mostly into short–chain carboxylic acids (including propionic and butyric acid), bacterial biomass and gases. Only acids can be are absorbed in the large intestine and subsequently metabolized in the liver. This is a less effective way of obtaining energy than when directly digesting sugars, hence the low calorific value of inulin [3,8,14].

Inulin has prebiotic properties – it supports the development of intestinal bacterial microflora, while inhibiting the growth of undesirable bacteria. Positive changes in the composition of intestinal bacterial flora can be observed even with small dietary changes (replacing 15 g of sucrose with the same mass of inulin every day for 15 days) [16].

1.3 Industrial applications

Due to its relatively easy and cheap production process, and occasionally unique properties, inulin is a desirable compound in various industries. It is used as an additive to food industry products, a prebiotic in medicine, a surfactant compound in the cosmetic industry. It is also an important substrate in the processes of obtaining inulin derivatives.

Food industry

Inulin is a dietary fiber and is not broken down by the human body into simple sugars, and as a result the saccharide has a reduced caloric value, so products enriched with this sugar can be used in dietetics as slimming aids. Its consumption does not affect blood glucose levels or insulin secretion, so it is used in diets for diabetics [17,18].

Solutions of inulin can be used as a fat substitute. Such fat–free additives are mainly found in dairy products (such as yoghurts, cheeses), meat products (such as sausages) and baked goods [1]. Cakes in which fats have been partially replaced by inulin do not lose their flavor and have a lower calorie content [19].

After adding inulin to most of the popular gelling agents, e.g. agar, gelatin, strengthening the action of gelling agents, increasing rigidity and stability of emulsions and foams are observed. Saccharide can be used as a fat-reducing stabilizer in ice cream, sandwich cheese and mayonnaise [20].

Medicine

Inulin is biochemically inert, non-toxic and indigestible by the humans. It can be used for urinary system tests. Intravenously introduced inulin is quickly excreted by the kidneys, with no metabolic processes or absorption in the renal tubules. The speed of such a process determines whether the kidney filtration processes are correct. Inulin can also be used as a carrier of active substances in medications targeting the urinary tract [14].

A diet rich in inulin may reduce the risk of developing cancer, especially colorectal cancer. This is due to prebiotic properties: saccharide selectively supports the growth of bacterial colonies in the large intestine, especially *Bifidobacterium infantis*, which produces cancer cell growth inhibitors [14,21].

Inulin has been shown to form stable dispersive systems with some drugs, improving solubility and assimilability. Inulin is also used in the production of ointments for wound healing and herpes, where it is an auxiliary ingredient. Due to its non-toxicity, simple purification process

and postvaccination-response enhancing properties, inulin is suggested as an adjuvant of preventive vaccines [9,22,23].

Cosmetics

Inulin used in cosmetics stabilizes emulsions, improves consistency and is also an emollient. It dissolves completely in washing detergents, improving stability of obtained solutions. The addition of saccharide reduces the risk of skin irritation caused by the detergent. The presence of hydrophilic and hydrophobic groups provides inulin with surfactant properties, making it a biodegradable alternative to ionic surfactants in cosmetics such as shampoos, conditioners and gels. Saccharide can also be used in soaps and antibacterial gels [24–26].

Technology

Obtained from plants in simple processes which do not require toxic solvents, inulin is a biodegradable and environmentally friendly raw material. Inulin derivatives often retain its positive properties. The saccharide undergoes many chemical modifications, the reactions carried out include: hydrolysis (total and partial), esterification, etherification, methylation and many others [3,27].

2. Inulin acetate

Hydroxyl groups present in the inulin rings may undergo an esterification reaction forming inulin esters. Dozens of scientific papers on inulin have been published. Although a much broader subject, inulin esters are less known and described. In this the work, we have tried to collect the most important information on inulin acetate.

2.1 Syntheses

Inulin acetate is mostly obtained in a reaction of inulin and acetic acid anhydride under different conditions (Tab. 6.3.1). It could be potentially synthesized in similar reactions to that of other esters, e.g. in reaction with carboxylic acid chloride or transesterification with carboxylic acids. Microemulsion methods are also used, in which the esters are dispersed in an inulin solution or in molten sugar [28,29].

To conduct the reaction one needs to first dissolve the inulin in a solvent (if used in a reaction) and add the acetic anhydride and a catalyst. As the solvents pyridine and dimethylformamide (DMF) are used, sodium acetate or ion exchange resin are used as catalysts. Solvents and catalysts are not used in every recipe, and occasionally the solvent also acts as a catalyst. The mixture should be intensively mixed and, depending on the reaction temperature, heated. The duration of the reaction is usually 24 h, though in 100 °C that time is reduced extremely, to just half an hour. After the reaction, ester is precipitated using a non-solvent (water), filtered and washed away from inulin residues and others. The washing liquid is removed by freeze-drying. The pure inulin acetate is obtained in the form of powder.

2.2 Properties

To the best of our knowledge, properties of inulin acetate were not yet widely researched and described. Inulin acetate is obtained as a white, odorless powder. It is insoluble in water and has hydrophobic properties. It is soluble in organic solvents such as methanol, ethanol, acetone, chloroform and other. The melting point of inulin acetate is reported as 87–92 °C, much lower than inulin. Its ester is biodegradable [32,33].

2.3 Industrial applications

Inulin acetate can be used both as a drug carrier and an adjuvant in vaccines. Its decomposition results in products that are non-toxic for human body: inulin and acetic acid. In the acylation reaction of water-soluble inulin with acetic anhydride, inulin acetate microparticles were obtained, later used as immunoactive polymers, closing the sample antigen, which is presented to the immune system. It has been proven that the inulin ester can be recognized as a pathogen by the antigen presenting cells, which trigger an appropriate immune response [31].

The emulsifying properties of inulin acetate have been previously researched. It causes good emulsion stability, though more research is required [33]. This feature makes this ester likely to be used as an emulsifier, similarly to inulin, in cosmetics or food industry.

The ester can also be used as a material for the production of capsules to enclose colon medicines. In order for medicinal substances contained in colorectal medications, e.g. mesalazine, to work effectively, the capsule compounds must not be digested in the organs of the digestive system preceding the colon. Acylation of inulin increases its resistance to the reduction caused by enzymes produced by the bacterial microflora of the large intestine. Inulin acetate is also a better drug carrier than unmodified inulin, due to the longer release time at the target site (an inulin capsule released mesalazine for 6 h, an inulin acetate capsule for 52 h) [34,35].

Inulin acetate succinate has been researched for the production of microspheres used as drug carriers. Such ester is biodegradable, hydrolysis of ester bonds occurs without the presence of enzyme catalyzing the decomposition, and results in non-toxic products: inulin, acetic acid and succinic acid. The microsphere formed from such material has the ability to release the medicine enclosed inside it [32].

Inulin acetate, as other inulin esters, can be used as a substitute for esters of other polysaccharides. Inulin esters are characterized by better solubility in water and thus, easier processing than esters of other polysaccharides, such as cellulose. Cellulose esters are used as additives to improve the moisture resistance of paper or adhesives in the paper industry and additives in the food industry. It is therefore expected that inulin esters could be used in these industries. Sheets made of cellulose acetate with the addition of inulin esters show less hardness and greater flexibility than sheets without additives [28].

Table 6.3.1: Inulin acetate syntheses conditions.

	Catalyst	Solvent	Temp. (°C)	Duration (h)	Washing with	Yield	Lit.
1	Ion exchange resin (acidic form)	–	100	0,5	Water	30%	[28]
2	–	Pyridine	25	24	Ethyl acetate, water	85%	[28]
3	CH_3COONa (0,1% v/w)	DMF	40	24	Water	~98%	[30,31]
4	CH_3COONa (0,5% w/w)	DMF	40	24	Diethyl ether	–	[32]

Conclusion

Inulin, a well-known polysaccharide of plant origin, is a commonly used compound, easily obtained and widely utilized in the food industry (as low calorie sweetener, emulsifier), medicine (urinary system examination, prebiotic), cosmetics industry (emulsifier, surfactant), chemical industry (reaction substrate for obtaining derivatives such as esters).

Inulin acetate, the ester of inulin and acetic acid, is usually obtained in reactions with acetic anhydride, either in the presence or in absence of a catalyst or solvent. Multiple research is being conducted on applications of inulin acetate in medicine (as drug carriers, adjuvant) or technology (replacement for other polysaccharides acetates). Because of its properties, inulin acetate could also become popular compound in cosmetics or a food emulsifier. Even though the ester is not yet popular, inulin acetate may prove to be an important, widespread compound in the future.

Acknowledgments

The authors would like to thank the Faculty of Chemistry of Warsaw University of Technology for providing laboratory equipment.

References

[1] Mensink M.A., Frijlink H.W., Van Der Voort Maarschalk K., Hinrichs W.L.J., Inulin, a flexible oligosaccharide I: Review of its physicochemical characteristics, *Carbohydrate Polymers*, 2015, 130, 405–419, doi:10.1016/j.carbpol.2015.05.026.

[2] Lewis D.H., Nomenclature and diagrammatic representation of oligomeric fructans — a paper for discussion, *New Phytologist*, 1993, 124, 583–594, doi:10.1111/j.1469-8137.1993.tb03848.x.

[3] Stevens C. V., Meriggi A., Booten K., Chemical modification of inulin, a valuable renewable resource, and its industrial applications, *Biomacromolecules*, 2001, 2, 1–16, doi:10.1021/bm005642t.

[4] Boeckner L.S., Schnepf M.I., Tungland B.C., in:, *Adv. Food Nutr. Res.*, vol. 43, 2001, pp. 1–63.

[5] Thomson T., A system of chemistry., London, 1817.

[6] Heinze T., Liebert T., Koschnella A., *Estrification of Polysaccharides*, Springer Laboratory, 2006.

[7] Kokubun S., Ratcliffe I., Williams P.A., Synthesis, characterization and self-assembly of biosurfactants based on hydrophobically modified inulins, *Biomacromolecules*, 2013, 14, 2830–2836, doi:10.1021/bm4006529.

[8] Franck A., *Inulin*, CRC Press Taylor & Francis Group, 2006.

[9] Chyc M., Ogonowski J., in:, 2014, pp. 719–732.

[10] Gupta A.K., Kaur N., Kaur N., Preparation of inulin from chicory roots, *Journal of Scientific and Industrial Research*, 2003, 62, 916–920.

[11] Ozimek L.K., Kralj S., van der Maarel M.J.E.C., Dijhuizen L., The levansucrase and inulosucrase enzymes of Lactobacillus reuteri 121 catalyse processive and non-processive transglycosylation reactions, *Microbiology*, 2006, 152, 1187–1196, doi:10.1099/mic.0.28484-0.

[12] Wada T., Sugatani J., Terada E., Ohguchi M., Miwa M., Physicochemical characterization and biological effects of inulin enzymatically synthesized from sucrose, *Journal of Agricultural and Food Chemistry*, 2005, 53, 1246–1253, doi:10.1021/jf048711u.

[13] Petkova N., Denev P., Methods for Determination of Inulin, *Monograph of 4rd European Young Engineers Conference 2015*, 2015, 135, doi:10.13140/RG.2.1.1790.4088.

[14] Barclay T., Ginic-Markovic M., Cooper P., Petrovsky N., Inulin - A versatile polysaccharide with multiple pharmaceutical and food chemical uses, *Journal of Excipients and Food Chemicals*, 2010, 1, 27–50.

[15] Blecker C., Fougnies C., Van Herck J.C., Chevalier J.P., Paquot M., Kinetic study of the acid hydrolysis of various oligofructose samples, *Journal of Agricultural and Food Chemistry*, 2002, 50, 1602–1607, doi:10.1021/jf010905b.

[16] Gibson G.R., Beatty E.R., Wang X.I.N., Cummings J.H., Oligofructose and Inulin, *Gastroenterology*, 1995, 975–982.

[17] Root H.F., Baker M.L., Inulin and artichokes in the treatment of diabetes, *Archives of Internal Medicine*, 1925, 36, 126–145, doi:10.1001/archinte.1925.00120130129012.

[18] Aidoo R.P., Depypere F., Afoakwa E.O., Dewettinck K., Industrial manufacture of sugar-free chocolates - Applicability of alternative sweeteners and carbohydrate polymers as raw materials in product development, *Trends in Food Science and Technology*, 2013, 32, 84–96, doi:10.1016/j.tifs.2013.05.008.

[19] Żbikowsa A., Rutkowska J., Possibility of Partial Replacement of Fat By Inuline in Cookies in Order To

Decrease Their Caloric Value, *Polish journal of food and nutrition sciences*, 2008, 58, 113–117.

[20] Franck A., Technological functionality of inulin and oligofructose, *British Journal of Nutrition*, 2002, 87, S287–S291, doi:10.1079/bjn/2002550.

[21] Taper H.S., Roberfroid M.B., Possible adjuvant cancer therapy by two prebiotics - Inulin or oligofructose, *In Vivo*, 2005, 19, 201–204.

[22] Visser M.R., Baert L., Klooster G. van t, Schueller L., et al., Inulin solid dispersion technology to improve the absorption of the BCS Class IV drug TMC240, *European Journal of Pharmaceutics and Biopharmaceutics*, 2010, 74, 233–238, doi:10.1016/j.ejpb.2009.10.004.

[23] Silva D.G., Cooper P.D., Petrovsky N., Inulin-derived adjuvants efficiently promote both Th1 and Th2 immune responses, *Immunology and Cell Biology*, 2004, 82, 611–616, doi:10.1111/j.1440-1711.2004.01290.x.

[24] Nizioł-Łukaszewska Z., Bujak T., Wasilewski T., Szmuc E., Inulin as an effectiveness and safe ingredient in cosmetics, *Polish Journal of Chemical Technology*, 2019, 21, 44–49, doi:10.2478/pjct-2019-0008.

[25] Levecke B., Booten K., Cosmetic Rinse-off Compositions Comprising Inulin-Type Fructan. EP 1 541 117 A1, 2005.

[26] Phong L., White D.W., Sturm M.A., Antimicrobial Foam Hand Soap Comprising Inulin or an Inulin Surfactant. US 7,803,746 B2, 2010.

[27] Kays S.J., Nottingham S.F., *Biology and Chemistry of Jerusalem Artichoke*, CRC Press, 2007.

[28] Begli H., Kunz M., Scheiwe L., Application F., et al., Aliphatic Carboxylate Esters of Inulin (United States Patent). 5,877,144, 1999.

[29] Rogge T.M., Stevens C. V., Facilitated synthesis of inulin esters by transesterification, *Biomacromolecules*, 2004, 5, 1799–1803, doi:10.1021/bm049869q.

[30] Tummala H., Kumar S., Kesharwani S.S., Kuppast B., Bakkari M.A., Pathogen-mimicking vaccine delivery system designed with a bioactive polymer (inulin acetate) for robust humoral and cellular immune responses, *Journal of Controlled Release*, 2017, 261, 263–274, doi:10.1016/j.jconrel.2017.06.026.

[31] Kumar S., Kesharwani S.S., Kuppast B., Rajput M., et al., Discovery of inulin acetate as a novel immune-active polymer and vaccine adjuvant: synthesis, material characterization, and biological evaluation as a toll-like receptor-4 agonist, *Journal of Materials Chemistry B*, 2016, 4, 7950–7960, doi:10.1039/C6TB02181F.

[32] Wu X.Y., Lee P.I., Preparation and characterization of inulin ester microspheres as drug carriers, *Journal of Applied Polymer Science*, 2000, 77, 833–840, doi:10.1002/(SICI)1097-4628(20000725)77:4<833::AID-APP17>3.0.CO;2-4.

[33] Petkova N., Arabadzhieva R., Vassilev D., Gencheva G., et al., Physicochemical characterization and antimicrobial properties of inulin acetate obtained by microwave-assisted synthesis, *Journal of Renewable Materials*, 2020, 8, 365–381, doi:10.32604/jrm.2020.09292.

[34] Walz M., Hagemann D., Trentzsch M., Weber A., Henle T., Degradation studies of modified inulin as potential encapsulation material for colon targeting and release of mesalamine, *Carbohydrate Polymers*, 2018, 199, 102–108, doi:10.1016/j.carbpol.2018.07.015.

[35] Poulain N., Dez I., Perrio C., Lasne M.C., et al., Microspheres based on inulin for the controlled release of serine protease inhibitors: Preparation, characterization and in vitro release, *Journal of Controlled Release*, 2003, 92, 27–38, doi:10.1016/S0168-3659(03)00251-7.

6.4 Pre- and probiotics as raw materials for cosmetic products

Anna Łętocha[*,1], Elżbieta Sikora[1]

1 Faculty of Chemical Engineering and Technology, Cracow University of Technology, Poland

Keywords: *skin microbiome*, *probiotics*, *prebiotics*, *cosmetic ingredients*.

Abstract

Human skin is a complex ecosystem colonised by bacteria, fungi and viruses collectively known as the skin microbiome. It plays crucial roles in skin health.

Several external factors negatively affect the skin microbiome balance, especially cleansing and daily skin care products or sanitizers. The necessity to use microbiome-friendly raw materials or the addition of pre- or/and probiotic ingredients to cosmetics formulations becomes desirable. The pre- and probiotics have been successfully used for years as ingredients in dietary supplements. In the case of cosmetics, these terms are used more widely.

In this work, the current state of knowledge on the skin microbiome and pre-/probiotic raw materials used in cosmetic formulations is presented.

Introduction

Human skin is a complex ecosystem, colonised by a wide variety of bacteria, fungi and viruses generally known as the skin microbiome or "*Stratum microbium*" (*SM*). Certain components of skin – hair follicles, sebaceous glands, sweat glands, and the stratum corneum – are colonised by unique microflora. The diversity of the skin microbiome was first described in 2011 by Elizabeth Grice and Julia Segre [1]. Currently, scientists are paying attention to the important role that the skin microbiome plays in skin's proper functioning, protection against pathogenic microorganisms, strengthening the immune system, and the ability to break down and produce various compounds [2–6].

Unfortunately, improper hygiene, cleansing and daily skin care can disrupt the proper functioning of *SM*, causing excessive skin dryness or lesions, e.g. atopic dermatitis. Therefore, the impact of cosmetic products on the skin microbiome and the need to use *SM*-friendly raw materials has become the subject of scientific research [7,8].

This subject is particularly important in the era of the *Corona virus* pandemic, where the requirement for cleansing and disinfecting hands is one of the elements of the sanitary regime. In turn, products for such purposes do not only effectively clean the skin by removing pathogenic microorganisms from its surface, they also remove components of the skin microbiome [9,10]. The occupational group that requires special care are healthcare workers who, as a result of disinfection, are exposed to damage to the skin and mucous membranes, which can cause acute and chronic dermatitis, secondary infections, and the aggravation of underlying skin diseases. One cross-sectional study conducted by the China Association of Dermatologists surveyed 330 healthcare workers battling COVID-19 cases. The results of the research showed that 71% of respondents reported damage to the epidermal barrier, with symptoms ranging from burning, itching and stinging to dryness, erythema and maceration [9]. One of the ways to reduce the side effects of disinfecting agents is the use of skin care products that soothe irritations and supplement the epidermal barrier, containing, for example active substances from the group of pre- and probiotics [11].

Skin microbiome

The skin is the human body's largest organ. It is an ecosystem of approximately 2 m^2 that supports the growth of microorganisms. The primary role of the skin is to act as a physical barrier protecting the body against potential attack by foreign organisms and toxic substances [1]. The skin is also an interface with the outside environment; is colonised by various groups of microorganisms (bacteria, fungi, viruses) and mites, which are classified as residents, temporary, and transient species [12,13]. Microorganisms and mites occur not only on the surface of the skin but also deep inside the hair or glands, creating the skin microbiome – "*Stratum microbium*" (*SM*) [1]. These microorganisms are mainly harmless, and in some cases, their presence provides vital functions, i.e. they are even useful for the host. Microorganisms that live "in harmony" with the host (i.e. symbiotic microorganisms) occupy many niches on the skin and protect against the colonisation of pathogenic and harmful organisms [1,14,15]. Until recently, the characterisation of cutaneous microbes was based on cell-culture techniques. However, less than 1% of bacterial species are able to grow under laboratory conditions, and many are suppressed by more competitive organisms. As a result, bacteria and fungi, including *Staphylococcus* and *Malassezia* species were overrepresented [16, 17]. Recent advances in DNA amplification and sequencing technology have omitted cell-culture steps and have revolutionised the way in which skin microbial communities are viewed. Using DNA sequencing methodology, it is possible to analyse the microbiome with greater precision and accuracy. This analysis is based on the sequencing of the 16S ribosomal RNA (rRNA) gene and shows that most dermal bacteria belong to one of four groups: *Actinobacteria*, *Firmicutes*, *Bacteroidetes* and *Proteobacteria*. Non-bacterial microorganisms were also isolated, including the fungal species – *Malassezia* and *Demodex* (mites) [1,12]. A molecular approach has also shown that bacterial colonisation is dependent upon site physiology in the human body. There are three main habitats on the skin (moist, sebaceous and dry), which influences the characteristic microflora of these areas [1,18]. Fig. 6.4.1 shows distribution of microenvironments of the human skin.

In addition to the differences resulting from anatomical conditions, the variability and abundance of skin microbiota depends on age, gender, seasons and ethnic origin, as well as on stressors such as physiological injuries and psychological anxiety. Factors contributing to the diver-

* Corresponding author, e-mail: *anna.letocha@doktorant.pk.edu.pl*

sity of the skin microbiome can also be environmental: climate, temperature, UV radiation and also lifestyle [14]. The skin is an organ that requires constant regeneration [19–20]. Differences in the properties of the stratum corneum can cause dysbiosis, which affects the diversity and abundance of commensal species [21]. In this way, the function of the skin barrier is disturbed, which in turn worsens chronic skin diseases, which include atopic dermatitis [14,17–19,22–25], psoriasis [14,17–19,22,25] and acne [14,17–19,22,26–28]. When there is dysbiosis on the skin and the diversity of the microbiome is disturbed, substances from the group of pre- and probiotics can be used as modulators to restore the microbiological balance [20].

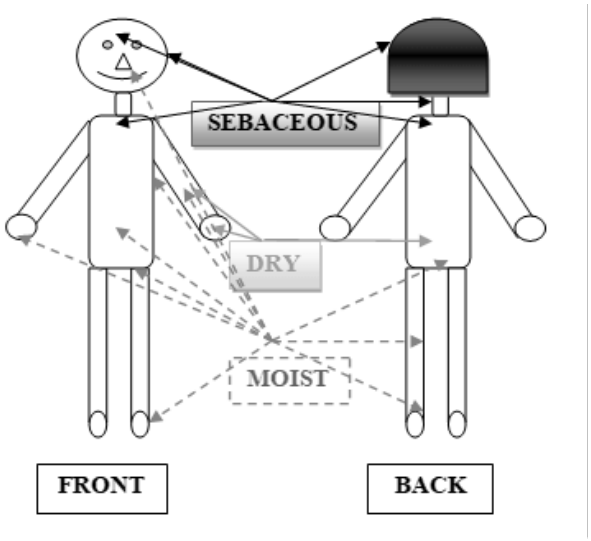

Figure 6.4.1: Distribution of microenvironments on the human skin (by author).

Pre- and probiotics in cosmetics

Prebiotics and probiotics are widely studied and applied in both the food and pharmaceutical industries because of the health benefits attributed to them. The global market for pre- and probiotics is constantly growing, which is partly attributed to consumer awareness of the health benefits of their consumption [12]. The current definitions of these terms have been developed on the basis of their use as dietary supplements.

Prebiotic ingredients

Prebiotics are commonly defined as "nondigestible food ingredients that, when consumed in sufficient amounts, selectively stimulate the growth and/or activity of one or a limited number of microbes in the colon resulting in documented health benefits" [29,30]. Prebiotics found in dietary supplements are carbohydrates made up of various types of short- or long-chain monomers. These monomers are linked by bonds that are not broken down by human digestive enzymes but are used by specific bacterial strains. The substances considered to be prebiotics in dietary supplements include mainly [31]:

- fructans, fructo-oligosaccharides and inulin
- galacto-oligosaccharides, composed of galactose monomers and a unit of terminal glucose groups
- lactulose, a disaccharide composed of galactose and fructose.

Prebiotics occur in natural sources, such as dahlia tubers, chicory root, garlic, onion, leek, artichoke, asparagus, flaxseed, soybeans and cow's milk [12].

Recently, the list of substances considered to be prebiotic has been expanded and in addition to the abovementioned carbohydrates, it includes conjugated linoleic acid, polyunsaturated fatty acids, polyphenols and phytochemicals [30,31].

In cosmetics, the term *prebiotic* is used in a broader context, i.e. as substances that can be used by "good" bacteria or as substances produced by microorganisms (these are also often referred to as probiotic ingredients in relation to cosmetics). Cosmetics manufacturers define prebiotic substances as follows: "Prebiotics are a food source for beneficial microbes to give them a competitive advantage. By giving them food, they proliferate and thrive, thereby excluding pathogenic (harmful) bacteria" [31].

Probiotic ingredients

According to the generally accepted definition established by FAO/WHO, "probiotics are live microorganisms that, when administered in appropriate amounts, provide the host with health benefits" [29,32]. The most common probiotics are representatives of the genera *Lactobacillus and Bifidobacterium*. Ingredients derived from *Lactococcus*, *Streptococcus*, *Leuconostoc*, *Pediococcus* and *Saccharomyces* are used much less frequently. It is important to note that only specific strains are probiotic, not the entire species [29,31]. Additionally, different strains may have different probiotic properties, and the parameters of one strain cannot be extrapolated to another, even if they belong to the same species [29]. This fact should be taken into account when selecting the appropriate strain for specific applications. In the cosmetics industry, the term *probiotic* is used more widely, because live microorganisms can only be used to a very limited extent in cosmetic products as their viability, purity and performance are difficult to control. In order to use live bacteria in cosmetic products, preservatives should be omitted, which is very difficult from the point of view of cosmetics safety and the requirements for cosmetic products (Regulation No. 1223/2009 on cosmetic products). The group of raw materials that combine health benefits for the skin may be substances that are not live bacteria themselves but are obtained with the help of probiotic bacteria. Among such probiotic cosmetic ingredients, four categories can be highlighted: fermentation products, cell lysates, raw materials obtained after tyndallization and live bacteria belonging to the fourth group presented below.

1. Fermentation products – in such a product, probiotic bacteria are grown in a special medium and subsequently filtered out from the solution, but the solution contains their metabolites, such as: amino acids, vitamins or antioxidants.

2. Cell lysates – bacteria are not filtered out of the medium, but they are destroyed and components of their cell structures can be found in solution.

3. Raw materials obtained after tyndallization – bacteria are killed by heating before being used in formulation. In this way, bacteria cannot multiply on the skin, and their cell components and excreted bacterial substances exert an immunomodulatory effect and thus contribute to the inhibition of pathogen development.

4. Live probiotic bacteria – live bacterial cultures are added to the cosmetic product, but in this case there are the above-mentioned limitations in the use of preservatives that can kill the "good" bacteria in the product. However, most products containing probiotics contain dead microbial cells, so this problem is not significant [31,33].

Among the above-mentioned categories, the first group of probiotic ingredients is the most popular. It has been observed that metabolites (vitamins, amino acids, antioxidants) obtained as a result of fermentation are common components of many cosmetic products.

With regard to the most commonly used lactic acid bacteria (*Lactobacillus*), there are four groups of ingredients in cosmetics:

- *Lactobacillus* bacteria (LACTOBACILLUS)
- *Lactobacillus* fermentation product (LACTOBACILLUS FERMENT)
- *Lactobacillus* fermentation product filtrate (LACTOBACILLUS FERMENT FILTRATE)
- *Lactobacillus* bacterial lysate (LACTOBACILLUS LYSATE) [31].

Research shows that probiotics composed of dead organisms may also exert beneficial pharmacological effects [34], which may also be reflected in cosmetology. Studies have been conducted on the influence of microorganisms or their metabolites on skin hydration, inflammation, protection against UV radiation and atopic dermatitis [12, 20–21,34–39]. In this way, probiotic substances consisting of both living and dead cells or metabolites of microorganisms can help prevent inflammatory and allergic diseases [40]. Some studies indicate that non-viable microorganisms such as heat-killed, UV-inactivated microorganisms or their metabolites may be better agents because the use of live microorganisms may be associated with undesirable side effects [41–43]. Clinical studies have shown that the use of *Bifidobacterium longum* lysate is effective in the treatment of sensitive and dry skin [36]. Furthermore, a study by Kim et al. [34] showed that a two-week application of *Lactobacillus sakei* probio 65 (live and dead) significantly inhibited the development of skin lesions resembling atopic dermatitis compared to the control group. In another study, Jung et al. [37] showed that *Lactobacillus rhamnosus* lysates can improve the skin barrier function using a Keraskin™ reconstructed epidermis model. A study by Khmaladze et al. [38], using live bacteria and a *Lactobacillus reuteri* DSM 17938 lysate, led the authors to conclude that the live form of *L. reuteri* DSM 17938 can be used to treat skin problems related to photoaging, bacterial overgrowth and skin hydration. Bacterial lysates can be used in skin care where an anti-inflammatory effect is needed. Due to the results of the above studies, it can be assumed that the local application of live microorganisms may bring about extraordinary effects [29]. There is great interest in the use of live bacteria in the care of dry and sensitive skin and in the treatment of inflammatory skin diseases [38]. However, current knowledge about the effects of probiotics and prebiotics on skin care is still quite limited [29]. A study by Peral et al. [44] showed that the topical application of live *Lactobacillus plantarum* inhibits inflammation and accelerates wound healing with patients with chronic venous ulcer leg wounds. Nevertheless, when planning to use live bacteria in cosmetic products, the following concerns are yet to be addressed: How can live bacteria be stored in a cosmetic? How can the safety of such a cosmetic be assessed and ensured? How will such a cosmetic containing live bacteria meet regulations with regard to microbial contamination limits? Currently, only a few products containing live bacteria (*Lactobacillus*) are available on the cosmetics market [33,45]. One biotechnology company proposes the use of encapsulated freeze-dried live *Lactobacillus* bacteria in an oil-in-water (O/W) cream [45]. According to the inventors of the product, bacteria are activated as a result of friction after the mechanical breakdown of the bacterial envelope. However, no literature supporting this theory is available yet. Microencapsulation used in the pharmaceutical and food industries may prove to be a method that can have a positive effect on the encapsulation of live bacteria in a cosmetic [46–48]. However, larger-scale studies are needed to confirm this concept.

Conclusions

This paper has presented the current state of knowledge on the skin microbiome with a particular emphasis on the influence of pre- and probiotic substances used in cosmetic products. Advances in DNA sequencing have been key to the current, although still limited, understanding of the structure of skin microbiota. The concept of using probiotics and prebiotics is still evolving. The available studies on the effects of microorganisms or their metabolites on skin hydration, inflammation, UV protection and atopic dermatitis suggest that in addition to the ability of probiotics to positively affect the digestive system, they may also exert their beneficial effects at the skin level. A new area of concern for skin health is the entrapment of live bacteria in a cosmetic product. Microencapsulation used in the pharmaceutical and food industries may be a method that provides positive results. However, larger-scale studies are needed to confirm this concept.

References

[1] Grice E.A., Segre J.A., The skin microbiome, *Nature Reviews Microbiology*, 2011, 9, 244–253

[2] Belkaid Y., Segre J., Dialogue between skin microbiota and immunity, *Science*, 2014, 346, 954–959

[3] Chen Y.E., Fischbach M.A., Belkaid Y., Skin microbiota–host interactions, *Nature*, 2018, 24, 427–436

[4] Grice E., The intersection of microbiome and host at the skin interface: genomic- and metagenomic-based insights, *Genome Res*, 2015, 25(10), 1514–1520

[5] Scharschmidt T.C., Fischbach M.A., What Lives On Our Skin: Ecology, Genomics and Therapeutic Opportunities Of the Skin Microbiome, *Drug Discov. Today Dis. Mech.,*. 2013, 10(3-4), e83–e89

[6] Butler E., Lundqvist Ch., Axelsson J., Lactobacillus reuteri DSM 17938 as a Novel Topical Cosmetic Ingredient: A Proof of Concept Clinical Study in Adults with Atopic Dermatitis, *Microorganisms*, 2020, 8, 1026, doi:10.3390/microorganisms8071026

[7] Paetzold B., Skin microbiome modulation induced by probiotic solutions, *Microbiome*, 2019, 7(1), 95–104

[8] Lee, H.J. et al., Effects of cosmetics on the skin microbiome of facial cheeks with different hydration levels, *Microbiology Open.* 2018; 7:e557, doi:10.1002/mbo3.557

[9] Yan Y., et al. Consensus of Chinese experts on protection of skin and mucous membrane barrier for health-care workers fighting against coronavirus disease 2019, *Dermatologic Therapy*, 2020, doi:10.1111/dth.13310

[10] Steventon K. et al., Biofilms and the Skin Microbiome - A 'Hot Spot' for Personal Care, Cosmetics & Toiletries, 2020, 135(1), 31–37

[11] Cinque B., et al., Use of Probiotics for Dermal Applications, *Probiotics*, 2011, 21, 221-241

[12] Bustamante M. et al., Probiotics and prebiotics potential for the care of skin, female urogenital tract, and respiratory tract, *Folia Microbiol (Praha)*, 2020, 65(2), 245-264

[13] Holland K.T., Bojar R.A., Cosmetics: what is their influence on the skin microflora?, *Am J Clin Dermatol.*, 2002, 3, 445–449

[14] Dréno B. et al., Microbiome in healthy skin, update for dermatologists, *J Eur Acad Dermatol Venereol*, 2016, 30(12), 2038–2047

[15] Singh P. et al., Intestinal microbial communities associated with acute enteric infections and disease recovery. *Microbiome*, 2015, 3, 45, doi:10.1002/jbm.a.34305

[16] Chen Y.E., Tsao H., The skin microbiome: current perspectives and future challenges, *J Am Acad Dermatol.*, 2013, 69(1), 143–155

[17] Staley J.T., Konopka A., Measurement of in situ activities of nonphotosynthetic microorganisms in aquatic and terrestrial habitats, *Annu Rev Microbiol.*, 1985, 39, 321–346

[18] Ellis S.R. et al., The Skin and Gut Microbiome and Its Role in Common Dermatologic Conditions, *Microorganisms*, 2019, 7(11), 550

[19] Salem I. et al., The Gut Microbiome as a Major Regulator of the Gut-Skin Axis, *Front Microbiol.*, 2018, 9, 1459

[20] Lopes E.G., Topical application of probiotics in skin: adhesion, antimicrobial and antibiofilm in vitro assays, *J Appl Microbiol.*, 2016, 122(2), 450–461

[21] Prescott S.L. et al., The skin microbiome: impact of modern environments on skin ecology, barrier integrity, and systemic immune programming, *World Allergy Organ J.*, 2017, 10(1), 29

[22] Grice E.A., The skin microbiome: potential for novel diagnostic and therapeutic approaches to cutaneous disease, *Semin Cutan Med. Surg.*, 2014, 33(2), 98–103 [23] Seité S., Zelenkova H., Martin R., Clinical efficacy of emollients in atopic dermatitis patients – relationship with the skin microbiota modification, Clin Cosmet Investing Dermatol., 2017, 10, 25–33

[23] Di Domenico E.G. et al., Staphylococcus aureus and the Cutaneous Microbiota Biofilms in the Pathogenesis of Atopic Dermatitis, *Microorganisms*, 2019, 7(9), 301

[24] Sanchez D.A., Nosanchuk J.D., Friedman A.J., The skin microbiome: is there a role in the pathogenesis of atopic dermatitis and psoriasis, *J Drugs Dermatol.*, 2015, 14, 127–130

[25] Zeeuwen P.L. et al., Microbiome and skin diseases, *Curr Opin Allergy Clin Immunol.*, 2013, 13, 514–520

[26] Nakatsuji T. et al., The microbiome extends to subepidermal compartments of normal skin, *Nat Commun*, 2013, 4, 1431

[27] Fitz-Gibbon S. et al., Propionibacterium acnes strain populations in the human skin microbiome associated with acne, *J Invest Dermatol.*, 2013, 133, 2152–2160

[28] Ouwehand A.C., Lahtinen S., Tiihonen K., The Potential of Probiotics and Prebiotics for Skin Health, *Textbook of Aging Skin*, 2016, 1299–1313

[29] Gibson G.R., Expert consensus document: The International Scientific Association for Probiotics and Prebiotics (ISAPP) consensus statement on the definition and scope of prebiotics, *Nature Reviews Gastroenterology & Hepatology*, 2017, 14, 491–502

[30] Warming M., Lassen C., Christensen F., Survey of cosmetics products with „probiotic" or „prebiotic" claims, *Ministry of Environment and Food of Denmark*, Denmark, 2018

[31] Hill C. et al., The International Scientific Association for Probiotics and Prebiotics consensus statement on the scope and appropriate use of the term probiotic, *Nature Reviews Gastroenterology & Hepatology*, 2014, 11, 506–514

[32] Sfriso R., Revealing the secret life of skin -- with the microbiome you never walk alone, *Int J Cosmet Sci.*, 2020, 42(2), 116–126

[33] Kim J.Y. et al., Atopic dermatitis – mitigating effects of new Lactobacillus strain, *Lactobacillus sakei* probio 65 isolated from Kimchi, *J Appl Microbiol.*, 2013, 115(2), 517–526

[34] Szöllősi A. G. et al., *Bifidobacterium longum* extract exerts pro-differentiating effects on human epidermal keratinocytes, in vitro, *Exp Dermatol.*, 2017, 26(1), 92–94

[35] Guéniche A. et al., *Bifidobacterium longum* lysate, a new ingredient for reactive skin, *Exp Dermatol.*, 2009, 19(8), e1–8

[36] Jung Y. et al., Lysates of a Probiotic, *Lactobacillus rhamnosus*, Can Improve Skin Barrier Function in a Reconstructed Human Epidermis Model, *Int J Mol Sci.*, 2019, 20(17), 4289

[37] Khmaladze I. et al., *Lactobacillus reuteri* DSM 17938 - A comparative study on the effect of probiotics and lysates on human skin, *Exp Dermatol.*, 2019, 28(7), 822–828

[38] Patra V.K., Sérézal I.G., Wolf P., Potential of Skin Microbiome, Pro- and/or Pre-Biotics to Affect Local Cutaneous Responses to UV Exposure, *Nutrients*, 2020, 12(6), 1795

[39] Adams C.A., The probiotic paradox: Live and dead cells are biological response modifiers, *Nutrition Research Reviews*, 2010, 23(1), 37–46

[40] Boyle R.J., Robins-Browne R.M., Tang, M.L., Probiotic use in clinical practice: what are the risks? *Am J Clin Nutr*, 2006, 83, 1256–1264

6.5 Ecological study of a mineral carbon capture and conversion process

Wanawan Pragot*,[1], Maria-Ara Carballo-Meilan[1], Waheed Afzal[1]

1 Chemical & Materials Engineering, School of Engineering, University of Aberdeen, Aberdeen, UK

Keywords: *carbon capture and utilisation (CCU)*, *mineral-CCU*, *mineral carbonation*, *precipitated calcium carbonate (PCC)*, *life cycle analysis (LCA)*, *environmental impacts*, *NaOH*, *fly ash*, *$CaSiO_3$*, *steel slag*.

Abstract

The rise in carbon dioxide emissions is creating environmental problems of unprecedented magnitude and impact. Current total global emissions of CO_2 from the fossil chemical use and industrial chemical processes are 38 GT CO_2-eq per year with growth rate of 2.7% during past decade. Due to COVID-19 pandemic and its impact, a temporary decrease in the global emissions is expected. Carbon capture and utilisation (CCU) strategies can aid a potential mitigation option for the reduction of greenhouse gas emissions.

This study presents a mineral CCU process that employed flue gas and an alkaline solution to develop an integrated absorption-based carbon removal and conversion process and then used an ion exchange reaction by using available brines to produce a useful form of precipitated calcium carbonate (PCC). Furthermore, this study compared the environmental impact of proposed mineral carbonation process with other three mineral CCU processes reported in the literatures [15], [37–39] ; mineral carbonation processes from; 1) fly ash from powerplants, 2) mineral wollastonite rock ($CaSiO_3$), and 3) steel slag using life cycle assessment (LCA) provided in ISO14044. The LCA was investigated using gate to gate (G-G) system boundary and 1 kg of $CaCO_3$ product as functional unit for comparison.

Results indicate that the cost estimation of the process operational cost of PCC-NaOH based process is £ 446 per ton of CO_2 removed and this is higher than other PCC based processes. The LCA results depict the PCC carbon capture technology using four different materials has a positive environmental impact. NaOH-based process has the lowest land use and water depletion impacts but it has the second largest global warming potential (GWP) within four options studied here due to NaOH solvent identified as the process hot-spot. The fly ash-based PCC has the highest environmental impact due to the process waste (direct emission), raw materials used and the energy consumption. The $CaSiO_3$ and steel slag-based PCC have comparable low toxicity impact as low chemical consumption and the waste generation in the process capture system. The overall environmental impact of carbon capture into PCC indicated that while mineral CCU presents long-term carbon sequestration potential and scalable markets but all of the processes studied here are far from being carbon negative.

* Corresponding author, e-mail: *r02wp17@abdn.ac.uk*

Acknowledgments

This work was financial supported by The Royal Embassy of Thailand.

Introduction

Carbon capture utilisation and storage (CCUS) situation

The overall greenhouse gas (GHG) emissions are currently at 54 $GTCO_2$-eq[6] with an annual growth rate of 2.7% (based on the past decade) [1,2]. It has been estimated that in order to maintain current emissions and to limit global warming within 2 °C above preindustrial levels by 2100, radical technologies will be required [1,3]. The greenhouse effect is a natural process of the Earth whereby some of the energy emitted by the Sun is reflected by the atmosphere and other is absorbed by the GHGs. The most abundant GHGs in our atmosphere are: water vapor (H_2O), carbon dioxide (CO_2), methane (CH_4), nitrous oxide (N_2O) and ozone (O_3) [4]. However, above a certain level of concentration, GHGs causes global warming by trapping too much solar heat through absorption and emission of infrared radiation with the consequent increase in the overall temperature of the atmosphere [3,5].

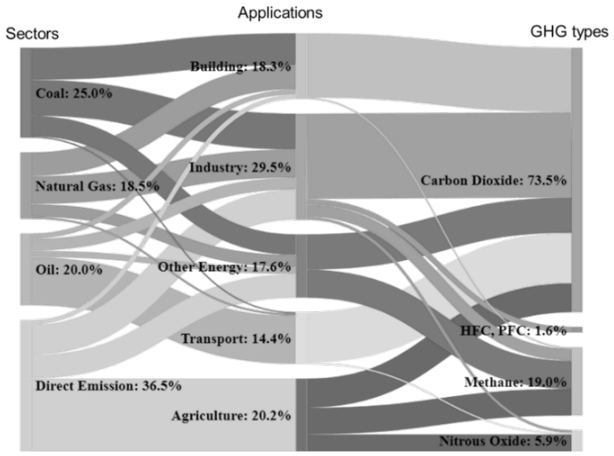

Figure 6.5.1: Total GHG by source, sector, and greenhouse gas type modified from ECOFYS (2014), EU-EDGAR (2017), EPA (2017).

Fig. 6.5.1 shows the share of total GHG emissions of 54 $GTCO_2$-eq including agricultural and forestry worldwide [1,2,6]. It is estimated that more than 30% of the contributions to global warming comes from direct emissions of GHGs as a result of using certain chemicals[7]. These chemicals produce goods and direct emission[8] of the fossil fuels combustion. The other remainder of that are from indirect emission[9] from fossil fuel production coal, natural

[6] $GTCO_2$-eq, refers to Gigaton CO_2 equivalent, is the unit of GHG emission by converting to carbon dioxide reference unit.

[7] 449 chemicals were reported as direct GHG emission sources in Total direct emissions from chemicals report 2019 [82].

[8] Fossil fuel combustion process led to the emission of CO_2, methane, as air emission and its defined as direct emission of fossil fuel application.

[9] Fossil fuel required energy and other resources for extraction, processing, refining, transportation process and that led to the GHG emission. Therefore, when using fossil fuel, the GHG emission from that processes are

gas, and oil. Anthropological applications such as transportation and electricity contribute to the total GHG emissions and almost 30% of those are produced by the industry. CO_2 is the largest GHG emitted from these human activities. Therefore, tackling the problem of the CO_2 emissions is likely to reduce global warming.

Specifically, anthropogenic CO_2 is released from the combustion of fossil fuels, including the energy produced for the residential and commercial sectors, automobile engines, as well as, large combustion units such as power generators, among others. Furthermore, the manufacture of cement, iron and steel, chemicals as well as petrochemicals emit significant quantities of CO_2 [7]. In 2016, global average concentrations of atmospheric CO_2 reached 403.3 ppm, an increase of 145% above pre-industrial levels (before 1750) (Kriegler et al., 2018; World Meteorological Organisation, 2020). Despite the global efforts to move towards greener energy sources, fossil fuels (i.e. coal, oil and natural gases) remain the main source of energy, accounting for up to 85% of the whole energy used [9]. Scientific predictions state that fossil fuels are likely to dominate the energy sector at least until the middle of the 21st century [10]. Drastic socioeconomic and institutional reforms will be needed to improve more adverse consequences.

The intense research in carbon-neutral technologies has gained increased momentum, not only due to the environmental concerns, but also because of the potential monetary impact on businesses caused by the increase in carbon emission taxes. The carbon taxation system is seen as a powerful financial disincentive to CO_2 emissions and it has been implemented in many countries across the globe after the agreements defined in the United Nations Framework Convention on Climate Change (UNFCCC) [11]. Most of these countries have implemented various energy taxes directly or have introduced at least one form of indirect taxation on energy products and motor vehicles [12,13].

Many efforts have been done in preventing and controlling the greenhouse gas emission levels. Several options have been proposed to mitigate the CO_2 concentrations in the atmosphere including: (i) energy saving improvements, (ii) the minimisation and reduction of offshore drilling, (iii) the development of renewable energy solutions, (iv) the enhancement of biological sinks [14–16], and more recently, (v) CO_2 capture and storage (CCS) and CO_2 capture and utilisation (CCU) technologies.

CCS usually describes various methods aiming at preventing the CO_2 from entering the atmosphere, usually by storing it underground in depleted oil and gas fields. CCS is very expensive and generally involves three steps; (i) CO_2 capture (ii) CO_2 separation and/or transportation to the site and (iii) CO_2 storage [10]. That includes several options such as carbon storage within geological formations in the ocean and carbon storage underground, in carefully selected storage sites. However, the storage of CO_2 could have a significant impact in the environment if, for instance, a leak take place. The stored CO_2 is sooner or later emitted, making this sequestration method of uncertain safety and effectiveness. While significant research has shown that CCS solutions are promising and safe, it's unlikely that it would reduce GHG emissions without legislations and subsidies. The economic burden imposed on industrial emitters exceed the reduction of net carbon emissions achieved by both geological and ocean storage processes. The reason lies on the increased energy output required to utilise a CCS system. Although economic studies are case-specific, it is generally agreed that a power plant equipped with a geological or ocean CCS system would require up to 10--40% more energy than one without it [2,14]. The economic impact affects other areas as well, such as transportation of the captured carbon[10].

Another potential technology is carbon capture and utilisation (CCU) which may provide a window to reduce carbon emissions and use it for the alternative materials as carbon capture and storage (CCS) could not, so far, deliver reduction of CO_2 emissions at an acceptable price despite significant research efforts and public opinion regarding global warming [17]. The difference between CCU and CCS is the final use. CCS technologies remove CO_2 from gas streams and transport it to a geological site for long-term storage, including depleted oil and gas reservoirs. CCU instead converts captured CO_2 into commercial products [18]. CCS suffers from unacceptably high cost, no economic return, fears of leakages, and unwillingness of governments to subsidy [19–22]. Therefore, CCU technologies can contribute to climate change mitigation and, at the same time, increase the economic profitability of carbon capture processes [23,24].

CO_2 capture and utilisation

There are several applications from the CO_2 utilisation: 1) CO_2 utilisation technologies into direct utilisation of CO_2 and 2) conversion of CO_2 into products. Pure CO_2 can be directly used in the food and beverage industries, extinguisher, and refrigerant. This includes the carbonation of beverages, a packaging gas and use as an extractant for the decaffeination of coffee and flavour and fragrances. Although a huge benefit to modern society, this technique will not fully sequester the gas and it will ultimately end up back in the atmosphere after customer application. CO_2 in these direct consumption processes also require a high purity (> 99.0% purity) [25], furthermore this is not effective in reducing CO_2 emissions. Another direct utilisation of CO_2 is CO_2 enhanced-oil recovery (EOR) that is the process of CO_2 injection into the pore spaces of rocks to help move immobile crude oil out [20]. The CO_2 will reduce the viscosity of the oil allowing for the easy removal of any oil that is left after the primary or secondary recovery has taken place, which then flows to the production well. However, as the oil and CO_2 mix reaches the surface, they must be separated from one another and there is opportunity for CO_2 to escape back into the atmosphere. This process requires high 95.0% purity [25] so consequently is not effective in reducing CO_2 emissions as the CO_2 will be emitted to the air. Therefore, both the direct CO_2 application by using in the food and beverage and EOR share the same problems as

counted as the indirect emission of fossil fuel application.

[10] Large source points are unlikely to be in a close geographical proximity to the suitable storage location.

the high CO_2 purity required and the non-permanent CO_2 storage.

CO_2 can be transformed into a wide range of products. CO_2 can then be utilised as valuable physical product as different alternative organic or inorganic compounds including fuels, chemicals feed stocks, and mineral carbonation products. However, the scope of CO_2 utilisation is limited. Therefore, most regions in Europe are currently funding research on the CO_2 mitigation and utilisation at various technology readiness level (TRLs) based on the projects progress [26,27] as shown in Fig. 6.5.2.

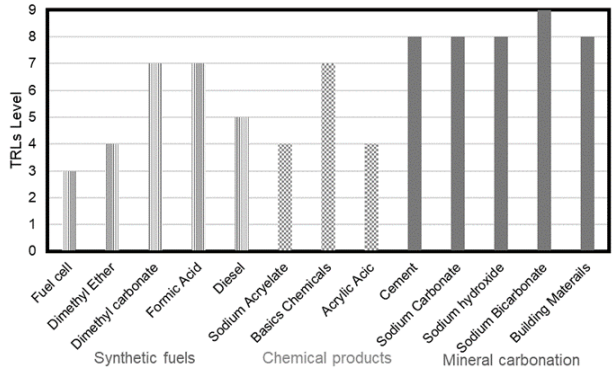

Figure 6.5.2: Technology readiness level (TRLs) of CCU applications adated from Eurostat (2018)

As shown in Fig. 6.5.2, currently, most regions in Europe are funding research on the CO_2 mitigation and utilisation at various technology readiness level (TRLs) [26,27]. Technology Readiness Levels (TRLs) are a type of measurement system used to assess the maturity level of a particular technology. Each technology project is evaluated against the parameters for each technology level and is then assigned a TRL rating based on the projects progress. There are nine technology readiness levels. TRL 1 is the lowest and TRL 9 is the highest. Fig. 6.5.2 shows the range of technology readiness level of CCU applications categorised into three major CO_2 utilisation pathways; synthetic fuels, chemical products, and mineral carbonation. Some process routes of CCU are now ranged in high TRLs level. For example, CCU for synthesis fuels routes[11] and chemical products are in TRLs of 7 that have been operating under pre-commercial scale environment. The mineral carbonation CO_2 utilisation are assigned in TRLs of 8 and TRLs of 9 that has now proved and enough technological study supports for the commercial application and a full-scale production in the industry [27].

Synthetic fuels from CO_2 can be produced that would directly replace liquid and gaseous fossil fuels. CO_2 is used as a carbon source replacing the carbon sourced from ordinary fossil fuels. One or both carbonate bonds C = O fully broken from CO_2 reduction reactions could be utilised in the production of methane [28], metanol [29], etanol, carbon monoxide, synthetic gas [30], formic acid, [22], [31] and acetone [32]. The reduction reactions are energy intensive to break down the C = O bond. The required energy can be provided by high-energetic reactants [19] such as hydrogen, by heat, electricity, sunlight or microwaves [33]. Apart from the reduction production, the biodiesel or kerosene could be produced in the microalgae CO_2 capture [23]. The capture of CO_2 from the air or the use of biogenic/biomass sources of carbon will provide carbon-neutral or negative liquid/gaseous fuels. Main impact is the low carbon footprint of the synthetic fuels by CO_2 utilisation compared to the ordinary fossil production process. However, since fuels are burned soon after production or during application process, the CO_2 will be released to the atmosphere. Therefore, the storage duration of this CO_2 utilisation via synthetic fuels is short.

The Chemical industry is a solution provider for many downstream sectors and end consumer areas. CO_2 source can be used as a chemical feedstock in the production of synthetic chemicals and intermediate chemicals. Ongoing research is primarily focusing on polymers [34], urea [35], carboxylates, carbonates, olefins, and the discovery of new catalysts and mechanisms for these reactions. The use of chemicals makes substantial contributions to reducing energy demand and emissions across many sectors. Synthetic chemicals (e.g. urea through the reaction with ammonia, methanol and synthetic gases) are heavily relied upon and are used daily throughout the world. The production of urea, a key ingredient in fertilisers [32] is the largest potential consumer of CO_2, with a maximum use potential of around 100 Mt/year. Other benefits for the chemical products sector include the potential of CO_2 utilisation processes to provide less toxic chemical synthesis routes compared to conventional methods e.g. replacing the use of the highly toxic phosgene with products derived from CO_2, and potentially using large quantities of CO_2 during production which is important when considering if a technique is effective in reducing emissions. Nevertheless, CO_2 utilised as a chemical feedstock does not come without its disadvantages. Chemical synthesis requires high CO_2 purity [25] and provides limited storage due to the product lifetime span being relatively low for most products. Furthermore, it is important to find a technique that can be utilised for longer periods of time such as mineral carbonation.

Mineral carbonation is the process of reacting captured CO_2 with minerals which are soluble in water, namely calcium and magnesium ion, to produce stable carbonates. Over extensive periods, and natural weathering processes, these carbonates have reduced concentrations of high CO_2 in the atmosphere resulting in around 80% of the world's carbon being present in the form of carbonate rocks [36,37]. Converting this to a large-scale industrial process to sequester CO_2 in natural materials is defined by mineral carbonation. Moreover, carbon sequestration via mineralization has been suggested as the safest and most stable way of locking away large amounts of CO_2 [36,37]. Materials that can be carbonated include industrial wastes [38–40] and naturally occurring silicates such as olivine, serpentine, or wollastonite [12,41–44]. Industrial mineralisation has the benefit of improving certain industrial wastes to create waste streams that are less toxic (improved leaching properties) and chemically stable, whilst at the same time sequestering CO_2. CO_2 utilisation technologies also offer

[11] such as, dimethyl carbonate and formic acid production

process integration opportunities with the potential to convert low-value materials into useful higher value products for the building sector (e.g. synthetic aggregate [45], Carbonate blocks[24]), which also provides a CO_2 utilisation route that can permanently sequester CO_2. Additionally, alkaline industrial residues can be carbonated in situ in the same plant where they are produced, avoiding waste transports to external treatment plants [1,24]. Moreover, mineral carbonation only requires medium to low CO_2 purity [25] which is significantly better than other techniques.

Mineral carbonation

Many CCU technologies have been developed already [22,23,33,46]. Technologies such as cryogenics, membrane separation, adsorption (temperature swing adsorption (TSA), pressure swing adsorption (PSA), vacuum swing adsorption (VSA)) and algal-based systems are all potential solutions [23]. However, they are currently not considered economically viable at this stage and do not store CO_2 permanently (Department of Energy, US, 2017). Except mineral carbonation, all the mentioned technologies provide only a temporal solution to carbon emissions because the product of these technologies can sequester CO_2 a maximum of 6 months [47].

The most promising technologies is mineral carbonation using amine solutions like monoethanolamide (MEA) [48,49] and diethanolamide (DEA) [35]. The amine process has been a successful method in terms of CO_2 capture performance thanks to a reaction highly selective with CO_2 [50,51]. This is a well establish process, developed and continuously improved over the years. However, thermal degradation and evaporation losses associated with the desorption process make this technology energy intensive, not to mention the energy penalty associated with its regeneration process [13]. Therefore, alternative mineral carbonation technologies have proved more advantageous than the ones using amine solutions. They have lower energy requirements and operate at lower temperatures.

One of these low energy intensive technologies is mineral carbonation with the sodium hydroxide (NaOH) solvent. The process is carried out at room temperature conditions and was first studied in 1940. Several researchers have focused on the capture of CO_2 taking advantage of its rapid reactivity with NaOH [52–57]. CO_2 is an acid gas that is converted to sodium carbonate (Na_2CO_3) and sodium bicarbonate ($NaHCO_3$) though reaction with NaOH solution. The chemical reactions of the carbonation process are defined as follows;

$$CO_2\,(g) + 2\,NaOH\,(aq) \rightleftharpoons Na_2CO_3\,(aq) + H_2O\,(l) \quad (1)$$
$$CO_2\,(g) + Na_2CO_3\,(aq) \rightleftharpoons 2\,NaHCO_3\,(aq) \quad (2)$$

The overall absorption process of CO_2 and NaOH can be summarized thus

$$NaOH\,(aq) + CO_2\,(g) \rightleftharpoons 2\,NaHCO_3\,(aq) \quad (3)$$

Thermodynamic parameters G, S and H are indicators of the possible nature of adsorption. Overall, the absorption process of CO_2 and NaOH is an exothermic (G < O) and involves a series of stepwise processes (Reaction 1 and 2). The reaction of CO_2 absorption in NaOH (Reaction 1) and Na_2CO_3 (Reaction 2) are exothermic (enthalpy of the reaction H < 0). As Tab. 6.5.1 shows, the Gibbs free energy value of Na_2CO_3 reaction is less than that of NaOH reaction revealing the rate of Na_2CO_3 reaction is very slow as compared with the NaOH reaction.

Table 6.5.1: Thermodynamic parameter of each reaction at room temperature [58]

Reaction	ΔH^* kJ/mol	ΔS^{**} kJ/mol	$\Delta G = H + S^{***}$
Reaction 1	−168.8	−0.137	−128.97
Reaction 2	−129.1	−0.334	−29.56

*ΔH is enthalpy change
**ΔS is entropy change
***ΔG is Gibbs free energy

Then, the carbonated aqueous solution is reacted with a brine containing calcium to precipitate the desired form of mineral carbonate. For example, calcium carbonate in the form of precipitated calcium carbonate (PCC) is commonly used as additive in the paper, rubber and plastic industries [46] and its equation is written like this

$$Ca^{2+}\,(aq) + {CO_3}^{2-}\,(aq) \rightleftharpoons CaCO_3\,(s) \quad (4)$$

PCC generally exists in six polymorphic forms. Three of these polymorphs are anhydrous: vaterite, aragonite and calcite as show in Fig. 6.5.3. This means that they have different crystal structure but the same $CaCO_3$ composition. Regarding the hydrous forms of PCC, the three polymorphs are named based on the number of molecules of water conforming the crystal structure (the general formula is $CaCO_3 \cdot xH_2O$). Thus, we find monomolecular bonding of water molecules as monohydrocalcite ($CaCO_3 \cdot H_2O$), Ikaite ($CaCO_3 \cdot 6\,H_2O$) where there is bonding of 6 water molecules, and amorphous calcium carbonate (ACC) with no established crystal structure [59].

The advantage of PCC over calcium carbonate produced from natural raw materials (ground calcium carbonate - GCC) is that the solid powder can be synthesised with specific requirements based on several properties such as polymorphic composition, morphology, crystal size distribution, surface area, degree of whiteness brightness, and so on [63]. Among its numerous uses, PCC can be converted into construction material and can sequester CO_2 long term, even for decades. The addition of PCC inside the cement to produce concrete improves the final characteristics of the product in different ways, affecting certain properties and conferring strength rather than just acting as a filler [64–66]. Traditionally, Portland cement is the most important construction material but it has a very high carbon footprint, 0.8 kg CO_2-eq per kg of product [67,68]. Integrating PCC with Portland cement can reduce the total carbon emissions of this application.

The carbonates produced after the mineral-CCU process have a competitive market with high demand. The global market of calcium carbonate products is estimated to grow 96 Mt/yr [25] and the UK market for calcium carbonate

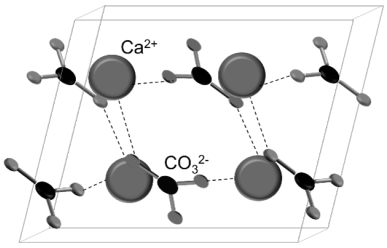

a. Calcite adapted from Donald L. (1961)

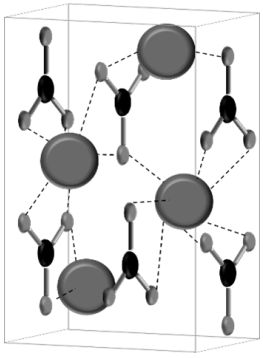

b. Aragonite adapted from Johan P.R. (1971)

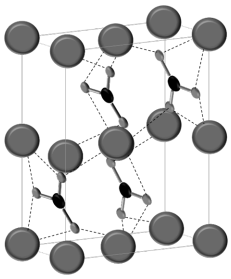

c. Vaterite adapted from Wang and Becker (2009)

Figure 6.5.3: Common forms of precipitate calcium carbonate; a) calcite, b) aragonite, and c) vaterite

products is 2 Mt/yr [25]. CCU products such as precipitated calcium carbonate (PCC) may be used along with cement to produce concrete where PCC can potentially improve certain properties such as the strength of the material rather than acting just as a filler. Similarly, hydrated forms of magnesium carbonate can be cemented to produce blocks and panels for buildings [69–73]. Precipitated magnesium carbonate (PMC) panels and blocks, along with favourable strength and thermal resistance can also act as fire extinguisher in the event of a fire [69–73]. These products have the potential to compete with other well-established products such as cladding, in the construction sector and partially replace high carbon intensive products with other low carbon intensive products such as the ones developed in this work.

Compared to the other sequestration options, mineral carbonation is a longer-term option. Mineral CCU where CO_2 is converted into stable and useful mineral carbonates of desired polymorphs of magnesium and calcium carbonates. In addition, mineral carbonation products could find beneficial reuse. For example, mineral carbonation could be used to produce aggregates, fills and other bulk building materials, and some have argued that mineral carbonation products could partially offset Portland Cement consumption [74]. These carbonates can be converted into construction material and they sequester CO_2 for long term ranging from decades to centuries [10]. Potential of CO_2 sequestration in carbonate form far exceeds demand for potential beneficial reuses, such opportunities could improve the economics of early implementations of CO_2 capture processes. It has some fundamental advantages, such as the permanent nature of the carbon dioxide storage and its theoretically vast capacity, but at this stage, there is insufficient knowledge to conclude whether a cost-effective and energetically acceptable process will be feasible.

The double benefit of mineral carbonation have already been described [22,23]. This includes, not only CO_2 capture and conversion but also a reduction of CO_2 emissions. Mineral carbonation can reduce CO_2 emissions in two ways [75]. Firstly, mineral carbonation affects the net emission because the mineral carbonation products, precipitate calcium carbonate (PCC) or precipitated magnesium carbonate (PMC), have lower CO_2 emission than calcium carbonate from traditional routes. Secondly, more CO_2 is removed from mineral carbonation process than is emitted. Mineral carbonation pathways should aim at reducing the net emissions or be carbon neutral, even so negative emissions are the best scenario. The option of avoiding CO_2 emission in comparison with traditional production route should be made clear in life cycle analysis (LCA).

Drawbacks to mineral carbonation include significant materials handling requirements and potentially high energy consumption. Mineral carbonation would require large amount of materials in order to sequester a significant quantity of CO_2 [76]. The energy demands of carbonation may result in emissions of CO_2 large enough to challenge the benefits of this sequestration process. The success of mineral carbonation depends critically on the cost and efficiency with which alkalinity can be extracted from feedstocks, and subsequently carbonated. If an energy efficient, scalable process for alkalinity extraction or generation exists, then mineral carbonation will be effective; otherwise, mineral carbonation is likely to be costly per tonne of CO_2 mitigated, and could even be a net CO_2 emission source instead of a sink. However, as the advantages of mineral carbonation outweigh those of alternative techniques and is most effective. Following this, a comparative assessment can be made using life cycle assessment studies found on mineral carbonation.

In this project, an integrated carbon capture and conversion process was developed to produce the mineral carbonate products and provide a partial solution for carbon emission control. The possible processes focus on the carbon capture via gas-liquid and direct carbonation process to produce useful mineral products. This research is based on experiments with synthetic flue gas at industrially relevant conditions to develop an absorption-based carbon removal process in an alkaline solution. Instead of regenerating the alkaline aqueous solution, like in conventional carbon capture processes, the carbonated aqueous solution is subjected to cation exchange to produce desired poly-

morphs of calcium carbonates (Precipitated Calcium Carbonate; PCC). Therefore, the ecological impact of the proposed process and its products was determined using life cycle assessment in order to compare the environmental impacts in this process with others with particular emphasis on mineral CCU.

Life cycle analysis

The environmental impact was used as well to assess the feasibility of the mineral carbon capture and conversion process. Fig. 6.5.4 shows the Life cycle assessment (LCA) framework based on the ISO standards [77–79]. Four major phases are mentioned and will be described below: goal and scope, Life Cycle Inventory (LCI), LCA and interpretation. This type of analysis is generally used to improve processes, support policies, and provide a sound basis for informed decision making.

As the Fig. 6.5.4 indicates, the first step was to define the goal and scope of the LCA analysis. In this stage of LCA, the main aim of the environmental assessment is decided. The scope included several stages such as the description of any assumptions, and selection of the functional unit or the unit of all inputs and outputs of the process. The goal of the study should describe the reasons for carrying out the study alongside the intended audience and applications. The goal of LCA is to compare the full range of environmental effects assignable to products and services. The scope defines the system boundaries and functional unit. It is important that when studies are compared, they must follow the same system boundaries to allow for an accurate comparison.

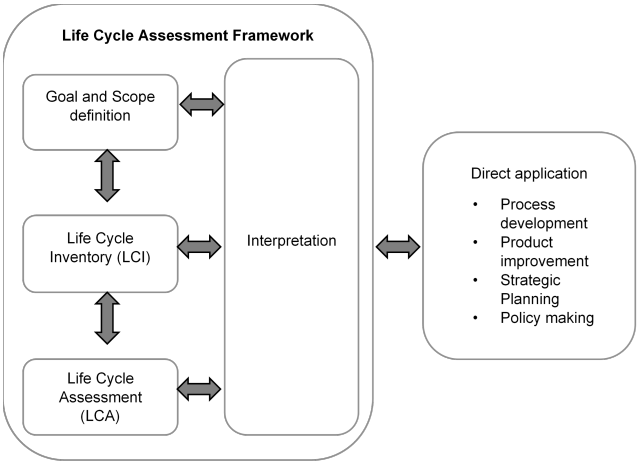

Figure 6.5.4: LCA framework adapted from ISO 14041 (1998) and ISO 14042 (2000)

Fig. 6.5.5 shows the LCA system boundary. The LCA study consists of 5 stages; i) the assessment of the environmental impact from raw material extraction and processing (cradle), ii) the product's manufacture, iii) the products distribution or the transport of the products, iv) the usage or the products application, v) the waste management of the products after their use and the waste of the process[12].

Such boundaries include cradle to grave, cradle to gate, gate to gate and gate to grave. Cradle to grave is a full LCA study applied to a supply chain or lifecycle from the origin of raw materials to the disposal of the products phase. Cradle to gate boundary focus on the sources of raw materials and the process for the product. Gate to grave boundary focus on the product production phase, the products distribution, the products use and the waste management. The gate to gate is an assessment of a partial product life cycle concerning the process mass balance and all activities associated with the production process. Furthermore, the LCA analysis at any boundary should define what was excluded (i.e. due to a lack of data, or inputs that were assumed negligible). In addition, the functional unit (FU) must provide a reference point at which the input and output of a process can be controlled and therefore allows for different systems to be treated as functionally equivalent. A reference flow can therefore be determined which allows for the quantification of product that can satisfy the function. It quantifies all inputs and outputs of material flows and assesses how these material flows affect the environment. The functional unit is a key element of LCA which has to be clearly defined. The definition should be precise and comparable enough so that the unit can be used throughout the study as reference. This enables comparison of different systems. The functional unit depends on the point of each research system boundary[13] interested, for example, 1) the number of products in kg of product, kWh of electricity produced, and lite of oil products, and 2) the economic value. As this research functional is 1 kg of $CaCO_3$ product, all mass and energy flows will be converted into how many of them needed to produce 1 kg of $CaCO_3$.

The second step is life cycle inventory (LCI) or process data collection that involves the compilation and quantification of inputs and outputs for a product throughout the life cycle of a process [78]. LCI accounts for everything involved in the system boundary or "system" of interest and it consists of detailed tracking information of all the flows (input and output) of the product system[14]. This means that the impact of the system can be determined and the data is used to reshape or redesign the system in order to reduce the impact. The forms to be used for data collection must be properly designed for optimal collection. Subsequently data is validated and related to the functional unit in order to allow the aggregation of results. Each LCA analysis need to clarify the source of data used in the analysis. There are

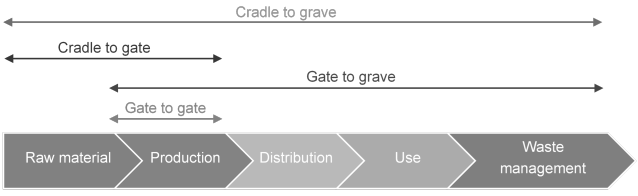

Figure 6.5.5: The system boundary of the LCA study based on ISO 14041 (1998)

[12] recycling or final disposal or composting (grave)

[13] System boundaries explains part life cycle is being considered for assessment

[14] Raw resources or materials, energy by type, water, and emissions to air, water and land by specific substance

Table 6.5.2: The correlation of midpoint impact and endpoint impact of LCA results

Midpoint impacts	Endpoint impacts		
	Human health	Ecosystems	Resource used
Global warming	√	√	
Stratospheric ozone depletion	√		
Ionizing radiation	√		
Ozone formation, Human health	√		
Fine particulate matter formation	√		
Ozone formation	√		
Terrestrial acidification		√	
Freshwater eutrophication		√	
Marine eutrophication		√	
Terrestrial ecotoxicity		√	
Freshwater ecotoxicity		√	
Marine ecotoxicity		√	
Human carcinogenic toxicity	√		
Human non-carcinogenic toxicity	√		
Land use			√
Mineral resource scarcity			√
Fossil resource scarcity			√
Water consumption			√

two types of the data which are 1) primary data, and 2) secondary data [77]. The primary data is the data that is collected by researchers directly from main sources like their experimental data or the production data from their company data log sheet. The secondary data is the data that is taken from other resources like the data from the report of journal publication. This research use the primary data of PCC produced by NaOH aqueous solution for LCA analysis. The results is compares with the secondary data of other PCC production processes from the available literatures : 1) fly ash[15] and ammonium chloride (NH_4Cl) [38], 2) Wollastonite ($CaSiO_3$) [15,37] ,3) steel slag, ammonium chloride (NH_4Cl) and hydrochloric acid (HCl) [39].

The later step is life cycle analysis (LCA) which converts or calculated the inputs and outputs for a functional unit into single unit environmental impacts such as global warming, fossil depletion, water depletion, human toxicity, etc. A very sensitive step in this calculation process is the allocation of flows. Most of the existing technical systems yield more than one product. Therefore, materials and energy flows regarding the process as a whole, as well as environmental releases must often be allocated to the different products. The allocation can be done whether in mass allocation, economic values allocation, or equity share[16]. The LCA can be done by using several available software, for instant, SimaPro, GaBi, openLCA, UmbertoLCA, Sphera, and etc. The reliability of the LCA results is depended on the method for the analysis and the right to access the relevant LCA emission factor[17] database.

SimaPro is a LCA software with many methods to analyse the environmental impact of the process using the mass and energy balance provided by the LCI. ReCiPe 2016 Midpoint(H) V1.02 method identifies eighteen key midpoint impact categories to convert LCI data into a limited number of characteristic factors that can be used on a global scale [79,80]. In the end, these categories can be narrowed down to three endpoint categories: Damage to human health, damage to ecosystems (natural environment) and damage to resource availability (natural resources). These three of endpoint impact categories, and the midpoint impact categories of this classification system are shown in Tab. 6.5.2.

Finally, interpretation was a vital stage. Results from the LCI and LCIA analysis were considered by the sensitivity analysis and suitable conclusions were drawn in line with the goal and scope of the study. The Interpretation phase of the LCA collated the overall findings of the LCI and delivered the results of the overall LCA. It gathered conclusions, identified limitations and gave recommendations for future research. The aim of an interpretation was to compare the results given by the goal and scope and make any revisions of that goal and scope to match with the overall result. The conclusion should discuss the methodology, limitations and results and check they sit in line with the goal and scope. If there were deviations from the intended results, the analysis should be carefully looked at and modified if needed.

Although LCA is frequently advocated for environmental evaluation of CCU, it is not yet a standard practice for CCU. A reliable environmental assessment of CCU is required to know whether a specific CCU process is environmentally favourable.

[15] From coal-fired plants
[16] The allocation by the right of ownership of the share holder
[17] Emission factor is used to convert the data to the relevant impact

Materials and methods

Mineral carbonation process based details

This research focuses on the mineral-carbon capture, conversion, and utilisation process. The carbon capture technology using both the absorption and crystallization processes. The reactants of these two processes included the flue gas and the waste brine[18] for the absorption and crystallisation steps, respectively. As it was mentioned above, there are 2 main processes involved in this system. In the first stage, a carbonation process takes place where the CO_2 from industrial flue gas is absorbed in NaOH aqueous solution. After that, a crystallization reaction takes place whereby the absorbed products from the previous stage reacts with $CaCl_2$ aqueous solution to produce precipitated $CaCO_3$ products (PCC). As the main process used NaOH to absorb CO_2 and convert to PCC, the process was assigned as the PCC-NaOH based process. The PCC-NaOH based process inputs required tap water for aqueous solution preparation and electricity for the functioning of the equipment. The process outputs are the precipitate $CaCO_3$ products, excess CO_2 gas emission to the air, and wastewater. All input and output data based on the primary data of the experiment results.

Lifecycle impacts analysis

The environmental impacts were calculated using a process based life cycle analysis (LCA) model [77–79]. The goal of this work was to determine the life cycle assessment of the PCC-NaOH based process as shown in Fig. 6.5.6 and compare the environmental impact of proposed mineral carbonation process with other three mineral CCU processes reported in the literatures; mineral carbonation into PCC processes from; 1) fly ash from power plants [38], 2) mineral wollastonite rock ($CaSiO_3$) [15,37], and 3) steel slag [39]. The LCA was investigated using gate to gate (G-G) system boundary and 1 kg of $CaCO_3$ product as functional unit for comparison.

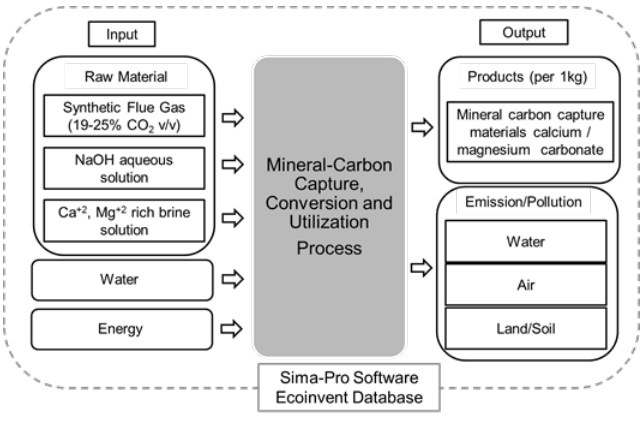

Figure 6.5.6: PCC-NaOH based process included in the details and boundaries of the ecological analysis

Part of the assumptions for the primary data in the present study was to consider the following inputs and raw materials: a synthetic flue gas, sodium hydroxide solution and a brine rich in Ca^{2+} and Mg^{2+} cations ($CaCl_2 \cdot 2\,H_2O$ and $MgCl_2 \cdot 6\,H_2O$). The energy and water used in this process was included in this analysis as an input of the system. This gate to gate system boundary LCA analysis is based on the following description and assumptions:

1. The pilot and lab scale absorption and crystallization processes were located at School of Engineering of the University of Aberdeen.
2. The tap water was delivered via a pipeline. This water is originated from Earth's surface waters. The emissions coming from the transport of the tap water were not considered or assumed to be negligible.
3. The electricity was produced by the UK grid mix. The emissions coming from the transport of electricity were not considered in this study or there were negligible.
4. The flue gas was associated with the emissions coming from an industrial source and transfer to the plant through the pipelines.
5. The brine rich in Ca and Mg are assumed to be of industrial origin as well. In this case, the waste brine from the industry is transferred to the plant through the pipeline system.
6. All the supplied electricity came from the EU low voltage grid.

The emission and pollution of the system was calculated using the database and guidelines from the Intergovernmental Panel on Climate Change (IPCC) [81]. The data was analysed with the SimaPro 8.5.2.0 LCA software. Data on resource (materials and energy) input, emissions and waste was collected from the primary data from the experiment for foreground PCC-NaOH based processes (Fig. 6.5.4) or collected from the literatures for other mineral carbonation into PCC process [15,37–39]. For background processes or where there was no data available in the LCI data, Ecoinvent 3 database was used containing all the input resources and energy, emissions and waste resulting from production all inputs and outputs per the functional unit. The ReCiPe 2016 Midpoint (H) V1.02 impact assessment method was selected for analysing the impact of lifecycle emissions. Although the results from the ReCiPe 2016 Midpoint analysis converts LCI data into eighteen key midpoint impact categories [79,80], this impact results are presented for six main categories; 1) GHG or climate change, 2) human toxicity, 3) ionising radiation, 4) land used change in term of agricultural land, 5) water depletion, and 6) fossil depletion.

Results and discussion

Mass and energy balance or the life cycle inventory (LCI) analysis

The environmental impact of the PCC-NaOH based process was carried out with an ecological analysis using the standard ISO 14044. The input and output data was obtained from the primary data of the experimental work to develop the life cycle inventory (LCI).

[18] Both from industrial emissions

The input and output data were taken from the average values of the experimental work. In the case of the energy usage, the data was taken in real time using the Mihome energy monitoring tool and software.

The data was obtained from a pilot scale carbon capture machine using the following settings: a volume of NaOH of 20 L, a solvent flow rate of $F_{solvent} = 3\,L/min$, a gas flow rate of $F_{Gas} = 1\,kg_{CO_2}/h$: $3.5\,kg_{Air}/h$. The overall reaction time was 65 min. The energy rate was fixed at 17 W during the preparation phase and at 75 W during the absorption phase (9th May, 2018). The mass of NaOH was calculated using the NaOH density value of 1.39 g/L corresponding to 47% NaOH solution. The dilution was accomplished using a common experimental mass balance: $C_1V_1 = C_2V_2$. The CO_2 mass was calculated from the operational time and the data from the mass controller.

The average mass in g/100ml was used as the conversion data. This corresponded to a total of 41 batch scale experiments. The carbonate products were mixed with the $CaCl_2$ solution at a mole ratio of 1:1. The $CaCl_2$ solution was prepared by dissolving $CaCl_2 \cdot 6\,H_2O$ (Tetra Chemicals, 77% purity) in distilled water. Each batch was prepared by mixing 50 ml of carbonate and 50 ml of brine to make in total a volume of 100 ml. The water content of the molecule ($CaCl_2 \cdot 6\,H_2O$) was taken into account to determine the mass of $CaCl_2$ during its reaction. However, the data was scaled up to consider 20L of brine as the LCI raw data. The overall conversion was 20 min and the energy rate was 54 W. A summary of every step of the process can be found in Tab. 6.5.3. Once the mass balance was completed (using a 40 L mixture), the data was converted to 1 kg $CaCO_3$ functional unit for the LCI of the process (Tab. 6.5.4).

The LCI results described in Tab. 6.5.4 revealed that the proposed process has high demand in terms of water consumption. To produce 1 kg of $CaCO_3$ product, the process required 12 L of water during the dilution of the NaOH aqueous solution. Additional water was consumed to wash the final PCC product. The process was performed under near-ambient conditions and the consumption of electric energy was quite small. Therefore, this could be considered a significant advantage of this process over other CCU technologies.

Life cycle analysis

Once the input data for the LCI analysis was compiled, the analysis took place using the LCA software SimaPro 8.5.2.0 with Ecoinvent 3 database and the ReCiPe 2016 Midpoint(H) V1.02 method. This LCA study assumed that the following information: i) Tap water was produced from the surface water and delivered via a pipeline without any emissions ii) The flue gas and brine were waste streams emitted from an industrial sector and transferred to the process plant without significant emissions. iii) All supplied electricity came from the UK low voltage grid. iv) The scope of LCA study was gate-to-gate. The LCA results provided in Fig. 6.5.5 of the PCC-NaOH based process include six main categories; 1) GHG or climate change, 2) human toxicity, 3) ionising radiation, 4) land used changes in term of agricultural land, 5) water depletion, and 6) fossil depletion.

Fig. 6.5.7 shows the main results of the ecological analysis. The process seems very resource intensive with a highly significant environmental impact coming from several categories of this analysis. Approximately, 80% of the total emissions in the PCC-NaOH based process came as a result of using the NaOH solvent. The total impact of the direct CO_2 emissions and the process waste was only 14%. Therefore, the use of NaOH can be considered the main hot-spot of this process. The emission factor of NaOH was calculated to be 0.9219 kg CO_2 equivalent per 1 kg of sodium hydroxide and can be considered high. This is the case because nearly all caustic soda is produced by the energy-intensive electrolysis of sodium chloride solution using one of the available cell types in the EU-27 and EFTA countries. This information was taken from the Euro Chlor 2013 database. A significant effort should be made to reduce the environmental impact produced by the caustic soda. Comparisons with other mineral carbonation into PCC production from the literature.

This section offers the comparison of operation cost environmental impacts between the absorption-based carbon capture and conversion process[19] and similar PCC production processes from secondary data from the literature, such as: i) fly ash[20] and ammonium chloride (NH_4Cl) [38], ii) wollastonite ($CaSiO_3$) [15,37], (iii) Steel slag, ammonium chloride (NH_4Cl) and hydrochloric acid (HCl) [39]. The literature data was retrieved and used in a way that allowed fair comparisons with the present experimental work.

Operation cost

The operation cost of the PCC-NaOH based process was calculated using the price of UK electricity, industrial water supply and sewage discharge, and the UK chemical supply. This cost was compared with the operation cost of similar PCC production processes of i) fly ash and ammonium chloride (NH_4Cl) [38], ii) wollastonite ($CaSiO_3$) [15,37], (iii) Steel slag, ammonium chloride (NH_4Cl) and hydrochloric acid (HCl) [39].

The operation cost of PCC-NaOH based process is £ 446 per ton of CO_2 removed that is higher than other PCC based process. The cost of the process operation mainly came from the cost of sodium hydroxide. This concluded that when the process relies on this alkaline solution the overall technology becomes expensive.

Environmental impact

The comparison of their environmental impact assessments was done adopting the gate to gate study boundary and a functional unit of 1 kg of $CaCO_3$ product. The system boundaries are shown in Fig. 6.5.5 and were consistent across all the studies. The raw material preparation, CO_2 capture, and separation process were considered. The infrastructure and the electricity used in these processes were also taken in consideration.

Starting from the top of the figure, the PCC production using a NaOH-based process consisted of the experimental data previously described (Fig. 6.5.8a). The first step

[19] Using NaOH and $CaCl_2$

[20] From coal-fired plants

Table 6.5.3: The raw mass and energy balance data for 20 L of the mixture solution

Input List	Amount	Unit	Process	Output List	Amount	Unit
CO_2 (flue gas)	0.8095	kg	Capture	CO_2 in	0.2478	kg
NaOH 47%	2.9574	kg		Excess gas		
Tab water	17.872	kg				
Electricity	0.0997	kWh				
$CaCl_2$ brine	20.922	kg	Conversion	$CaCO_3$	1.4503	kg
Electricity	0.018	kWh		Wastewater	40.863	kg

Table 6.5.4: The mass energy balance or LCI of PCC-NaOH based process based on 1 kg $CaCO_3$ as a functional unit

Input List	Amount	Unit	Process	Output List	Amount	Unit
Raw materials				**Product**		
CO_2 (flue gas)	0.5581	kg	1. Capture	$CaCO_3$	1.0000	kg
NaOH 47%	2.0392	kg	2. Conversion	**Waste**		
Tap water*	12.3229	kg		*Emission to water*		
$CaCl_2$ brine	14.4254	kg		Wastewater	28.1748	kg
Energy				*Emission to air*		
Electricity	0.0811	kWh		CO_2	0.1708	kg

*The water from washing process was excluded so, the mass of water was solely used for NaOH dilution 2solution.

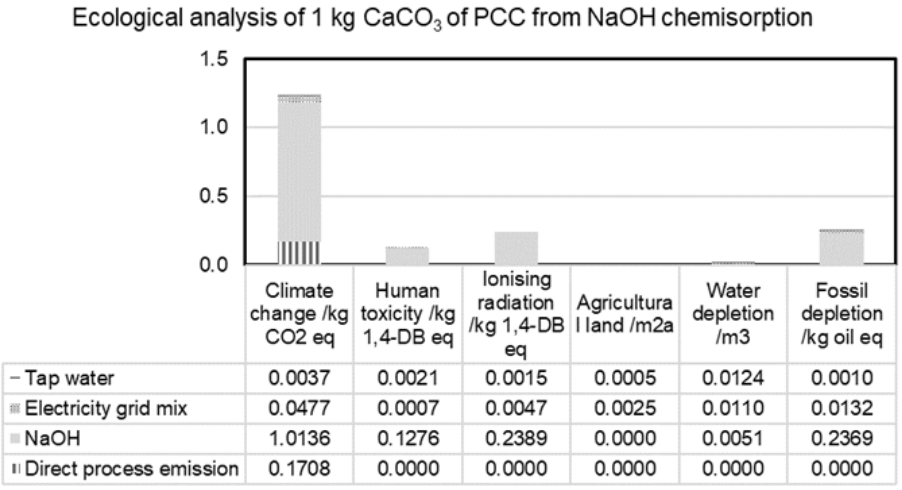

Figure 6.5.7: Ecological impact of the functional unit of 1 kg $CaCO_3$ product from PCC-NaOH based process

Table 6.5.5: The operation cost of PCC production processes

Process	Operation cost (£ per ton of CO_2 removed)	Reference
PCC-NaOH based process	446	This study
PCC-fly ash based process	101–816*	[38]
PCC-$CaSiO_3$ based process	102	[37]
PCC-steel slag based process	65	[39]

*The price in pound based on the conversion rate at $1 equal to £0.75 (data provided by Morningstar for Currency and Coinbase for Cryptocurrency on 8 Dec 2020)

corresponded to the carbonation process of CO_2 from industrial flue gas absorbed in a NaOH aqueous solution. The second stage consisted of a crystallization process between the absorbed products generated in the previous stage and the $CaCl_2$ aqueous solution. Inputs included the use of tap water for dilution of the reactants and the use of electricity for the well-functioning of the equipment. The outputs were the precipitate $CaCO_3$ products, excess CO_2 gas emitted to the air and wastewater.

The second process described in the figure was the fly ash-based process (Fig. 6.5.8b). This is a muti-step process with three distinctive steps. Initially, NH_3Cl solvent is used during the reaction and dissolution of the fly ash. Then during the second step, the solid residue (or solid waste) is separated by doing a solid-liquid separation process. Finally, in the third stage, there is a carbonation reaction whereby the

calcium ions react with the CO_2 flue gas stream to form $CaCO_3$. The NH_4Cl is recovered through a leaching process[21]. This process also requires the input of electricity associated with the equipment consumption. The input and output data was taken from the Aspen simulation results studied by Hosseini et al. (2016).

In the case of the $CaSiO_3$-based process, there is a pretreatment step of Wollastonite rocks whereby the $CaSiO_3$ material is crushed and grinded to a suitable particle size distribution (Fig. 6.5.8c). Then, $CaSiO_3$ is reacted with CO_2 using a wet process. This carbonation stage produced $CaCO_3$ as the main product, but also SiO_2 as the by-product of the reaction. The solid product is then recovered doing a solid-liquid separation and the wastewater discarded. The energy consumption corresponding to the crushing and grinding steps was obtained from Khoo and Tan (2006) and the energy coming from the solid-liquid saperation was given by Sanna et al. (2014).

Finally, the steel slag-based process from Fig. 6.5.8d is considered. In the direct carbonation with CO_2, various multi-step processes have been proposed for extracting calcium from slags before the precipitation of calcium carbonate takes place. For instance, calcium ions can be selectively dissolved from steelmaking slag in ammonium salt solutions (NH4Cl). Then, calcium carbonate is precipitated by bubbling CO_2-containing flue gas through the solution. The final calcium carbonate product is recovered by filtration and the solvent containing the ammonium salt is recirculated to the extractor where is finally regenerated. The results corresponding to the optimal reaction parameters and the process modelling was based on the Outotec HSC Chemistry software of Teir et al. (2016).

The compiled data regarding the LCI analysis of the three PCC processes described above can be read in Tab. 6.5.6 to Tab. 6.5.8 for the fly ash, Wollastonite and steel lag processes, respectively. Although the processes included different raw materials and gate to gate boundaries, the study used a common functional unit of 1 kg of $CaCO_3$ product to allow comparisons.

Further analysis of this data took place in the LCA software using SimaPro 8.5.2.0 with Ecoinvent 3 database and the ReCiPe 2016 Midpoint(H) V1.02 method. Thus, the methodology, tools and LCA assumptions described in the previous section were reproduced in this analysis. This included: i) Tap water was produced from the surface water and delivered via a pipeline without any emissions ii) The flue gas and brine were waste streams emitted from an industrial factory and transferred to the process plant without significant emissions. iii) All supplied electricity came from the UK low voltage grid. iv) the scope of LCA study was gate-to-gate.

The environmental impact calculated from these processes is shown in Fig. 6.5.9. The global warming potential (GWP) of the synthesized PCC was calculated and compared. The impact of this technology seems positive. By comparison, the fly ash-based PCC had a relatively higher impact than the others. The emissions from

[21] Leaching involves the use of a solvent to extract a solute from its carrier fluid.

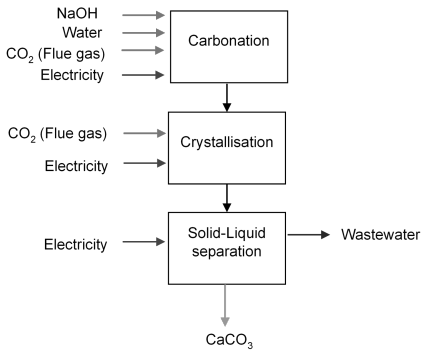

PCC-NaOH based process (our study)

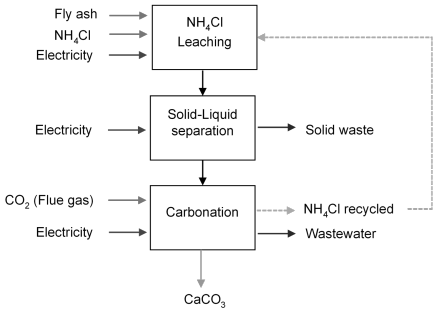

PCC-Fly ash based process [38]

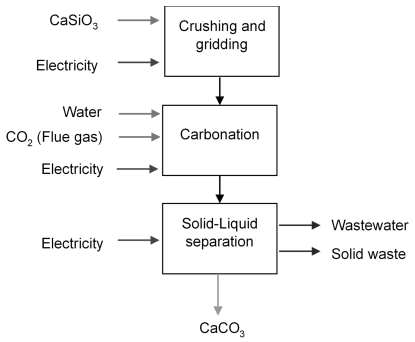

PCC-$CaSiO_3$ based process [15,37]

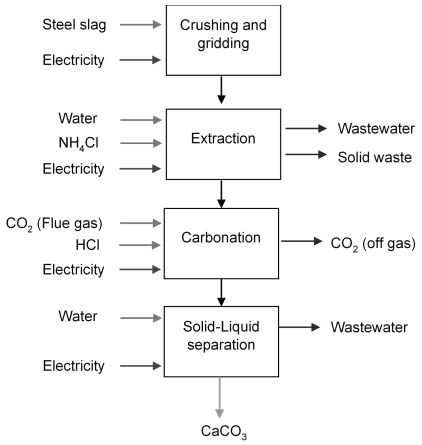

PCC-Steel slag based process [39]

Figure 6.5.8: CO2 utilisation as mineral carbonation into PCC process boundaries; (a) based on NaOH, and (b) based on fly ash, (c) based on $CaSiO_3$, and (d) based on Steel slag.

Table 6.5.6: LCI data for the Fly ash (from coal-fired plants) and ammonium chloride (NH_4Cl) process [38]

Input List	Amount	Unit
Raw materials		
Fly ash	5.0201	kg
NH_4Cl	0.2209	kg
Water	0.4096	kg
CO_2	3.3133	kg
Energy		
Electricity	3.6205	kWh

Process
1. NH_4 leaching
2. Solid-Liquid separation
3. Carbonation

Output List	Amount	Unit
Product		
$CaCO_3$	1.0000	kg
By Product		
$MgCO_3$	0.9739	kg
Waste		
Emission to water		
Wastewater	0.4157	kg
Emission to air		
CO2	2.4699	kg
Emission to soil		
$CaSO_4$	0.8855	kg
$CaCO_3$	0.5100	kg
MgO	0.9900	kg
CaO	0.2369	kg
SiO_2	0.2470	kg
Fe_2O_3	0.2952	kg
$CaFe_2O_5$	0.6888	kg
Other	0.3534	kg

the fly ash-based PCC were 3.5276 kg_{CO_2} eq/kg_{CaCO_3} while in the case of the NaOH-based PCC were 1.2358 kg_{CO_2} eq/kg_{CaCO_3}. The GWP of the steel slag-based and $CaSO_3$-based PCC were similar; their values were 0.5680 and 0.3809 kg_{CO_2} eq/kg_{CaCO_3}, respectively. Fly ash-based and NaOH-based PCC emissions were higher than $CaSO_3$ and steel slag-based PCC emissions because of the high emission of fly ash and NaOH. In the case of the fly ash-based PCC process, around 35% of total emissions came from the direct CO_2 emissions and the process waste. The fly ash and electricity contributions cannot be underestimated either. They corresponded to approximately 30% of total impact, and this could be considered a significant contribution. The remaining 4% and 1% contributions to the total impact were associated with the ammonium salt solution and water consumption, respectively. The GHG impacts of fly ash-based PCC could be significantly reduced once the waste from the process is minimized and there is a decrease in fly ash and energy penalty.

Table 6.5.7: LCI data for the Wollastonite ($CaSiO_3$) process [15,37]

Input List	Amount	Unit
Raw materials		
$CaSiO_3$	1.1607	kg
CO_2	0.4396	kg
Tab water	5.8033	kg
Energy		
Electricity	0.2054	kWh

Process
1. Crushing and gridding
2. Carbonation
3. Solid-Liquid separation

Output List	Amount	Unit
Product		
CaCO3	1.0000	kg
By Product		
SiO2	0.6003	kg
Waste		
Emission to water		
Wastewater	5.8033	kg
Emission to air		
CO2	0.0879	kg

However, when taking into account the impact categories indicated in Fig. 6.5.9, NaOH-based PCC could be a better choice given its lowest impact on agricultural land at 0.0029 m^2 per year. The reason behind lies in the fact that the NaOH-based PCC has a different contributor to the used impact than other PCC technologies. The main contributor to land used in a NaOH-based PCC process is generally associated with the source of energy. However, the source of raw materials is considered to have a greater contribution to the land used impact in the case of the other PCC based processes. The following components contributed to the land used impact in non NaOH technologies: fly ash for fly ash-based PCC, CaSiO3 for $CaSiO_3$-based PCC, and ammonium salts for steel slag-based PCC. NaOH-based PCC had lower water used impact as compared to other PCC based process. The water impact for NaOH-based PCC was affected by the water consumption in the process and by the energy source. For the human toxicity impact, the $CaSO_3$ and steel slag-based PCC toxicity were comparably low. The main contribution to toxicity was attributed to the chemical consumption and the waste generation in the capture system.

If the overall environmental impact of carbon capture technology is compared across the four different based materials[22], results indicate that steel slag-based PCC leads

[22] NaOH, fly ash, $CaSiO_3$ and steel slag

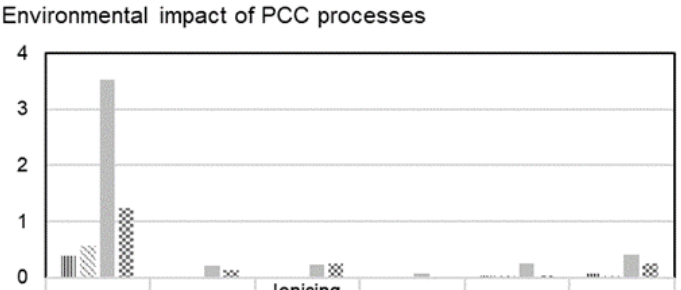

	Climate change /kg CO2 eq	Human toxicity /kg 1,4-DB eq	Ionising radiation /kg 1,4-DB eq	Agricultural land /m2a	Water depletion /m3	Fossil depletion /kg oil eq
PCC ,CaSO3 (Khoo, 2006)	0.3809	0.0094	0.0161	0.0064	0.0340	0.0618
PCC , Steel Slag (Tier 2016)	0.5680	0.0081	0.0131	0.0067	0.0288	0.0383
PCC , Fly ash (Hosseini 2016)	3.5276	0.2012	0.2252	0.0723	0.2540	0.4017
PCC , NaOH (Wanawan 2020)	1.2358	0.1303	0.2451	0.0029	0.0285	0.2512

Figure 6.5.9: Environmental impact from PCC production process based on different raw materails per 1 kg of $CaCO_3$ product

Table 6.5.8: LCI data for the Steel slag, ammonium chloride (NH_4Cl) and hydrochloric acid (HCl) process [39]

Input List	Amount	Unit
Raw materials		
Slag	2.1667	kg
NH_4Cl	0.0048	kg
Water	0.7000	kg
HCl solution	0.0115	kg
CO_2	0.8733	kg
Energy		
Electricity	0.2049	kWh

Process
1. Crushing and gridding
2. Extraction
3. Carbonation
4. Solid-Liquid separation

Output List	Amount	Unit
Product		
$CaCO_3$	1.0000	kg
Waste		
Emission to water		
Wastewater	3.1189	kg
Emission to air		
CO_2	0.4333	kg
Emission to soil		
Residual Slag	1.3890	kg

to the lowest environmental impact and fly ash-based PCC to the highest. This is largely due to the energy and raw materials used during the NH_3 leaching process [38] in the synthesis of fly ash-based PCC. In the NaOH-based process, results suggest that NaOH-based process had the lowest land used and water depletion impacts but had the second largest GWP. This was attributed to the use of NaOH solvent during the carbonation process.

The GWP impact of these four mineral CCU processes calculated in ton of CO_2 emission per ton of CO_2 removed (t CO_2 eq./t CO_2 removed) is presented in Fig. 6.5.10.

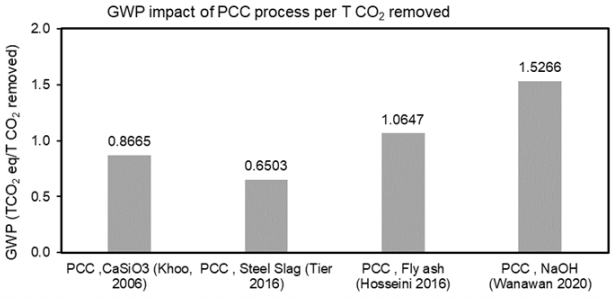

Figure 6.5.10: CO_2 emission of PCC production process based on different raw materails in ton of CO_2 emission per ton of CO_2 removed (t_{CO_2} eq/t_{CO_2}).

The worst mineral – CCU option appeared to be the PCC production from NaOH-based process which had the GWP at 1.5266 t_{CO_2} eq/t_{CO_2} removed. This was almost 2 times higher than PCC product from $CaSiO_3$ and steel slag based process. The second worst option was fly ash-based process PCC with the GWP 1.0647 t_{CO_2} eq/t_{CO_2} removed. Concluding, although a priori the mineral carbonation using NaOH seems promising, the fact is that when the process relies on this alkaline solution the overall technology becomes expensive and with high carbon emissions. All LCA used in this study were partial LCA analysis using gate to gate boundary study. Therefore, the results were changed if the full LCA analysis took into account the cradle to grave approach. However, it is worth mentioning that there were

many limitations to access the primary data for the full LCA analysis.

All CO_2 capture and utilisation (CCU) required substantial amount of energy the caused both direct CO_2 emission and indirect CO_2 emission. The direct CO_2 emissions are from the use of energy resources. The indirect emissions are from the burning of the energy resources such fossil burning; coal, diesel, gasoline and petroleum gas. In addition, some mineral process pathway required make-up of the chemical substrates like CO_2 absorbents, CO_2 adsorbents, and water. Apart from CO_2 emission that led to GHG problem, these energy resources and make up chemicals for mineral-CCU also cause resources depletion. In addition, the waste generation from the process such as solid waste, wastewater, and air pollution, could have an effect on the toxicity impact. The challenge of mineral-CCU is not only to reduce the emitting of CO_2 in comparison with the amount captured. It is also important to enable the lower energy consumption and fewer waste generation in the processes.

Conclusion

The process parameters from a NaOH based carbon capture and conversion process were determined in this chapter. This technology used available brines to produce precipitated calcium carbonate (PCC) with useful applications as construction material. A detailed life cycle analysis (LCA) of the process was included to determine the environmental impact of this technology, including six of the most important impacts; 1) GHG or climate change, 2) human toxicity, 3) ionising radiation, 4) land used change in term of agricultural land, 5) water depletion, and 6) fossil depletion. The main goal was to determine the environmental impact and the process hot-spot of the mineral carbonation when NaOH was used to synthesize $CaCO_3$. The boundary scope used in this study was gate to gate (G-G). The PCC synthesized with the NaOH-based process had a positive environmental impact. Results indicated that the NaOH solution used during the carbonation stage was the process hotspot in all the analysed impact categories. Based on the information provided by the Euro Chlor 2013 database, the NaOH solution produced by the electrolysis of a sodium chloride solution was an energy-intensive process. Significant efforts should be made to reduce the environmental impact of NaOH. The operation cost of PCC-NaOH based process is £ 446 per ton of CO_2 removed and it is more expensive than other PCC based process.

The environmental impacts from different technologies were compared with the results obtained from the NaOH-based mineral carbonation used to synthesize $CaCO_3$ (PCC). This corresponded to three similar technologies found in the literature [15,37–39]: fly ash-based, $CaSiO_3$-based and steel slag-based. The literature data was extracted and modelled with the same methodology and conditions that were used with the experimental NaOH-based process. This provided the basis for the environmental impact assessment. Comparisons of the processes were accomplished using the G-G study boundary and a functional unit of 1 kg of $CaCO_3$ product in every case. These PCC processes were different in several ways like they used different based materials: NaOH, fly ash, $CaSiO_3$ and steel slag. This difference showed a positive environmental impact. The fly ash-based PCC had the highest environmental impact due to the process waste streams (direct emission), the raw materials and the greater energy consumption. The NaOH-based PCC process displayed the lowest land used and water depletion impacts but had the second largest GWP. This was attributed to the use of NaOH solvent during the carbonation process. The $CaSO_3$ and steel slag-based PCC process were comparable and showed low toxicity impact thanks to their lower chemical consumption and lower waste generation in the capture system. Thus, processes that rely on this NaOH solution, have high carbon emissions and are expensive. The overall environmental impact of these four carbon capture technologies indicated not only long-term carbon sequestration potential and scalable markets, but also a technology that is still far from being environmental impact negative.

References

[1] IPCC, "Project Overview | Global Carbon Atlas," 2020. *http://www.globalcarbonatlas.org/en/content/project-overview* (accessed Jun. 17, 2020).

[2] G. Etiope, G. Ciotoli, S. Schwietzke, and M. Schoell, "Gridded maps of geological methane emissions and their isotopic signature," Earth Syst. Sci. Data, vol. 11, no. 1, pp. 1–22, Jan. 2019, doi:10.5194/essd-11-1-2019.

[3] E. Kriegler et al., "Pathways limiting warming to 1.5°C: A tale of turning around in no time?," Philos. Trans. R. Soc. A Math. Phys. Eng. Sci., vol. 376, no. 2119, May 2018, doi:10.1098/rsta.2016.0457.

[4] T. M. L. Wigley, P. D. Jones, and P. M. Kelly, "Global warming?," Nature, vol. 291, no. 5813, p. 285, 1981, doi:10.1038/291285a0.

[5] C. Figueres et al., "Emissions are still rising: ramp up the cuts," Nature, vol. 564, no. 7734. Nature Research, pp. 27–30, Dec. 06, 2018, doi:10.1038/d41586-018-07585-6.

[6] T. Gao, L. Shen, M. Shen, F. Chen, L. Liu, and L. Gao, "Analysis on differences of carbon dioxide emission from cement production and their major determinants," J. Clean. Prod., vol. 103, pp. 160–170, 2015, doi:10.1016/j.jclepro.2014.11.026.

[7] J. Wilcox, Carbon Capture Textbook. 2012.

[8] World Meteorological Organization, "World Meteorological Organization," 2020. *https://public.wmo.int/en* (accessed Sep. 15, 2020).

[9] C. Le Quéré et al., "Global carbon budget 2013," Earth Syst. Sci. Data Discuss., vol. 6, no. 2, pp. 689–760, Nov. 2013, doi:10.5194/essdd-6-689-2013.

[10] P. C. Chiang and S. Y. Pan, "Carbon dioxide mineralization and utilization," Carbon Dioxide Miner. Util., pp. 1–452, 2017, doi:10.1007/978-981-10-3268-4.

[11] UNFCCC, "United Nations Framework Convention on Climate Change," 2020. *https://unfccc.int/* (accessed Sep. 15, 2020).

[12] L. C. Pasquier, G. Mercier, J. F. Blais, E. Cecchi, and S. Kentish, "Technical & economic evaluation of a mineral carbonation process using southern Québec mining wastes for CO_2 sequestration of raw flue gas with by-product recovery," Int. J. Greenh. Gas Control, vol. 50, pp. 147–157, 2016, doi:10.1016/j.ijggc.2016.04.030.

[13] P. C. Psarras, S. Comello, P. Bains, P. Charoensawadpong, S. Reichelstein, and J. Wilcox, "Carbon Capture and Utilization in the Industrial Sector," Environ. Sci. Technol., vol. 51, no. 19, pp. 11440–11449, 2017, doi:10.1021/acs.est.7b01723.

[14] D. W. Keith, G. Holmes, D. St. Angelo, and K. Heidel, "A Process for Capturing CO_2 from the Atmosphere," Joule, 2018, doi:10.1016/j.joule.2018.05.006.

[15] A. Sanna, M. Uibu, G. Caramanna, R. Kuusik, and M. M. Maroto-Valer, "A review of mineral carbonation technologies to sequester CO_2," Chemical Society Reviews, vol. 43, no. 23. Royal Society of Chemistry, pp. 8049–8080, Dec. 07, 2014, doi:10.1039/c4cs00035h.

[16] J. H. Leie, J. H. Lee, I. K. Park, and C. H. Lee, "Techno-economic and environmental evaluation of CO_2 mineralization technology based on bench-scale experiments," J. CO_2 Util., vol. 26, no. June, pp. 522–536, 2018, doi:10.1016/j.jcou.2018.06.007.

[17] K. Arning et al., "Same or different? Insights on public perception and acceptance of carbon capture and storage or utilization in Germany," Energy Policy, vol. 125, no. November 2018, pp. 235–249, 2019, doi:10.1016/j.enpol.2018.10.039.

[18] T. Bruhn, H. Naims, and B. Olfe-Kräutlein, "Separating the debate on CO_2 utilisation from carbon capture and storage," Environ. Sci. Policy, vol. 60, pp. 38–43, 2016, doi:10.1016/j.envsci.2016.03.001.

[19] C. Fernández-Dacosta et al., "Prospective techno-economic and environmental assessment of carbon capture at a refinery and CO_2 utilisation in polyol synthesis," J. CO_2 Util., vol. 21, pp. 405–422, Oct. 2017, doi:10.1016/j.jcou.2017.08.005.

[20] R. J. Thorne et al., "Technical and environmental viability of a European CO_2 EOR system," Int. J. Greenh. Gas Control, vol. 92, Jan. 2020, doi:10.1016/j.ijggc.2019.102857.

[21] M. Fasihi, O. Efimova, and C. Breyer, "Techno-economic assessment of CO 2 direct air capture plants," J. Clean. Prod., vol. 224, pp. 957–980, Jul. 2019, doi:10.1016/j.jclepro.2019.03.086.

[22] R. Aldaco et al., "Bringing value to the chemical industry from capture, storage and use of CO 2: A dynamic LCA of formic acid production," Sci. Total Environ., vol. 663, pp. 738–753, May 2019, doi:10.1016/j.scitotenv.2019.01.395.

[23] R. M. Cuéllar-Franca and A. Azapagic, "Carbon capture, storage and utilisation technologies: A critical analysis and comparison of their life cycle environmental impacts," J. CO_2 Util., vol. 9, pp. 82–102, 2015, doi:10.1016/j.jcou.2014.12.001.

[24] A. Di Maria, R. Snellings, L. Alaert, M. Quaghebeur, and K. Van Acker, "Environmental assessment of CO_2 mineralisation for sustainable construction materials," Int. J. Greenh. Gas Control, vol. 93, p. 102882, Feb. 2020, doi:10.1016/j.ijggc.2019.102882.

[25] T. Pieri, A. Nikitas, A. Castillo-Castillo, and A. Angelis-Dimakis, "Holistic Assessment of Carbon Capture and Utilization Value Chains," Environments, vol. 5, no. 10, p. 108, Sep. 2018, doi:10.3390/environments5100108.

[26] Eurostat, "Renewable energy statistics - Statistics Explained," Eurostat, 2018. *https://ec.europa.eu/eurostat/statistics-explained/index.php/Renewable_energy_statistics* (accessed Sep. 15, 2020).

[27] SCOT Project, "SCOT Project," 2015. *http://www.scotproject.org/images/SCOT SERIA.pdf* (accessed Sep. 15, 2020).

[28] J. Patricio, A. Angelis-Dimakis, A. Castillo-Castillo, Y. Kalmykova, and L. Rosado, "Method to identify opportunities for CCU at regional level - Matching sources and receivers," J. CO_2 Util., vol. 22, no. September, pp. 330–345, 2017, doi:10.1016/j.jcou.2017.10.009.

[29] M. Matzen and Y. Demirel, "Methanol and dimethyl ether from renewable hydrogen and carbon dioxide: Alternative fuels production and life-cycle assessment," J. Clean. Prod., vol. 139, pp. 1068–1077, Dec. 2016, doi:10.1016/j.jclepro.2016.08.163.

[30] D. Parra, X. Zhang, C. Bauer, and M. K. Patel, "An integrated techno-economic and life cycle environmental assessment of power-to-gas systems," Appl. Energy, vol. 193, pp. 440–454, 2017, doi:10.1016/j.apenergy.2017.02.063.

[31] M. Shemfe et al., "Life cycle, techno-economic and dynamic simulation assessment of bioelectrochemical systems: A case of formic acid synthesis," Bioresour. Technol., vol. 255, pp. 39–49, May 2018, doi:10.1016/j.biortech.2018.01.071.

[32] N. von der Assen, From life-cycle assessment towards life-cycle design of carbon dioxide capture and utilization. 2015.

[33] N. Von Der Assen, J. Jung, and A. Bardow, "Life-cycle assessment of carbon dioxide capture and utilization: Avoiding the pitfalls," Energy Environ. Sci., vol. 6, no. 9, pp. 2721–2734, 2013, doi:10.1039/c3ee41151f.

[34] S. Kaiser and S. Bringezu, "Use of carbon dioxide as raw material to close the carbon cycle for the German chemical and polymer industries," J. Clean. Prod., vol. 271, p. 122775, 2020, doi:10.1016/j.jclepro.2020.122775.

[35] P. Styring, H. Le Connunck, and K. Armstrong, Carbon Capture and Utilisation in the green economy Using CO_2 to manufacture fuel, chemicals and materials. 2011.

[36] H. H. Khoo et al., "Carbon capture and mineralization in singapore: Preliminary environmental impacts and costs via LCA," Ind. Eng. Chem. Res., vol. 50, no. 19, pp. 11350–11357, 2011, doi:10.1021/ie200592h.

[37] H. H. Khoo and R. B. H. Tan, "Life cycle evaluation of CO_2 recovery and mineral sequestration alternatives," Environ. Prog., vol. 25, no. 3, pp. 208–217, 2006, doi:10.1002/ep.10139.

[38] T. Hosseini, N. Haque, C. Selomulya, and L. Zhang, "Mineral carbonation of Victorian brown coal fly ash using regenerative ammonium chloride - Process simulation and techno-economic analysis," Appl. Energy, vol. 175, pp. 54–68, 2016, doi:10.1016/j.apenergy.2016.04.093.

[39] S. Teir, T. Kotiranta, J. Pakarinen, and H. P. Mattila, "Case study for production of calcium carbonate from carbon dioxide in flue gases and steelmaking slag," J. CO_2 Util., vol. 14, pp. 37–46, 2016, doi:10.1016/j.jcou.2016.02.004.

[40] J. Li and M. Hitch, "Economic analysis on the application of mechanical activation in an integrated mineral carbonation process," Int. Biodeterior. Biodegrad., vol. 128, pp. 63–71, 2018, doi:10.1016/j.ibiod.2016.08.026.

[41] R. M. Santos, P. C. M. Knops, K. L. Rijnsburger, and Y. W. Chiang, "CO 2 Energy reactor - integrated mineral carbonation: Perspectives on lab-scale investigation and products valorization," Front. Energy Res., vol. 4, no. FEB, pp. 1–6, 2016, doi:10.3389/fenrg.2016.00005.

[42] R. M. Santos, W. Verbeeck, P. Knops, K. Rijnsburger, Y. Pontikes, and T. Van Gerven, "Integrated mineral carbonation reactor technology for sustainable carbon dioxide sequestration: 'CO2 Energy Reactor,'" Energy Procedia, vol. 37, pp. 5884–5891, 2013, doi:10.1016/j.egypro.2013.06.513.

[43] S. Teir, S. Eloneva, and R. Zevenhoven, "Production of precipitated calcium carbonate from calcium silicates and carbon dioxide," Energy Convers. Manag., vol. 46, no. 18–19, pp. 2954–2979, 2005, doi:10.1016/j.enconman.2005.02.009.

[44] H. Zhao, Y. Park, D. H. Lee, and A. H. A. Park, "Tuning the dissolution kinetics of wollastonite via chelating agents for CO_2 sequestration with integrated synthesis of precipitated calcium carbonates," Phys. Chem. Chem. Phys., vol. 15, no. 36, pp. 15185–15192, Sep. 2013, doi:10.1039/c3cp52459k.

[45] Y. Jiang and T. C. Ling, "Production of artificial aggregates from steel-making slag: Influences of accelerated carbonation during granulation and/or postcuring," J. CO_2 Util., vol. 36, pp. 135–144, Feb. 2020, doi:10.1016/j.jcou.2019.11.009.

[46] P. Markewitz et al., "Worldwide innovations in the development of carbon capture technologies and the utilization of CO_2," Energy Environ. Sci., vol. 5, no. 6, pp. 7281–7305, 2012, doi:10.1039/c2ee03403d.

[47] I. Dimitriou, P. García-Gutiérrez, R. H. Elder, R. M. Cuéllar-Franca, A. Azapagic, and R. W. K. Allen, "Carbon dioxide utilisation for production of transport fuels: Process and economic analysis," Energy Environ. Sci., vol. 8, no. 6, pp. 1775–1789, Jun. 2015, doi:10.1039/c4ee04117h.

[48] C. C. Lin and B. C. Chen, "Carbon dioxide absorption in a cross-flow rotating packed bed," Chem. Eng. Res. Des., vol. 89, no. 9, pp. 1722–1729, 2011, doi:10.1016/j.cherd.2010.11.015.

[49] N. A. Odeh and T. T. Cockerill, "Life cycle GHG assessment of fossil fuel power plants with carbon capture and storage," Energy Policy, vol. 36, no. 1, pp. 367–380, 2008, doi:10.1016/j.enpol.2007.09.026.

[50] B. R. Gurjar, C. S. P. Ojha, R. Y. Surampalli, T. C. Zhang, and P. P. Walvekar, "Carbon capture and storage: An overview," Carbon Capture Storage Phys. Chem. Biol. Methods, pp. 7–36, 2015, doi:10.1061/9780784413678.

[51] G. R. M. Dowson, D. G. Reed, J. M. Bellas, C. Charalambous, and P. Styring, "Fast and selective separation of carbon dioxide from dilute streams by pressure swing adsorption using solid ionic liquids," Faraday Discuss., vol. 192, pp. 511–527, 2016, doi:10.1039/c6fd00035e.

[52] J. Ma and R. H. Yoon, "Use of reactive species in water for CO_2 mineralization," Energy and Fuels, vol. 27, no. 8, pp. 4190–4198, 2013, doi:10.1021/ef400201a.

[53] C. C. Lin and C. R. Chu, "Feasibility of carbon dioxide absorption by NaOH solution in a rotating packed bed with blade packings," Int. J. Greenh. Gas Control, vol. 42, pp. 117–123, 2015, doi:10.1016/j.ijggc.2015.07.035.

[54] J. G. Shim, D. W. Lee, J. H. Lee, and N. S. Kwak, "Experimental study on capture of carbon dioxide and production of sodium bicarbonate from sodium hydroxide," Environ. Eng. Res., vol. 21, no. 3, pp. 297–303, 2016, doi:10.4491/eer.2016.042.

[55] M. Krauß and R. Rzehak, "Reactive absorption of CO_2 in NaOH: An Euler-Euler simulation study," Chem. Eng. Sci., vol. 181, pp. 199–214, 2018, doi:10.1016/j.ces.2018.01.009.

[56] M. Krauβ and R. Rzehak, "Reactive absorption of CO_2 in NaOH: Detailed study of enhancement factor models," Chem. Eng. Sci., vol. 166, pp. 193–209, 2017, doi:10.1016/j.ces.2017.03.029.

[57] Y. Tavan and S. H. Hosseini, "A novel rate of the reaction between NaOH with CO_2 at low temperature in spray dryer," Petroleum, vol. 3, no. 1, pp. 51–55, 2017, doi:10.1016/j.petlm.2016.11.006.

[58] H. Bustos-serrano, "The Carbonate System in Natural Waters," System, no. 2010, 2010.

[59] S. W. Lee, Y. J. Kim, Y. H. Lee, H. Guim, and S. M. Han, "Behavior and characteristics of amorphous calcium carbonate and calcite using $CaCO_3$ film synthesis," Mater. Des., vol. 112, pp. 367–373, Dec. 2016, doi:10.1016/j.matdes.2016.09.099.

[60] Donald L. Graf, "Crystallographic tables for the rhombohedral carbonates," Am. Mineragist, vol. 46, pp. 1283–1386, 1961, Accessed: Nov. 05, 2020. [Online]. Available: https://rruff.info/doclib/am/vol46/AM46_1283.pdf.

[61] Johan P.R. De Villiers, "Crystal structures of aragonite, strontianite, and witherite," American mineralogist, 1971. *https://rruff.info/doclib/am/vol56/AM56_758.pdf* (accessed Nov. 05, 2020).

[62] J. Wang and U. Becker, "Structure and carbonate orientation of vaterite (CaCO3)," Am. Mineral., vol. 94, pp. 380–386, 2009, doi:10.2138/am.2009.2939.

[63] N. Lippiatt, T. C. Ling, and S. Y. Pan, "Towards carbon-neutral construction materials: Carbonation of cement-based materials and the future perspective," Journal of Building Engineering, vol. 28. Elsevier Ltd, p. 101062, Mar. 01, 2020, doi:10.1016/j.jobe.2019.101062.

[64] L. McDonald, F. P. Glasser, and M. S. Imbabi, "A new, carbon-negative precipitated calcium carbonate admixture (PCC-A) for low carbon Portland cements," Materials (Basel)., vol. 12, no. 2, Feb. 2019, doi:10.3390/ma12040554.

[65] J. Ma, Z. Yu, C. Ni, H. Shi, and X. Shen, "Effects of limestone powder on the hydration and microstructure development of calcium sulphoaluminate cement under long-term curing," Constr. Build. Mater., vol. 199, pp. 688–695, Feb. 2019, doi:10.1016/j.conbuildmat.2018.12.054.

[66] T. Matschei, B. Lothenbach, and F. P. Glasser, "The role of calcium carbonate in cement hydration," Cem. Concr. Res., vol. 37, no. 4, pp. 551–558, Apr. 2007, doi:10.1016/j.cemconres.2006.10.013.

[67] M. B. Ali, R. Saidur, and M. S. Hossain, "A review on emission analysis in cement industries," Renew. Sustain. Energy Rev., vol. 15, no. 5, pp. 2252–2261, 2011, doi:10.1016/j.rser.2011.02.014.

[68] M. Tiong, R. Gholami, and M. E. Rahman, "Cement degradation in CO 2 storage sites: a review on potential applications of nanomaterials," Journal of Petroleum Exploration and Production Technology, vol. 9, no. 1. Springer Verlag, pp. 329–340, Mar. 01, 2019, doi:10.1007/s13202-018-0490-z.

[69] F. P. Glasser, G. Jauffret, J. Morrison, J. L. Galvez-Martos, N. Patterson, and M. S. E. Imbabi, "Sequestering CO 2 by Mineralization into Useful Nesquehonite-Based Products," Front. Energy Res., vol. 4, no. FEB, pp. 1–7, 2016, doi:10.3389/fenrg.2016.00003.

[70] Z. Cao, L. Shen, L. Liu, and S. Zhong, "Analysis on major drivers of cement consumption during the urbanization process in China," J. Clean. Prod., vol. 133, pp. 304–313, 2016, doi:10.1016/j.jclepro.2016.05.130.

[71] C. Unluer and A. Al-Tabbaa, "Impact of hydrated magnesium carbonate additives on the carbonation of reactive MgO cements," Cem. Concr. Res., vol. 54, pp. 87–97, 2013, doi:10.1016/j.cemconres.2013.08.009.

[72] R. Liu, F. Liu, S. Zhao, Y. Su, D. Wang, and Q. Shen, "Crystallization and oriented attachment of monohydrocalcite and its crystalline phase transformation," CrystEngComm, vol. 15, no. 3, pp. 509–515, 2013, doi:10.1039/c2ce26562a.

[73] S. A. Walling and J. L. Provis, "Magnesia-Based Cements: A Journey of 150 Years, and Cements for the Future?," Chem. Rev., vol. 116, no. 7, pp. 4170–4204, 2016, doi:10.1021/acs.chemrev.5b00463.

[74] A. Kirchofer, A. Brandt, S. Krevor, V. Prigiobbe, and J. Wilcox, "Impact of alkalinity sources on the life-cycle energy efficiency of mineral carbonation technologies," Energy Environ. Sci., vol. 5, no. 9, pp. 8631–8641, Sep. 2012, doi:10.1039/c2ee22180b.

[75] P. K. Naraharisetti, T. Y. Yeo, and J. Bu, "New classification of CO_2 mineralization processes and economic evaluation," Renew. Sustain. Energy Rev., vol. 99, no. August 2018, pp. 220–233, 2019, doi:10.1016/j.rser.2018.10.008.

[76] S. Giannoulakis, K. Volkart, and C. Bauer, "Life cycle and cost assessment of mineral carbonation for carbon capture and storage in European power generation," Int. J. Greenh. Gas Control, vol. 21, pp. 140–157, 2014, doi:10.1016/j.ijggc.2013.12.002.

[77] ISO 14042, "ISO14042," Environ. Manag. - Life Cycle Assess. - Life Cycle Impact Assess., vol. 1999, 2000.

[78] ISO 14041, "ISO14041," Environ. Manag. - Life Cycle Assess. - Goal Scope Defin. Invent. Anal., vol. 1998, 1998.

[79] ISO 14044, "ISO14044," Int. J. Life Cycle Assess., vol. 2006, no. 7, pp. 652–668, 2006, doi:10.1007/s11367-011-0297-3.

[80] S. Islam, S. G. Ponnambalam, and H. L. Lam, "Review on life cycle inventory: methods, examples and applications," J. Clean. Prod., vol. 136, pp. 266–278, 2016, doi:10.1016/j.jclepro.2016.05.144.

[81] IPCC, "2006 IPCC Guidelines for National Greenhouse Gas Inventories — IPCC," 2006. *https://www.ipcc.ch/report/2006-ipcc-guidelines-for-national-greenhouse-gas-inventories/* (accessed Jan. 15, 2021).

[82] US EPA, "GHGRP Chemicals | Greenhouse Gas Reporting Program (GHGRP) | US EPA," United States Environmental Protection Agency, 2019. *https://www.epa.gov/ghgreporting/ghgrp-chemicals#2019-subsector* (accessed Nov. 17, 2020).

6.6 Preparation of polycaprolactone nanoparticles via nanoprecipitation method and evaluation of their properties

Ewa Rybak[*,1] Tomasz Ciach[1]

1 Faculty of Chemical and Process Engineering, Warsaw University of Technology, Warsaw, Poland

Keywords: *polymeric nanoparticles*, *nanoprecipitation*, *polycaprolactone*, *drug-carriers*.

Abstract

In the field of pharmaceutical research, nanoprecipitation has been used as an alternative for common drug-carrier formulations. In this method, the nanoparticles (NPs) are formed by precipitation from dissolved polymer mixture after exposure to a polymer non-solvent. The use of polymeric nanoparticles as drug nanocarriers is a promising strategy for anticancer targeted therapy. The formulated particles' size significantly impacts drug loading, distribution in vivo, diffusion into the tumor, and cell uptake. Thus, it is essential for the successful progression of a drug delivery system.

The presented work concerns formulation of polymeric nanoparticles via polymer nanoprecipitation in a non-solvent (water) environment. A syringe pump was used to dose the organic phase into the aqueous phase. Different concentrations of polymer (polycaprolactone) and surfactant (Pluronic®F-127) were evaluated. The impact of studied parameters on the size and polydispersity of obtained nanoparticles were analyzed by Dynamic Light Scattering (DLS). Moreover, the cytotoxicity of the produced NPs was investigated by the in vitro cell culture of the human cervical tumor HeLa cells.

Preliminary results confirm that nanoparticles formed in the presence of surfactants are characterized by better stability in the water phase as well as after the lyophilization process, which was confirmed by DLS measurements. The increasing polymer concentration in the organic phase resulted in decreasing particle size depending on the concentration of surfactant.

Introduction

In the past decades, polymeric nanoparticles (NPs) have gained importance in many areas of industry. The reason for this trend is related to their unique properties, which meet a wide range of applications. In recent years, the evolution of polymeric nanoparticles as a drug delivery carrier has promoted the development of nano- and micromedicine [1]. Due to their size, NPs can move freely through the body via the smallest capillary vessels, and they are capable of transporting high doses of the drug directly into the cancerous cells while sparing healthy ones [2]. Thanks to these features of NPs, the biodistribution and pharmacokinetic properties of the transported drug molecules can be modified, leading to improved drug efficacy, reduction of side effects, and increased patient compliance [3]. NPs can make a significant change in medicine because of the ability of cell-targeting and controlled drug release [4]. They offer simple administration via oral, pulmonary, vascular, and parenteral injection. They do not need surgical removal upon complete drug release.

Nanoparticles can be formulated from inorganic or polymeric materials. Polymeric NPs are more common as they can be chemically modified to be biodegradable and biocompatible [5]. Enzymatic or non-enzymatic degradation in vivo of biodegradable substances results in toxicologically safe side products that are further removed by the normal metabolic pathways. The biodegradable polymers can be generally classified as natural polymers such as chitosan, hyaluronan, etc., and synthetic polymers that include polylactic-co-glycolic acid (PLGA), polycaprolactone (PCL), and others [6]. In general, synthetic polymers have many inherent advantages since their structures can be manipulated to generate specialized carriers to suit particular applications [7]. PCL is a semi-crystalline polyester that is hydrophobic, biodegradable and biocompatible. When compared to other polymers, the biodegradation of PCL is slow; hence, it can be highly suitable for the design of controlled release delivery systems [8-10]. The glass transition temperature (T_g) of – 60 °C and low melting point (59–64 °C) of PCL allows for the easy fabrication of delivery systems at reasonably low temperatures [10]. Furthermore, PCL has excellent blend compatibility with other polymers, facilitating tailoring of desired properties like degradation kinetics, hydrophilicity, and mucoadhesion [11,12].

The NPs' properties need to be optimized depending on the particular application, and to achieve the required characteristics of NPs, the method of a formulation is crucial [13]. There are various methods for NPs' formulation using biodegradable polymers, such as salting out, emulsification solvent evaporation, monomer polymerization, nanoprecipitation, etc. [14]. The nanoprecipitation method was first described by Fessi et al. [15]. The term refers to a simple process for the fabrication of polymeric nanoparticles. It involves the precipitation of a dissolved material into nanoparticles after exposure to a polymer non-solvent, that is miscible with the solvent [16]. The rapid diffusion of the solvent into the non-solvent phase results in the decrease of interfacial tension between the two phases, which increases the surface area and leads to the formation of small droplets of organic solvent [15,17]. The nanoprecipitation system consists of three basic components: the polymer (synthetic, semi synthetic, or natural), the polymer-solvent and the non-solvent of the polymer. The organic solvent (i.e., ethanol, acetone, toluene, or tetrahydrofuran), which is miscible in water and easy to remove by evaporation, is chosen as a polymer solvent. Due to this reason, acetone is the most frequently employed polymer solvent in this method [15,18,19]. However, in this study, tetrahydrofuran (THF) was chosen as a polymeric solvent. The melting point of THF is similar to acetone, and it can be removed from the reaction easily. Moreover, the solubility of

* Corresponding author, e-mail: *Ewa.Rybak.dokt@pw.edu.pl*

PCL in THF is better than its solubility in acetone. The non-solvent phase consists of a non-solvent (usually water) and surfactant. The polymers commonly used are biodegradable polyesters, especially PCL [20–24], polylactide (PLA) [25,26] and PLGA [27,28]. NPs are produced by slow addition of the organic phase to the aqueous phase under moderate stirring. The nanoparticles with a well-defined size are characterized by a narrow distribution formed instantaneously during the polymer solution's rapid diffusion in the non-solvent phase. The key variables determining the success of the method and affecting the physicochemical properties of NPs are those associated with the conditions of adding the organic phase to the aqueous phase, such as organic phase injection rate, aqueous phase agitation rate, the method of organic phase addition and the organic phase to aqueous phase ratio. Although a surfactant is not necessary to ensure the formation of NPs by nanoprecipitation, the particle size is influenced by the surfactant nature and concentration [20,23]. The surfactant's role is to stabilize the NPs of the dispersed phase after mixing two phases together. Moreover, the addition of surfactants helps to preserve the nanoparticle suspensions from agglomeration over long storage periods [15].

There are 3 stages of the formulation of nanoparticles: nucleation, growth by condensation, and growth by coagulation, which leads to the formation of polymer nanoparticles or aggregates [29,30]. The rate of each step determines the particle size, and the ratio of polymer concentration over the solubility of the polymer in the solvent mixture is the driving force of these phenomena. The key factor for uniform particle formation is a separation between the nucleation and the growth stages [31]. Preferably, operating conditions should allow a high nucleation rate strongly dependent on supersaturation and low growth rate. Nanoprecipitation is a simple, fast and reproducible method that is widely used for the preparation of both nanospheres and nanocapsules.

There are still many challenges for successful adjustment of nanoparticle formulation, i.e., low production efficiency, shorter residence time, and substandard scale-up feasibility of the manufacturing process. Therefore, an advanced approach that can produce nanoparticles with the desired physicochemical properties in an efficient manner is highly required [32]. The aim of the presented research was to investigate the production process of polymeric NPs, which can potentially be used as an anti-cancer drug carrier. For that purpose, the nanoprecipitation method, combined with a modification of process parameters, was employed. Moreover, the in vitro cell culture of the human cervical tumor HeLa cells was used to evaluate the cytotoxicity of formulated NPs.

Materials

Polycaprolactone (PCL) with a weight average molar mass of 14 000 g/mol was purchased from Sigma Aldrich/Merck (Poznan, Poland). Tetrahydrofuran (THF) (HPLC grade, purity 99.9%) was obtained from Chempur (Poland). Pluronic®F-127 was purchased from Sigma Aldrich/Merck (Poznan/Poland). Ultrapure water (MilliQ, Millipore) was used throughout the experiment. All other chemicals used were of reagent grade.

Methods

Preparation of polymeric nanoparticles

For the preparation of polymeric NPs, PCL was dissolved in tetrahydrofuran to form an organic phase with various polymer concentrations (1.0, 2.0, 5.0% w/v). 2 ml of the organic phase was added dropwise (0.15 ml/min) to 100 ml of the aqueous phase (ultrapure water MilliQ, Millipore) containing 0.04 mM and 0.08 mM of surfactant (Pluronic®F-127) under magnetic stirring (1000 rpm) at room temperature. NPs were formed and turned the solution into milky colloidal suspension. The obtained suspension was stirred magnetically for 10 min. Solvent evaporation was carried out subsequently under high temperature and reduced pressure conditions. The obtained suspension was subjected to filtration (0.45 μm).

Particle size analysis

The average particle sizes and polydispersity index (PDI) were measured by dynamic light scattering (DLS) using a Malvern Zetasizer (Nano ZS, Malvern Instruments), equipped with a detector to measure the intensity of the scattered light at 173° to the incident beam. All measurements were replicated at least three times and presented as mean values with standard deviations.

Cytotoxicity evaluation

For the cytotoxicity evaluation, an MTT cell proliferation assay (Thiazolyl Blue Tetrazolium Bromide, Sigma-Aldrich), according to ISO 10993–5 standard, was performed [33]. First, the human cervical tumor HeLa cell line was cultured in Dulbecco's Modified Eagle Medium (DMEM, Life Technologies) supplemented with bovine serum (10% v/v, Life Technologies) and a mixture of penicillin-streptomycin antibiotics (1% v/v, Life Technologies) in an incubator (37 °C, 5% CO_2). Cells were seeded in a 96-well plate at a concentration of 1×10^4 cells/well and incubated for 24 h. For this assay, a sample of NPs formulated with 5.0 % of PCL and 0.04 mM of surfactant was prepared as mentioned in the Preparation of polymeric nanoparticles section and then lyophilized. Later, the sample was sterilized with UV for 60 minutes. The NPs were suspended in DMEM, a series of dilutions was prepared (10, 5, 1, 0.1 mg/ml), and the suspensions were placed in the wells (100 μl/well). Samples were incubated for the next 24 h. DMEM medium was used as a negative control. Then, the MTT solution (1 mg/ml in DMEM without supplements and phenol red) was added. Plates were incubated for 4 h in an incubator. Afterward, the medium was gently removed, isopropanol was added to dissolve the resulting crystals. The absorbance of the obtained solution was measured at 570 nm with the use of a plate reader (Epoch, BioTek, USA). Cell viability was calculated using the following formula:

$$cell\ viability\ (\%) = \frac{A_{S570}}{A_{C570}} \cdot 100\% \qquad (6.6.1)$$

where: A_{S570} is the mean value of the sample absorption measured at 570 nm, A_{C570} is the mean value of the negative control absorption measured at 570 nm.

Results

Particle size, size distribution and polydispersity index

The mean size and polydispersity of formulated nanoparticles with different concentration of PCL and Pluronic®F-127 was determined. Fig. 6.6.1 presents the mean diameter and PDI of NPs obtained with 1.0, 2.0, 5.0% PCL with 0.04 mM of surfactant. Both mean diameter and PDI decrease with the increase of polymer concentration.

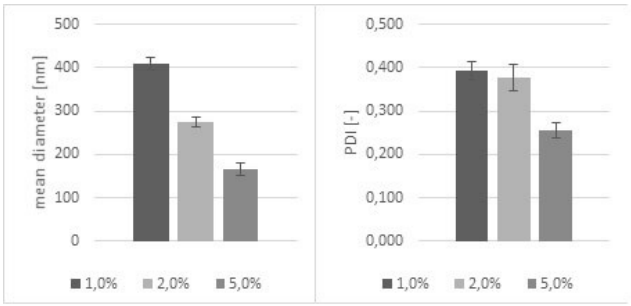

Figure 6.6.1: Mean values of nanoparticle sizes and PDI of nanoparticles formulated with different concentration of PCL and 0.04 mM of Pluronic®F-127.

The nanoprecipitation of 5.0% PCL from THF into the aqueous phase with 0.04 mM Pluronic ®F-127 gave 166 ± 15 nm particles (PDI 0.256 ± 0.016). With the increase of surfactant's concentration (Fig. 6.6.2), the smallest particles occurred with 1.0% of PCL (132 ± 10 nm), but with a high polydispersity index (0.424 ± 0.069). 2.0% of PCL gave almost monodisperse suspension of particles with 176 ± 12 nm mean diameter. Higher concentration of surfactant allowed to obtain a narrow size distribution of NPs for all 3 polymer concentrations. The smallest particles (100–280 nm) were formulated with the highest PCL concentration (Fig. 6.6.4).

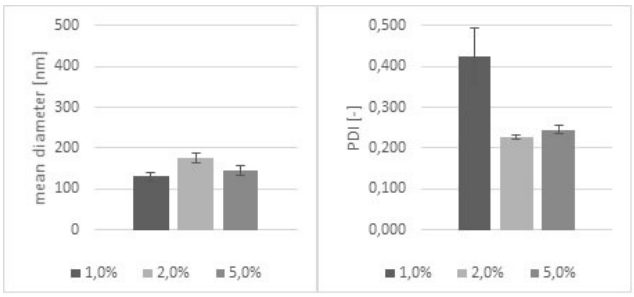

Figure 6.6.2: Mean values of nanoparticle sizes and PDI of nanoparticles formulated with different concentration of PCL and 0.08 mM of Pluronic®F-127.

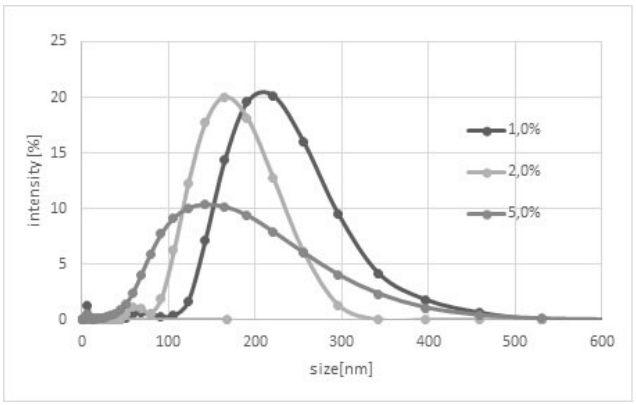

Figure 6.6.3: Size distribution by Intensity for PCL NPs obtained with different concentration of polymer and 0.04 mM Pluronic®F-127.

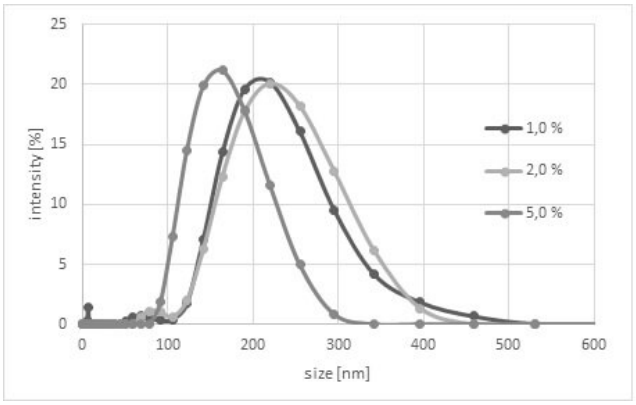

Figure 6.6.4: Size distribution by Intensity for PCL NPs obtained with different concentration of polymer and 0.08 mM Pluronic®F-127.

Cytotoxicity evaluation

The results of the cytotoxicity assay are presented in Fig. 6.6.5. Values were normalized against a negative control (cells with cell culture medium). Based on those results, it can be concluded that with the increase in NPs concentration, cell viability decreases. According to the ISO standard [33], the material can be considered non-toxic if the cell viability after contact with materials is above 70%. Therefore, it can be assumed that PCL NPs were cytotoxic for HeLa cells at all concentrations apart from 0.1 mg/ml.

Discussion

The preparation of PCL nanoparticles and factors affecting the mean size and PDI of NPs formulated by the nanoprecipitation method were investigated. The conducted experiments confirmed that if the mixing in the system is at the appropriate speed, the particles are kinetically blocked, and their diameters and polydispersity can be controlled [16, 34]. Such control is difficult to achieve in large systems where mixing is slower and aggregation of nanoparticles occurs, and Ostwald ripening increases polydispersity [35]. Therefore, the main goal of this research was to develop optimal conditions for the preparation of nanoparticles. It was found that polymer concentration has a significant

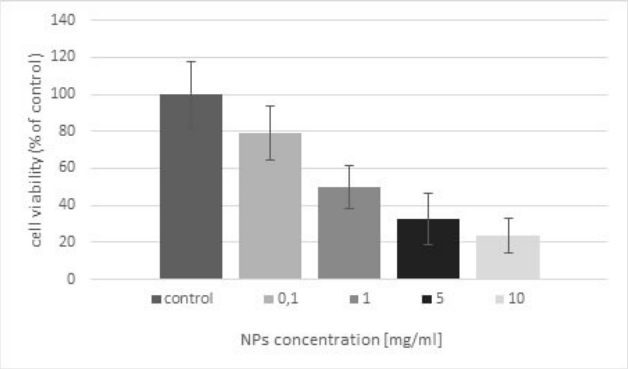

Figure 6.6.5: MTT assay results for evaluation of cell toxicity for PCL nanoparticles. The measured size of NPs in this assay was 140 ± 3 nm (PDI 0.294 ± 0.030).

effect on particle size. Moreover, the type and concentration of surfactant affect NPs' size to a certain limit. It is assumed that nanoparticle formation occurs when both the organic and aqueous phases are in contact. The solvent diffuses from the organic into the aqueous phase and takes along some polymer chains which are still in solution, then as the solvent spreads through the water, the polymer chains aggregate, forming nanoparticles [13]. Increasing the polymer content in the organic phase consequently increases its viscosity which is associated with a higher mass transfer resistance, which leads to a negative effect on the distribution efficiency of the polymer-solvent composition to the outer aqueous phase and the formulation of large nanoparticles [36]. Here, the results obtained with a low concentration of surfactant (0.04 mM, Fig. 6.6.1) were opposite to those presented by Ajiboye et al. [36], as with the increase of polymer concentration, the mean size of NPs decreases. This may be justified by the fact that at the highest polymer concentration (Fig. 6.6.1), more nuclei were obtained to formulate NPs with small sizes but high polydispersity value (over 0.200) due to uneven growth. The particle size was found to decrease (Fig. 6.6.2) upon an increase in the surfactant concentration. This might be attributed to the surfactant's ability to reduce the interfacial tension between the aqueous and organic phases so that a higher amount of surfactant results in an emulsion with a high interfacial area, which means a smaller particle size with good stability. The results were in agreement with those reported by Srikar et al. in the case of aqueous core nanocapsules containing tenofovirdisoproxil fumarate [37] and also with those reported by Gupta et al. in the case of solid lipid nanoparticles [38]. Moreover, with 0.08 mM of Pluronic®F-127, the size distribution was narrow for all 3 concentrations of PCL in contrast to 0.04 mM of surfactant, where a high concentration of PCL resulted in wide size distribution while low PDI. The aggregation of PCL NPs during the solvent evaporation process is a notable problem. In order to prevent PCL NPs aggregation, polymer stabilizers are often used, such as poly (vinyl alcohol) (PVA) [39], poly (vinyl pyrrolidone), Tween®80 [40]. Here, Pluronic®F-127 was applied in 2 different concentrations that resulted in preventing NPs aggregation. It is assumed that the particle size can be further decreased to less than 100 nm by minimizing the concentration of polymer in the solvent used for nanoprecipitation with a high concentration of surfactant. In addition, the cytotoxicity analysis demonstrated that the prepared PCL nanoparticles are nontoxic for HeLa cells only in small concentration (0.1 mg/ml). After incubation with higher NPs' concentration, the viability of Hela cells was below 70%. Such results were expected, as the high surfactant concentration used in the experiment may be toxic to cancerous cells. Moreover, polymeric NPs as drug nanocarriers may themselves be toxic to cancerous cells, especially in high concentrations [41].

In conclusion, the fundamental knowledge about the processes in the preparation of polymeric NPs is still limited. The effects of the homogenization conditions and the control of droplet size distribution, which determines the particle size and morphology, are not plain. Future research work should focus on the precise control over the properties of the produced NPs depending on the subsequent application. However, taking into account the presented research, it can be concluded that nanoprecipitation is a suitable method for the formulation of polymeric nanoparticles. Still, the influence of all the process parameters should be carefully examined in order to optimize the production process.

Acknowledgements

This work was supported by the Dean's grant, Faculty of Chemical and Process Engineering, Warsaw University of Technology (nr PSP 504/04430/1070/44.000000).

References

[1] Wang, Y., Li, P., Truong-Dinh Tran, T., Zhang, J., & Kong, L. (2016). Manufacturing Techniques and Surface Engineering of Polymer Based Nanoparticles for Targeted Drug Delivery to Cancer. *Nanomaterials*, 6(2), 26. doi:10.3390/nano6020026

[2] Liu Z, Jiao Y, Wang Y, Zhou C, Zhang Z. (2008) Polysaccharides-based nanoparticles as drug delivery systems. Adv Drug Deliv Rev.; 60:1650. doi:10.1016/j.addr.2008.09.001

[3] Gonçalves C, Pereira P, Gama M. (2010) Self-assembled hydrogel nanoparticles for drug delivery applications. *Materials.*; 3:1420

[4] Sun J., et al. (2014) Encapsulating magnetic and fluorescent mesoporous silica into thermosensitive chitosan microspheres for cell imaging and controlled drug release in vitro, *Colloids and Surfaces B: Biointerfaces*, 113, 1–9. doi:10.1016/j.colsurfb.2013.08.015

[5] Yang YY, Wang Y, Powell R, Chan P. (2006) Polymeric core-shell nanoparticles for therapeutics. *Clin Exp Pharmacol Physiol.*;33:557. doi:10.1111/j.1440-1681.2006.04408.x

[6] Makadia HK, Siegel SJ. (2011) Poly lactic-co-glycolic acid (PLGA) as biodegradable controlled drug delivery carrier. *Polymers*;3:1377. doi:10.3390/polym3031377

[7] Crucho C, Barros MT. (2015) Formulation of functionalized PLGA polymeric nanoparticles for targeted drug delivery. *Polymer.*; 68:41. doi:10.1016/j.polymer.2015.04.083

[8] Seremetaa KP, Chiappettaa DA, Sosnik A. (2013) Poly (ε-caprolactone), Eudragit® RS 100 and poly(ε-caprolactone)/Eudragit® RS100 blend submicron particles for the sustained release of the antiretroviral efavirenz. *Colloids Surf B: Biointerfaces.*; 102:441. doi:10.1016/j.colsurfb.2012.06.038

[9] Woodruff MA, Hutmacher DW. (2010) The return of a forgotten polymer polycaprolactone in the 21st century. *Prog Polym Sci.*; 35:1217. 11. doi:10.1016/j.progpolymsci.2010.04.002

[10] Karuppuswamy P, Venugopal JR, Navaneethan B, Laiva AL, Ramakrishna S. (2015) Polycaprolactone nanofibers for the controlled release of tetracycline hydrochloride. *Mater Lett.*; 141:180; doi:10.1016/j.matlet.2014.11.044

[11] Bilensoy E, Sarisozen C, Esendagli G, Dogan AL, Aktas Y, Sen M, et al. (2009) Intravesical cationic nanoparticles of chitosan and polycaprolactone for the delivery of mitomycin C to bladder tumors. *Int J Pharm.*; 371:170. 13. doi:10.1016/j.ijpharm.2008.12.015

[12] Payyappilly SS, Panja S, Mandal P, Dhara S, Chattopadhyay S. (2015) Organic solvent-free low temperature method of preparation for self-assembled amphiphilic poly(ε-caprolactone)–poly(ethylene glycol)block copolymer based nanocarriers for protein delivery. *Colloids Surf B: Biointerfaces.*; 135:510. doi:10.1016/j.colsurfb.2015.07.075

[13] Rao, J. P., & Geckeler, K. E. (2011). Polymer nanoparticles: Preparation techniques and size-control parameters. *Progress in Polymer Science (Oxford)*, 36(7), 887–913. doi:10.1016/j.progpolymsci.2011.01.001

[14] Kumar, A., & Sawant, K. (2013). Encapsulation of exemestane in polycaprolactone nanoparticles: Optimization, characterization, and release kinetics. *Cancer Nanotechnology*, 4(4–5), 57–71. doi:10.1007/s12645-013-0037-4

[15] Fessi H, Puisieux F, Devissaguet JP, Ammoury N, Benita S. (1989) Nanocapsule formation by interfacial polymer deposition following solvent displacement. *Int J Pharm*; 55:R1–4. doi:10.1016/0378-5173(89)90281-0

[16] Karnik, R. et al. (2008) Microfluidic platform for controlled synthesis of polymeric nanoparticles. *Nano Letters 8*, 2906–2912. doi:10.1021/nl801736q

[17] Mishra B, Patel BB, Tiwari S. (2010) Colloidal nanocarriers: a review on formulation technology, types and applications toward targeted drug delivery. *Nanomedicine: NBM*; 6:9–24. doi:10.1016/j.nano.2009.04.008

[18] Dalpiaz A, Vighi E, Pavan B, Leo E. (2009) Fabrication via a nonaqueous nanoprecipitation method, characterization and in vitro biological behavior of N6-cyclopentyladenosine-loaded nanoparticles. *J Pharm Sci*; 98:4272–84. doi:10.1002/jps.21710

[19] Fong-Yu C, Saprina Ping-Hsien W, Chio-Hao S, Tsung-Liu T, Ping- Ching W, Dar-Bin S, Jyh-Horng C, Patrick Ching-Ho H, Chen-Sheng Y. (2008) Stabilizer-free poly(lactide-co-glycolide) nanoparticles for multimodal biomedical probes. *Biomaterials*; 29:2104–12. doi:10.1016/j.biomaterials.2008.01.010

[20] Limayem I, Charcosset C, Sfar S, Fessi H. (2006) Preparation and characterization of spironolactone-loaded nanocapsules for paediatric use. *Int J Pharm*; 325:124–31. doi:10.1016/j.ijpharm.2006.06.022

[21] Zili Z, Sfar S, Fessi H. (2005) Preparation and characterization of poly- ε -caprolactone nanoparticles containing griseofulvin. *Int J Pharm*; 294:261–7. doi:10.1016/j.ijpharm.2005.01.020

[22] Kim E, Yang J, Choi J, Jin-Suck S, Yong-Min H, Haam S. (2009) Synthesis of gold nanorod-embedded polymeric nanoparticles by a nanoprecipitation method for use as photothermal agents. *Nanotechnology*; 20:365602. doi:10.1088/0957-4484/20/36/365602

[23] Moinard-Chécot D, Chevalier Y, Briancon S, Beney L, Fessi H.(2008) Mechanism of nanocapsules formation by the emulsion–diffusion process. *J Colloid Interface Sci*; 317:458–68. doi:10.1016/j.jcis.2007.09.081

[24] Ferranti V, Marchais H, Chabenat C, Orecchioni AM, Lafont O. (1999) Primidone-loaded poly- ε -caprolactone nanocapsules: incorporation efficiency and in vitro release profiles. *Int J Pharm*; 193:107–11. doi:10.1016/s0378-5173(99)00325-7

[25] Seyler I, Appel M, Devissaguet JP, Legrand P, Barratt G. (1999) Macrophage activation by a lipophilic derivative of muramyldipeptide within nanocapsules: investigation of the mechanism of drug delivery. *J Nanopart Res*; 1:91–7.

[26] Legrand P, Lesieur S, Bochot A, Gref R, Raatjes W, Barratt G, Vauthier C. (2007) Influence of polymer behaviour in organic solution on the production of polylactide nanoparticles by nanoprecipitation. *Int J Pharm*; 344:33–43. doi:10.1016/j.ijpharm.2007.05.054

[27] Nehilla BJ, Bergkvist M, Popat KC, Desai TA. (2008) Purified and surfactant- free coenzyme Q10-loaded biodegradable nanoparticles. *Int J Pharm*; 348:107–14. doi:10.1016/j.ijpharm.2007.07.001

[28] Yallapu MM, Gupta BK, Jaggi M, Chauhan SC. (2010) Fabrication of curcumin encapsulated PLGA nanoparticles for improved therapeutic effects in metastatic cancer cells. *J Colloid Interface Sci*; 351:19–29. doi:10.1016/j.jcis.2010.05.022

[29] Rao, J. P., & Geckeler, K. E. (2011). Polymer nanoparticles: Preparation techniques and size-control parameters. *Progress in Polymer Science*, 36(7), 887–913. doi:10.1016/j.progpolymsci.2011.01.001

[30] Marchiso, D. L., Barresi, A. A., & Garbero, M. (2002). Nucleation, growth, and agglomeration in barium sulfate turbulent precipitation. *AIChE Journal*, 48(9), 2039–2050. doi:10.1002/aic.690480917

[31] Johnson, B. K., & Prud'homme, R. K. (2003). Flash NanoPrecipitation of Organic Actives and Block Copolymers using a Confined Impinging Jets Mixer. *Australian Journal of Chemistry*, 56(10), 1021–1024. doi:10.1071/CH03115

[32] Gardouh, A. & Ghorab, M. (2015) Polymeric-nanoparticles: Influence of polymer, surfactant and composition on particle size. *Word Journal of Pharmaceutical Sciences*., 3(12), 2308-2322

[33] International Organization for Standardization, (2009) "Biological Evaluation of Medical Devices – Part 5: Tests for in Vitro Cytotoxicity, 5"

[34] Liu, Y., Cheng, C., Liu, Y., Prud'homme, R. K., & Fox, R. O. (2008). Mixing in a multi-inlet vortex mixer (MIVM) for flash nano-precipitation. *Chemical Engineering Science*, 63(11), 2829–2842. doi:10.1016/j.ces.2007.10.020

[35] D'Addio, S. M., & Prud'homme, R. K. (2011). Controlling drug nanoparticle formation by rapid precipitation. *Advanced Drug Delivery Reviews*, 63(6), 417–426. doi:10.1016/j.addr.2011.04.005

[36] Ajiboye, A. L., Trivedi, V., & Mitchell, J. C. (2018). Preparation of polycaprolactone nanoparticles via supercritical carbon dioxide extraction of emulsions. *Drug Delivery and Translational Research*, 8(6), 1790–1796. doi:10.1007/s13346-017-0422-3

[37] Srikar, G., & Rani, A. P. (2019). Study on influence of polymer and surfactant on in vitro performance of biodegradable aqueous-core nanocapsules of tenofovirdisoproxil fumarate by response surface methodology. *Brazilian Journal of Pharmaceutical Sciences*, 55, 1–11. doi:10.1590/s2175-97902019000118736

[38] Gupta B, Poudel BK, Pathak S, Tak JW, Lee HH, Jeong JH, Choi HG, Yong CS, Kim JO. Effects of formulation variables on the particle size and drug encapsulation of imatinib-loaded solid lipid nanoparticles. *AAPS PharmSciTech.* 2015;17(3):652-62. doi:10.1208/s12249-015-0384-z

[39] Abdelwahed, W., Degobert, G., Fessi, H. (2006) A pilot study of freeze drying of poly(ε -caprolactone) nanocapsules stabilized by poly(vinyl alcohol): formulation and process optimization. *Int. J. Pharm.* 309, 178–188

[40] Alyautdin, R.N., Petrov, V.E., Langer, K., Berthold, A., Kharkevich, D.A., Kreuter, J. (1997) Delivery of loperamide across the blood–brain barrier with polysorbate 80-coated polybutylcyanoacrylate nanoparticles. *Pharm. Res.* 14, 325–328. doi:10.1023/A:1012098005098

[41] Voigt, N., Henrich-Noack, P., Kockentiedt, S., Hintz, W., Tomas, J., & Sabel, B. A. (2014). Toxicity of polymeric nanoparticles in vivo and in vitro. *Journal of Nanoparticle Research*, 16(6). doi:10.1007/s11051-014-2379-1

6.7 CFD study of monolithic structures with enhanced transport properties

Katarzyna Sindera*,1

1 Institute of Chemical Engineering, Polish Academy of Sciences, Gliwice, Poland

Keywords: *short-channel structures*, *computational fluid dynamics*, *turbulence models*, *heat transport*.

Abstract

Heat transfer properties of short-channel monolith of hexagonal channel cross-section shape were CFD modeled. Different turbulence models were introduced: $k-\varepsilon$ standard, $k-\varepsilon$ Realizable, $k-\varepsilon$ RNG, $k-\omega$ SST and laminar. The structure tested displays more beneficial heat transfer properties than long monolith, but not as high as packed bed. Choice of the proper turbulence model for the flow simulations through the structure tested is important when considering $Re > 800$. Heat transfer coefficients calculated on the basis of $k-\varepsilon$ models are visibly greater than in the case of laminar and $k-\omega$ SST models.

Introduction

Importance of catalysis for the human health and environment

Rapid industrial and civilisational development have increased the amount of dangerous substances emitted to the atmosphere. Examples of such substances include methane, nitrogen oxides (NO_x), sulfur oxides (SO_x,), particulate matter (for example, $PM_{2.5}$ and PM_{10}), and a wide group of volatile organic compounds (VOCs). Catalytic processes enable the effective elimination of toxic emissions. Heterogeneous catalysts are of particular importance, and are used in most chemical and environmental processes [1]. In atmospheric air protection processes, catalytic combustion and catalytic reduction of NO_x are of utmost importance. These technologies are integrated with automobile catalysts, which are the most commonly used catalytic reactors and are extremely technologically advanced [2].

The last decades have seen the rapid development of catalysis. New catalysts of better selectivity and much faster reaction rates have been developed. This is an element of research aimed at improving the efficiency of catalytic processes (increased conversion, shorter reactors, greater selectivity of the process). Great achievements have been made in this field, but the design of the catalytic converter has not changed significantly.

Catalyst components and their importance in catalysis

The catalyst consists of a catalytic phase and a support. Various substances are used as active components of catalysts. In the case of catalytic combustion and deNO_x processes, effective (but expensive) noble metals such as platinum, palladium or rhodium are often used [3].

The most commonly used catalytic carriers include monoliths and packed beds (which may consist of elements of various shapes, such as grains, rings, etc.). Monoliths have been used in the car industry for years. They consist of many long, parallel channels. They are characterised by the possibility to modify properties depending on channel density. Their surface area can even exceed 4000 m^2m^{-3} [4]. The automotive industry uses 400–1200 cpsi monoliths (channels per square inch) [5]. They can be made of ceramics, for example cordierite (which gives them good resistance to thermal shock and low thermal conductivity), or from metal (for much more favourable thermal conductivity). The monolith channels may have different cross-section shapes (square, round, triangular, hexagonal, etc.) [5,6]. Compared to monoliths, packed-beds have more intense mass and heat transport and much higher flow resistance [6,7]. Their properties depend on the shape and diameter of the grains, although the porosity (free volume) of the most commonly used deposits is low (about 30–50 %).

The industry is still dominated (especially on a larger scale) by packed-bed reactors. The result is high flow resistance. The internal diffusional resistance in relatively large grains limits the use of the catalytic active phase. The exception is the egg-shell type catalyst in which a thin catalytically active layer has been deposited on the inert grains. In case of monolith low flow resistance is a positive feature here, but the mass (and heat) transport between the catalytic layer and the flowing gas is relatively weak (in long channels there is a developed laminar flow). The development of catalysts led to the rate of chemical reaction becoming very high. Catalytic processes could, in many cases, be much more intense. However, the diffusion of reactants has become a limitation. Many tests are carried out on very fine catalysts (powder), which is usually impossible to implement in large-scale industrial practice (due to very high flow resistance).

Gas flow through the reactor brings flow resistance (pressure drop) and therefore requires energy for the fluid pumping. Flow resistance is also related to the geometry of the carrier. Moreover, it is proportional to the intensity of heat and mass transfer (see analogies, such as Lévêque [8]). However, gas flow in any case can be forced if the compressor has appropriate energy (despite the costs), so this is not an absolute process limitation.

The literature includes several works indicating the possibility of designing new geometries for catalytic carriers. In this respect, one may mention wire meshes, monoliths with fins [9] and solid foams. It is also important to increase the specific surface area S_v, as this increases the amount of catalyst and the surface through which the diffusion of reagents occurs. Transport intensification thus can be achieved by significantly reducing the length of monolith channels [10,11].

Concept of short-channel structures

Kołodziej et al. [10,11] proposed and experimentally confirmed the possibility of effectively increasing the value of

* Corresponding author, e-mail: *katarzyna.sindera@iich.gliwice.pl*

mass transfer coefficient k_C for monoliths by shortening the length of their channels. This is based on the theory of developing laminar flow [12]. The flow of fluid through long monolith channels is, due to their small diameters, of laminar nature. Velocity and temperature profiles over the majority of the channel length are fully developed (parabolic), and the intensity of heat and mass transport is low. However, the velocity profiles are not fully developed near the channel inlet (their central part is flat; see Fig. 6.7.1). Heat and mass transport occur there over shorter distance, which guarantees much higher transport intensity. After passing a certain inlet section, the developed (parabolic) profiles are formed.

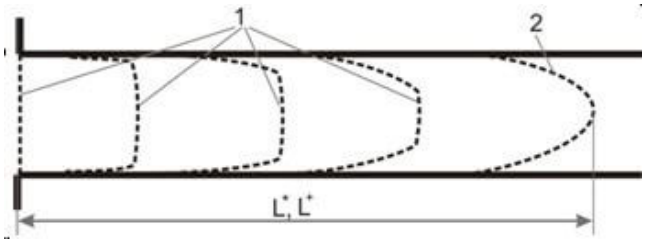

Figure 6.7.1: Formation of the fluid velocity/temperature profile: 1 - developing flow, 2 - developed flow.

If the structure of the monolith is cut into many shorter sections, the transport coefficients per unit of volume will be much greater than in the case of a single, long channel. The correctness of this approach has been confirmed by many subsequent works [13–17]. This is accompanied by, of course, higher unit flow resistance, but the value of this increase is acceptable, taking into account other benefits. In conclusion - a significant reduction in the channel length of the classic monolith is the first option for improving the properties of the carriers.

The shape of the cross-section of the channels also plays an important role. Its impact can be assessed by comparing the values of, for example, Nusselt numbers (Nu) for laminar developed flow, because in this case their value is a function of the channel shape only. These values are listed in Tab. 6.7.1.

Table 6.7.1: Transport-flow parameters for different geometries of the cross-section of the channels, f – Fanning friction factor, Re – Reynolds number, fd (fully developed) – value given for developed flow, $< H >$ – boundary condition (constant heat flux).

Shape of the cross-section of the channel	$Nu_{fd<H>}$	$(fRe)_{fd}$	$\frac{Nu_{fd<H>}}{(fRe)_{fd}}$	Ref.
Square	3.608	14.227	0.254	[18]
Equilateral triangle	3.111	13.333	0.233	[12,18]
Circle	4.364	16	0.273	[12]
Regular hexagon	4.002	15.054	0.266	[19,20]

Analysis of the data presented in Tab. 6.7.1 shows that a circle is the most preferred shape of the channel. This channel shape, however, has a significant disadvantage concerning the spatial distribution of many circular channels: the volume of inter-channel space is greater than in the case of other shapes. Theoretically, the circular shape has much better parameters than the others if only a single channel is considered. While considering the entire structured carrier it would be more beneficial to use regular hexagons, which have a better degree of spatial filling than circles and better transport parameters than squares or triangles. There are no research papers published concerning on short-channel structures of hexagonal cross-section shape heat/mass transfer or pressure drop properties.

Computational Fluid Dynamics (CFD)

The CFD software is a powerful tool for simulating process. It enables the impact of geometry on transport properties can be assessed numerically (and therefore much faster than experimentally). The usefulness of CFD have been proven in many works focusing on classic and short-channel monoliths [13,14,21,22]. It has also been confirmed that the simulation results for short-channel structures are in sufficient agreement with the experimental ones [13,14]. The method consists of pre-processing (preparation of geometry and mesh for simulation), simulation and post-processing (processing of results). Numerical modeling were carried out using ANSYS FLUENT software.

Pre-processing

Fig. 6.7.2 shows the image and dimensions of structure that transport properties were CFD modeled (hexagonal cross-section shape short-channel monolith). It's morphological parameters are shown in Tab. 6.7.2.

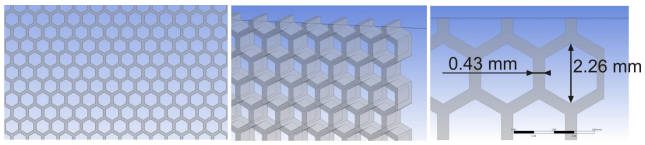

Figure 6.7.2: Dimensions of short-channel structure of hexagonal channel cross-section.

Table 6.7.2: Morphological parameters of simulated structure (L - channel length, S_v - specific surface area, ε_p - porosity of the structure).

L, m	S_v, $m^2 \cdot m^{-3}$	ε_p
$1 \cdot 10^{-3}$	1743.66	0.73

The CAD (Computer Aided Design) geometry of the carrier created reflects all the above mentioned parameters. It was created using the ANSYS DesignModeler module. All structure's channels behave essentially alike, so only one channel was simulated. The control regions of 50 mm upstream and downstream the channel were introduced. Only fluid gas domain was created. Image of the domain is shown in Fig. 6.7.3.

Next step was to divide the domain into small elements of finite volume (meshing) – see Fig. 6.7.4, which are used

to conserve relevant quantities such as mass, momentum and energy. It was done using the ANSYS MESHING module. Mesh was consisted of hexahedral elements in channel part and tetrahedrons in control regions. Total number of volume elements was about 480000.

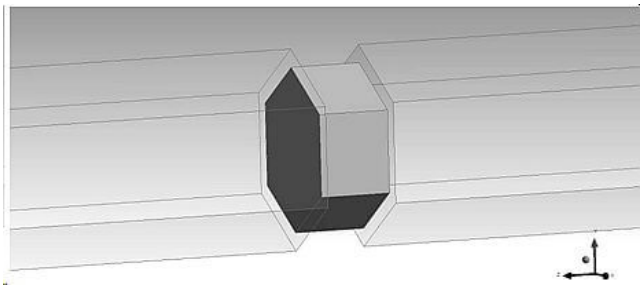

Figure 6.7.3: CAD geometry of the fluid inside the carrier's channel (marked) and control regions.

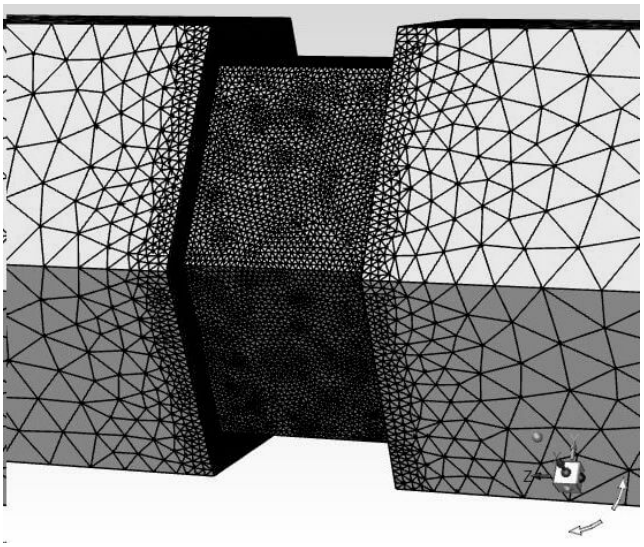

Figure 6.7.4: The fluid domain meshed.

Simulations

The simulations were carried out using the ANSYS FLUENT module. The Cartesian coordinate system was used in order to solve governing equations for flow and heat transfer. The equations are continuity, momentum and energy as follows:

$$\frac{\partial\left(\rho \cdot w_j\right)}{\partial x_j} = 0 \tag{6.7.1}$$

$$\frac{\partial\left(\rho \cdot w_j \cdot w_i\right)}{\partial x_j} = -\frac{\partial p}{\partial x_i} + \frac{\partial}{\partial x_j}\left(\eta\frac{\partial w_i}{\partial x_j} + \frac{\partial w_j}{\partial x_i}\right) \tag{6.7.2}$$

$$\frac{\partial\left(\rho \cdot c_p \cdot w_j \cdot T\right)}{\partial x_j} = \lambda\frac{\partial^2 T}{\partial x_j^2} \tag{6.7.3}$$

where $i, j \in 1, 2, 3$, ρ – density, w – fluid axial velocity, x – coordinate, p – pressure, η – viscosity, c_p – specific heat, T – temperature, λ – thermal conductivity.

Although inside the channel developing laminar flow occurs, turbulent zones are formed at the channel inlet and outlet. Velocity components perpendicular to the flow direction (reactor axis) occur at frontal and back surfaces of the channel wall. This brings about important drag force, static zones and eddies that appear near the channel inlet and outlet. ANSYS FLUENT software enables the use of different turbulence models during the simulations. In order to examine turbulent zones depending on differrent turbulence models few of them were introduced to the study. The models are: laminar, $k-\omega$ SST, standard $k-\varepsilon$, Realizable $k-\varepsilon$ and RNG $k-\varepsilon$. Although the Re range is between 80–2100, what is typical for laminar flow through long monolith channels, there are studies concerning low-Reynolds simulation that prove the importance of the model chosen (e.g. flow in straight blood vessels for $400 < Re < 1500$ [23] or [24]).

$k-\varepsilon$ models consist of transport equations for turbulent kinetic energy k and for dissipation rate ε. Governing equations for the $k-\varepsilon$ standard model are presented below [25,26]:

$$\frac{\partial}{\partial t}(\rho k) + \frac{\partial}{\partial x_j}(\rho k w_i) = \frac{\partial}{\partial x_j}\left[\left(\mu + \frac{\mu_t}{\sigma_k}\right)\frac{\partial k}{\partial x_j}\right] + \\ + G_k + G_b - \sigma\varepsilon - Y_M + S_k \tag{6.7.4}$$

$$\frac{\partial}{\partial t}(\rho\varepsilon) + \frac{\partial}{\partial x_j}(\rho\varepsilon w_i) = \frac{\partial}{\partial x_j}\left[\left(\mu + \frac{\mu_t}{\sigma_\varepsilon}\right)\frac{\partial \varepsilon}{\partial x_j}\right] + \\ + C_{\varepsilon 1}\frac{\varepsilon}{k}\left(G_k + C_{\varepsilon 3}G_b\right) - C_{\varepsilon 2}\rho\frac{\varepsilon^2}{k} + S_\varepsilon \tag{6.7.5}$$

where: t – time , k – turbulent kinetic energy, μ – dynamic viscosity, G_k – generation of turbulence kinetic energy due to the mean velocity gradients, G_b – generation of turbulence kinetic energy due to buoyancy, Y_M – contribution of the fluctuating dilatation in compressible turbulence to the overall dissipation rate, ε – dissipation rate, S_k, S_ε – user defined source terms, $C_\mu = 0.09$, $C_{\varepsilon 1} = 1.44$, $C_{\varepsilon 2} = 1.92$, $\sigma_k = 1.0$, $\sigma_\varepsilon = 1.3$. Description of each $k-\varepsilon$ model is shown in Tab. 6.7.3 [26–28].

$k-\omega$ models use equation for the turbulent energy dissipation rate ω instead of dissipation rate ε. $k-\omega$ models describe well the near-wall flows, however generate some problems with jet streams. Applied successfully for cases including large pressure gradient. $k-\omega$ SST (Shear Stress Transport) model, introduced by Menter [33], connects $k-\varepsilon$ and $k-\omega$ models. Flow patterns inside fluid core are calculated according to $k-\varepsilon$ equation while for near-flow region – with the use of $k-\omega$ equations [27]. Equations for $k-\omega$ are presented below [28,34,35]:

$$\frac{\partial}{\partial t}(\rho k) + \frac{\partial}{\partial x_j}\left(\rho w_j k\right) = \tau_{ij}\frac{\partial w_i}{\partial x_j} - \beta^*\rho\omega k + \\ + \frac{\partial}{\partial x_j}\left[\left(\mu + \sigma^*\mu_t\right)\frac{\partial k}{\partial x_j}\right] \tag{6.7.6}$$

$$\frac{\partial}{\partial t}(\rho\omega) + \frac{\partial}{\partial x_j}\left(\rho\omega x_j\right) = \left(\frac{\gamma\omega}{k}\right)\tau_{ij}\frac{\partial w_i}{\partial x_j} - \beta\rho\omega^2 + \\ + \frac{\partial}{\partial x_j}\left[\left(\mu + \sigma\mu_t\right)\frac{\partial \omega}{\partial x_j}\right] \tag{6.7.7}$$

Table 6.7.3: $k-\varepsilon$ models description [26,29].

k-ε model	standard	Realizable	RNG
Proposed by	Launder and Spalding [30]	Shih et al [31]	Yakhot et al [32]
Features	– semiempirical, – fully turbulent flow assumed, – molecular viscosity effects are negligible, – transport equations are not integrated to the walls, – turbulent viscosity is determined by a single characteristic linear turbulence scale, – the most popular model for turbulent flow simulations	– improved standard $k-\varepsilon$ model, – "realizable" means that model satisfies certain mathematical constraints on the Reynolds stresses, – alternative formulation for the turbulent viscosity, – ε equation is derived from the exact equation for the transport of the mean square vorticity fluctuation, – better accuracy in cases of large pressure, separated and recirculating flows in comparison to standard $k-\varepsilon$ model	– improved standard $k-\varepsilon$ model, – developed with using statistical mathematic technique called "renormalization", – turbulent viscosity determined by more different scales of turbulent motion, – improvements concerning on swirl on turbulence – higher accuracy in simulations of swirl and rapidly strained flow in comparison to standard $k-\varepsilon$ model

where τ – sum of molecular and Reynolds stress tensors, ω – specific dissipation rate, constants for $k-\omega$ SST are: $\sigma^* = 0.85$, $\sigma = 0.5$, $\beta = 0.9$, $\beta^* = 0.075$, $\gamma = -0.005$.

The process is assumed to be steady state, air is operating fluid, channel walls are made of steel, gravitational and radiative effects are negligible. Air density is calculated according to incompressible ideal gas law:

$$\rho_a = \frac{p \cdot M}{R \cdot T} \tag{6.7.8}$$

where M - molecular weight, R - universal gas constant. Air viscosity is defined by Sutherland's equation:

$$\eta_a = \frac{1.716 \cdot 10^{-5} T^{\frac{3}{2}}}{T + 114} \tag{6.7.9}$$

Air thermal conductivity and spefific heat are a function of temperature:

$$\lambda_a = -4 \cdot 10^{-8} T^2 + 9 \cdot 10^{-5} T + 0.0018 \tag{6.7.10}$$

$$c_{p.a} = 1009 + 0.126(T - 273) \tag{6.7.11}$$

Steel properties are defined as: $\rho_s = 8030\,\mathrm{kg \cdot m^{-3}}$, $c_{p.s} = 502.48\,\mathrm{J \cdot kg^{-1} \cdot K^{-1}}$, $\lambda_s = 16.27\,\mathrm{W \cdot m^{-1} \cdot K^{-1}}$. The abovementioned steel and air data (equations 9–11) are defined according to FLUENT database.

Boundary conditions are defined as: pressure outlet at domain outlet, air velocity (in range of 0.6–15 $\mathrm{m \cdot s^{-1}}$) and temperature (300 K) at inlet, constant heat flux along structure walls (heating in range of 5000–25 000 $\mathrm{W \cdot m^{-2}}$, walls of control regions are assumed to be the symmetry boundary condition.

Post-processing

The comparison of different turbulent models applied in numerical modeling is presented in Fig. 6.7.5. Additionally, Nusselt numbers of classic monolith and packed bed are shown as well. Short-channel structure of hexagonal cross section shape tested displays much more intense heat transport properties than classic long monolith, but not so intense as in the case of packed bed. This result is similar for short-channel structures of triangular or sinusoidal channel cross-section shapes [11,13,36]. The monolith of 100 cpsi was chosen for the comparison because of similar specific surface area (about 1340 $\mathrm{m^2 \cdot m^{-3}}$ [5] and 1744 $\mathrm{m^2 \cdot m^{-3}}$ for short-channel structure).

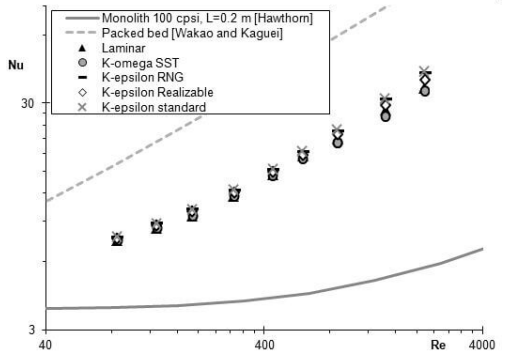

Figure 6.7.5: Nu vs. Re (correlation for packed bed and monolith: [37,38]).

It can be easily noticed that in the range of $80 > Re > 800$ there is slight difference between the models. The higher the velocity, the more divergent the results are. Nusselt numbers calculated on the basis of $k-\varepsilon$ standard and $k-\varepsilon$ RNG models results are visibly greater than in the case of laminar and $k-\omega$ SST models. The use of $k-\varepsilon$ Realizable turbulence model gives intermediate values.

Figs 6.7.6, 6.7.7 and 6.7.8 show air particles' pathlines colored by velocity magnitude for all the turbulence models tested. The figures differ in the air inlet velocity used (0.6, 6 or 15 $\mathrm{m \cdot s^{-1}}$ respectively for Fig 6.7.7, 6.7.8 and 6.7.9). Inlet velocity of 0.6 $\mathrm{m \cdot s^{-1}}$ is the lowest of all the velocities tested

while $15\,\mathrm{m}\cdot\mathrm{s}^{-1}$ is the highest one.

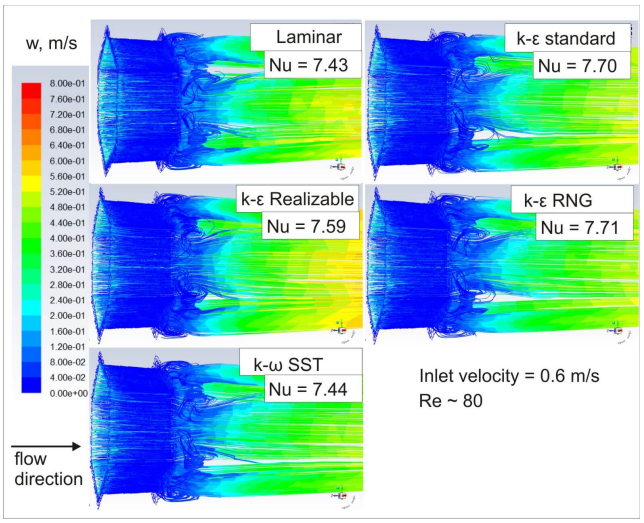

Figure 6.7.6: Velocity distribution behind the channel for $w = 0.6\,\mathrm{m}\cdot\mathrm{s}^{-1}$

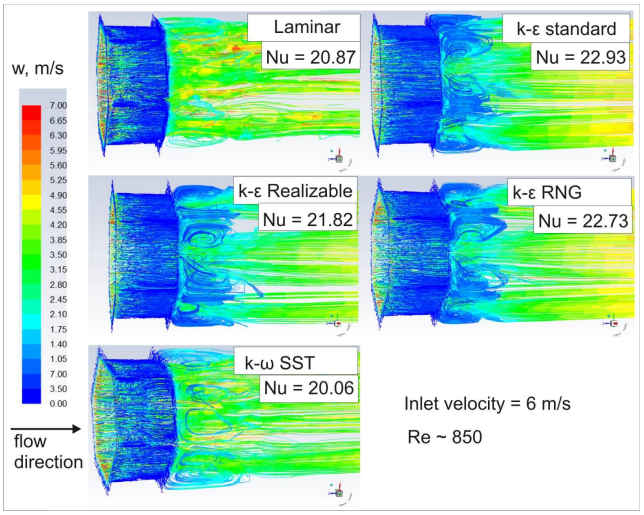

Figure 6.7.7: Velocity distribution behind the channel for $w = 6\,\mathrm{m}\cdot\mathrm{s}^{-1}$

Pathlines of all the models considering inlet velocity equal to $0.6\,\mathrm{m}\cdot\mathrm{s}^{-1}$ shown in Fig. 6.7.6 look alike. This explains slight differences in Nusselt numbers calculated for low Reynolds numbers. As expected, turbulent zones behind the structure occur, but their size and distribution is similar for all the models. In the case of higher velocity – $6\,\mathrm{m}\cdot\mathrm{s}^{-1}$, differences between the models used are more pronounced. The greatest turbulences can be noticed for the $k-\varepsilon$ models. On the other hand, the largest turbulences produced by the $k-\varepsilon$ models result in the highest Nu results given by the $k-\varepsilon$ ones (cf. Fig. 6.7.5). The question arises: are the turbulences (i.e. Nu values as well) are real or produced only by the CFD procedures; this can only be answered by the experiments. $k-\omega$ SST model application leads to less intense turbulences with little more elongate shape in comparison to those produced with application of $k-\varepsilon$ models. As expected, laminar model leads to the least disturbed flow in that case. Considering simulations results for the highest inlet velocity of $15\,\mathrm{m}\cdot\mathrm{s}^{-1}$, the differences

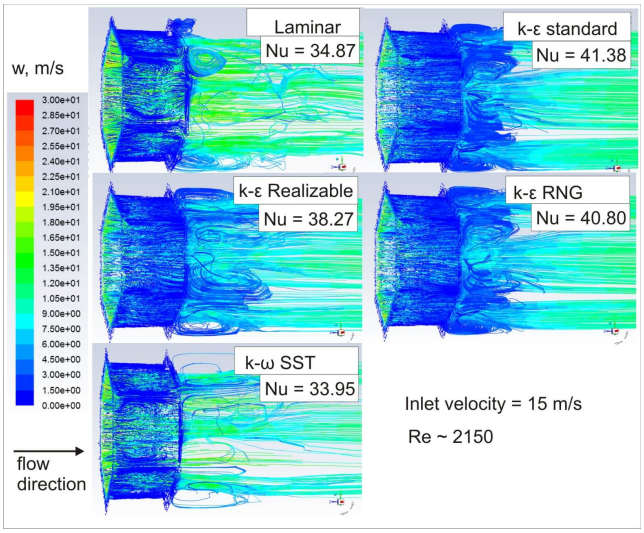

Figure 6.7.8: Velocity distribution behind the channel for $w = 15\,\mathrm{m}\cdot\mathrm{s}^{-1}$

between the turbulence models are even more important. Moreover, particle pathlines' shape differs for each $k-\varepsilon$ model. This proves that the greater the fluid velocity, the choice of turbulence model used is more significant. Turbulence calculated by $k-\omega$ SST model behind the structure seems more outstretched than for other models except laminar.

Fig. 6.7.9 shows temperature distribution at the structure. Only one exemplary case is shown because the distribution looks similar for the all the velocity and models tested. For all the cases the warmest zones were placed in the corners inside the channel (Fig. 9B) as well as at the outlet frontal edge of the structure, mainly in the middle part (Fig. 6.7.9A, C). This regions display the lowest heat transfer intensity.

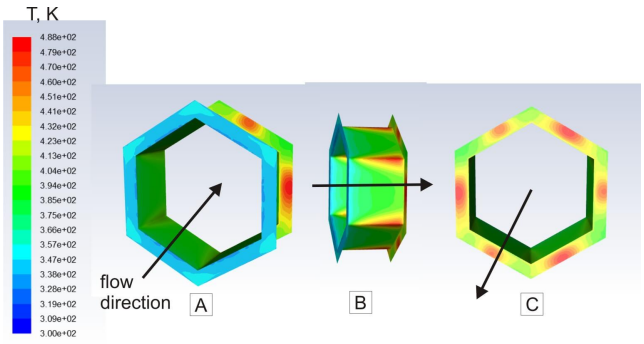

Figure 6.7.9: Temperature distribution at the structure tested: A – inlet, B – side, C – outlet view (laminar flow, $w = 6\,\mathrm{m}\cdot\mathrm{s}^{-1}$)

Conclusions

The analysis of CFD results leads to the following conclusions:

- short-channel monolith of hexagonal cross-section shape displays more beneficial heat transfer properties than long monolith, but not as high as packed bed;
- CFD is a very useful tool for simulating fluid flow, it enables to obtain information not available by direct experimental measurement;
- choice of the proper turbulence model for the flow simulations through the hexagonal short-channel structures is important when considering $Re > 800$
- air velocity influence strongly on turbulence shape. When considering the lowest velocity of $0.6\,\mathrm{m \cdot s^{-1}}$, there is almost no difference between the pathlines for the models used. Higher velocity pronounce the differences between models. Those calculated by $k-\omega$ SST and laminar ones seems more outstretched than for $k-\varepsilon$ models for the higher tested velocity;
- air velocity does not significantly affect the temperature distribution of the structure tested – for all the cases the warmest zones were placed in the corners inside the channel.

Symbols

c_p	specific heat, $\mathrm{J \cdot kg^{-1} \cdot K^{-1}}$
d_h	channel hydraulic diameter, m
f	Fanning friction factor
h	heat transfer coefficient, $\mathrm{W \cdot m^{-2} \cdot K^{-1}}$
k	turbulent kinetic energy, $\mathrm{J \cdot kg^{-1}}$
M	molecular weight, $\mathrm{kg \cdot mol^{-1}}$
Nu	Nusselt number, $= \mathrm{h \cdot d_h \cdot \lambda^{-1}}$
p	pressure, Pa
Pr	Prandtl number, $= \mathrm{c_p \cdot \eta \cdot \lambda^{-1}}$
R	universal gas constant, $\mathrm{J \cdot mol^{-1} \cdot K^{-1}}$
Re	Reynolds number, $= \mathrm{w_0 \cdot d_h \cdot \rho \cdot \eta^{-1}}$
t	time, s
T	temperature, K
w	fluid axial velocity, $\mathrm{m \cdot s^{-1}}$
w_0	fluid superficial velocity, $\mathrm{m \cdot s^{-1}}$
x	coordinate
ε	dissipation rate, $\mathrm{m^2 \cdot s^{-3}}$
η	viscosity, Pa·s
λ	thermal conductivity, $\mathrm{W \cdot m^{-1} \cdot K^{-1}}$
μ	dynamic viscosity, $\mathrm{kg \cdot m^{-1} \cdot s^{-1}}$
μ_t	turbulent dynamic viscosity, $\mathrm{kg \cdot m^{-1} \cdot s^{-1}}$
ρ	density, $\mathrm{kg \cdot m^{-3}}$
τ	sum of molecular and Reynolds stress tensors
υ_t	turbulent kinematic viscosity, $\mathrm{m^2 \cdot s^{-1}}$
ω	specific dissipation rate, $\mathrm{s^{-1}}$

Subscripts:

a	air
s	steel

Acknowledgements

This work was supported by the Polish National Science Centre (Project No. 2016/21/B/ST8/00496).

References

[1] Dumesic, J., G. Huber, and M. Boudart, Chapter in the book: Handbook of Heterogeneous Catalysis, *Principles of Heterogeneous Catalysis*, in. 2008, Wiley-VCH Verlag GmbH & Co. KGaA.

[2] Leman, A.M., et al. Catalytic Converter Developed By Washcoat Of gamma-Alumina On Nickel Oxide (Nio) Catalyst In FeCrAl Substrate For Exhaust Emission Control : A Review. in 2nd International Conference on Green Design and Manufacture (IConGDM), 2016, Phuket, THAILAND: E D P Sciences

[3] Pardiwala, J., F. Patel, and S. Patel. Review paper on Catalytic Converter for Automotive Exhaust Emission, in International Conference on Current Trends in Techology, Nuicone,. 2011, Ahmedabad

[4] Kolodziej, A. and J. Lojewska, Optimization of structured catalyst carriers for VOC combustion. Catalysis Today, 2005, 105, 3-4, 378-384, doi:10.1016/j.cattod.2005.06.029

[5] Williams, J.L., Monolith structures, materials, properties and uses, *Catalysis Today*, 2001, 69, 1-4, 3-9, doi:10.1016/S0920-5861(01)00348-0

[6] Cybulski, A. and J.A. Moulijn, Monoliths in heterogeneous catalysis, *Catalysis Reviews-Science and Engineering*, 1994, 36, 2, 179-270, doi:10.1080/01614949408013925

[7] Allen, K.G., T.W. von Backstrom, and D.G. Kroger, Packed bed pressure drop dependence on particle shape, size distribution, packing arrangement and roughness, *Powder Technology*, 2013, 246, 590-600. doi:10.1016/j.powtec.2013.06.022

[8] Lévêque, A., Les lois de la transmission de chaleur parconvectio,. *Ann. Mines.*, 1928, 13, 201-299, 305-362,381-415

[9] Lebens, P.J.M., et al., Potentials of internally finned monoliths as a packing for multifunctional reactors, *Chemical Engineering Science*, 1999, 54, 10, 1359-1365, doi:10.1016/S0009-2509(99)00060-3

[10] Kolodziej, A. and J. Lojewska, Short-channel structured reactor for catalytic combustion: Design and evaluation, *Chemical Engineering and Processing*, 2007, 46, 7, 637-648, doi:10.1016/j.cep.2006.08.009

[11] Kolodziej, A., et al., Short-channel structured reactor: Experiments versus previous theoretical design, *Chemical Engineering and Processing*, 2011, 50, 8, 869-876, doi:10.1016/j.cep.2011.05.003

[12] Shah, R.K. and A.L. London, *Laminar flow forced convection in ducts.* 1978, New York: Academic Press.

[13] Iwaniszyn, M., et al., Flow resistance and heat transfer in short channels of metallic monoliths:

Experiments versus CFD, *International Journal of Heat and Mass Transfer*, 2017, 109, 778-785, doi:10.1016/j.ijheatmasstransfer.2017.02.019

[14] Iwaniszyn, M., et al., Novel intense metallic monolith for automotive applications: Experimental versus numerical studies, *Comptes Rendus Chimie*, 2015, 18, 10, 1030-1035, doi:10.1016/j.crci.2015.03.010

[15] Iwaniszyn, M., et al., Short-Channel Structured Reactor as a Catalytic Afterburner, *Topics in Catalysis*, 2013, 56, 1-8, 273-278, doi:10.1007/s11244-013-9966-8

[16] Iwaniszyn, M., et al., Very short monoliths of triangular cross-sectional channel shape for fast catalytic reactions, *Przemysl Chemiczny*, 2012 91, 7, 1435-1438

[17] Kolodziej, A., et al., Mass transfer and flow resistance for sinusoidal short-channel catalytic internals, *Przemysl Chemiczny*, 2012, 91, 10, 2074-2078

[18] Shah, R.K., Laminar-flow friction and forced-convection heat-transfer in ducts of arbitrary geometry, *International Journal of Heat and Mass Transfer*, 1975, 18, 7-8, 849-862, doi:10.1016/0017-9310(75)90176-3

[19] Marin, O., et al., Characterization of the secondary flow in hexagonal ducts, *Physics of Fluids*, 2016, 28, 12, 26, doi:10.1063/1.4968844

[20] Turgut, O., Numerical investigation of laminar flow and heat transfer in hexagonal ducts under isothermal and constant heat flux boundary conditions, *Iranian Journal of Science and Technology-Transactions of Mechanical Engineering*, 2014, 38, M1, 45-56, doi:10.22099/IJSTM.2014.1926

[21] Liu, H., et al., Conceptual design and CFD simulation of a novel metal-based monolith reactor with enhanced mass transfer, *Catalysis Today*, 2005, 105, 3-4, 401-406, doi:10.1016/j.cattod.2005.06.060

[22] Maffei, T., et al., CFD Analysis of the Channel Shape Effect in Monolith Catalysts for the CH4 Partial Oxidation on Rh, *Chemie Ingenieur Technik*, 2014, 86, 7, 1099-1106, doi:10.1002/cite.201400013

[23] Ghalichi, F., et al., Low Reynolds number turbulence modeling of blood flow in arterial stenoses. *Biorheology*, 1998, 35, 4-5, 281-294, doi:10.1016/S0006-355X(99)80011-0

[24] Bauchire, J.M., J.J. Gonzalez, and A. Gleizes, Modeling of a DC plasma torch in laminar and turbulent flow, *Plasma Chemistry and Plasma Processing*, 1997, 17, 4, 409-432, doi:10.1023/A:1021847113956

[25] Rouaud, O. and M. Havet, Computation of the airflow in a pilot scale clean room using K-epsilon turbulence models, *International Journal of Refrigeration-Revue Internationale Du Froid*, 2002, 25, 3, 351-361, doi:10.1016/S0140-7007(01)00014-7

[26] Soe, M.T. and S.Y. Khaing, Comparison of Turbulence Models for Computational Fluid Dynamics Simulation of Wind Flow on Cluster of Buildings in Mandalay, *International Journal of Scientific and Research Publications*, 2017, 7

[27] Bulat, M.P. and P.V. Bulat, Comparison of Turbulence Models in the Calculation of Supersonic Separated Flows, *World Applied Sciences Journal*, 2013, 27, 10, 1263-1266, doi:idosi.wasj.2013.27.10.13715

[28] Voigt, L.K., Comparison of Turbulence Models fornumerical Calculation of Airflow in an Annex 20 Room, I.C.f.I.E.a. Energy, D.o.E. Engineering, and D. Technical University of Denmark, Editors 2000

[29] Bardina, J.E., P.G. Huang, and T.J. Coakley, Turbulence Modeling Validation,, T.a.D.N.T.M. 110446, Editor, 1997

[30] Launder , B.E. and D.B. Spalding, The numerical computation of turbulent flows. *Computer Methods in Applied Mechanics and Engineering*, 1974. 3(2): p. 269-289, doi:10.1016/0045-7825(74)90029-2

[31] Shih, T.H., et al., A new kappa-epsilon eddy viscosity model for high reynolds-number turbulent flows. *Computers & Fluids*, 1995, 24, 3, 227-238

[32] Yakhot, V., et al., Development of turbulence models for shear flows by a double expansion technique, *Physics of Fluids a-Fluid Dynamics*, 1992, 4, 7, 1510-1520, doi:10.1063/1.858424

[33] Menter, F.R. Zonal Two Equation k-[omega] Turbulence Models for Aerodynamic Flows. in AAIA 24th Fluid Dynamics Conference, 1993

[34] Wilcox, D.C., Reassessment of the scale-determining equation for advanced turbulence models, *AIAA Journal*, 1988, 26, 11, 1299-1310, doi:10.2514/3.10041

[35] Menter, F.R., 2-equation eddy-viscosity turbulence models for engineering applications. *AIAA Journal*, 1994, 32, 8, 1598-1605

[36] Kolodziej, A., et al., Short-channel structures of triangular cross-section. *International Journal of Heat and Mass Transfer*, 2011, 54, 15-16, 3291-3295, doi:10.1016/j.ijheatmasstransfer.2011.03.058

[37] Wakao, N., S. Kaguei, and T. Funazkri, Effect of fluid dispersion coefficients on particle-to-fluid heat-transfer coefficients in packed-beds - correlation of nusselt numbers, *Chemical Engineering Science*, 1979, 34,3, 325-336, doi:10.1016/0009-2509(79)85064-2

[38] Hawthorn, R.D., Afterburner catalysis-effects of heat and mass transfer between gas and catalyst surface, in *AIChE Symp. Ser.* 1974, 428-438

6.8 Investigations on magnetic nanoparticles surface modifications suitable for nucleic acids extraction

Anna Szymczyk*,1, Robert Ziółkowski[1], Marcin Drozd[1,2], Elżbieta Malinowska[1,2]

1 Faculty of Chemistry, Warsaw University of Technology, Warsaw, Poland
2 Centre for Advanced Materials and Technologies, Warsaw University of Technology, Warsaw, Poland

Keywords: *iron(II,III) oxide*, *modified magnetic nanoparticles*, *nucleic acids extraction*, *polymers*.

Abstract

Human infections require rapid diagnosis which prevent them from spreading in society. Assays based on nucleic acid detection turned out to be an effective approach for such a challenge. The portable diagnostic tools for DNA/RNA extraction and minimizing sample preparation time are needed. One of the approaches that can meet these requirements is using magnetic nanoparticles in the extraction of DNA from samples. The aim of this study was to synthesize Fe_3O_4 magnetic nanoparticles (MNPs) with chosen modifications and evaluate their ability to adsorb DNA from the solutions of various ionic strength. MNPs coated with PEI, GO and derivatives, SiO_2 or Au shell were characterized by long-term stability in solution and good magnetism. Surface properties of MNPs have been examined by measuring the zeta potential, size distribution profile and UV-Vis absorption spectra. This research should contribute to development of sample preparation methods for the rapid diagnosis of infectious diseases.

Introduction

Fast, reliable and cost efficient molecular diagnostic tests which could be performed outside laboratories in most cases are still only in the research phase. However, in the point of view of even recent COVID-19 pandemic, wide availability of such tests would significantly reduce the spread of viral infections. However, to perform the diagnostics based on specific nucleic acid fragment detection, it is indispensable to develop efficient methods for DNA/RNA extraction and purification. This is the first and crucial step in the whole procedure, as inhibitors present in the biological samples could influence the DNA amplification reaction (PCR) and the subsequent product detection [1]. To date, to obtain high purity nucleic acids for diagnostic procedure the appropriate benchtop equipment (e.g. centrifuges) and labor intensive procedure is needed. These can be however successfully replaced by appropriately prepared magnetic nanoparticles (MNPs) which exhibit high affinity towards nucleic acids.

A classical procedure for the isolation of genomic DNA involves phenol/chloroform extraction and DNA precipitation in ethanol [2]. To date several modifications of this extraction procedure have been described in the literature [3]. However it still has severe limitations like extended time, requirement for benchtop equipment e.g. centrifuges, and skilled personnel [4]. Simplification of this process would be very beneficial in the point of view of limiting the infection diseases spread. This can be achieved by the use of appropriately designed magnetic nanoparticles (MNPs), where the whole extraction and purification procedure could be reduced only to adsorption of the DNA or RNA at the MNPs surface (in standard procedure DNA is adsorbed onto a silica column), its magnetic separation and washing, followed by nucleic acids desorption back to appropriate buffer (Fig. 6.8.1).

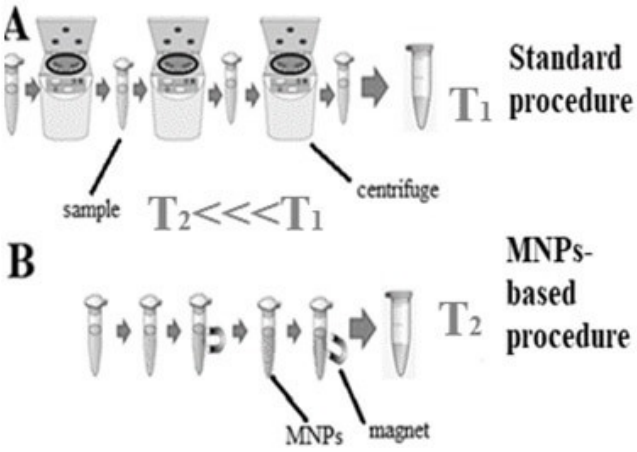

Figure 6.8.1: Classical research procedure (A) and magnetic nanoparticles-based approach of DNA extraction (B).

Modified magnetic nanoparticles properties like good dispersion, low cost, ease of modification suitable for specific adsorption of nucleic acids, and most important also facility of its separation from the whole sample could overcome limitations of traditional method of e.g. nucleic acids isolation from physiological samples (blood, saliva, plasma).

In the presented study several types of Fe_3O_4 coatings (in the form of solid shells as well as surface ligands) were analyzed in the point of view of its interaction with calf thymus DNA (ctDNA). These were polyethyleneimine (PEI), silica/aminated silica, gold, as well as graphene oxide (GO) and carboxylated graphene oxide (GO-COOH).

Experimental

Materials

Graphite, tetramethyl orthosilicate, branched polyethylenimine, (PEI) $M_w = 25\,\text{kDa}$, deoxyribonucleic acid from calf thymus, $FeSO_4 \cdot 7\,H_2O$, $FeCl_3 \cdot 6\,H_2O$, $FeCl_2 \cdot 4\,H_2O$, KNO_3, chloroacetic acid, ammonia, $K_2S_2O_8$, P_2O_5, NaOH, $NaBH_4$, $HAuCl_4$, sodium citrate, hydroxylamine hydrochloride, $KMnO_4$, H_2SO_4, HCl, H_2O_2, ethanol, NaCl, $MgCl_2$ were purchased from Sigma-Aldrich. Iron(II,III) oxide suspension (3%)(MNPs) and (3-aminopropyl)trimethoxysilane were from Alfa Aesar. The water used throughout this work was reagent-grade water produced by Purix. For separation of nanoparticles, cylindrical neodymium magnet ($d = 70\,\text{mm}$, $H = 50\,\text{mm}$) N42 was used.

* Corresponding author, e-mail: *anna.szymczyk.dokt@pw.edu.pl*

Synthesis of PEI-coated iron(II,III) oxide nanoparticles

Synthesis of iron oxide nanoparticles was carried out using two different methods (co-precipitation and controlled oxidation). It was decided to use these two types of cores to choose nanoparticles that combine satisfactory stability in solution and magnetic properties. Hence, the type of core subjected to particular types of further modification was selected individually. In general the nanoparticles obtained by controlled oxidation method were expected as characterized by a larger size, better magnetism and slightly worse stability in solution compared to nanoparticles obtained by co-precipitation.

The co-precipitation method was performed according to modified procedure described by H. Zhou et al. [6]. Reaction was carried out at room temperature under an inert gas (argon) atmosphere with continuous stirring with a mechanical stirrer at 2000 rpm. In a 250 ml three-necked flask, 4.886 g $FeCl_3 \cdot 6\,H_2O$ and 2.982 g $FeCl_2 \cdot 4\,H_2O$ were dissolved in 120 ml of water. Then, after the iron salt had completely dissolved, 15 ml of a 25% aqueous ammonia solution was quickly added to the flask. After 2 minutes, the temperature was increased to 90 °C. After 10 minutes, 20 mL of PEI (20 mg/ml) was added as a stabilizer. The process was carried out for 2 hours. After the synthesis was completed, the cooled nanoparticle suspension was purified five times by magnetic decantation. Finally MNPs were suspended in ultrapure water. Next, 40 ml of a 20 g/l PEI solution was placed in a 60 ml vial attached to a magnetic stirrer. While stirring continuously, 10 ml of the purified NPs suspension was added slowly in small portions. Synthesis relied on simultaneous precipitation of iron(II) and iron(III) hydroxide as a result of alkalization of iron salt solutions by adding ammonia. Then, due to heating, precipitated hydroxides decompose mainly into mixed iron(II) and iron(III) oxide forming at the same Fe_3O_4 nanoparticles.

The controlled oxidation approach was based on the initial precipitation of iron(II) hydroxide followed by its partial oxidation to Fe_3O_4 mediated by KNO_3. The synthesis was carried out in accordance with the methodology described by Chuah et al. [7] using PEI as capping ligand. The reaction was carried out at 90 °C, under an inert gas (argon) atmosphere, with constant stirring with a mechanical stirrer at a speed of 2000 rpm. In a 250 ml three-necked flask were placed: 80 ml of water, 0.7 g of $FeSO_4 \cdot 7\,H_2O$, and 10 ml of a 2 M KNO_3 solution. After the system was completely purged by argon, 10 ml of 1 M NaOH solution was rapidly injected. After 10 minutes of vigorous stirring, 20 ml of PEI solution with a concentration of 20 mg/ml were added. The process was carried out for 2 hours. After the synthesis, the purification procedure was the same as in the case of the above-described co-precipitation method.

Such obtained magnetic nanoparticles, called further as MNPs+PEI, were subjected for further modification or used as obtained. Detailed types of MNPs obtained in presented study and the core type used for their synthesis are summarized in Tab. 6.8.1.

Table 6.8.1: Magnetic nanoparticles and its modifications.

Nanoparticle type (abbreviation)	MNPs outer layer	Method of magnetic core synthesis
MNPs+PEI	PEI	co-precipitation
MNPs+GO	GO	co-precipitation
MNPs+GOCOOH	GO-COOH	co-precipitation
MNPs+ TMOS	TMOS	controlled oxidation
MNPs+ APTMS	APTMS	controlled oxidation
MNPs+ Au	Au	co-precipitation
MNPs	unknown	co-precipitation (commercial nanoparticles)

MNPs+GO and MNPs+GOCOOH synthesis

Graphene oxide (GO) was prepared by oxidation of natural graphite according to Hummers method [8,9]. Prior to the GO preparation a preliminary graphite oxidation was carried out. The graphite powder (4 g) was put into an solution containing concentrated H_2SO_4 (6 ml), $K_2S_2O_8$ (2 g), P_2O_5 (2 g) and heated up to 80 °C. The resultant dark blue dispersion was allowed to cool to room temperature. Then the solution was diluted with 5 l of distilled water, filtered, and washed on the filter until the pH of rinse water became neutral. The product was dried in air at ambient temperature overnight. The resultant powder was subjected to oxidation by Hummers' method. The preliminary oxidized graphite powder (4 g) was put into cold (0 °C), concentrated H_2SO_4 (92 ml). Then the $KMnO_4$ (12 g) was gradually added with stirring and cooling, so that the temperature was not allowed to reach 20 °C. Then the dispersion was heated and stirred at 35 °C for 2 h. After that the distilled water (185 ml) was added. After 15 min, the reaction was terminated by addition of a large amount of distilled water (0.6 l) and 30% H_2O_2 solution (10 ml). The color changed to bright yellow. Dispersion was filtered with 1:10 (v/v) HCl solution (1 l). The GO product was then suspended in distilled water to give a viscous, brown, 2% dispersion. Then it was subjected to dialysis to completely remove residual metal ions and acids. As obtained, purified GO suspension has been used for MNPs decoration.

Initially 10 mg/ml GO solution in water was prepared and sonicated for 15 minutes. Then, 5 ml of respective iron oxide nanoparticles (see Tab. 6.8.1) was added to 5 ml of GO, and the whole mixture was vigorously stirred magnetically for 30 minutes. Then the nanoparticles were washed three times and separated with a neodymium magnet.

GOCOOH solution was prepared based on the methodology described in the article [10]. Graphene oxide (GO) was prepared by oxidation of natural graphite according to Hummers' method. Then, the as prepared GO was dispersed in ultrapure water to form GO aqueous suspension with a concentration of 2 mg/ml, and then the bath was sonicated for 1 h. Afterwards, the resultant 2 mg/ml GO suspension (100 ml) was mixed with NaOH (1.2 g, 30 mM) and chloroacetic acid ($Cl-CH_2-COOH$) (1.0 g, 10.6 mM), and then the bath was sonicated for 2 h to convert the

–OH groups in the GO to –COOH moieties. The resulting GO–COOH solution was neutralized with dilute hydrochloric acid and purified by repeated rinsing and filtrations until the product was well dispersed in water. MNPs+GOCOOH nanoparticles were modified in a similar manner as MNPs+GO, by simply covering them with carboxylated graphene oxide instead of graphene oxide. The synthesis and purification of MNPs+GOCOOH was analogous to that for nanoparticles coated with graphene oxide.

MNPs+TMOS (SiO_2 shell) and MNPs+APTMS (amine SiO_2 shell)

MNPs+TMOS nanoparticles were prepared by the method carried out according to modified procedure described by Z. Zhao [11]. 0.3 g of PEI-coated MNPs, 7.5 ml of deionized water and 6 ml of ammonium hydroxide were added into 75 ml of ethanol, followed by a continuous sonication for 30 min at room temperature. 0.6 ml of TMOS was then added into the solution mixture after sonication (in portions of 100 µl, with 10 min intervals), and vigorously stirred for another 4 h at room temperature to allow the formation of silica layers on the surface of MNPs. The obtained nanoparticles were washed several times by means of repeated magnetic separation and resuspension in water.

MNPs+APTMS nanoparticles have been prepared in a similar way. Briefly, mixture containing 450 µl TMOS and 150 µl APTMS was added to MNPs instead of TMOS.

Synthesis of MNPs+Au

Synthesis of spherical gold nanoparticles (Au seeds)

Synthesis of gold seeds was carried out by reduction of Au(III) by means of NaBH4 in the presence of sodium citrate using the method described by Brown et al.[12]. 10 ml of 1% $HAuCl_4$ and 900 ml of H_2O were placed in a 1-liter beaker, in room temperature, with intensive stirring by means of a magnetic stirrer. After a minute of mixing with a magnetic stirrer, 20 ml of 38.8 M sodium citrate was added followed by 4.5 ml of freshly prepared 0.075% $NaBH_4$. The solution was stirred for another 10 min and stored in a darkened place.

Preparation of MNPs+PEI decorated with spherical gold nanoparticles

150 ml of obtained Au nanoparticles were placed in a 300 ml beaker. During intensive stirring with a magnetic stirrer, 80 ml of a suspension of MNPs synthesized by the modified co-precipitation method were added dropwise. The mixture was vigorously stirred for 4 hours at room temperature. Purification was performed by magnetic separation using 0.5 mM citrate buffer pH = 5.5. Part of the nanoparticles so obtained was suspended in 10 mM NaOH for further modification.

Synthesis of MNPs + Au

Solid gold coating was created around the nanoparticles previously decorated with gold seeds by means of the secondary reduction of $HAuCl_4$ with hydroxylamine hydrochloride according to method proposed by Kenneth R. Brown [12]. MNPs+PEI decorated with spherical gold nanoparticles suspended in 10 mM NaOH were placed in a glassy vial. With intensive, continuous stirring, 100 µl of 10 mM $HAuCl_4$ and 30 mM $NH_2OH \cdot HCl$ were added alternately, together with monitoring the spectra of as obtained nanostructures. The modification was completed after adding 2 ml of both solutions. The obtained nanoparticles were purified three times by magnetic decantation and suspended in 0.5 mM citrate buffer pH 5.5.

Finally, all types of nanoparticles after purification were suspended in the buffer to obtain the optical density of $OD_{380\,nm} = 5$.

Characterization of magnetic nanoparticles

The magnetism of nanoparticles was characterized by visual method. The nanoparticles were placed on a neodymium magnet and their rate of magnetic decantation was observed.

To evaluate the MNPs modification, size and zeta potential of functionalized nanoparticles were measured by Malvern Zetasizer Nano ZS. 1 ml of solution was prepared in the PS cuvette (950 µl of water and 50 µl of nanoparticles). The absorbance spectrum of Fe_3O_4+Au nanoparticles was measured in the wavelength range 200–800 nm. Spectra of all remaining nanoparticles were measured in the wavelength range 210–325 nm by using UV-Vis LAMBDA 25 spectrophotometer (Perkin Elmer) with the use of quartz microcuvette.

Preliminary DNA adsorption testing

To evaluate the efficiency of the DNA adsorption by various MNPs 200 µl of 0.0786 mg/ml DNA solution was prepared (2 M NaCl or 2 M $MgCl_2$). Then 100 µl was mixed with 100 µl of nanoparticles solution in water. After 5 min, the sample was placed on the magnet and the approximate time of collecting nanoparticles was examined. The supernatant for measurement was taken when it was considered that most of the nanoparticles had collected on the magnet-after about 5 min of magnetic separation. In the case of MNPs+Au nanoparticles, this time was extended to about 10 minutes. The efficiency of magnetic separation (presence of residual MNPs) was assessed on the basis of the background absorbance at 345 nm.

Results and discussion

The basic criterion taken into account in selection of nanoparticles for further investigations is their magnetic properties. The Tab. 6.8.2 shows results of magnetic separation in time. As it can be seen, after 5 seconds, MNPs+TMOS and MNPs+GO nanoparticles are completely deposited on the vial bottom, beneath which the magnet was placed. After 2 minutes from the initial magnetic field introduction, it can be seen the complete separation of all nanoparticles except MNPs+Au and MNPs+GOCOOH. The first mentioned were not separated even after 5 minutes (most likely the gold layer weakens the magnetic properties).

As was shown in Fig. 6.8.2, the surface modification of MNPs results in the change of their size. This was measured with the use of Dynamic Light Scattering method

(DLS). The method provides information about the size of nanoparticles in solution together with its electric double layer surrounding (hydrodynamic diameter), as opposed to microscopic methods [13].

Table 6.8.2: Magnetic characterization of nanoparticles.

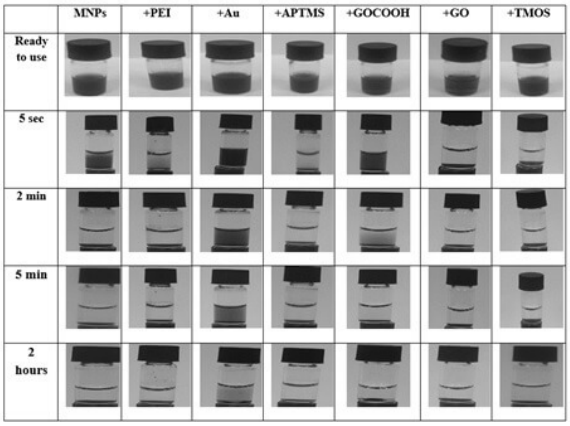

The results presented in Fig. 6.8.2 does not reflect the exact size of nanoparticles, but correspond to the relationship between the individual types nanoparticles, both with their hydrodynamic diameter. It should be underlined that the free movement of nanoparticles is influenced by magnetic phenomena, so the values of hydrodynamic diameters may differ from the real dimensions of nanoparticles. However as we can see, the smallest diameters were observed for MNPs coated with gold, commercial MNPs, graphene oxide and carboxylated graphene. On the other side, the highest values were obtained for MNPs where the outer layer was composes only with PEI or silica (TMOS and APTMS), which could indicate on slight agglomeration of Fe_3O_4 cores at the coating/silanization stage.

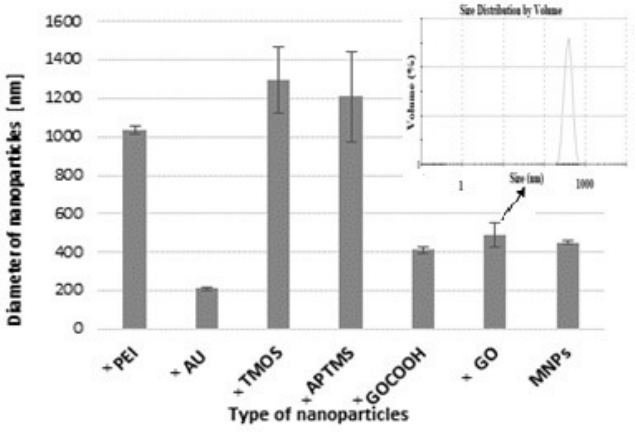

Figure 6.8.2: Hydrodynamic diameter of nanoparticles.

To further evaluate the nanoparticles modifications with chosen ligands or solid shells, it was decided to measure the zeta potential (Fig. 6.8.3). It is the potential that exists in the double layer at the surface of the dispersed particles. It is defined as the slip limit, related to the in-depth potential of the continuous phase [13].

As can be seen in Fig. 6.8.3 all modifications were successful as nanoparticles gained the charge determined by their coatings. From all modifications, only MNPs+PEI and MNPs+APTMS are characterized with positive charge. Iron oxide MNPs possess intrinsic negative charge which significantly increases after addition of a stabilizer containing numerous amino groups (PEI). The reason for the increase in the surface potential is compensation of negative charge by amino groups, which are protonated under the measurement conditions. The positive charge of MNPs+APTMS nanoparticles is also caused by the presence of protonated $-NH_3^+$ groups on the surface. The negative charge of MNPs+GO and MNPs+GOCOOH confirms that iron nanoparticles are efficiently incorporated into structure of graphene oxide, which negative charge derives from carboxyl and other oxygen-containing groups on its surface.

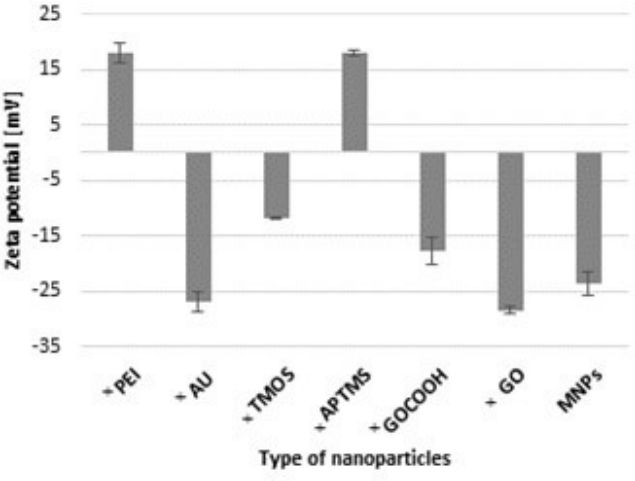

Figure 6.8.3: Characterization of MNPs surface properties.

Spherical gold nanoparticles used as seeds for Au shell growth were also characterized by UV-Vis spectroscopy (Fig. 6.8.4). The maximum absorption at a wavelength of 520 nm was obtained, which confirms preparation of spherical gold nanoparticles. Its presence proves the small diameter of gold seeds. On this basis it was concluded that they could be successfully used for decoration of MNPs for MNPs+Au preparation.

Above results allow us to confirm the composition and surface properties of prepared magnetic nanoparticles, which are schematically presented in Fig. 6.8.5. PEI on MNPs nanoparticles is characterized by a high degree of branching, which increases the hydrodynamic diameter of nanostructures. APTMS and TMOS form a silica shell on the surface of the nanoparticles. Gold covers the nanoparticles in the form of a solid shell of uniform thickness over the entire surface of the nanoparticle. On the other hand, graphene oxide and carboxylated graphene oxide nanohybrids, due to their large size in comparison to Fe_3O_4 creates more complex structures in which nanoflakes are surface decorated with Fe_3O_4 nanoparticles.

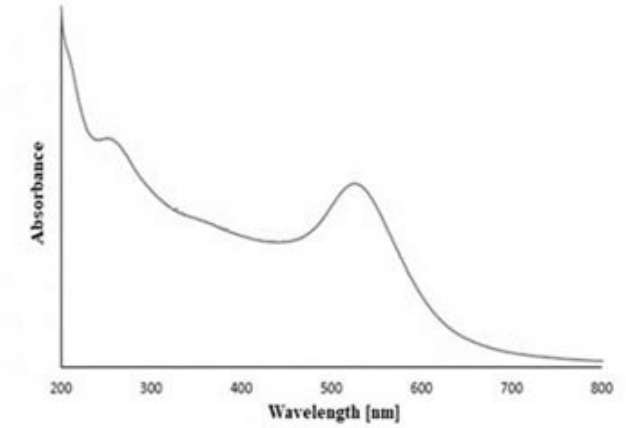

Figure 6.8.4: Absorption spectrum of gold nanoparticles (seeds).

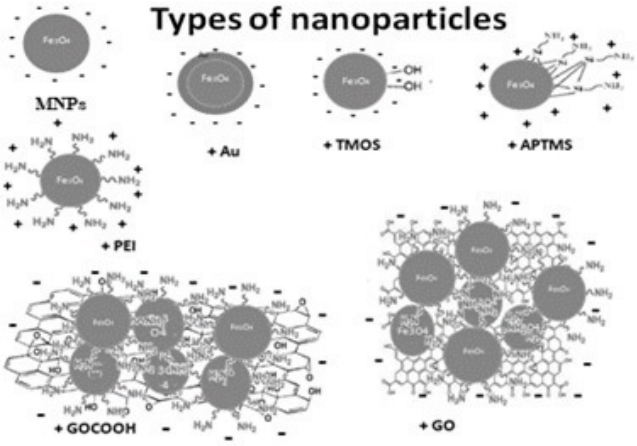

Figure 6.8.5: Schematic illustration of investigated MNPs types.

Preliminary DNA adsorption testing

Nanoparticles characterized by different coatings exhibit different capabilities to interact with DNA. The surface chemistry also determines the dominant mechanism of interaction. Thus, the efficiency of magnetic extraction can be adjusted by careful selection of nanosorbent. Measurement of the absorbance spectrum in the wavelength range of 210–325 nm was used as a method for determining the DNA binding efficiency of nanoparticles. At first, however, also UV spectra of modified MNPs in this range were registered (Fig. 6.8.6). As can be seen, the absorption in the range of approximately 260 nm, characteristic for nucleic acids range could be observed. That is why the crucial step in evaluation of the DNA adsorption studies and the same the possibility of its extraction by modified MNPs is the appropriate magnetic sedimentation.

Initially the DNA adsorption on the surface of modified MNPs was studied in deionized water (Fig. 6.8.7). For comparison the UV spectrum of calf thymus DNA was also provided. As can be seen the absorption intensity after the DNA interaction with magnetic nanoparticles does not change significantly. The decrease in absorbance at the maximum characteristic of DNA would proves its bonding to modified MNPs. Relatively small drop in absorbance can be seen for all MNPs types except MNPs+GO and MNPs+GOCOOH, where the UV absorption intensity was slightly increased. However, the presented results may indicate that DNA adsorb at the nanoparticles surfaces only in small manner ,while in the case of graphene derivatives, the increase in absorbance intensity could indicate most likely ineffective separation.

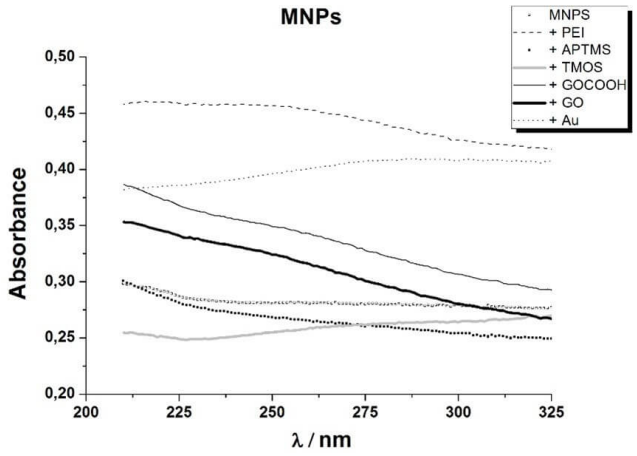

Figure 6.8.6: Absorption spectrum of investigated MNPs.

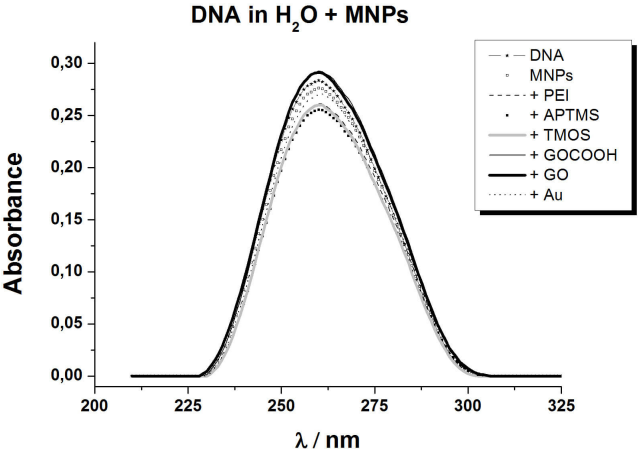

Figure 6.8.7: Absorption spectrum of DNA in H_2O + MNPs.

An ineffective nucleic acids adsorption at the as prepared MNPs may result from the electrostatic repulsion between the negatively charged nucleic acids and nanoparticles. This made us to increase the ionic strength of DNA adsorption medium [14]. It is crucial factor in binding and elution of nucleic acids by magnetic nanoparticles. The main driving force for DNA adsorption is high concentration of ions which decrease the Debye Length in binding solution, what in turn effectively shields the negative charges and intensively weakens the repulsive electrostatic force between DNA and nanoparticles. Cations present in solution are important for the stability of two negative strands in dsDNA molecule. The presence of Mg^{2+} and Na^{+} cations in the solution induces attraction forces between the positive and negative charges. This enables the adsorption of negative DNA on the modified surfaces of nanoparticles, which also show a negative charge. What is more, a divalent ion provides greater DNA stability than a monovalent one. Divalent

cations can neutralize large negative surface charge density of DNA through counterion condensation and can bridge adjacent phosphate anions [15,16]. Wu M. et. al. proved that DNA adsorption time strictly depends on buffer composition and is significantly higher for divalent ions like Mg^{2+} than for Na^{+}.

Result of DNA adsorption in 1 M NaCl was shown in Fig. 6.8.8. In this case, the observed maximum absorbances with the use of all nanoparticle types is smaller than for DNA alone. This means that DNA was deposited at the nanoparticles surfaces and its concentration in the solution has decreased.

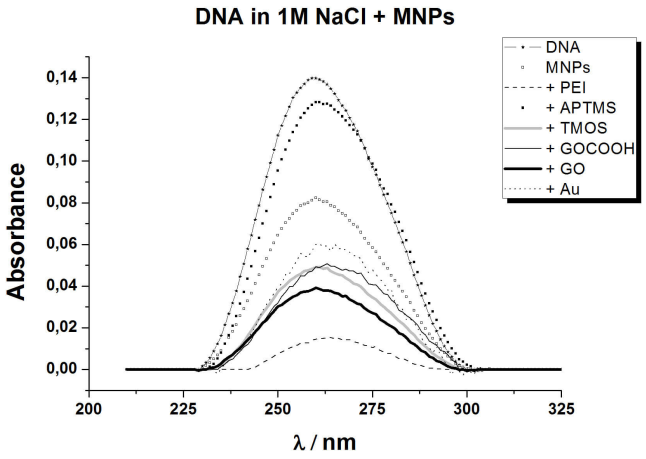

Figure 6.8.8: Absorption spectrum of DNA in 1 M NaCl + MNPs.

The influence of divalent ion on the long, double stranded DNA adsorption is presented in Fig. 6.8.9. This time, the maximum absorbance of supernatant collected after calf thymus DNA adsorption on modified MNPs in most cases significantly diminish when compared to ctDNA alone. This indicates its adsorption at the nanoparticles surfaces. The least amount of DNA was adsorbed by silica nanoparticles, evidenced by peak heights close to the DNA peak. On the other hand, MNPs, MNPs+GO and MNPs+GOCOOH allowed for almost complete DNA adsorption and removal from the solution, as evidenced by the very low peak height for the collected supernatant.

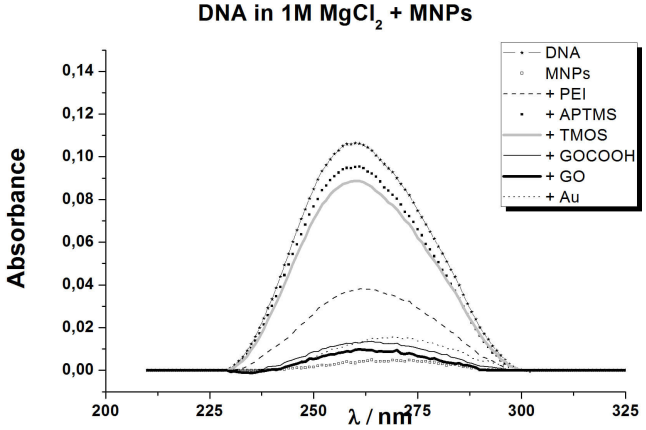

Figure 6.8.9: Absorption spectrum of DNA in 1 M $MgCl_2$ + MNPs.

To better show the efficiency in DNA adsorption at modified nanoparticles (expressed as their removal from investigated solutions), relative changes in absorption intensity was calculated and summarized (Tab. 6.8.3 and Tab. 6.8.4). This value can be correlated with the DNA amount decrease in the extracted sample. As could be observed, depending on the environment (the presence of Na^{+} or Mg^{2+} ion) different results could were obtained. The best adsorption was observed for commercial MNPs (the highest percentage decrease) in the presence of $MgCl_2$ salt. Satisfactory values were also observed for nanoparticles coated with GO, GOCOOH and Au (in the presence of Mg^{2+} ions), and those coated with PEI (in the presence of Na^{+} ions), which proves the possibility of using it in further investigations.

Table 6.8.3: Calculation of the quantity of the adsorbed DNA.

$$\Delta A = \frac{A_0 - A}{A_0} \cdot 100\% \qquad (1)$$

where:
ΔA – relative change of DNA absorbance (%);
A_0 – absorbance for pure DNA;
A – absorbance of the tested sample.

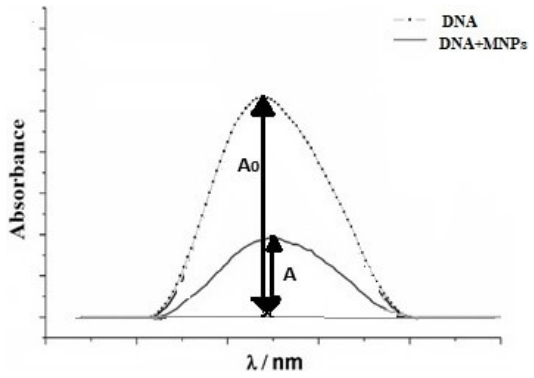

Table 6.8.4: Percentage change of DNA absorption peaks intensities.

	H_2O	1 M NaCl	1 M $MgCl_2$
DNA	100.00%	100.00%	100.00%
MNPs	97.35%	58.82%	4.56%
+PEI	92.11%	11.02%	35.91%
+APTMS	90.01%	91.77%	89.61%
+TMOS	91.69%	35.19%	83.44%
+GOCOOH	103.26%	36.31%	12.77%
+GO	102.70%	28.00%	9.19%
+Au	95.42%	43.13%	14.71%

The efficiency of DNA adsorption was influenced by many factors such as the surface of nanoparticles (solid shell, branched polymer), their charge (positive or negative), as well as different concentrations of nanoparticles. Currently, the concentration is expressed by optical density, and thus the observed effect may be influenced by different surface areas of nanoparticles available for DNA adsorption. The influence of MNPs specific surface areas on the efficiency of DNA-binding will be further investigated.

Conclusions

In the presented study various surface modifications were used to investigate the ability of the prepared magnetic nanoparticles to bind DNA. Various MNPs surface coatings and shells, including polymers, metal and silica shells as well as GO and GOCOOH decoration allowed for the comparative examination of efficiencies of DNA binding on the surface of nanoparticles characterized by various surface chemistries. As could be seen, we successfully obtain nanoparticles that are stable in solution and have satisfactory magnetic and colloidal properties, which enabled their use as DNA sorbents. The successful modification of MNPs with PEI, Au, SiO_2 and amine SiO_2 shells has been confirmed. PEI-coated nanoparticles were used for decoration of GO and GOCOOH nanoflakes to obtain hybrid magnetic-graphene-like material. The nanoparticles exhibit differences in hydrodynamic diameters and surface charges, which allowed the examination of several types of DNA-surface interaction mechanisms, that are crucial in bioanalytical applications. At this moment, the most promising are nanoparticles coated with PEI, GO and GOCOOH, due to their good magnetic properties and the high efficiency in DNA adsorption on its surface. The results demonstrated that processes of DNA adsorption by nanoparticles were greatly affected by the ionic strength where the effective binding require the presence of high salt concentration (preferably containing divalent cation). From the point of view of further sample processing in medical diagnostics, it would be more advantageous to use a solution containing Mg^{2+} ions, because they are used in the polymerase chain reaction (PCR). However for specific applications also Na^{+} ions could be applicable in separation medium. Further work will be focused on the investigation of the best conditions for DNA desorption from the surface of nanoparticles.

The research show potential applicability of as prepared surface-modified magnetic nanoparticles for isolation of DNA/RNA from biological samples.

Acknowledgements

This work was financially supported by the Warsaw University of Technology and the IDUB project "Against COVID-19".

References

[1] Grassly N.C., Pont-Salort M., Parker E.P.K., White P.J., Ferguson N.M., Comparison of molecular testing strategies for COVID-19 control: a mathematical modeling study, *Lancet Infectious Diseases*, 2020, 20, 12, 1381–1389

[2] Sambrook J., Russell D.W., *Molecular Cloning: A Laboratory Manual*, Cold Spring Harbor Laboratory Press, 2001

[3] Doyle J.J., Doyle J.L., A rapid DNA isolation procedure for small quantities of fresh leaf tissue, *Phytochemical Bulletin*, 1987, 19, 1, 11–15

[4] Rittich B., Španová A, Horák D., Beneš M.J., Klesnilová L., Petrová K., Rybnikář A., Isolation of microbial DNA by newly designed magnetic particles, *Colloids and Surfaces B: Biointerfaces*, 2006, 52, 2, 143–148

[5] Yi L., Huang Y., Wu T. and Wu J., A magnetic nanoparticles- based method for DNA extraction from the saliva of stroke patients, *Neural Regeneration Research*, 2013, 8, 32, 3036–3046

[6] Zhou H., Lee J., Park T.J., Lee S.J., Park J.Y. and Lee J., Ultrasensitive DNA monitoring by Au-Fe3O4 nanocomplex, *Sensors and Actuators B: Chemical*, 2012,163,1, 224–232

[7] Chuah K., Lai M.H., Goon I.Y., Perker S.G., Amal R. and Gooding J. J., Ultrasensitive electrochemical detection of prostate- specific antygen (PSA) using gold-coated magnetic nanoparticles as dispersable electrodes, *Chemical Communications*, 2012, 48, 29, 3503–3505

[8] Hummers W.S., Offeman R.E., Preparation of graphitic oxide, *Journal of the American Chemical Society*, 1958, 80, 6, 1339.

[9] Ziółkowski R., Górski Ł., Malinowska E., Carboxylated graphene as a sensing material for electrochemical uranyl ion detection, *Sensors and Actuators B-chemical*, 2017, 238, 540–547

[10] Song M., Xu J., Preparation of Polyethylenimine-Functionalized Graphene Oxide composite and Its Application in Electrochemical Ammonia Sensors, *Electroanalysis*, 2013, 25, 2, 523-530

[11] Zhao Z. , Cui H., Song W., Ru X., Zhou W., Yu X., A Simple magnetic nanoparticles-based Vidal RNA extraction method for efficient detection of SARS-CoV-2, *bioRxiv*, 2020,

[12] Brown K.R., Walter D.G. and Natan M.J., Seeding of colloidal Au nanoparticles solutions. Improved control of particie size and shape, *Chemistry of Materials*, 2000, 12, 2, 306–313

[13] Świderska-Środa A., Łojkowski W., Lewandowska M., Kurzydłowski K.J., *Świat nanocząstek*, PWN, 2016

[14] Wu M., Kempaiah R., Huang, P.J. Adsorption and desorption of DNA on graphene oxide studied by fluorescently labeled oligonucleotides, *Langmuir* 2011, 27, 6, 2731-2738

[15] Melzak K.A., Sherwood C.S., Turner R.F.B., Haynes C.A., Driving forces for DNA adsorption to silica in perchlorate solutions, *Journal of Colloid Interface Science*, 1996, 181, 635–644

[16] Nguyen T.H., Elimelech M., Plasmid DNA Adsorption on Silica: Kinetics and Conformational Changes in Monovalent and Divalent Salts, *Biomacromolecules* 2007, 8, 1, 24–32

6.9 Application of population balance to modelling particle breakdown in batch homogenizers

Krzysztof Wojtas [*,1], Radosław Krzosa[1], Radosław Adamek[2], Wojciech Orciuch[1], Łukasz Makowski[1]

1 Faculty of Chemical and Process Engineering, Warsaw University of Technology, Warsaw, Poland
2 ICHEMAD – Profarb, Gliwice, Poland

Keywords: *population balance*, *quadrature method of moments*, *homogenization*, *computational fluid dynamics*.

Abstract

The main aim of this paper is to present a new model that describes particle breakdown in homogenizers with high shear stress. The studies were carried out in a batch tank mixer, both experimentally and using computational fluid dynamics. Homogenizers of this type are characterized by high energy consumption, which is influenced mainly by the process time and system geometry. The research allowed to determine the necessary parameters of the theoretical model, such as starting values (e.g. initial particle size distributions), instantaneous and final values (e.g. particle sizes during and after the homogenization process) or parameters characterizing particles. The developed breakdown kinetics model, which takes into account the suspension rheology, enabled to identify key process parameters and to determine favourable conditions of the homogenization process, and therefore, can be considered as a useful tool in real-life engineering applications.

Introduction

The literature review indicates the importance of developing a new, extended model describing the breakdown of particles in tank homogenizers. Computational fluid dynamics (CFD) coupled with the population balance, together with the experimental verification, seem to be an ideal choice to achieve this goal. CFD is a method that allows to determine the flow field in the studied system (velocity or component concentration distribution), as well as provide much easier way to investigate the effect of process parameters (temperature, reactant concentrations, process duration, impeller speed, system geometry, etc.) on the course of the process. The population balance, which provides a statistical description of particles in the system and its evolution in space and time, can be determined by numerous methods proposed in the literature [1–6], among which the quadrature approximation methods are nowadays more commonly used due to their relatively low computational requirements.

High shear impellers are a type of agitators commonly used in unbaffled tanks for dispersing particle agglomerates in a system [7]. Used together with typical tank mixers, they allow long residence times to be achieved. As a consequence, the process continues until a uniform, desired degree of homogenization of the suspension is achieved throughout the entire batch. The principle of operation of such devices is that the impeller generates high values of hydrodynamic stresses in suspension, that in consequence break bonds in agglomerates [8]. Generally, choosing the right impeller is application dependent, and is strictly related to the process requirements. Impellers with particular designs that are used in the homogenization process, provide substantial improvements over standard designs, such as the Rushton turbine, because very specific requirements of shear, energy dissipation and pumping are desirable in this process [9].

In this study, the break up process of titanium dioxide particles is investigated using a batch tank homogenizer equipped with a high shear impeller (sawtooth impeller). Results obtained over a range of processing conditions are analysed to study the break up kinetics and identify the dominating mechanism. Two impellers of different geometry were used in this work in order to tune the break up kinetics model (by choosing more universal model constant values), and therefore, to allow using the model in the future to assess also different designs. A titanium dioxide suspension in water (a fluid of non-Newtonian rheology) was used as a test suspension. This is a typical fluid used in the industry, among others, in paint and coatings, cleaning products, food and cosmetics industries where it is usually used as a white pigment and antimicrobial additive [10].

The main objectives of the present work are the development of a detailed titanium dioxide particle breakdown model in homogenizers characterized by high shear stress values and the application of population balance method combined with computational fluid dynamics to predict the course of the homogenization process. A further goal involves investigation of deagglomeration performance and efficiency using different impeller designs, and the development of a method, which could be used in the future to simplify process design and improve or even create new industrial equipment.

Methods

Population balance modelling

To model evolution of the dispersed phase system properties one can use population balance equations [1]:

$$\frac{\partial f}{\partial t} + \sum_{i=1}^{3} \frac{\partial \left[u_i(x,t)\, f\right]}{\partial x_i} + \sum_{j=1}^{N} \frac{\partial \left[G_j(r,t)\, f\right]}{\partial r_i} = B(x,r,t) - D(x,r,t) \tag{6.9.1}$$

where f denotes the probability density function of the dispersed phase properties distribution, u_i is the particle velocity, G_j is the velocity of the particle in the properties space, B and D are the birth and death functions of nonlinear processes such as breakage.

This way we can express the change of particle properties in time and space, however, solving this function for complex processes is not possible. To solve population balance with reasonable computational effort a number

* Corresponding author, e-mail: *krzysztof.wojtas@pw.edu.pl*

of methods were proposed, such as the method of moments [1], which is based on the moment transformation of Eq. 6.9.1, the class method [2], and various quadrature based methods [3–6]. The quadrature approximation methods are currently very popular due to their balance between accuracy and computational resource requirements, especially when the population balance is solved together with computational fluid dynamics. For the same reason, in this work the quadrature method of moments (QMOM) [3] is used. The method uses an approximation that substitutes continuous particle size distribution by a sum of several Dirac deltas with weights and abscissas as parameters. This way we obtain transport equations for statistical moments that can be solved using CFD software:

$$\frac{\partial m_k}{\partial t} + \overline{u_j}\frac{\partial m_k}{\partial x_j} - \frac{\partial}{\partial x_j}\left[D_x \frac{\partial m_k}{\partial x_j}\right] = \overline{B_k} - \overline{D_k} \tag{6.9.2}$$

where $\overline{B_k}$ and $\overline{D_k}$ are the moment transformed birth and death functions, D_x is the diffusive term.

Moment values can be approximated by the following quadrature:

$$m_k = \int_0^\infty L^k f(L)\, dL \approx \sum_{i=1}^{N} w_i L_i^k \tag{6.9.3}$$

where w_i and L_i are weights and abscissas respectively, and their values can be determined using, e.g., the product-difference algorithm [11].

The closure for aggregation and breakage for QMOM was introduced by Marchisio et al. [12]. In this work, in the experiments we observed that the breakage mechanism is the dominating one, and therefore we neglected aggregation. The source terms for breakage, i.e., the right hand side of Eq. 6.9.2, can be then finally written as:

$$\overline{B_k^b} - \overline{D_k^b} = \sum_i^N \Gamma_i \bar{b}_i^{(k)} w_i - \sum_i^N L_i^k \Gamma_i w_i \tag{6.9.4}$$

where Γ is the breakage kernel, $\bar{b}^{(k)}$ the daughter (fragment) distribution function.

Based on the experimental PSDs, we identified that shattering is the dominating deagglomeration mechanism in the studied process. Therefore, only shattering was taken into account in the simulations and the following breakage kernel (Eq. 6.9.5) and daughter function (Eq. 6.9.6) were employed:

$$L_i > \lambda_K : \Gamma_i = \begin{cases} C_b \left(\frac{\varepsilon}{L_i^2}\right)^{1/3} & \text{if} \quad \rho\left(\varepsilon L_i\right)^{2/3} > \sigma_T \\ 0 & \text{if} \quad \rho\left(\varepsilon L_i\right)^{2/3} \leq \sigma_T \end{cases} \tag{6.9.5}$$

$$L_i \leq \lambda_K : \Gamma_i = \begin{cases} C_b \left(\frac{\varepsilon}{\nu}\right)^{1/2} & \text{if} \quad \mu\left(\frac{\varepsilon}{\nu}\right)^{1/2} > \sigma_T \\ 0 & \text{if} \quad \mu\left(\frac{\varepsilon}{\nu}\right)^{1/2} \leq \sigma_T \end{cases}$$

$$\bar{b}_i^{(k)} = \int_0^\infty L^k b\left(L|\lambda\right) dL \tag{6.9.6}$$

$$b\left(L|\lambda\right) = N\left(\lambda\right)\delta\left(L - L_a\right) \tag{6.9.7}$$

where λ_K is the Kolmogorov scale, C_b is the proportionality constant, ε is the turbulence dissipation rate, ρ is the suspension density, μ and ν is the suspension dynamic and kinematic viscosity respectively, σ_T is the tensile strength of agglomerates. The number of aggregates that form an agglomerate, N, can be estimated by [13]:

$$N\left(\lambda\right) = \left(\frac{k_v}{k_{va}}\right)^{D_f/3} \left(\frac{\lambda}{L_a}\right)^{D_f} \tag{6.9.8}$$

where k_v and k_{va} are the volume shape factors, L_a is the aggregate size.

The breakage kernel (Eq. 6.9.5) includes the effect of process parameters. One should note, however, that the proportionality constant, C_b, is an experimental one. Hence, in order for the kernel to work properly, one has choose C_b value to best fit experimental data. In the simulations, C_b was equal to 2×10^{-5}.

Experimental system

The course of the titanium dioxide deagglomeration process was investigated both numerically and experimentally in the ICHEMAD-Profarb tank homogenizer system, whose geometry is shown in Fig. 6.9.1. The flat-bottomed tank diameter was equal to 240 mm and the liquid level was at the height of 115 mm. This corresponded to approximately 5 litres of TiO_2 suspension per run. The tank was equipped with a water jacket, which allowed the thermostatting of experiments.

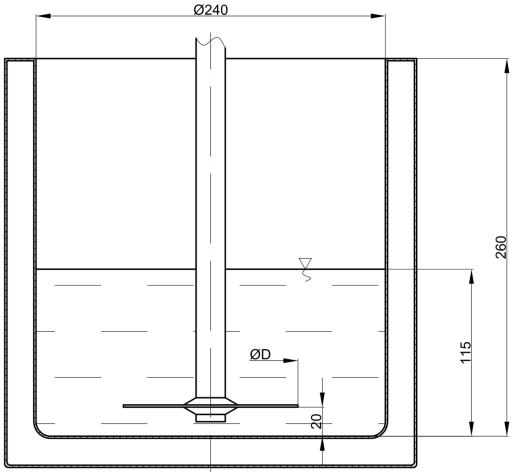

Figure 6.9.1: Tank homogenizer geometry.

Two saw impellers of equal diameter of 120 mm were used, referred in this work as M01 (Fig. 6.9.2a) and M02 (Fig. 6.9.2b). The main difference between the impellers was the shape of teeth and the presence of holes that increase shear and circulation in the tank.

In this work, the suspension of 40% mass concentration of titanium dioxide was used to study the efficiency of deagglomeration process. To prepare suspensions for the process, demineralized water and industrial grade chemicals were used. The suspension's density was equal to 1440 kg m^{-3} and with regards to viscosity, it can be characterized as a non-Newtonian, shear-thinning liquid

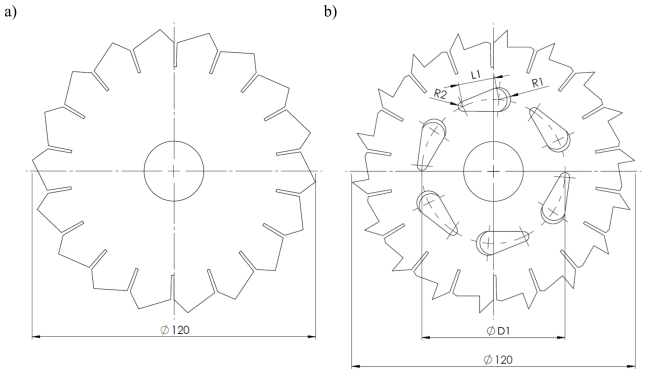

Figure 6.9.2: Impeller geometry: a) M01; b) M02.

(Fig. 6.9.3). To properly describe its rheology, in the simulations the Carreau model (Eq. 6.9.9) was employed to define the suspension viscosity:

$$\mu(\gamma) = \mu_\infty + (\mu_0 - \mu_\infty)\left[1 + (\lambda\gamma)^2\right]^{\frac{n-1}{2}} \tag{6.9.9}$$

where γ is the shear rate, λ is the time constant, n is the power-law index, μ_0 and μ_∞ are, respectively, the zero- and infinite-shear viscosities. All model parameters are presented in Tab. 6.9.1.

Table 6.9.1: Rheology model parameters.

μ_∞	0.11 Pa s
μ_0	14.09 Pa s
λ	1.73 s
n	0.1

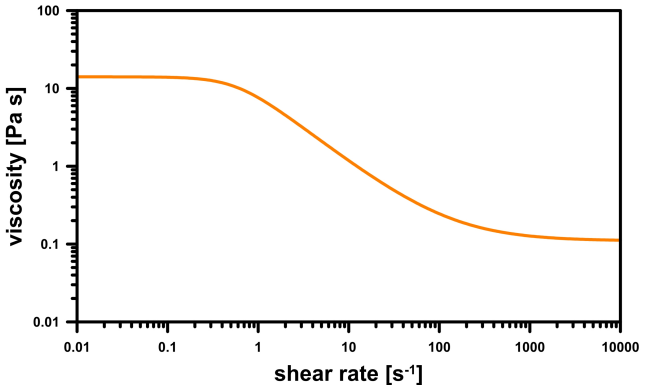

Figure 6.9.3: Effect of shear rate on viscosity of studied suspension.

The experiments were carried out at 293 K. During the measurements, the effect of both mixing (impeller speed) and impeller geometry on the particle breakdown was studied. Product samples were collected at the level of impeller before, during and after the process was finished. Particle size distribution of particles was measured using Beckman&Coulter LS 13320. The device uses laser diffraction and polarization intensity differential scattering techniques and has the measuring range from 40 nm to 2 mm.

Numerical method

Commercial CFD software ANSYS Fluent 2020R2 was used to predict the course of the deagglomeration process in the tank homogenizer. The realizable $k-\varepsilon$ turbulence model, together with the enhanced wall treatment wall function, was used in steady-state hydrodynamics simulations to determine the distribution of process parameters (velocity, viscosity, turbulence dissipation rate, etc.) in the tank. Impeller motion was represented using Moving Reference Frame method with periodic boundaries, i.e., one-sixth of the tank was used in the simulations.

The simulations were divided into two steps. The first step consisted in determining the shape of swirl in the tank for given impeller speed. For this purpose Volume of Fluid multiphase model were used. Next, the swirl shape was extracted and used as a free-shear top wall in individual tank geometries for each impeller-impeller speed combination. The second step included single-phase simulations in thus defined tank geometries. It was checked that the average value of the crucial process parameters for homogenization (viscosity and turbulence dissipation rate) in the liquid phase was equal for both multi- and single-phase predictions.

In the second step, again steady-state simulations were used to predict the flow field of suspension, while the evolution of population balance was solved in transient computations, i.e., a time step value equal to 1 s was set for each tested case. In this work, six moments were tracked in space and time in the QMOM method, and this value can be considered sufficient to obtain accurate results [12]. This equals to three weights and three abscissas that were computed in each iteration. Weights and abscissas were calculated using the Long Quotient-Modified Difference Algorithm [14] and the QL with implicit shifts algorithm [15] to determine eigenvalues and eigenvectors of the tridiagonal matrix. The diffusive term in the transport equations of scalars (Eq. 6.9.2) includes turbulent diffusion. The turbulent diffusion coefficient, D_T, can be determined using the analogy of component, momentum or energy physical transfer. In this work, the expression based on the turbulent Schmidt number was used:

$$D_T = \frac{\nu_T}{Sc_T} = \frac{\nu_T}{0.9} \tag{6.9.10}$$

where ν_T is the turbulent viscosity and is computed with the use of the realizable $k-\varepsilon$ model.

The numerical mesh was generated using ANSYS Fluent Meshing 2020R2 and consisted of approximately 600 000 and 400 000 poly-hexcore cells for “multiphase” and “single-phase” step respectively. The average cell size in the impeller zone was equal to 1 mm and in the bulk region to 4 mm. The inflation layer on each wall consisted of 10 cells and was generated using smooth-transition method with a growth ratio equal to 1.1. This allowed to satisfy the $y^+ \sim 1$ condition for all studied cases. To check mesh independence, an average value of turbulence energy dissipation rate at the highest tested impeller speed was used. It was observed that the results of the computations were not sensitive to a further increase in the number of cells, i.e., the

average energy dissipation rate value was constant (~1–3% difference) despite further increase in mesh density.

The coupled solver was used for the pressure-velocity coupling and the second-order discretization schemes were used for all variables to minimize numerical diffusion effects. Computations were regarded as satisfactorily converged when the total normalized residuals were smaller than 10^{-6} and a constant value of the average wall shear stress was achieved on each wall.

Results and discussion

The effect of impeller speed on the PSD evolution was studied in the range from 500 to 1200 rpm for both impellers. For higher impeller speeds the suspension was becoming strongly aerated, due to strong circulation generated by the impeller motion and lack of baffles in the tank (Fig. 6.9.4). It is not a beneficial phenomenon, because in such situation impellers do not work with full efficiency, and also blurs the differences between impeller designs. Moreover, for these cases the swirl's shape could not be reproduced, and thus making it impossible to conduct "single-phase" simulations for population balance.

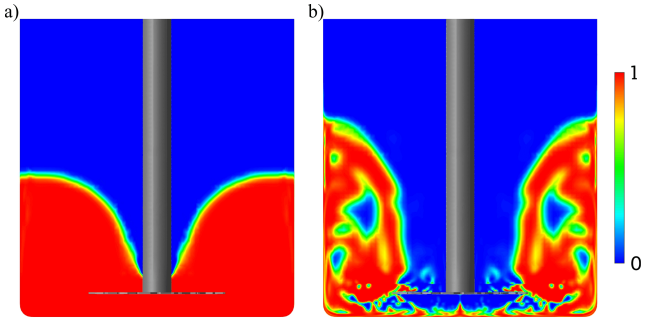

Figure 6.9.4: Swirl shape during homogenization process, red and blue indicate liquid and gas phase volume fraction respectively, M02 impeller: a) 800 rpm; b) 2500 rpm.

Fig. 6.9.5 shows contours of dynamic viscosity in the suspension at 1000 rpm for the M01 and M02 impellers. The difference between the impellers is not significant, however, for the M02 impeller the area of lower viscosity is larger and the "dead zone" below the shaft, i.e., the region with high viscosity values and low circulation, is smaller. What is more, the presence of holes in the disc of the M02 impeller generates a low viscosity region, just below the impeller. This is of course a beneficial phenomenon, which increase circulation in the tank and results in "steeper" and higher swirl.

In the case of turbulence dissipation rate (Fig. 6.9.6), one can observe analogous trends. Again, the region of high energy dissipation (reddish colours) is larger for the M02 impeller. Also, the average value of turbulence dissipation rate is visually higher than in the case of the M01 impeller (more yellow-orange tint in the figures).

Both these two process parameters have a key impact on the homogenization performance. However, an analysis based only on visual observations is insufficient to assess the impeller geometry. A much better indication can

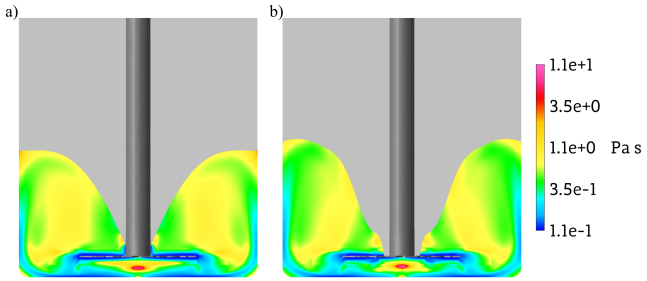

Figure 6.9.5: Contours of dynamic viscosity of suspension in the tank at 1000 rpm: a) M01; b) M02.

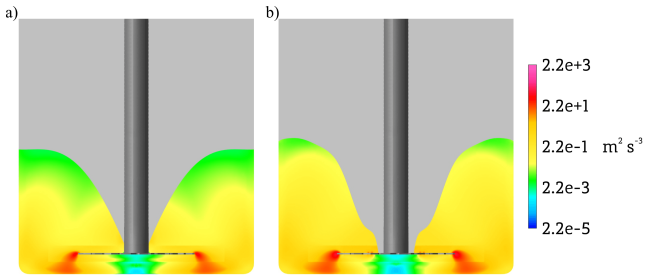

Figure 6.9.6: Contours of turbulence dissipation rate in suspension at 1000 rpm: a) M01; b) M02.

be given by contours of the initial value of zero moment, i.e., at 0 seconds (Fig. 6.9.7). In the figure one can see that the region where particle breakage actually occurs is mainly around the impeller. And, as one could conclude from the results presented in Fig. 6.9.5 and Fig. 6.9.6, that for the M02 impeller this region is as well larger and more visible (red and pink colour), not only at the tip of the teeth as for the M01 impeller. Based on the data presented so far, one can quite accurately estimate the relative impeller performance, i.e., that the M02 impeller will be a better choice for the homogenization process.

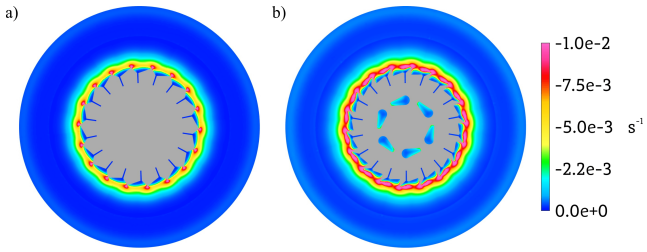

Figure 6.9.7: Contours of the initial m_0 source term at 1000 rpm: a) M01; b) M02.

In fact, both experiments and simulations show this impeller behaviour as well. Fig. 6.9.8 and Fig. 6.9.9 show a comparison of relative impeller performance at 800 and 1200 rpm respectively. As expected, smaller average particle size is obtained using the M02 impeller for both cases. The results also indicate that the breakdown kinetics model used works properly, accurately reflecting the effect of process parameters and impeller geometry on the deagglomeration performance.

Fig. 6.9.10 shows the evolution of the mean particle size during the homogenization process for the M02 impeller at

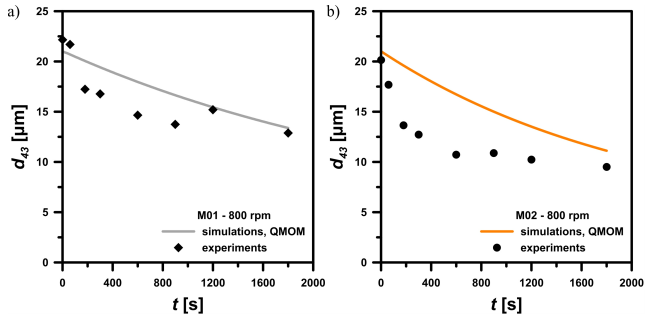

Figure 6.9.8: Evolution of the mean particle size during the homogenization process – comparison of impellers at 800 rpm.

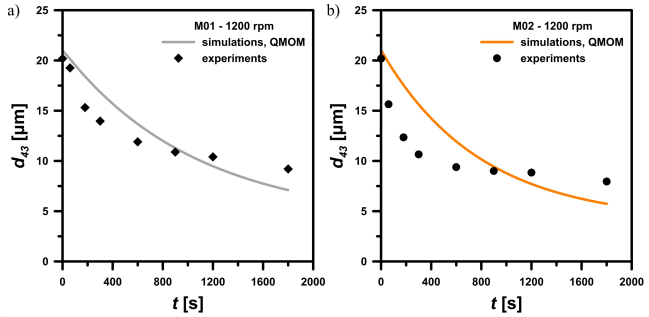

Figure 6.9.9: Evolution of the mean particle size during the homogenization process – comparison of impellers at 1200 rpm.

four tested impeller speeds. One can see that the used particle breakdown kinetics model fits the experimental data fairy well and that the trend of change is predicted accurately. Also, that deagglomeration is more prominent in the early stages of the process, what was not reproduced in the simulations. Hence, further improvement to the breakage model can be introduced to correctly predict this effect, e.g., by including a second breakdown mechanism, erosion, or a more complex particle-wall interactions.

A different representation of the previous data, and a better visualization of the comparison of the impeller performance is presented in Fig. 6.9.11. The figure shows the effect of impeller speed on the mean particle size during, and each sub-figure corresponds to a different process time, from 1 to 30 minutes. Although the difference between the impellers is visible at all process times in the experiments, in the simulations only about 3 to 5 minutes after the process starts differences become apparent. This again indicates that some improvements to the breakdown kinetics model should be introduced to accurately predict the course of the early stages of the homogenization process.

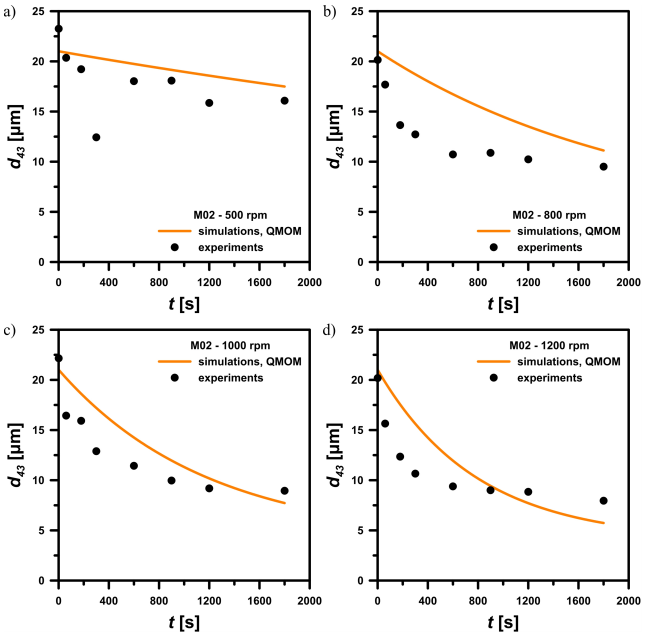

Figure 6.9.10: Evolution of the mean particle size during the homogenization process, M02 impeller:a) 500 rpm; b) 800 rpm; c) 1000 rpm; d) 1200 rpm.

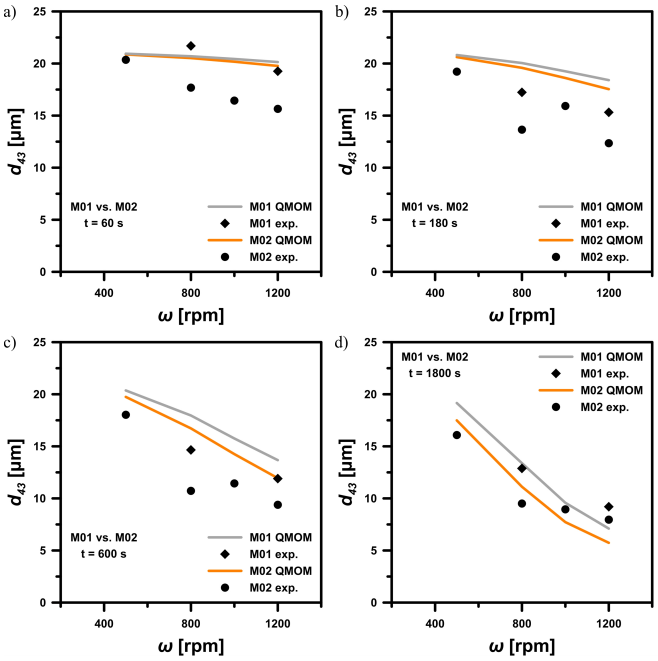

Figure 6.9.11: Effect of impeller speed on the homogenization performance – comparison of impellers. Results at time intervals: a) 60 s; b) 180 s; c) 600 s; d) 1800 s.

Discussion and conclusions

Despite wide application of the homogenization process in the industry, there are not many attempts in the literature to employ population balance in the CFD simulations to predict the course of the process. This is partially related to the fact that there is no universal breakdown kinetics, which would be suitable to predict evolution of dispersed phase properties. In other words, experimental results and a proper analysis is still necessary to achieve accurate predictions. Therefore, this paper is focused on a proper application of population balance to simulate the experimental data of batch homogenization of titanium dioxide. To achieve this goal, the breakage kinetics model was developed and tested using computational fluid dynamics. The dominating mechanism of titanium dioxide breakdown has been recognized based on the experimental data and implemented in the kinetics model. The deagglomeration process is mainly affected by process parameters (viscosity and

density of suspension, turbulence dissipation rate), however, the trends observed in the simulations strongly depends on the experimental constant, whose value was determined to best fit all the available data. Finally, the quadrature approximation method (QMOM) implementation in Fluent allowed to study the effect of process parameters and impeller geometry on the deagglomeration performance (defined here as the smallest possible average particle size after 30 minutes of the process).

In this work, among the two tested impellers, the M02 impeller was found to be a better choice for the homogenization process in this respect. The better mixing characteristics, i.e., increased turbulence, higher shear rates leading to lower suspension's viscosity, resulted in the smaller average particle size after 30 minutes of the process. Considering these observations, impellers with more complex geometry (teeth shape and holes in the impeller disc) should be used to increase deagglomeration efficiency.

The simulations resulted in accurate predictions of the deagglomeration process. The predicted trends were also observed in the experiments, and this was shown for both studied cases. The effect of impeller speed is rather obvious, since increasing impeller speed increases turbulence in the system (Reynolds number) and turbulence energy dissipation, which strongly affects particle breakdown. Therefore, the simulations allowed to observe the effect of impeller geometry and impeller speed on the key process parameters for homogenization. Even such limited data was sufficient to predetermine relative impeller performance. However, such assumptions are usually limited to one specific system and cannot be extrapolated for different systems, especially in larger or smaller scale. Taking this into account, the described approach can be considered as a universal method to compare impellers and, in general, impeller design efficiency, at least for titanium dioxide homogenization.

On the other hand, the deagglomeration is more prominent in the early stages of the process, and was not reproduced accurately in the simulations. This does not exclude developed breakage kinetics from further use, however, indicates the necessity of further development of the model. Based on the available experimental data, a second mechanism could be included here, and the erosion mechanism seems to be a proper choice to better reflect the observed evolution of particle sizes. The population balance simulations were conducted only for a single phase, and this of course is a rather large simplification of the problem at hand. Even though the average values of process parameters in the liquid phase were almost equal, this also could resulted in less accurate predictions. Therefore, in the nearest future we plan to implement the QMOM method for multiphase simulations in Fluent.

The last thing that should be discussed is the computational time needed for the QMOM procedure, which in fact was very low. The average time to calculate moment source terms was about 1.1 s on AMD Ryzen 3700X CPU unit (using single core, up to 4.4 GHz) averaged over a set of 1 000 000 repeated procedures. Of course solving the transport equations for moments is more demanding, but what is really important is that the numerical procedure is not the bottleneck here.

Summing up, the results obtained with the described modelling approach, showed that CFD coupled with population balance methods can be successfully used in the simulations of industrial processes. The results enabled us to assess the impeller design in terms of homogenization performance, and, hopefully in the future, will allow us to further optimize or even create new solutions for industrial homogenization. All the advantages of the modelling method clearly show that quadrature approximation methods coupled with CFD can be a compelling tool in practical, real-life engineering applications, for process optimization, industrial equipment design, and many more.

Acknowledgements

This work was supported by the National Science Centre, Poland (Decision No. DEC-2019/03/X/ST8/01261).

References

[1] Hulburt, H.M.; Katz, S. Some Problems in Particle Technology. *Chemical Engineering Science* 1964, 19, 555–574, doi:10.1016/0009-2509(64)85047-8.

[2] Marchal, P.; David, R.; Klein, J.P.; Villermaux, J. Crystallization and Precipitation Engineering—I. An Efficient Method for Solving Population Balance in Crystallization with Agglomeration. *Chemical Engineering Science* 1988, 43, 59–67, doi:10.1016/0009-2509(88)87126-4.

[3] McGraw, R. Description of Aerosol Dynamics by the Quadrature Method of Moments. *Aerosol Science and Technology* 1997, 27, 255–265, doi:10.1080/02786829708965471.

[4] Marchisio, D.L.; Fox, R.O. Solution of Population Balance Equations Using the Direct Quadrature Method of Moments. *Journal of Aerosol Science* 2005, 36, 43–73, doi:10.1016/j.jaerosci.2004.07.009.

[5] Yuan, C.; Fox, R.O. Conditional Quadrature Method of Moments for Kinetic Equations. *Journal of Computational Physics* 2011, 230, 8216–8246, doi:10.1016/j.jcp.2011.07.020.

[6] Yuan, C.; Laurent, F.; Fox, R.O. An Extended Quadrature Method of Moments for Population Balance Equations. *Journal of Aerosol Science* 2012, 51, 1–23, doi:10.1016/j.jaerosci.2012.04.003.

[7] Ramírez-Muñoz, J.; Martínez-de-Jesús, G.; Soria, A.; Alonso, A.; Torres, L.G. Assessment of the Effective Viscous Dissipation for Deagglomeration Processes Induced by a High Shear Impeller in a Stirred Tank. *Advanced Powder Technology* 2016, 27, 1885–1897, doi:10.1016/j.apt.2016.06.019.

[8] Özcan-Taşkin, N.G.; Padron, G.; Voelkel, A. Effect of Particle Type on the Mechanisms of Break up of Nanoscale Particle Clusters. *Chemical Engineering Research and Design* 2009, 87, 468–473, doi:10.1016/j.cherd.2008.12.012.

[9] Zhang, J.; Xu, S.; Li, W. High Shear Mixers: A Review of Typical Applications and Studies on Power Draw, Flow Pattern, Energy Dissipation and Transfer Properties. *Chemical Engineering and Processing: Process Intensification* 2012, 57–58, 25–41, doi:10.1016/j.cep.2012.04.004.

[10] Titanium Dioxide (Tio2) and Its Applications; Palmisano, L., Parrino, F., Korotcenkov, G., Eds.; 1st ed.; Elsevier: Cambridge, 2021; ISBN 978-0-12-819960-2.

[11] Gordon, R.G. Error Bounds in Equilibrium Statistical Mechanics. *Journal of Mathematical Physics* 1968, 9, 655–663, doi:10.1063/1.1664624.

[12] Marchisio, D.L.; Vigil, R.D.; Fox, R.O. Quadrature Method of Moments for Aggregation–Breakage Processes. *Journal of Colloid and Interface Science* 2003, 258, 322–334, doi:10.1016/S0021-9797(02)00054-1.

[13] Bałdyga, J.; Orciuch, W.; Makowski, Ł.; Malik, K.; Özcan-Taşkin, G.; Eagles, W.; Padron, G. Dispersion of Nanoparticle Clusters in a Rotor–Stator Mixer. *Ind. Eng. Chem. Res.* 2008, 47, 3652–3663, doi:10.1021/ie070899u.

[14] Sack, R.A.; Donovan, A.F. An Algorithm for Gaussian Quadrature given Modified Moments. *Numer. Math.* 1971, 18, 465–478, doi:10.1007/BF01406683.

[15] Press, W.H.; Flannery, B.P.; Teukolsky, S.A.; Vetterling, W.T. *Numerical Recipes in C: The Art of Scientific Computing*; 2nd ed.; Cambridge University Press: Cambridge, 1992; ISBN 978-0-521-43108-8.

6.10 Testing two different synthetic pathways towards linear poly(glycerol sebacate) production

Michal Wrzecionek[*,1], Krzysztof Kolankowski[1], Agnieszka Gadomska-Gajadhur[1]

1 Faculty of Chemistry, Warsaw University of Technology, Warsaw, Poland

Keywords: *poly(glycerol sebacate)*, *biomaterial*, *synthesis*, *polycondensation*, *polytransesterification*.

Abstract

Poly(glycerol sebacate) – PGS – is the first glycerol polyesters used as a biomaterial. Today it is commonly used in tissue engineering. Because of glycerol trifunctionality, it is naturally branched. However, the linear glycerol polyester should be much better for biomedical application than highly branched. In this work, two possibilities of obtaining linear PGS were tested. Polytransesterifcation and polycondensation were studied. Also, a catalyst (aluminum oxide) and excess of glycerol influence on polymer structure were checked. Finally, PGS with only a 4% degree of branching and an 85.89% esterification degree was obtained. Moreover, the presented synthetic pathway is cheap, environment-friendly, and allows for obtaining material for biomedical uses.

Introduction

Materials for biomedical applications are currently the subject of interest of many scientists. Commonly used in this field polyesters are poly(lactic acid), polycaprolactone, and poly(3-hydroxybutyrate) [1–9]. However, they are very hydrophobic, usually degrade slowly under physiological conditions, and chemical functionalization of them is hard to do. Because of these factors, their applications in the biomedical field could be badly restricted [10].

The solution to these problems could be polyesters of glycerin. The first time synthesized material of this group was poly(glycerol sebacate) – PGS [11,12]. After that, it was immediately proposed as a biomaterial for tissue engineering [12,13]. Today, it is widely studied material that is effectively used in cardiac tissue engineering [14–17], vascular tissue engineering [18,19], cartilage tissue engineering [20–22], retinal tissue engineering [23–25], nerve tissue engineering [26–29], repair of tympanic membrane perforation [30–32]. Even more, other medical uses are published as scientific articles and patents [33]. All this emphasizes how valuable poly(glycerol sebacate) has become in recent years.

Usually, this polyester is synthesized through classical polycondensation of glycerol and sebacic acid [11,33–39]. Also, kinetic of this reaction was studied [40]. Because of the different functionality of reactants glycerol – 3 and sebacic acid – 2, there is the natural possibility of creating a branched structure. In most works, scientists report that the prepolymer is first created, which is generally linear and, because of that, very soluble in organic solvents. Such prePGS is commonly used for electrospinning [41]. During a longer reaction from the prepolymer, the polymer is created (Fig. 6.10.1). However, the production of the polymer involves a high degree of branching product. This increases the risk of the chains rapidly cross-linking into an insoluble product, which is called gelation. However, there is a possibility for hyperbranched PGS structure synthesis with avoiding gelation [42,43].

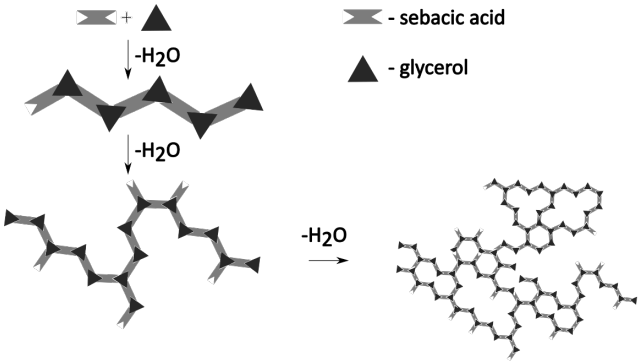

Figure 6.10.1: Graphical presentation of glycerol and sebacic acid polycondensation.

In fact, Wang Yadong, who synthesized PGS first, mention that the best for tissue engineering polyester should have a low density of cross-linking. Such material should be elastic and durable, opposite to be rigid and brittle, which is not desirable [11]. Because of the mentioned glycerol functionality, it is almost impossible to create linear PGS with high molecular weight. However, in one work with the use of the catalyst PGS with less than 1% degree of branching and 24 kDa molecular weight was obtained [44]. Unfortunately, the authors did not study the catalyst interactions with living cells, and they used acid chloride of sebacic acid, which could be negative for biomedical applications.

The goal of this work is to try two different synthetic pathways to obtain linear PGS. There is know that aluminum oxide, a transesterification catalyst, is selective for primary hydroxyl groups [45]. Moreover, the excess of glycerol could impact PGS linearity because the secondary hydroxyl group is less reactive than the primary. In this work polytransesterification of dimethyl sebacate and polycondensation of sebacic acid (both with glycerol) were tested if adding glycerol excess or aluminum oxide catalyst will help with creating linear PGS. Suppose linear polyester could be obtained in these ways. In that case, these methods will be the most appropriate methods for obtaining biomedical linear PGS because of using cheaply available reactants and solid-state catalyst, which could be easy removed from the polymer solution.

To sum up briefly, main hypothesis of this work are:

1. Investigation of the possibility of obtaining linear PGS by poly-transesterification and polycondensation reactions.

* Corresponding author, e-mail: *6824@pw.edu.pl*

Table 6.10.1: Parameters of performed reactions.

No	Glycerol	Second reactant	Catalizator	Temperature (℃)	Time (h)
S1	0,22 mol 20,26 g	dimethyl sebacate (Sigma-Aldrich, 99%)	0%	170	24
S2	16,07 mL	0,22 mol 50,67 g; 51,29 mL	10%	170	24
S3	0,22 mol 20,26 g 16,07 mL	sebacic acid (Sigma-Aldrich, 95%) 0,22 mol; 44,50 g	10%	150	22
S4	0,26 mol 23,94 g 18,98 mL	sebacic acid (Sigma-Aldrich, 95%) 0,13 mol; 26,29 g	10%	150	22
S5	0,22 mol 20,26 g 16,07 mL	sebacic acid (Sigma-Aldrich, 95%) 0,22 mol; 44,50 g	0%	150	22
S6	0,26 mol 23,94 g 18,98 mL	sebacic acid (Sigma-Aldrich, 95%) 0,13 mol; 26,29 g	0%	150	22

2. Investigation of the influence of alumina oxide on the reactivity of secondary hydroxyl groups of glycerol.
3. Investigation of the effect of an excess of glycerin on the reactivity of the secondary hydroxyl group of glycerin.

Materials and methods

All substances were used without further purification. The purity and the producer of the substances used are further specified in the description of the analyzes and experiments.

Acid Number (AN) was determined by titration with the use of thymol blue as an indicator according to the following formula:

$$AN\,(\mathrm{mg_{KOH}/g}) = \frac{(V - V_0) \cdot M_{\mathrm{NaOH}} \cdot 56.1}{m} \qquad (6.10.1)$$

where V - the volume of used 0.1 M NaOH(aq) (CHEMPUR, analytical standard) for sample titration, V_0 – the volume of used 0.1 M NaOH(aq) for blank sample titration, M_{NaOH} – titer of used NaOH(aq), 56.1 – molecular weight of KOH, m – sample weight.

For this analysis, the sample (ca. 0.25 g) was dissolved in 20 mL of methanol (CHEMPUR, analytical standard). According to the definition of AN, the equation consists of converter because of using for the titration NaOH(aq) instead of KOH(aq).

Ester Number (EN) was determined by titration with use of phenolphthalein as an indicator according to the following formula:

$$EN\,(\mathrm{mg_{KOH}/g}) = \frac{(V - V_0) \cdot M_{\mathrm{HCl}} \cdot 56.1}{m} - AN \qquad (6.10.2)$$

where V – the volume of used 0.1 M HCl(aq) (CHEMPUR, analytical standard) for sample titration, V_0 – the volume of used 0.1 M HCl(aq) for blank sample titration, M_{HCl} – titer of used HCl(aq), 56.1 – molecular weight of KOH, m – sample weight.

As before sample was dissolved in 20 mL of methanol, then 20 mL of 0.1 M NaOH(aq) was added. Before titration solution was heated and refluxed for 1 hour after that cooled.

Esterification Degree (*ED*) was calculated based on *AN* and *EN*'s values, as shown in equation 6.10.3. For each sample, three repetitions were done. The end result is an average of them.

$$EN = \frac{EN}{AN + EN} \cdot 100\% \qquad (6.10.3)$$

FTIR spectroscopy was done to confirm ester bond forming in performed reactions. For this purpose, Bruker Alpha II Platinium spectrometer was used. Spectras were collected with the use of the Attenuated Total Reflectance (ATR) technique. 32 scans in the range 400–4000 $\mathrm{cm^{-1}}$ were performed and averaged for each sample.

Nuclear Magnetic Resonance spectroscopy was used for the determination of chemical structure. Sample (ca. 150 mg) was dissolving in 1 mL of DMSO-d6 (Sigma-Aldrich, 99.8%) for 24 h, and then 700 µL of this solution was transferred to testing tube. Spectras were collected by Agilent 400 MHz spectrometer.

Degree of Branching (DB) was calculated based on integrals for characteristic signals for dendritic structure and each repetitive unit structure from ^{1}H NMR spectra as fallow:

$$DB = \frac{D/1}{A/4} \cdot 100\% \qquad (6.10.4)$$

where D – integral of characteristic signal from methine proton in dendritic glycerol structure, A – integral of characteristic signal from an acid part of the repetitive unit structure. The integrals have been normalized in accordance with the number of protons.

Table 6.10.2: Degree of branching and esterification degree of obtained polyesters.

No	Integrals D	A	DB (%)	AN (mg_{KOH}/g)	EN (mg_{KOH}/g)	ED (mg_{KOH}/g)
S3	0,08	1	32%	61,3	325,1	84,13%
S4	0,03	1	12%	39,4	247,6	86,27%
S5	0,05	1	20%	72,1	327,8	81,97%
S6	0,01	1	4%	42,0	255,7	85,89%

Synthetic Pathways. Due to three different pathways various reactants and amounts of catalyst were used, but in each case, the same laboratory equipment has been applied. Also always anhydrous glycerol (Fisher BioReagents, 99.50%) was used as a reactant. As catalyst aluminum oxide (Sigma-Aldrich, standard chromatography grade) was used, which amount was calculated as a percentage of reactants weight sum. The composition of each reactant mixture is shown in Tab. 6.10.1. Reactants were carefully weighed into a three-neck 100 mL bottom flask. The flask was equipped with a magnetic mixing element, a temperature sensor and a Dean-Stark apparatus. The unused neck was tightly closed with a glass stopper. The reaction was carried out under the conditions specified in Tab. 6.10.1. Each reaction mixture was stirred at 200 rpm.

Product purification. Due to catalyst use, it is necessary to purified product after the reaction. Post-reaction mixture was mixed with 30 mL of THF. After sedimentation of the catalyst, the solution was decanted. The product was dried of solvent on a rotary evaporator.

Results

Reactions S1 and S2 both yield with the two-phase product. One of the phases was clear solid crystals. The second phase was a clear liquid. No matter the presence of the used catalyst, the reaction did not happen, because the solid crystals could be only one – unreacted dimethyl sebacate. From this, it follows that transesterification (S1, S2) is not as eases as we thought. For this reason, we decide to give up this synthetic pathway and do not perform further analyses.

Other reactions yields with white soft wax. The presence of ester groups is confirmed by FTIR spectroscopy in each case (S3–S6). There are the fallowing characteristic bands of each spectra (Fig. 6.10.2) at similar wavenumbers:

- 3429.26 cm^{-1}, a wide band characteristic of the vibrations of the O-H bond in alcohols and acids, proves that the glycerol part of the polyester is not esterified in 100% of the hydroxyl groups and that all carboxyl groups of the acid are not reacted, they are polymer ending groups;
- 2927.31 and 2854.75 cm^{-1}, two narrow bands characteristic for the vibration of C – H sp^3 bonds occurring in the glycerin and sebacic parts of polyester;
- 1733.57 cm^{-1}, a narrow band characteristic of carbonyls with a narrow band of 1164.33 cm^{-1} characteristic of the acyl group and a weak band of 1050.02 cm^{-1} characteristic of the alkoxy group, prove the production of polyester.

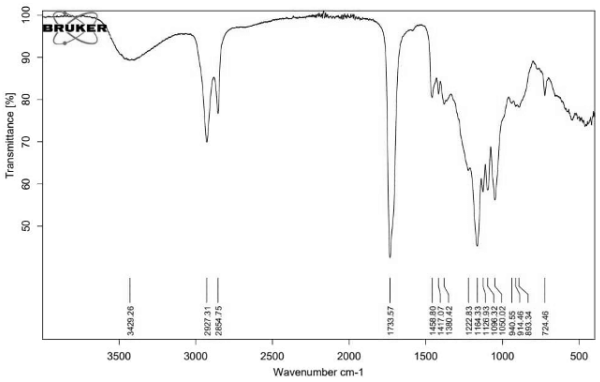

Figure 6.10.2: FTIR spectrum of S3 product.

On ^{1}H NMR are observed several signals (Fig. 6.10.3). Their detailed interpretation is presented in our previous work [41]. In this work, the most important are signals 1.55 ppm (A) and 5.19 ppm. Based on them, the degree of branching is estimated (Tab. 6.10.2). Moreover, 2.17 ppm signal is the characteristic signal for protons bonded to α carbons in the sebacic part of poly(glycerol sebacate), which prove obtaining of this polyester. These signals are observed in each case (S3–S6). High esterification degree (Tab. 6.10.2) also confirms that these pathways yield with polyesters.

To summarizes, the transesterification reactions (S1 and S2) are not suitable for obtaining poly(glycerol sebacate), the reason may be that the substrates are not miscible (two phases are formed). In the case of polycondensation, adding a catalyst to the reaction has a positive effect on the degree of acid conversion, which can be equated with the degree of esterification. For reactions that contain the same acid/glycerin molar ratio: 1:1 S3 and S5; 1:2 S4 and S6; reactions carried out with the catalyst show a slightly higher degree of esterification (2.16 pp and 0.38 pp respectively). The excess of glycerin, both in the case of syntheses with and without a catalyst, allows to obtain a product with a higher degree of esterification (2.14 pp and 3.92 pp respectively). It is surprising that the use of the catalyst yields polyester with a higher degree of branching than in the case of non-catalyzed reactions (12 pp and 8 pp respectively). As we assumed, excess glycerin significantly lowers the degree of branching regardless of the use of the catalyst (20 pp and 16 pp respectively). The S4 reaction is the most satisfactory, it allows to obtain a polymer with a high degree of esterification (85.89%) and a low degree of branching (4%).

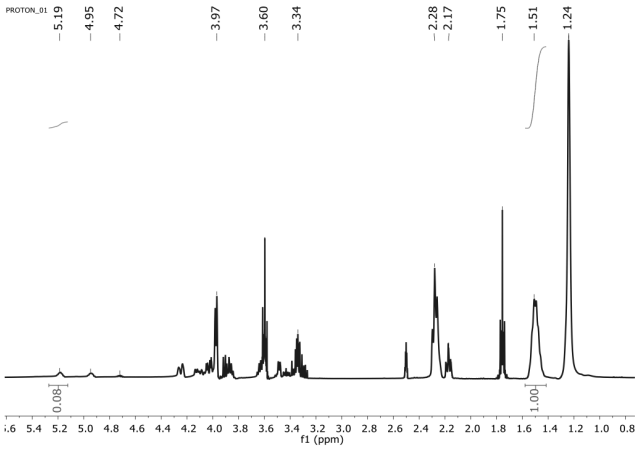

Figure 6.10.3: ^{1}H NMR spectrum of S3 product.

Conclusions

In this work, two different synthetic pathways were tested toward the production of linear poly(glycerol sebacate). The presented transesterification pathway (S1, S2) did not allow for obtaining desirable polyester. Dimethyl sebacate poorly reacts, probably because of this reaction's heterogeneous character – not mixable reactants even in high temperature. In this case, using aluminum oxide as a catalyst does not help much.

According to the literature data, the polycondensation of sebacic acid and glycerin (S3–S6) allows to obtain poly(glycerol sebacate), which was confirmed by spectral methods. The addition of the catalyst has a positive effect on the degree of esterification of the obtained polyester, especially in the case of a 1:1 molar ratio of the substrates. The addition of glycerin (2:1 molar ratio) also has a positive effect on the degree of esterification and allows obtaining a similar effect to the use of a catalyst. The impact of the catalyst addition for the 2:1 molar ratio of the substrates is insignificant.

Based on the ^{1}H NMR spectra, it can be assumed that the catalyst affects the branch growth, acts contrary to the expectations. The use of glycerin addition allows to significantly reduce the degree of branching in both catalyzed and non-catalyzed reactions.

It is most advantageous to carry out the synthesis without the use of a catalyst and with an excess of glycerin. This synthetic pathway allows obtaining poly(glycerol sebacate) with only a 4% degree of branching and 85.89% esterification degree. This is a satisfactory result and the product obtained in this way could be used in medicine as it does not contain any solvent or catalyst contamination.

Founding sources

This scientific research was financed from the budgetary funds on science projected for 2018–2022 as a research project under the "Diamond Grant" program (DI 2017 000347 (ID 395680)).

Acknowledgements

The authors would like to thank the Faculty of Chemistry of the Warsaw University of Technology for providing laboratory equipment.

References

[1] Place E.S., George J.H., Williams C.K., Stevens M.M., Synthetic polymer scaffolds for tissue engineering, *Chemical Society Reviews*, 2009, 38, 1139–1151, doi:10.1039/b811392k

[2] Place E.S., Evans N.D., Stevens M.M., Complexity in biomaterials for tissue engineering, *Nature Materials*, 2009, 8, 457–470, doi:10.1038/nmat2441

[3] Budnicka M., Trzaskowska J., Gadomska-Gajadhur A., Ruśkowski P., Synoradzki L., Preparation of polylactide scaffolds for cancellous bone regeneration-preliminary investigation and optimization of the process, *Pure and Applied Chemistry*, 2019, doi:10.1515/pac-2018-0708

[4] Abdul Karim A., Loh X.J., Design of a micellized α-cyclodextrin based supramolecular hydrogel system, *Soft Matter*, 2015, 11, 5425–5434, doi:10.1039/c5sm00665a

[5] Chen G.Q., A microbial polyhydroxyalkanoates (PHA) based bio- and materials industry, *Chemical Society Reviews*, 2009, 38, 2434–2446, doi:10.1039/b812677c

[6] Kruk A., Gadomska-Gajadhur A.A., Ruśkowski P., Przybysz A., et al., Optimization of the preparation of neomycin-containing polylactide spheres by mathematical methods of design of experiments, *Przemysl Chemiczny*, 2016, 95, 766–769, doi:10.15199/62.2016.4.10

[7] Kruk A., Gadomska-Gajadhur A., Dulnik J., Ruśkowski P., The influence of the molecular weight of polymer on the morphology, functional properties and L929 fibroblasts growth on polylactide membranes for tissue engineering, International Journal of Polymeric Materials and *Polymeric Biomaterials*, 2020, 1–13, doi:10.1080/00914037.2020.1798440

[8] Li Z., Loh X.J., Water soluble polyhydroxyalkanoates: Future materials for therapeutic applications, *Chemical Society Reviews*, 2015, 44, 2865–2879, doi:10.1039/c5cs00089k

[9] Drury J.L., Mooney D.J., Hydrogels for tissue engineering: Scaffold design variables and applications, *Biomaterials*, 2003, doi:10.1016/S0142-9612(03)00340-5

[10] Kai D., Loh X.J., Polyhydroxyalkanoates: Chemical modifications toward biomedical applications, *ACS Sustainable Chemistry and Engineering*, 2014, 2, 106–119, doi:10.1021/sc400340p

[11] Wang Y., Ameer G.A., Sheppard B.J., Langer R., A tough biodegradable elastomer, *Nature Biotechnology*, 2002, 20, 602–606, doi:10.1038/nbt0602-602

[12] Wang Y., Sheppard B.J., Langer R., Poly(glycerol sebacate)—A Novel Biodegradable Elastomer for Tissue Engineering, *MRS Proceedings*, 2002, 724, N11.1, doi:10.1557/PROC-724-N11.1

[13] Wang Y., Kim Y.M., Langer R., In vivo degradation characteristics of poly(glycerol sebacate) 2003, 192–197, doi:10.1002/jbm.a.10534

[14] Chen Q.Z., Bismarck A., Hansen U., Junaid S., et al., Characterisation of a soft elastomer poly(glycerol sebacate) designed to match the mechanical properties of myocardial tissue, *Biomaterials*, 2008, 29, 47–57, doi:10.1016/j.biomaterials.2007.09.010

[15] Masoumi N., Jean A., Zugates J.T., Johnson K.L., Engelmayr G.C., Laser microfabricated poly(glycerol sebacate) scaffolds for heart valve tissue engineering, *Journal of Biomedical Materials Research Part A*, 2013, 101A, 104–114, doi:10.1002/jbm.a.34305

[16] Engelmayr G.C., Cheng M., Bettinger C.J., Borenstein J.T., et al., Accordion-like honeycombs for tissue engineering of cardiac anisotropy, *Nature Materials*, 2008, 7, 1003–1010, doi:10.1038/nmat2316

[17] Jean A., Engelmayr G.C., Finite element analysis of an accordion-like honeycomb scaffold for cardiac tissue engineering, *Journal of Biomechanics*, 2010, 43, 3035–3043, doi:10.1016/j.jbiomech.2010.06.032

[18] Gao J., Crapo P.M., Wang Y., Macroporous Elastomeric Scaffolds with Extensive Micropores for Soft Tissue Engineering, *Tissue Engineering*, 2006, 12, 917–925, doi:10.1089/ten.2006.12.917

[19] Motlagh D., Yang J., Lui K.Y., Webb A.R., Ameer G.A., Hemocompatibility evaluation of poly(glycerol-sebacate) in vitro for vascular tissue engineering, *Biomaterials*, 2006, 27, 4315–4324, doi:10.1016/j.biomaterials.2006.04.010

[20] Kemppainen J.M., Hollister S.J., Tailoring the mechanical properties of 3D-designed poly(glycerol sebacate) scaffolds for cartilage applications 2010, 9–18, doi:10.1002/jbm.a.32653

[21] Liu Y., Tian K., Hao J., Yang T., et al., Biomimetic poly(glycerol sebacate)/polycaprolactone blend scaffolds for cartilage tissue engineering, *Journal of Materials Science: Materials in Medicine*, 2019, 30, 1–11, doi:10.1007/s10856-019-6257-3

[22] Lin D., Cai B., Wang L., Cai L., et al., A viscoelastic PEGylated poly(glycerol sebacate)-based bilayer scaffold for cartilage regeneration in full-thickness osteochondral defect, *Biomaterials*, 2020, 253, 120095, doi:10.1016/j.biomaterials.2020.120095

[23] Ghosh F., Neeley W.L., Arnér K., Langer R., Selective Removal of Photoreceptor Cells In Vivo Using the Biodegradable Elastomer Poly(Glycerol Sebacate), *Tissue Engineering Part A*, 2011, 17, 1675–1682, doi:10.1089/ten.tea.2008.0450

[24] Pritchard C.D., Arnér K.M., Langer R.S., Ghosh F.K., Retinal transplantation using surface modified poly(glycerol-co-sebacic acid) membranes, *Biomaterials*, 2010, 31, 7978–7984, doi:10.1016/j.biomaterials.2010.07.026

[25] Gultekinoglu M., Öztürk Ş., Chen B., Edirisinghe M., Ulubayram K., Preparation of poly(glycerol sebacate) fibers for tissue engineering applications, *European Polymer Journal*, 2019, 121, 109297, doi:10.1016/j.eurpolymj.2019.109297

[26] Saravani S., Ebrahimian-Hosseinabadi M., Mohebbi-Kalhori D., Polyglycerol sebacate/chitosan/gelatin nano-composite scaffolds for engineering neural construct, *Materials Chemistry and Physics*, 2019, 222, 147–151, doi:10.1016/j.matchemphys.2018.10.010

[27] Saudi A., Rafienia M., Zargar Kharazi A., Salehi H., et al., Design and fabrication of poly (glycerol sebacate)-based fibers for neural tissue engineering: Synthesis, electrospinning, and characterization, *Polymers for Advanced Technologies*, 2019, 30, 1427–1440, doi:10.1002/pat.4575

[28] Sundback C.A., Shyu J.Y., Wang Y., Faquin W.C., et al., Biocompatibility analysis of poly(glycerol sebacate) as a nerve guide material, *Biomaterials*, 2005, 26, 5454–5464, doi:10.1016/j.biomaterials.2005.02.004

[29] Hu J., Kai D., Ye H., Tian L., et al., Electrospinning of poly(glycerol sebacate)-based nanofibers for nerve tissue engineering 2017, 70, 1089–1094

[30] Wieland A.M., Sundback C.A., Hart A., Kulig K., et al., Poly(glycerol sebacate)-engineered plugs to repair chronic tympanic membrane perforations in a chinchilla model, *Otolaryngology - Head and Neck Surgery*, 2010, 143, 127–133, doi:10.1016/j.otohns.2010.01.025

[31] Sundback C.A., McFadden J., Hart A., Kulig K.M., et al., Behavior of poly(glycerol sebacate) plugs in chronic tympanic membrane perforations, *Journal of Biomedical Materials Research Part B: Applied Biomaterials*, 2012, 100B, 1943–1954, doi:10.1002/jbm.b.32761

[32] Aydin H.M., Salimi K., Rzayev Z.M.O.O., Pişkin E., Microwave-assisted rapid synthesis of poly(glycerol-sebacate) elastomers, *Biomaterials Science*, 2013, 1, 503–509, doi:10.1039/c3bm00157a

[33] Rai R., Tallawi M., Grigore A., Boccaccini A.R., Synthesis, properties and biomedical applications of poly(glycerol sebacate) (PGS): A review, vol. 37, 2012

[34] Gadomska-Gajadhur A., Wrzecionek M., Matyszczak G., Piętowski P., et al., Optimization of Poly(glycerol sebacate) Synthesis for Biomedical Purposes with the Design of Experiments, *Organic Process Research & Development*, 2018, 22, doi:10.1021/acs.oprd.8b00306

[35] Liu L.L., Yi F.C., Cai W., Synthesis and Shape Memory Effect of Poly(Glycerol-Sebacate) Elastomer, *Advanced Materials Research*, 2012, 476–478, 2141–2144, doi:10.4028/www.scientific.net/AMR.476-478.2141

[36] Liu Q., Tian M., Ding T., Shi R., et al., Preparation and characterization of a thermoplastic poly(glycerol sebacate) elastomer by two-step method, *Journal*

of Applied Polymer Science, 2007, 103, 1412–1419, doi:10.1002/app.24394

[37] Loh X.J., Abdul Karim A., Owh C., Poly(glycerol sebacate) biomaterial: synthesis and biomedical applications, vol. 3, *Royal Society of Chemistry*, 2015

[38] Li Y., Huang W., Cook W.D., Chen Q., A comparative study on poly(xylitol sebacate) and poly(glycerol sebacate): Mechanical properties, biodegradation and cytocompatibility, *Biomedical Materials (Bristol)*, 2013, 8, doi:10.1088/1748-6041/8/3/035006

[39] Kafouris D., Kossivas F., Constantinides C., Nguyen N.Q., et al., Biosourced amphiphilic degradable elastomers of poly(glycerol sebacate): Synthesis and network and oligomer characterization, *Macromolecules*, 2013, 46, 622–630, doi:10.1021/ma3016882

[40] Matyszczak G., Wrzecionek M., Gadomska-Gajadhur A., Ruśkowski P., Kinetics of Polycondensation of Sebacic Acid with Glycerol, *Organic Process Research and Development*, 2020, 24, 1104–1111, doi:10.1021/acs.oprd.0c00110

[41] Denis P., Wrzecionek M., Gadomska-Gajadhur A., Sajkiewicz P., Poly(Glycerol Sebacate)–Poly(l-Lactide) Nonwovens. Towards Attractive Electrospun Material for Tissue Engineering, *Polymers*, 2019, 11, 2113, doi:10.3390/polym11122113

[42] Zamboulis A., Nakiou E.A., Christodoulou E., Bikiaris D.N., et al., Polyglycerol Hyperbranched Polyesters: Synthesis, Properties and Pharmaceutical and Biomedical Applications, *International Journal of Molecular Sciences*, 2019, 20, 6210, doi:10.3390/ijms20246210

[43] Martín Cabezuelo R., Monitoring of the Parameters of Synthesis of Poly(Glycerol Sebacate) and Influence on the Physicochemical and Biological Properties of Its Elastomer. Universitat Politècnica de València, 2020

[44] Slavko E., Taylor M.S., Catalyst-controlled polycondensation of glycerol with diacyl chlorides: linear polyesters from a trifunctional monomer, *Chemical Science*, 2017, 8, 7106–7111, doi:10.1039/C7SC01886J

[45] Otera J., Nishikido J., *Esterification*, Wiley, 2009

6.11 N-doped carbon nanoparticles: properties and influence on mouse fibroblast L929 cells

Piotr Wyrębiak[*,1], Aleksandra Poniatowska [1], Tomasz Ciach [1]

1 Faculty of Chemical and Process Engineering, Warsaw University of Technology, Warsaw, Poland

Keywords: *citric acid*, *nitrogen doped*, *carbon nanoparticles*, *fluorescence*, *cytotoxicity*.

Abstract

Carbon dots (CDs), which are the newly discovered fluorescent nanomaterials, have become popular in the last decade due to their unique optical properties, good biocompatibility, possible low toxicity, high stability in water, and facility of synthesis. One of the types of CDs are nitrogen doped carbon nanoparticles (NCNPs). NCNPs have a non-zero bandwidth and with good fluorescent properties, can have much potential use in various fields.

The aim of the research was to synthesize NCNPs from citric acid with nitrogen atoms incorporated in the structure of NCNPs and to study its effect on the viability of cells cultured in vitro. The nitrogen sources were urea, ammonia, ethanolamine, tris (2-amino-2-(hydroxymethyl)propane-1,3-diol). Homogeneous, mixed solutions were pyrolyzed in 200 °C and various time variants: 1h, 1h 40 min, 2h 30 min, which is novelty to related articles. The analysis of the carbon nanoparticles physicochemical properties was investigated by Fourier transform infrared spectroscopy (FTIR), dynamic light scattering technique (particle size distribution), and fluorescence measurement. The acid-base characteristics were also examined. Because of the potential use in medicine, a commonly known short cytotoxicity test MTT was used for this purpose. The mouse fibroblasts cell line L929 was incubated at 37 °C for 24h with suspensions of nitrogen modified CNPs at a concentration of 1 mg/ml and 0.5 mg/ml.

Particle size analysis showed that a wide distribution of diameter characterizes the obtained particles, especially NCNPs after synthesis with ammonia and urea. The highest relative fluorescence was obtained for carbon nanoparticles with nitrogen groups derived from Tris. The viability for cells incubated with this material was over 70%, so it is supposed that it has no negative influence on the viability of cells. On the contrary, NCNPs obtained with the addition of urea and ammonia turned out to be toxic to cells (viability below 40%). The research also shows differences between carbon-based materials with nitrogen depending on nitrogen sources and its properties are strongly dependent on the synthesis conditions and confirmed that carbon nanoparticles could be a promising material in medical applications, for example, cancer diagnostics or anti-cancer therapy.

[*] Corresponding author, e-mail: *wyrebiakpiotr@gmail.com*

Introduction

The research into the engineering and application of new functional nanomaterials has been explored in various fields such as chemistry, engineering, and biomedicine. Carbon, present in all forms of organic life, performs an essential role in nanomaterials design. Beginning with 3D graphite, through 2D graphene and graphene oxide, to 1D carbon nanotubes, carbon-based nanomaterials continue to arouse interest in the research environment with their superb properties and vast application potential [1]. Graphene and its derivatives: graphene oxide (GO), graphene nanoparticles (GNPs), graphene oxide nanoparticles (GONPs) and other carbon based nanomaterials have potential applications in many fields such as fuel cell technology [2], sensors for monitoring environment [3], energy storage [4], use in biosensors, bioimaging, drug delivery, systems for cell differentiation [5]. Moreover, graphene and its derivatives have inherent antibacterial properties due to their structure [6].

The synthesis methods of carbon nanoparticles can be classified into two categories: "top-down" and "bottom-up". The "top-down" process means decomposition of larger carbon structures such as nanodiamonds [7], graphite [8], carbon nanotubes [9], carbon blacks [10], graphene oxide [11] in an electric arc, by laser ablation, or electrochemical oxidation. The "bottom-up" method is characterized by the synthesis of CNPs starting from precursors at the molecular level, such as citric acid salts, carbohydrates, silica nanocomposites subjected to combustion, hydrothermal or microwave heating [12].

Particular attention should be paid to obtaining CNPs from citric acid, which was used in this work. It belongs to uncomplicated and cheap methods of production of carbon nanoparticles. The simplicity of this synthesis is based on hydrothermal treatment of citric acid solution with appropriate modifiers. In this work, modifiers containing nitrogen were used. The solutions of citric acid with ammonia, urea, ethanolamine, tris (2-amino-2-(hydroxymethyl)propane-1,3-diol) were used and pyrolyzed in different time variants, which is novelty in relation to articles. In literature, it is possible to find modifications in the form of ethylenediamine, diethylamine, urotropine(hexamethylenetetramine), and the above mentioned [13]. Many studies have shown that CNPs have excellent biocompability and low toxicity [14,15,16], but others have shown then to have high cytotoxicity [17]. The biocompatibility of CNPs depends strictly on their properties and the method of synthesis. It is difficult to compare different particles with each other. We decided to compare four types of nanoparticles with different nitrogen donors, but obtained by the same method, at the same temperature to study these differences in terms of their effects on L929 cells. We investigated physicochemical properties by Fourier-transform infrared spectroscopy and acid-base titration to determine amount of –COOH groups. Dynamic light scattering allowed to specify the size of obtained nitrogen-modified-carbon nanoparticles (NCNPs). The fluorescent properties, important in applications in cellular imaging, also were determined. Cytotoxicity was performed by MTT assay.

Table 6.11.1: Summary of reagents and conditions for pyrolysis.

Mixture	Water	Citric acid	Amount of nitrogen source	Pyrolysis time	Temperature (°C)
citric acid with ammonia	20 ml	20 g	21.4 ml s. 25% (v/v)	1 h, 1h 40 min, 2h 30 min	200
citric acid with urea	30 ml	20 g	10 g	1 h, 1h 40 min, 2h 30 min	200
citric acid with ethanolamine	20 ml	20 g	1.88 ml	1 h, 1h 40 min, 2h 30 min	200
citric acid with tris	20 ml	20 g	1.88 g	1 h, 1h 40 min, 2h 30 min	200

Materials and methods

Synthesis of carbon nanoparticles modified with nitrogen atoms

Nitrogen-modified-carbon nanoparticles were produced during the hydrothermal treatment of citric acid (Chempur) with the addition of compounds that are a source of nitrogen in a temperature-controlled drying oven (Binder FD 115) according to a reported method [18–21]. Compared to the above articles, different pyrolysis time variants were used. All chemicals used were of analytical reagent grade. Four nitrogen compounds were selected: ammonia (s. v/v 25%, Chempur), urea (Chempur), ethanolamine (2-aminoethanol) (Sigma), tris (2-amino-2-(hydroxymethyl)propane-1,3-diol) (Sigma). The solutions were prepared as follows: citric acid was thoroughly dissolved in distilled water in concentration according to Tab. 6.11.1. Next nitrogen compounds were added to the dissolved citric acid and stirred until complete dissolution. Then the obtained solutions were pyrolyzed in a drying oven. After the time specified in Tab. 6.11.1, they were taken out of the oven and left to cool down. The solution of 80 ml 0.1 M NaOH was prepared, in which the obtained particles were mixed until a homogeneous suspension was obtained. The obtained suspensions were placed in dialysis tubes with 1 kDa pores (Roth) and dialyzed in deionized water for two days. After one day, the water was changed. The obtained dialyzed suspensions were concentrated by evaporation of the solvent at 60 °C. Then solutions were dried for two days in a freeze-dryer (Christ Alpha 2-4 LSC).

Physicochemical properties of obtained NCNPs

Several analytical techniques were used to determine the quality of the NCNPs produced. The first one is Fourier transform infrared spectroscopy (FTIR). Powders of obtained NCNPs in room temperature were used to determine the spectra on a Nicolet 6700 Spectrometer (Thermo Scientific). Particle size distribution was determined by Zetasizer (Malvern, Nano -ZS) with using dynamic light scattering (DLS). All samples were prepared as 0.5% w/w water suspensions. The suspensions of 0.5% NCNPs w/w in water suspensions were prepared, and fluorescence was collected using TECAN Spark 10M spectrofluorometer. Fluorescence of NCNPs was tested in the emission wavelength range 330 nm–630 nm, and the excitation wavelength range 280 nm, CNPs show strong optical absorption in excitation wavelength in UV region (230–320 nm) [22]. Titration curves were determined with using the Mettler Toledo Seven Compact pH-meter. In all variants, 10 ml of 0.5% w/w water suspensions of obtained NCNPs were titrated by 0.1 M NaOH solution to a final pH of around 12.

Biological properties of NCNPs

In the next step cytotoxicity of obtained NCNPs was measured. An adherent mouse fibroblasts cell line L929 (Sigma Aldrich) was used. Firstly, cells were subcultured in a sterile laminar chamber (Thermo Scientific MSC-Advantage). After dilution to concentration 105 cells/ml with medium (Dulbecco's Modified Eagle Medium without phenol red, Gibco) containing penicillin/streptomycin (Pen/Strep, 1%, Gibco) and L-glutamine (Gln, 1%, Gibco), 100 µl/well of the cells suspension was seeded in 96-well cell culture plates. Plates were incubated at 37 °C, 5% CO_2 in the incubator (Hera Cell 150) for 24 h. All materials were sterilized with 70% ethanol and UV-light for 30 min. On the second day, NCNPs suspensions with phenol red free DMEM medium were prepared according to the data in Tab. 6.11.2. All obtained NCNPs suspensions were filtered through a 0.2 µm syringe filter. After preparing desired suspensions medium was removed from the wells and $100 l/well$ of NCNPs suspensions were contacted with cells for 24h at 37 °C 5% $CO_2 \cdot$ On the third day suspensions were removed from all wells and 50 µl of MTT (Sigma) 1 mg/ml mixture with phenol red free DMEM medium was added to each well. All culture plates were incubated for 4h at 37 °C 5% CO_2. After this period, the MTT solution was removed from wells, then isopropyl alcohol was added, and plates were shaken (Ika Vortex 4). Absorbance was measured at 570 nm and 650 nm using a spectrophotometric microplate reader (Biotek Epoch). The data collected from the spectrophotometer allowed to calculate cell viability, the absorbance of the solution is directly proportional to cell viability. The viability was calculated according to the following formula 6.11.1:

$$C_v = \frac{A_W}{A_{ANC}} \cdot 100\% \tag{6.11.1}$$

where C_v – cell viability, A_W – well absorbance, A_{ANC} – the average negative control absorbance. Then the average value for the holes of the same variant was calculated.

Table 6.11.2: Summary of reagents and conditions for pyrolysis.

Type of NCNPs	Concentration (mg/ml)	
NCNPs prepared with the addition of ammonia, 1h 40 min	1	0.5
NCNPs prepared with the addition of urea, 1h	1	0.5
NCNPs prepared with the addition of ethanolamine, 2h 30 min	1	0.5
NCNPs prepared with the addition of tris, 1h 40 min	1	0.5

Results and discussion

Chemical compound of NCNPs

Carbon nanoparticles are characterized by the absorption in the range of 3050–3800 cm^{-1}, that comes from a hydroxyl group, 3200–3600 cm^{-1} – amine group, 1750–1850 cm^{-1} – carbonyl group, 1650–1750 cm^{-1} – carboxyl group, 1500–1600 cm^{-1} – double carbon bond, 1000–1280 cm^{-1} – ether or epoxy group [19].

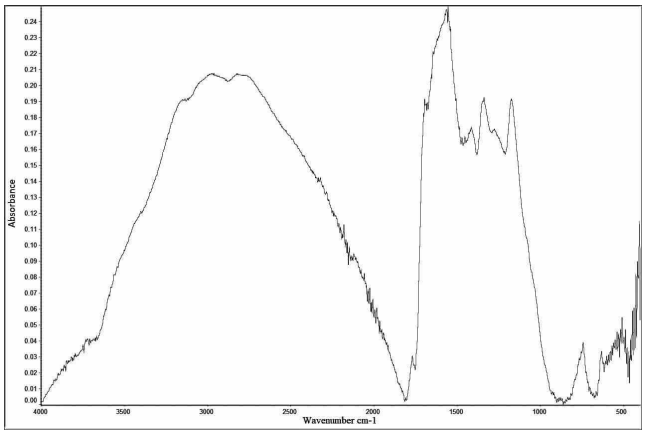

Figure 6.11.1: FTIR spectra for selected NCNPs formed from citric acid and ammonia.

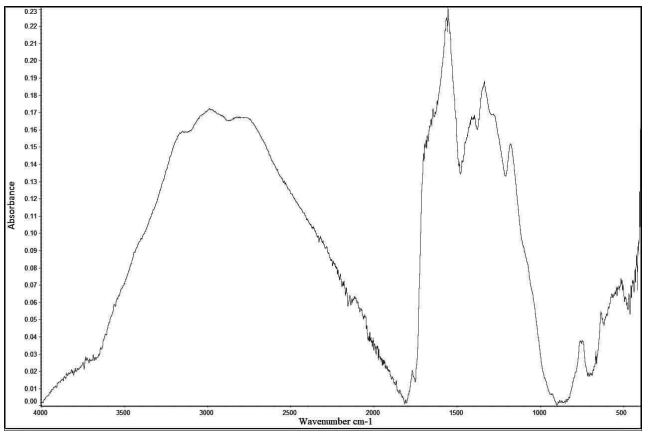

Figure 6.11.2: FTIR spectra for selected NCNPs formed from citric acid and urea.

For the following graphs of absorbance NCNPs (Fig. 6.11.1, Fig. 6.11.2, Fig. 6.11.3, Fig. 6.11.4), it can be seen that all synthesized materials have peaks, which are characteristic of carbon nanoparticles. Therefore, it can be concluded that in all of the tested variants, the expected product was obtained. Strong and broad signals at the hydroxyl and amine groups site suggest a high content of these groups in NCNPs. Figure 6.11.1 shows that NCNPs formed from citric acid and ammonia have the highest vibration band intensity of hydroxyl and amino groups than other NCNPs. Figure 6.11.3 shows a very high and sharp peak at a wavenumber of about 1650 cm^{-1}, for NCNPs formed from citric acid and ethanolamine. It is responsible for the vibrations of the carboxylic groups, which indicates a large number of them. Another characteristic feature of NCNPs is the distinct signal from epoxy groups and double carbon bond. The lowest signals and low signals of the vibrations of the carboxylic groups, the double bond, and the epoxy group can be seen for NCNPs formed from citric acid and ammonia. Comparing spectra from obtained NCNPs with carbon nanoparticles obtained by hydrothermal synthesis, it can be observed that NCNPs has peaks at similar wavenumbers. The amino moieties peaks overlap in the spectrum with other signals, which may be the reason for the similar appearance of the spectra [19].

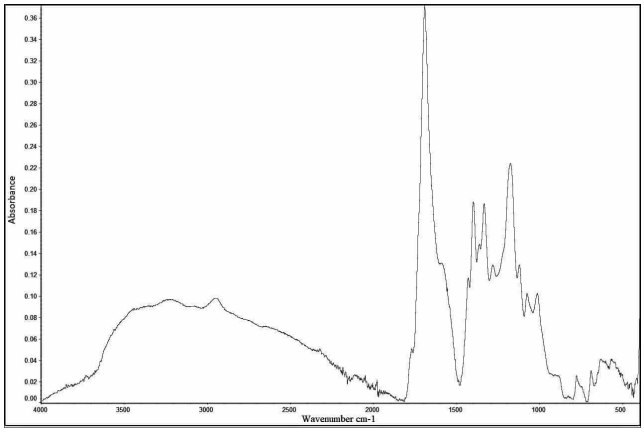

Figure 6.11.3: FTIR spectra for selected NCNPs formed from citric acid and ethanolamine.

Size measurement of NCNPs

The following figures (Fig. 6.11.5, Fig. 6.11.6) show diagrams concerning the particle size distribution by number and volume of NCNPs produced by the pyrolysis of citric acid and nitrogen atoms containing additives. In the volume distribution diagram (Fig. 6.11.5, A) for the NCNPs synthesized with ammonia addition, it can be observed that the pyrolysis variants 1h 40 min and 2h 30 min have a wide volume distribution concerning particle size, at the same time, for the pyrolysis time of 1h, the narrowest volume distribution and the largest percentage have particles of size about 615 nm. The smallest size of carbon nanoparticles by the number can be seen for pyrolysis 1h 40 min and 2h 30 min about

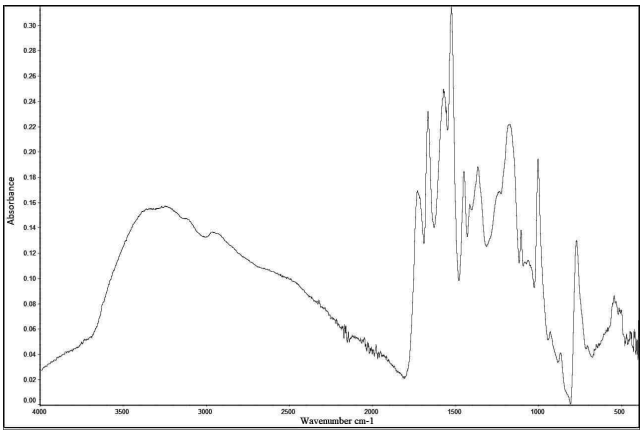

Figure 6.11.4: FTIR spectra for selected NCNPs formed from citric acid and tris.

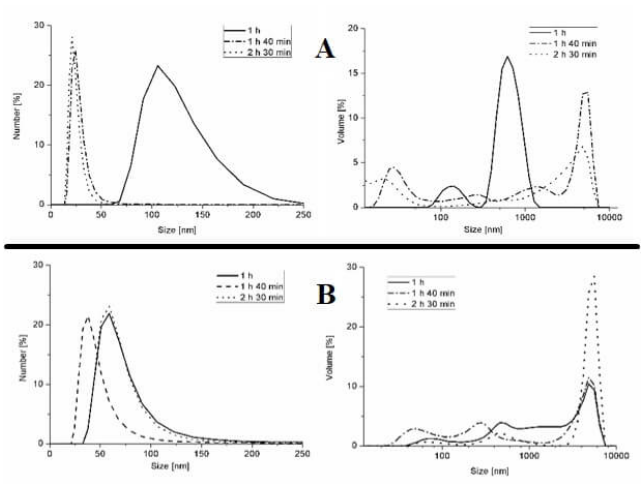

Figure 6.11.5: Particle size distribution by number and volume for the cabon nanoparticles formed from citric acid and ammonia (A) and urea (B) with different pyrolysis time.

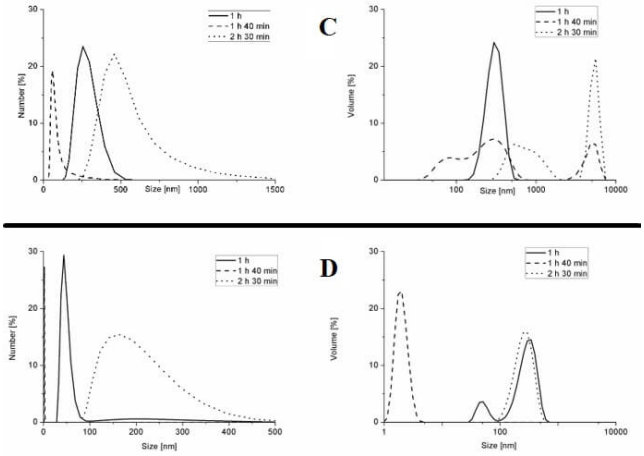

Figure 6.11.6: Particle size distribution by number and volume for the carbon nanoparticles formed from citric acid and ethanolamine (C) and tris (D) with different pyrolysis time.

25 nm. The biggest nanoparticles by number for this type of carbon nanoparticles can be observed for 1h pyrolysis time it is about 106 nm. In figure 6.11.5 for the volume distribution plot (B) for the carbon nanoparticles with urea addition, a wide volume distribution of NCNPs can be seen for all pyrolysis times. The particles formed in the 2h 30 min pyrolysis have the highest percentage of particles by 4801 nm. The particles synthesized at 1h and 1h 40 min also have a wide particle volume distribution, but the largest percentage of particles also has a diameter of 4801 nm. In the graph showing the particle size distribution of the carbon nanoparticles with urea addition, all particle pyrolysis variants have a similar distribution. Structures with a size of about 43 nm have the largest percentage. The volume versus particle size distribution for CNPs with ethanolamine (Fig. 6.11.6, C) shows the widest size range in percentage volume for a pyrolysis time of 1h 40 min, sequentially, the particles with a pyrolysis time of 2h 30 min has the smaller width of the volume distribution, while the NCNPs with a pyrolysis time of 1h has the smallest width. For the particle size distribution for this luminophore, it can be seen that the largest percentage for the pyrolysis time of 2h 30 min have particles with a size of about 458 nm. The next smaller sizes with the highest percentage share have particles synthesized at 1h 40 min – 255 nm and 1h – about 59 nm. Figure 6.11.6 (D) shows a plot of volume versus particle size distribution for carbon particles formed with tris addition. It can be seen that the largest share of 23% for the pyrolysis time of 1h 40 min have particles with very small size – about 2 nm. Correspondingly, for the pyrolysis time of 1h and 2h 30 min, the largest share of about 15% was for particles with a size of about 255 nm. From the above data, it can be concluded that pyrolysis time has no visible effect on particle size distribution. In all cases the obtained particles are heterogeneous. We also not clearly observed the phenomena of increasing with a longer time of pyrolysis. For all variants, we observed large structures, however, most particles have a diameter below 500 nm [23].

Fluorescence of NCNPs

Fig. 6.11.7 shows the fluorescence of different NCNPs variants depending on the pyrolysis time. Fluorescence of NCNPs was tested in the emission wavelength range 330 nm–630 nm and the excitation wavelength – 280 nm. Tab. 6.11.3 shows the results obtained by fluorescence measurement.

Fig. 6.11.7 shows the relative fluorescence of NCNPs produced from citric acid and ammonia for different pyrolysis time variants. It can be seen that the highest fluorescence was obtained for the NCNPs synthesized in 1h 40 min. As shown in Tab. 6.11.3, the lowest fluorescence was observed for NCNPs synthesized in 2h 30 min and slightly higher for 1h. The highest maximum of emission is located at about 510–520 nm. For carbon nanoparticles with urea, the highest fluorescence was achieved for NCNPs obtained within 2h 30 min, then NCNPs obtained in 1h pyrolysis. The lowest relative fluorescence was shown by the NCNPs produced for 1h 40 min. The obtained particles emitted light by a wavelength of about 530 - 540 nm. The spectrum of emission of fluorescence of NCNPs formed from citric acid and ethanolamine shows, very similar to the previous variant

Table 6.11.3: Summary of results obtained using fluorescence.

NCNPs prepared with the addition	Pyrolysis time	Wavelength at the highest relative fluorescence (nm)	Maximum relative fluorescence value (RFU)
Ammonia	1h	510	7000
	1h 40 min	510	24000
	2h 30 min	520	4000
Urea	1h	540	16000
	1h 40 min	530	5000
	2h 30 min	530	18600
Ethanolamine	1h	430	28000
	1h 40 min	430	30000
	2h 30 min	430	37500
Tris	1h	400	280000
	1h 40 min	390	342500
	2h 30 min	420	85000

that the highest fluorescence was emitted by structures obtained in 2h 30 min. The other two variants have similar maximum peak values for 1h 40 min and 1h. In this variant of compound additives, as in the previous ones, the particles emitted radiation in one wavelength, which was 430 nm. The last variant is NCNPs formed from citric acid and tris. The most appropriate time of fluorophore formation for this type of NCNPs is 1h 40 min. Variants with a lower maximum RFU are respectively: 1h and 2h 30 min.

The optical properties of carbon nanoparticles are strongly related to the carbon core of particles and surface modification. The photoluminescence phenomenon is determined by the π states of the sp^2 hybridization states of carbon skeleton influenced by the bandgap of the σ states of the sp^3 matrix. The blue emission may be due to the quantum confinement effect of electrons inside the sp^2 carbon domains. In contrast, the more extended wavelength emission is associated with a mixed structure containing functional groups (at the edges and/or surface) and a graphene core. In particular with the increasing amount of $-NH_2$ moieties cause an extension of the emission wave [22]. Greenlight emission suggests that NCNPs with ammonia and urea contain a large number of amine groups at the edges/surface. Violet-blue emission light suggests that carbon nanoparticles formed from citric acid and ethanolamine and tris have lower contains amino moieties at the edges of structure or connected alkylamines transferred epoxy and –COOH groups into –CONHR and –CNHR, which causes reduction of non-radiative recombination induced by the –COOH and epoxy moieties [24]. It can be observed that pyrolysis time has no significant effect on the location of maximum emission in the area of a variant. This may indicate that the emission of the light wave originates from groups attached to the carbon skeleton [22].

Characteristics of acidic properties

Titration curves for carbon nanoparticles produced by pyrolysis are shown in the figure below (Fig. 6.11.8). Acid-base titration were used to determine amount of -COOH groups in carbon nanoparticles. Titration endpoints (TE) and pKa values were determined graphically.

Titration endpoints and pKa values were determined in those variants where this was possible. TE and pKa were not determined for NCNPs formed from ammonia (1h, 2h 30 min) and urea (1h, 2h 30 min), because the starting pH of the solutions was higher than the others. Respectively for NCNPs made of citric acid and ammonia: 2h 30 min – 6.55. For NCNPs with ammonia pyrolysed for 1h the yield was too low to perform the titration. For NCNPs obtained with urea starting pH was: 1h - 5.57, 2h 30 min – 5.04. This may be due to the high amount of nitrogen-containing groups and possible impurities left after dialysis. The aim of the titration was to verify the amount of -COOH groups, so the titration with the acid was not investigated. TE and pKa were determined for NCNPs from ammonia and urea for 1 h 40 min time of pyrolysis. The values of these points are respectively for ammonia: TE – 209 µl TE, pKa – 4.8, and for NCNPs with urea: TE – 300 µl, pKa – 4.6. The curves for NCNPs (Fig. 6.11.8) made of citric acid and ethanolamine and tris have the characteristic appearance of a weak acid strong base titration curve. It is noticeable that the TE for NCNPs with ethanolamine and tris for different time variants occur at a similar pH value, but with a different volume of titrant added. After graphical determination, for NCNPs with ethanolamine, TE and pKa are respectively: 1h– TE– 1883 µl and pKa– 4.5; 1h 40 min– TE– 2550 µl, pKa– 4.5; 2h 30 min– TE– 916 µl, pKa– 5.2. For NCNPs made from citric acid and tris data are as follows: 1h– TE– 3358 µl and pKa– 4.4; 1h 40 min– TE– 998 µl, pKa– 5.7; 2h 30 min– TE– 1111 µl, pKa– 5.5. From the above data, it can be assumed that the strongest acidic properties for NCNPs from citric acid and ethanolamine pyrolyzed during 1h and 1h 40 min and for NCNPs from citric acid and tris pyrolyzed in 1h. The results obtained cannot be determined whether the pyrolysis time affects the acid-base properties of the carbon nanoparticles.

Cytotoxicity of NCNPs

After analyzing physicochemical properties (especially size distribution and fluorescence) of obtained particles, NCNPs used for cytotoxicity studies were selected: NCNPs with the addition of ammonia, pyrolysis time 1h 40 min; NCNPs with urea addition, 1h; NCNPs with ethanolamine addition, 2h 30 min; NCNPs with tris addition, 1h 40 min. Fig. 6.11.9 shows cell viability after 24-hour incubation with NCNPs suspen-

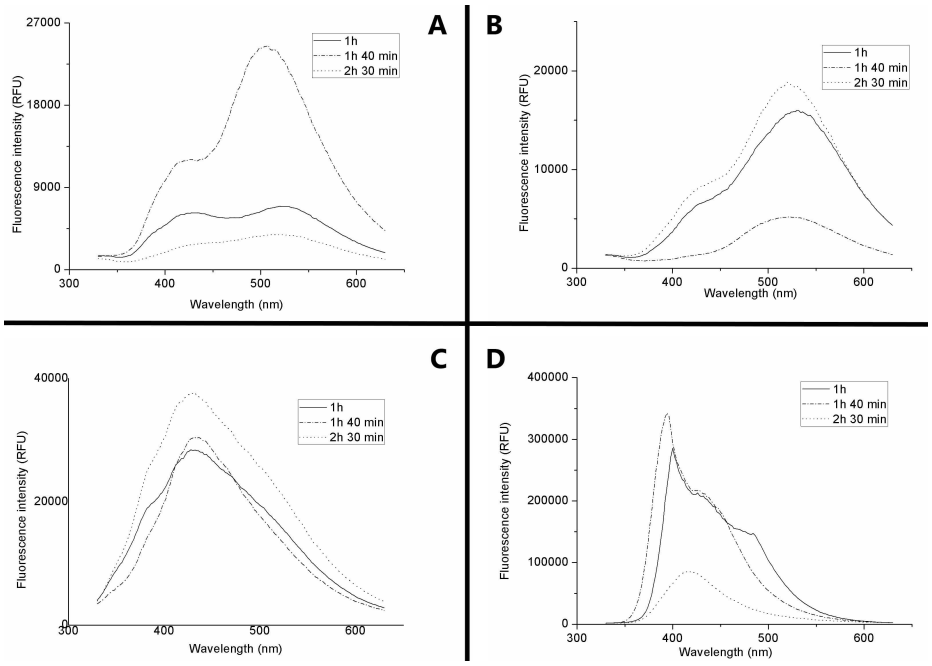

Figure 6.11.7: Fluorescence of carbon nanoparticles derived from citric acid and ammonia (A), urea (B), ethanolamine (C), tris (D) with different time of pyrolysis

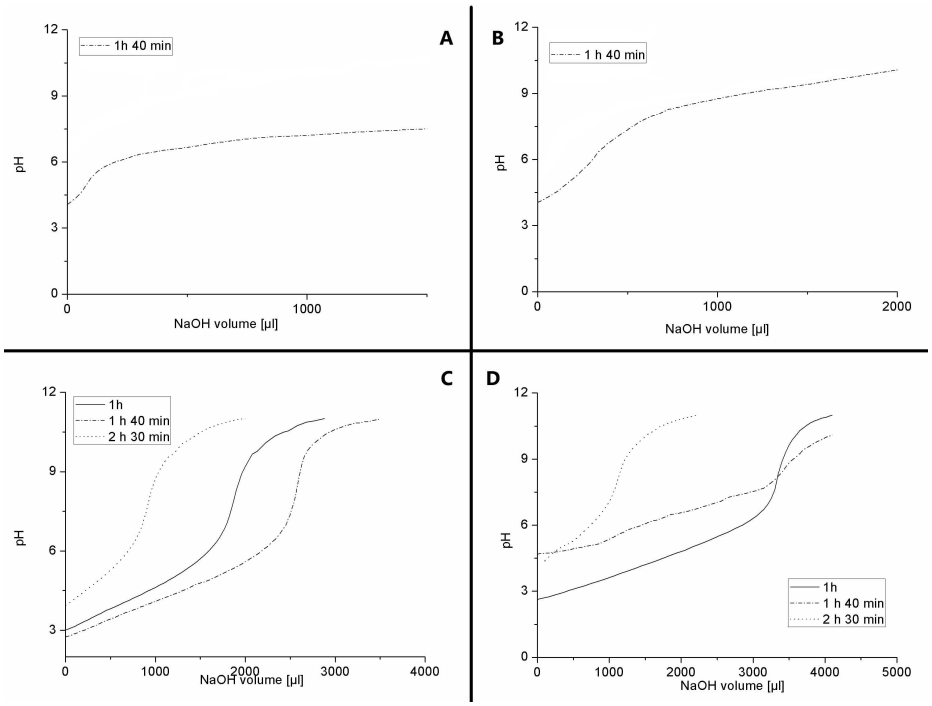

Figure 6.11.8: Titration curves for graphene oxide obtained from citric acid and ammonia (A), urea (B), ethanolamine (C), tris (D) with different time of pyrolysis.

sions. The graph shows that the cells treated with NCNPs suspensions with ammonia and urea had a low survival rate after 24h incubation.

Cells tested with these suspensions had a survival rate below 40%. One of the possible reasons for the low cell survival rate is oxidative stress. The high content of -OH groups in NCNPs with ammonia and urea increases cell death. A second possible reason for increased cell death is the antibacterial properties of carbon nanoparticles. Sharp ends from attached groups disrupt cell membranes [25]. In our view, the first mechanism is essential, but additional research is needed. It is considered that the substance is not toxic when the cell survival rate is over 70% [26]. It can be seen that in the case of NCNPs suspensions with tris with a pyrolysis time of 1h 40 min, the cells had a 60% survival rate. This variant with a concentration of 0.5 mg/ml caused a significant increase in cell viability than a suspension with a concentration of 1 mg/ml. The viability value was 83%, i.e. about 20% more than the suspension with a higher concentration. The highest viability was observed for cells treated

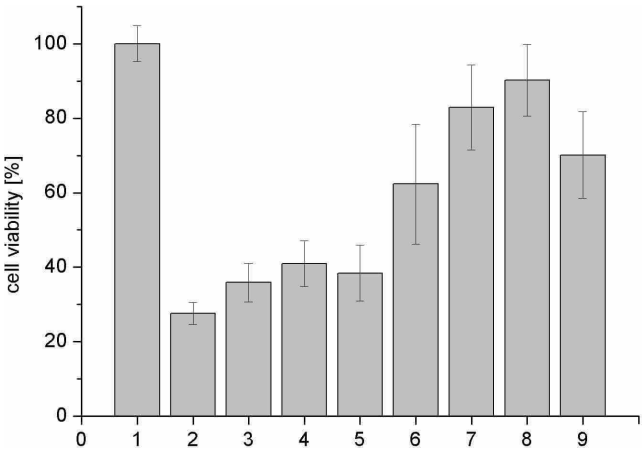

Figure 6.11.9: Cell viability diagram after 24-hour incubation with NCNPs suspensions. 1- negative control; 2 – NCPNs with ammonia, 1h 40 min, 1 mg/ml; 3 – NCNPs with ammonia, 1h 40 min, 0.5 mg/ml; 4 – NCNPs with urea, 1h, 1 mg/ml; 5 – NCNPs with urea, 1h, 0.5 mg/ml; 6 – NCNPs with tris, 1h 40 min, 1 mg/ml; 7 – NCNPs with tris, 1h 40 min, 0.5 mg/ml; 8 – NCNPs with ethanolamine, 2h 30 min, 1 mg/ml; 9 – NCNPs with ethanolamine, 2h 30 min, 0.5 mg/ml.

with NCNPs suspension with ethanolamine with pyrolysis time of 2h 30 min and 1 mg/ml concentration. The cell survival rate was 90%, a very good result. A less concentrated variant, 0.5 mg/ml, had viability at 70%, less than a more concentrated variant. Smaller particles were likely taken up during dilution of the solution, which better penetrate cell organelles and reduced cell viability. In literature Zhang et al. co-cultured for 24h adherent mouse fibroblasts cell line L929 with carbon nanoparticles formed in hydrothermal synthesis with citric acid and ethylenediamine as a nitrogen source. In a concentration of 1 mg/ml, the viability of L929 cells was above 75%, in a high concentration of 2 mg/ml viability was reduced to 60% [27]. Yuan et al. reported that A549 cells incubated for 24h with graphene nanoparticles in concentration 200 μg/ml with $-NH_2$ groups attached had viability above 80% [16].

Conclusions

In the presented work, carbon nanoparticles modified with nitrogen were produced using a bottom-up method by pyrolysis of citric acid with ammonia, urea, ethanolamine, or tris. All the NCNPs obtained have desirable chemical and physical properties, especially fluorescence. FTIR and acid-base analysis confirm that nanoparticles with different groups and chemical properties are obtained depending on the nitrogen source. Based on the above studies, the effect of pyrolysis on the chemical properties of obtained nanoparticles cannot be unequivocally stated. Particle size analysis showed that the NCNPs obtained have a wide diameter distribution and are very heterogeneous in size. Based on the results obtained, the effect of pyrolysis time on particle size cannot be clearly stated due to the high randomness in the DLS results. Pyrolysis time did not affect the wavelength location of the highest fluorescence in all cases. This may indicate that the emission of the light wave originates from groups attached to the carbon skeleton. The most promising nanoparticles with good fluorescence and uniform size were obtained from citric acid and ethanolamine and tris. The cytotoxicity test showed the toxicity of selected nanoparticles synthesized with ammonia and urea. Good viability results for NCNPs from ethanolamine and tris indicate biocompatibility and further studies can be carried out to better understanding their properties. They have the potential to be used in medicine, e.g. in bioimaging of stem or cancer cells in anti-cancer therapies, diagnostics, or the development of sensors.

References

[1] Peng Z., Han X., Li S., Al-Youbi A. O., Bashammakh A. S., El-Shahawi M. S., Leblanc R. M.: Carbon dots: Biomacromolecule interaction, bioimaging and nanomedicine, *Coordination Chemistry Reviews*, Volume 343, 2017, Pages 256-277, doi:10.1016/j.ccr.2017.06.001.

[2] Tong X., Wei Q., Zhan X., Zhang G., Sun S.: The New Graphene Family Materials: Synthesis and Applications in Oxygen Reduction Reaction, *Catalysts*. 7 (2016) 1, doi:10.3390/catal7010001.

[3] Novikov S., Lebedeva N., Satrapinski A., Walden J.: Graphene based sensor for environmental monitoring of NO2, in: *Procedia Eng.*, 2015, doi:10.1016/j.proeng.2015.08.731.

[4] Wei Q., Fu Y., Zhang G., Sun S.: Rational design of carbon-based oxygen electrocatalysts for zinc-air batteries, *Curr. Opin. Electrochem.* 4 (2017) 45–59, doi:10.1016/j.coelec.2017.09.006.

[5] Kotchey G. P. et al.: The enzymatic oxidation of graphene oxide. *ACS Nano* 2011, 5, 2098–2108, doi:10.1021/nn103265h.

[6] Hu W., Peng C., Luo W., Li M., Li X., Li D., Huang Q., Fan C.: Graphene-based antibacterial paper. *ACS Nano* 2010, 4, 4317–4323, doi:10.1021/nn101097v.

[7] Yu S. J., Kang M. W., Chang H. C., Chang K. M. and Yu Y. C.: *J. Am. Chem. Soc.*, 2005, 127, 17604–17605, doi:10.1021/ja0567081.

[8] Sun Y. P., Zhou B., Lin Y., Wang W., Fernando K.A.S., Pathak P., Meziani M.J., Harruff B. A., Wang X., Wang H., Luo P.G., Yang H., Kose ME, Chen B., Veca L.M., Xie S. Y.: Quantum-sized carbon dots for bright and colorful photoluminescence, *J. Am. Chem. Soc.*, 128(2006), 7756-7757, doi:10.1021/ja062677d.

[9] Zhou J. G., Booker C., Li R. Y., Zhou X. T., Sham T. K., Sun X. L. and Ding Z. F.: *J. Am. Chem. Soc.*, 2007, 129, 744–745, doi:10.1021/ja0669070.

[10] Liu H. P., Ye T. and Mao C. D.: *Angew. Chem., Int. Ed.*, 2007, 46, 6473–6475, doi:10.1002/anie.200701271.

[11] Wang Q. L., Zheng H. Z., Long Y. J., Zhang L. Y., Gao M. and Bai W. J.: *Carbon*, 2011, 49, 3134–3140, doi:10.1016/j.carbon.2011.03.041.

[12] Bourlinos B., Stassinopoulos A., Anglos D., Zboril R., Karakassides M. and Giannelis E. P.: *Small*, 2008, 4, 455–458, doi:10.1002/smll.200700578.

[13] Qu D., Zheng M., Zhang L., Zhao H., Xie Z., Jing X., Sun Z.: Formation mechanism and optimization of highly luminescent N-doped graphene quantum dots, 2014, *Scientific Reports*, 4(1), doi:10.1038/srep05294.

[14] Fasbender, S., Zimmermann, L., Cadeddu, RP. et al.: The Low Toxicity of Graphene Quantum Dots is Reflected by Marginal Gene Expression Changes of Primary Human Hematopoietic Stem Cells. *Sci Rep* 9, 12028 (2019), doi:10.1038/s41598-019-48567-6.

[15] Chunyan Z., Chen Z., Gao S., Goh B., Samsudin I., Lwe K., Wu Y., Wu C., Su X.: Recent advances in non-toxic quantum dots and their biomedical applications. *Prog. Nat. Sci.: Mater. Int.*, 2019, 29(6), 628–640, doi:10.1016/j.pnsc.2019.11.007.

[16] Yuan X., Liu Z., Guo Z. et al.: Cellular distribution and cytotoxicity of graphene quantum dots with different functional groups. *Nanoscale Res Lett 9*, 108 (2014), doi:10.1186/1556-276X-9-108.

[17] Murugan K., Nataraj D., Jaganathan A., Dinesh D., Jayashanthini S., Samidoss C. M., Paulpandi M., Panneerselvam C., Subramaniam J. and Nicoletti M.: Nanofabrication of graphene quantum dots with high toxicity against malaria mosquitoes, Plasmodiumfalciparum and MCF-7 cancer cells: impact on predation ofnon-target tadpoles, odonate nymphs and mosquito fishes, *J. Cluster Sci.*, 2017, 28(1), 393–411. doi:10.1007/s10876-016-1107-7.

[18] Fan Y. Z., Zhang Y., Li N., Liu S.G., Liu T., Li N.B., Luo H.Q.: A facile synthesis of water-soluble carbon dots as a label-free fluorescent probe for rapid, selective and sensitive detection of picric acid. *Sensors and Actuators B: Chemical*, 2017, 240, 949-955, doi:10.1016/j.snb.2016.09.063.

[19] Zhang Y., Wang Y. , Feng X. , Zhang F. , Yang Y. , Liu X.: Effect of reaction temperature on structure and fluorescence properties of nitrogen-doped carbon dots. *Applied Surface Science*, 2016, 387, 1236-1246. doi:10.1016/j.apsusc.2016.07.048.

[20] S. Chen, Chen X., Zhang L., Gao J., Ma Q.: Electrochemiluminescence Detection of Escherichia coli O157:H7 Based on a Novel Polydopamine Surface Imprinted Polymer Biosensor. ACS *Applied Materials & Interfaces* 2017 9 (6), 5430-5436, doi:10.1021/acsami.6b12455.

[21] Zhang J. P., Na L. H., Jiang Y. X., Lou D. W., Jin L.: *Anal. Methods* 2016, 8, 7242, doi:10.1039/C6AY02203K.

[22] Song, Yubin & Zhao, Xiaohuan & Shao, Jieren & Zhang, Junhu & Yang, Bai: The photoluminescence mechanism in carbon dots (graphene quantum dots, carbon nanodots, and polymer dots): current state and future perspective. *Nano Research.* 2015, 8, 355-381, doi:10.1007/s12274-014-0644-3.

[23] Dong Y., Shao J., Chen C., Li H., Wang R., Chi Y., Lin X., Chen G.: Blue luminescent graphene quantum dots and graphene oxide prepared by tuning the carbonization degree of citric acid, *Carbon*, Volume 50, Issue 12, 2012, 4738-4743, doi:10.1016/j.carbon.2012.06.002.

[24] Zhu S. J., Zhang J. H., Tang S. J., Qiao C. Y., Wang L., Wang H. Y., Liu X., Li B., Li Y. F., Yu W. L. et al.: Surface chemistry routes to modulate the photoluminescence of graphene quantum dots: From fluorescence mechanism to up-conversion bioimaging applications. *Adv. Funct. Mater.* 2012, 22, 4732–4740, doi:10.1002/adfm.201201499.

[25] Liu S., Zeng T. H., Hofmann M., Burcombe E., Wei J., Jiang R., Kong J., Chen Y.: Antibacterial activity of graphite, graphite oxide, graphene oxide, and reduced graphene oxide: membrane and oxidative stress. *ACS Nano.* 2011 Sep 27;5(9):6971-80, doi:10.1021/nn202451x.

[26] ISO 10993-5:2009, *https://www.iso.org/standard/36406.html*.

[27] Zhang S., Pei X., Xue Y., Xiong J., Wang J.: Bio-safety assessment of carbon quantum dots, N-doped and folic acid modified carbon quantum dots: A systemic comparison, *Chinese Chemical Letters*, Volume 31, Issue 6, 2020,Pages 1654-1659, doi:10.1016/j.cclet.2019.09.018.

7 Scientific articles

7.1 Modeling and simulation of CO_2 capture using MEA in hollow fiber membrane contactors

Alexandru-Constantin Bozonc*,1, Ana-Maria Cormos[1]

1 Department of Chemical Engineering, Faculty of Chemistry and Chemical Engineering, Babes-Bolyai University, Cluj-Napoca, Romania

Keywords: *mathematical modeling*, *CO_2 capture process*, *hollow fiber membrane contactors*.

Abstract

In this work, a mathematical model is developed in order to evaluate the CO_2 capture process into hollow fiber membrane contactors. To analyze the performance of the system, the mathematical model was implemented in Matlab/Simulink. Comparing the simulation results with the experimental data presented in literature we obtained similar mass transfer coefficients. At the same time, the CO_2 removal capacities for the experimental and simulation data showed a good correlation, the R^2 factor has a value of 0.9374. The simulation results indicate that hollow fiber membrane contactors have better efficiency to remove CO2 from flue gases in comparison with packed bed contactors. On this basis, the developed model would be used to evaluate CO_2 capture process in hollow fiber membrane contactors for wide domain of operating conditions in order to predict with accuracy the process parameters (liquid and gaseous flows, composition of the streams, mass transfer area, mass transfer coefficient, etc.).

Introduction

Global warming and climate change caused by CO_2 emissions is an important issue today. Of all greenhouse gases, carbon dioxide has the highest impact on global warming, it contributes more than 60% to global warming due to the huge amounts released into the atmosphere. Most of the carbon dioxide emissions come from fossil fuels and industrial processes [1].

Carbon capture represents a promising option of reducing CO_2 emissions and allows the continuation of fossil fuels for at least a short to medium period of time. The most common process for removal of CO_2 from flue gases is the absorption into a solvent using conventional gas–liquid contactor such as packed bed absorber. Traditionally, gas-liquid contacting operations are carried out in columns or towers. For the past decades packed columns have been used successfully, being designed to maximize mass transfer rate from gas to liquid by increasing the interfacial area. This conventional chemical absorption processes for CO_2 capture suffers many drawbacks such as flooding, foaming, entraining, channeling, and because of their size they have high construction and operating costs [2,3]. In order to solve the operational problems related to the usage of conventional gas–liquid contactors, the gas-liquid microporous membrane contactor was developed, which is a promising and effective CO_2 capture technology. Since the mid-1980s, membrane contactors have been investigated for a wide range of applications. One of the biggest advantages of this technology is the membrane modularity, achieving a substantially larger interfacial area than conventional packed bed absorber [2,4]. Some other advantages of using membrane contactors are [4,5]:

- The absorbent solution and the gas mixture flow independently compared to traditional packed bed absorbers, where the two fluid phases must be in contact, thus avoiding some difficulties such as emulsions, foaming, discharge and flooding.
- Because the two fluids flow through different sections, the available transfer area remains the same at low and high flow rates.
- Scale-up is more simple with membrane contactors, increase in capacity is achieved simply by adding membrane modules.

However, the mass transfer is done by diffusion across the interface just as in traditional packed bed absorber. The membrane contactor consists of three sections presented in Fig. 7.1.1: tube side, membrane and shell side. The gas mixture flows through the tube side, while the solvent flows through the shell side in a countercurrent arrangement.

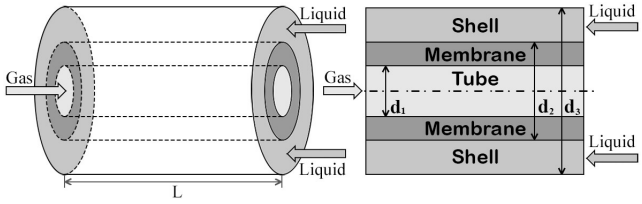

Figure 7.1.1: A schematic diagram of a fiber for the membrane contactor.

Model development

The developed model constitues in equations that describe the complex nature of the process, referring not only to the mass transfer between the gas and the liquid phase, but also to the kinetics of absorption of CO_2.

1. Absorption is performed in isothermal conditions;
2. The gaseous phase in the tube is considered to behave as an ideal gas;
3. The Henry's law is applied for calculating the gas-liquid interface concentration;

* Corresponding author, e-mail: *alexandrubozonc0@gmail.com*

4. Laminar flow regime for the gas mixture in the tube and for the absorbent solution in the shell;
5. The gas and liquid velocity profile are assumed to be fully developed.

Reaction kinetics for CO_2 with Monoethanolamine (MEA)

The chemical reaction equations between CO_2 and MEA (chemical absorbent) and CO_2 with H_2O (physical absorbent) are the following [6,7,8]:

$$CO_2 + 2\,MEA \xrightarrow{k_{CO_2-MEA}} MEA^+ + MEACOO^- \tag{7.1.1}$$

$$H_2O + CO_2 \longleftrightarrow H^+ + HCO_3^- \tag{7.1.2}$$

The reaction rate of CO_2 with MEA in the shell compartment can be determined at different temperatures according to the following empirical equation [9]:

$$N_R = \frac{10^{\left(10.99-\frac{2152}{T}\right)}}{1000} \cdot C^L_{CO_2} \cdot C_{MEA} \tag{7.1.3}$$

where T – temperature in kelvin.

Mass transfer coefficient

An important part of the developed model is the calculation procedure of the mass transfer coefficients.

Mass transfer coefficient of CO_2 inside the gas phase ($k_{CO_2,g}$) – Tube side

The tube side mass transfer coefficient for the CO_2 can be described by the Yang and Cussler correlation as follows [10]:

$$Sh = \frac{k_{CO_2,g} \cdot d_1}{D_{CO_2,g}} = 1.25\left(Re\frac{D_h}{L}\right)^{0.93} Sc^{0.93} \tag{7.1.4}$$

According to the equation, the CO_2 mass transfer coefficient inside the gas phase is calculated as $5.2 \times 10^{-3}\ m\,s^{-1}$, inline with the values presented in literature [11].

Mass transfer coefficient of CO_2 in membrane compartment ($k_{CO_2,m}$)

The membrane mass transfer coefficient of CO_2 in the non-wetted membrane mode of operation can be calculated by [12]:

$$k_{CO_2,m} = \frac{D_{CO_2,g,m} \cdot \epsilon}{\delta \cdot \tau} \tag{7.1.5}$$

The CO_2 diffusion coefficient ($D_{CO_2,g,m}$) can be calculated with the following equation [13]:

$$D_{CO_2,g,m} = \frac{1}{D_{CO_2,M}} + \frac{1}{D_{CO_2,Kn}} \tag{7.1.6}$$

Calculation of the molecular diffusion coefficient of CO_2 ($D_{CO_2,M}$) is based on the kinetic gas theory as the following [6]:

$$D_{CO_2,M} = 1200\frac{R \cdot T \cdot \Omega_\mu}{M \cdot P \cdot \Omega_D}\mu_{CO_2} \tag{7.1.7}$$

coefficient to the equation, the molecular diffusion coefficient is calculated as $1.455 \times 10^{-5}\ m^2\,s^{-1}$, inline with the values presented in literature [6]. The Knudsen diffusion coefficient ($D_{CO_2,Kn}$) is calculated with the following equation [6]:

$$D_{CO_2,Kn} = \frac{d_p}{3}\sqrt{\frac{8 \cdot R \cdot T}{\pi \cdot M}} \tag{7.1.8}$$

Acording to the equation mentioned above, the CO_2 Knudsen diffusion coefficient is $3.991 \times 10^{-7}\ m^2\,s^{-1}$. Additionally, on the basis of Eq. 7.1.6, the CO_2 diffusion coefficient in the gas filled membrane pores ($D_{CO_2,g,m}$) is $3.885 \times 10^{-7}\ m^2\,s^{-1}$ and on the basis of Eq. 7.1.6 the CO_2 mass transfer coefficient in the membrane compartment of hollow fiber ($k_{CO_2,m}$) is $0.0053\ m\,s^{-1}$, inline with the values presented in the literature [6,11].

Mass transfer coefficient of CO_2 inside the liquid phase ($k_{CO_2,liq}$) – shell side

In order to estimate the mass transfer coefficient in the liquid phase, Graetz-Lévêque solution is applied as the following [14]:

$$Sh = \frac{k_{CO_2,liq} \cdot d_e}{D_{CO_2,liq}} = 1.62\left(\frac{d_e^2 \cdot v_L}{D_{CO_2,liq} \cdot L}\right)^{\frac{1}{3}} \tag{7.1.9}$$

where $D_{CO_2,liq}$ is the CO_2 diffusion coefficient in the MEA solution and can be calculated from N_2O analogy [15]:

$$D_{CO_2,MEA} = D_{N_2O,MEA} \cdot \frac{D_{CO_2,H_2O}}{D_{N_2O,H_2O}} \tag{7.1.10}$$

The diffusivity correlations of CO_2 and N_2O in H_2O have been proposed by Versteeg and Van Swaaij [15]:

$$D_{CO_2,H_2O} = 2.35 \cdot 10^{-6} \cdot \exp\left(-\frac{2119}{T}\right) \tag{7.1.11}$$

$$D_{N_2O,H_2O} = 5.07 \cdot 10^{-6} \cdot \exp\left(-\frac{2371}{T}\right) \tag{7.1.12}$$

The N_2O diffusivity in MEA solution can be calculated with the following equation [15]:

$$\begin{aligned} D_{N_2O,MEA} &= 5.07 \cdot 10^{-6} + 8.65 \cdot 10^{-7} \cdot C_{MEA} + \\ &+ 2.78 \cdot 10^{-7} C^2_{MEA} \cdot \exp\left(\frac{-2371 - 93.4 \cdot C_{MEA}}{T}\right) \end{aligned} \tag{7.1.13}$$

On the basis of Eq. 7.1.13 the CO_2 mass transfer coefficient in the liquid phase ($k_{CO_2,liq}$) is $2.2 \times 10^{-4}\ m\,s^{-1}$, inline with the values presented in the literature [10,11].

Overall mass transfer coefficients, K_L and K_G [16]

$$\frac{1}{K_L \cdot d_2} = \frac{1}{k_{CO_2,liq} \cdot d_2} + \frac{1}{k_{CO_2,m} \cdot H \cdot d_{lm}} + \frac{1}{k_{CO_2,g} \cdot H \cdot d_1} \tag{7.1.14}$$

$$\frac{1}{K_G \cdot d_2} = \frac{H}{k_{CO_2,liq} \cdot d_2} + \frac{1}{k_{CO_2,m} \cdot d_{lm}} + \frac{1}{k_{CO_2,g} \cdot d_1} \tag{7.1.15}$$

Mass balance equations – tube side

There is no chemical reaction in the tube compartment of microporous hollow fiber membrane contactors. The continuity equation for gas flow rate (Q_G) in tube side is as follows:

$$\frac{dQ_G}{dz} = -\frac{A_G \cdot M_G \cdot N_{CO_2}}{\rho_G} \tag{7.1.16}$$

where N_{CO_2} is the mass transfer parameter from the gas phase to the liquid coefficient and is calculated as follows [3,17,18]:

$$N_{CO_2} = a_e \cdot E \cdot K_G \cdot (C^g_{CO_2} - H \cdot C^L_{CO_2}) \tag{7.1.17}$$

In order to determinate the solubility of CO_2 in MEA solution, the N_2O analogy is used [11]:

$$H_{CO_2,MEA} = H_{N_2O,MEA} \cdot \frac{H_{CO_2,H_2O}}{H_{N_2O,H_2O}} \tag{7.1.18}$$

The Henry's constant for N_2O in pure MEA can be calculated from the following expressions [11]:

$$H_{N_2O,MEA} = 1.207 \cdot 10^5 \cdot \exp\left(-\frac{1126.5}{T}\right) \tag{7.1.19}$$

$$H_{CO_2,H_2O} = 2.82 \cdot 10^6 \cdot \exp\left(-\frac{2044}{T}\right) \tag{7.1.20}$$

$$H_{N_2O,H_2O} = 8.55 \cdot 10^6 \cdot \exp\left(-\frac{2284}{T}\right) \tag{7.1.21}$$

The continuity equation for CO_2 concentration in the tube side, where is no chemical reaction, is written as below:

$$\frac{dC^G_{CO_2}}{dz} = -\frac{N_{CO_2}}{v_G} \tag{7.1.22}$$

Mass balance equations – shell side

The chemical reaction between CO_2 and MEA takes place inside the shell side. The continuity equation for liquid flow rate (Q_L) in shell side is:

$$\frac{dQ_L}{dz} = \frac{A_L \cdot M_L \cdot N_{CO_2}}{\rho_L} \tag{7.1.23}$$

The continuity equations for CO_2 and MEA concentration in shell side, where the chemical reaction takes place, are the following:

$$\frac{dC^L_{CO_2}}{dz} = -\frac{N_R}{v_L} + \frac{N_{CO_2}}{v_L} \tag{7.1.24}$$

$$\frac{dC_{MEA}}{dz} = -\frac{2 \cdot N_R}{v_L} \tag{7.1.25}$$

Results and discussion

The developed model was implemented in Matlab/Simulink using the process parameters presented in Tab. 7.1.1.

The simulation results of CO_2 removal in a wide range of gas flow rates are presented in Fig. 7.1.2. Increasing the gas flow rate, thus increasing the amount of CO_2 in the gas phase, leading to a considerable decrease in CO_2 removed. As can be seen from the Fig. 7.1.2, by increasing the gas flow rate from 1 to 2.8 L/min, the CO_2 removal % decreased from 98% to 57%. The simulation results of CO_2 removal for different liquid flow rates are presented in Fig. 7.1.3. As can be seen from the Figure, an increase of the liquid flow rate from 15 to 30 L/h leads to an increase of CO_2 removal from 65% to 80Åt the same time, the CO_2 removal capacities were compared for the experimental and simulation data and showed a good correlation, the R^2 factor has a value of 0.9374.

Based on simulation results the CO_2 concentration in the gas phase and the gas flow rate along the membrane was determined (Fig. 7.1.4). As it was expected, the CO_2 concentration in the gas phase decreases from 10 vol% to 2.3 vol%

Table 7.1.1: Membrane module dimensions, properties and model parameters [6].

Parameter	Value
Inner fiber diameter, d_1 (m)	$3.5 \cdot 10^{-4}$
Outer fiber diameter, d_2 (m)	$4 \cdot 10^{-4}$
Effective diameter of shell, d_3 (m)	$1.512 \cdot 10^{-3}$
Average pore diameter, d_p (m)	10^{-7}
Module inner diameter (m)	0.035
Module length, L (m)	0.27
Porosity, ε	0.17
Number of fibers, n	510
Membrane thickness, δ (m)	$2.5 \cdot 10^{-5}$
Diffusion coefficient of CO_2 in tube, $D_{CO_2,g}$ ($m^2\ s^{-1}$)	$1.8 \cdot 10^{-5}$
Dynamic viscosity of CO_2, μ_{CO_2} (Pa s)	$1.52 \cdot 10^{-5}$
Viscosity collision integrals, Ω_μ	1.7
Diffusion collision integrals, Ω_D	1.2
Temperature, T (K)	298.15
Pressure, P (Pa)	10^5
Gas flow rate, Q_G ($L\ min^{-1}$)	1–2.8
Liquid flow rate, Q_L ($L\ h^{-1}$)	15–30
CO_2 intel concentration, $C_{CO_2,0}$	10 vol%
MEA intel concentration, C_{MEA}	5 wt%

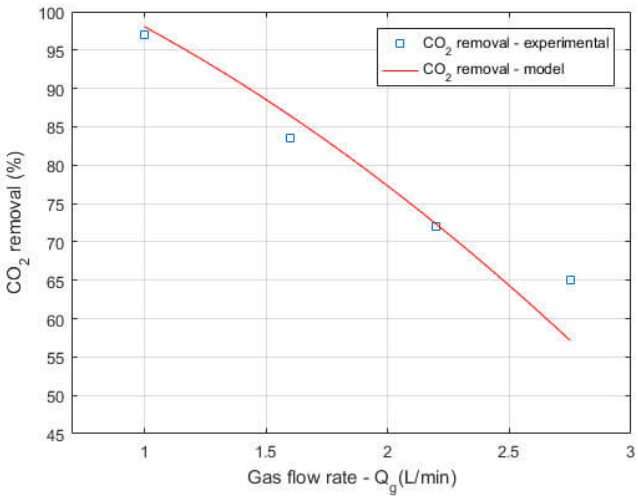

Figure 7.1.2: Effect of gas flow rate on the CO_2 removal. $Q_L = 25\ L\ h^{-1}$, $C_{CO_2,0} = 10$ vol%, $C_{MEA} = 5$ wt%.

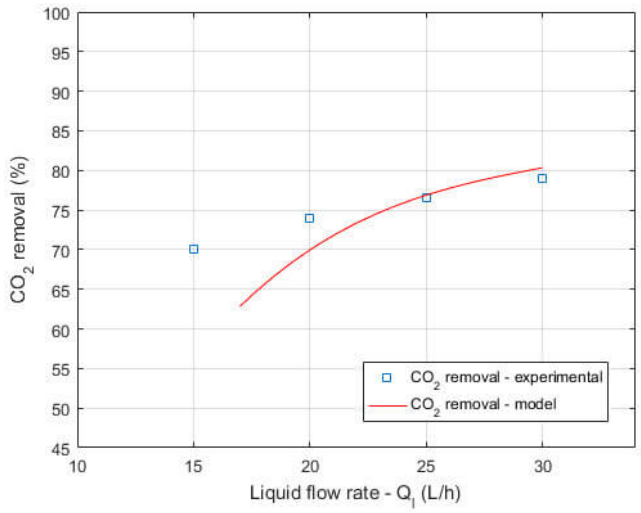

Figure 7.1.3: Effect of liquid flow rate on the CO_2 removal. $Q_G = 2\,\mathrm{L\,min^{-1}}$, $C_{CO_2,0} = 10$ vol%, $C_{MEA} = 5$ wt%.

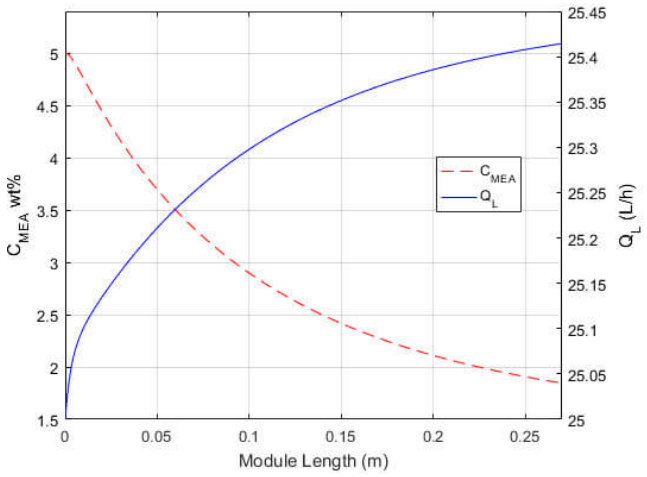

Figure 7.1.5: Profile of MEA concentration in liquid phase and liquid flow rate along the module. $Q_G = 2\,\mathrm{L\,min^{-1}}$, $C_{CO_2,0} = 10$ vol%, $C_{MEA,0} = 5$ wt%.

due to the absorption in the MEA solution. It is also observed that the gas flow rate decreases from 2 L/min to nearly 0.3 L/min because most of the CO_2 is absorbed in the liquid phase. As can be seen from Fig. 7.1.5 the concentration of MEA decreases from 5 wt% to 1.8 wt% because it reacts with CO_2 transferred from the gas phase. The liquid flow increases along the module due to the amount of CO_2 absorbed from the gas phase.

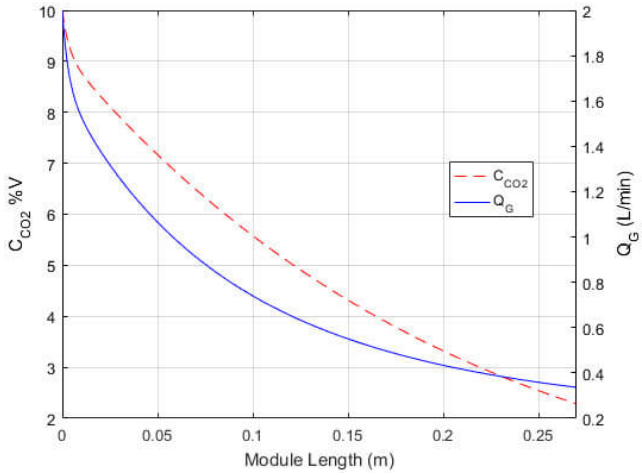

Figure 7.1.4: Profile of CO_2 concentration in gas and gas flow rate along the module. $Q_L = 25\,\mathrm{L\,h^{-1}}$, $C_{CO_2,0} = 10$ vol%, $C_{MEA} = 5$ wt%.

Conclusion

A mathematical model for CO_2 capture using MEA in hallow fiber membrane contactors has been developed. The mass transfer coefficients were calculated and compared with those presented in literature and similar values were obtained. The developed model was validated by comparing the CO_2 removal efficiency from the simulation with the experimental data from literature, where a good correlation was observed. It was observed that the model underestimates the amount of CO_2 removed from the gas phase at gas flows rate higher than 2.5 L/min and liquid flows rate lower than 23 L/h.

The developed model would be used to evaluate CO_2 capture process in hollow fiber membrane contactors for wide domain of operating conditions in order to predict with accuracy the process parameters (liquid and gaseous flows, composition of the streams, mass transfer coefficient, etc.).

Acknowledgement

The research leading to these results has received funding from the NO Grants 2014–2021, under Project contract no. 13/2020.

Nomenclature

$C^L_{CO_2}$	concentration of CO_2 in the liquid phase ($\mathrm{mol\,m^{-3}}$)
C_{MEA}	concentration of MEA in the liquid phase ($\mathrm{mol\,m^{-3}}$)
$C^G_{CO_2}$	concentration of CO_2 in the gas phase ($\mathrm{mol\,m^{-3}}$)
a_e	effective transfer area ($\mathrm{m^2/m^3}$)
A_G, A_L	area of tube and shell side ($\mathrm{m^2}$)
$D_{CO_2,liq}$	diffusion coefficient of CO_2 in MEA absorbent ($\mathrm{m^2\,s^{-1}}$)
$D_{CO_2,g}$	diffusion coefficient of CO_2 in gas phase ($\mathrm{m^2\,s^{-1}}$)
$D_{N_2O,\mathrm{MEA}}$	diffusivity correlations of N_2O in MEA ($\mathrm{m^2\,s^{-1}}$)
D_{CO_2,H_2O}	diffusivity correlations of CO_2 in water ($\mathrm{m^2\,s^{-1}}$)
D_{N_2O,H_2O}	diffusivity correlations of N_2O in water ($\mathrm{m^2\,s^{-1}}$)
d_1	inside diameter of membrane (m)
d_2	outside diameter of membrane (m)
d_3	effective diameter of shell (m)
d_e	average inner diameter of shell (m)
d_{lm}	logarithmic mean diameter of membrane (m)

d_h	hydraulic diameter (m)
d_p	average pore diameter (m)
v_L	liquid velocity ($m\,s^{-1}$)
v_G	gas velocity ($m\,s^{-1}$)
ϵ	membrane porosity (–)
δ	membrane thickness (m)
τ	membrane tortuosity (–)
L	module length (m)
T	temperature (K)
Ω_μ	viscosity collision integrals (–)
Ω_D	diffusion collision integrals (–)
P	pressure (Pa)
μ_{CO_2}	dynamic viscosity of CO_2 (Pa s)
E	enhancement factor (–)
H	Henry's law constant (–)
$H_{CO_2,MEA}$	Henry's constant of CO_2 in MEA (–)
$H_{N_2O,MEA}$	Henry's constant of N_2O in MEA (–)
H_{CO_2,H_2O}	Henry's constant of CO_2 in water (–)
H_{N_2O,H_2O}	Henry's constant of N_2O in water (–)
Q_G	gas flow rate ($L\,min^{-1}$)
Q_L	liquid flow rate ($L\,h^{-1}$)
ρ_L, ρ_G	liquid phase and gas phase density ($kg\,m^{-3}$)
M, M_G, M_L	molecular weight of CO_2, gas and liquid phase (kg/kmol)
n	number of fibers (–)
Re	Reynolds number (–)
Sc	Schmidt number (–)
Sh	Sherwood number (–)

References

[1] Tuckett, R., Greenhouse Gases. Reference Module in Chemistry, *Molecular Sciences and Chemical Engineering*, 2018, doi:10.1007/978-3-319-71062-4_65-1.

[2] A. Bottino, G. Capannelli, A. Comite, R. Di Felice, R. Firpo, CO_2 removal from a gas stream by membrane contactor, *Sep. Purif. Technol.* 59 (2008) 85–90, doi:10.1016/j.seppur.2007.05.030.

[3] D. deMontigny, P. Tontiwachwuthikul, A. Chakma, Using polypropylene and polytetrafluoroethylene membranes in a membrane contactor for CO_2 absorption, *J. Membr. Sci.* 277 (2006) 99–107, doi: 10.1016/j.memsci.2005.10.024.

[4] A. Gabelman, S.T. Hwang, Hollow fiber membrane contactors, *J. Membr. Sci.* 159 (1999) 61–106, doi:10.1016/S0376-7388(99)00040-X.

[5] P.H.M. Feron, A. Jansen, CO_2 separation with polyolefin membrane contactors and dedicated absorption liquids: performances and prospects, (2002) 231–242, doi:10.1016/S1383-5866(01)00207-6.

[6] A.T. Nakhjiri, A. Heydarinasab, O. Bakhtiari, T. Mohammadi, Experimental investigation and mathematical modeling of CO_2 sequestration from CO_2/CH_4 gaseous mixture using MEA and TEA aqueous absorbents through polypropylene hollow fiber membrane contactor, *J. Membr. Sci.* 565 (2018) 1–13, doi:10.1016/j.memsci.2018.07.095.

[7] P.M.M. Blauwhoff, G.F. Versteeg, W.P.M. van Swaaij, A study on the reaction between CO_2 and alkanolamines in aqueous solution, *Chem. Eng. Sci.* 39 (1984) 207–225, doi:10.1016/0009-2509(84)80021-4.

[8] S. Paul, A.K. Ghoshal, B. Mandal, Removal of CO_2 by Single and Blended Aqueous Alkanolamine Solvents in Hollow-Fiber Membrane Contactor: Modeling and Simulation, *Ind. Eng. Chem. Res.* 46 (2007) 2576–2588, doi:10.1021/ie061476f.

[9] R. Faiz, M. Al-Marzouqi, Mathematical modeling for the simultaneous absorption of CO_2 and H_2S using MEA in hollow fiber membrane contactors, *J. Membr. Sci.* 342 (2009) 269–278, doi:10.1016/j.memsci.2009.06.050.

[10] M.C. Yang, E. Cussler, Designing hollow-fiber contactors, *AIChE J.* 32 (1986) 1910–1916, doi:10.1002/aic.690321117.

[11] S. Khaisri, D. deMontigny, P. Tontiwachwuthikul, R. Jiraratananon, CO_2 stripping from monoethanolamine using a membrane contactor, *J. Membr. Sci.* 376 (2011) 110–118, doi:10.1016/j.memsci.2011.04.005.

[12] Z. Qi, E.L. Cussler, Microporous hollow fibers for gas absorption: II. Mass transfer across the membrane, *J. Membr. Sci.* 23 (1985) 333–345, doi:10.1016/S0376-7388(00)83150-6.

[13] H. Kreulen, C.A. Smolders, G.F. Versteeg, W.P.M. Van Swaaij, Determination of mass transfer rates in wetted and non-wetted microporous membranes, *Chem. Eng. Sci.* 48 (1993) 2093–2102, doi:10.1016/0009-2509(93)80084-4.

[14] A. Gabelman, S.T. Hwang, Hollow fiber membrane contactors, *J. Membr. Sci.* 159 (1999) 61–106. doi:10.1016/S0376-7388(99)00040-X.

[15] J.J. Ko, T.C. Tsai, C.Y. Lin, H.M. Wang, M.H. Li, Diffusivity of Nitrous Oxide in Aqueous Alkanolamine Solutions, *J. Chem. Eng. Data* 46 (2001) 160–165. doi:10.1021/je000138x.

[16] J. Ghobadi, D. Ramirez, R. Jerman, M. Crane, S. Khoramfar, CO_2 separation performance of different diameter polytetrafluoroethylene hollow fiber membranes using gas-liquid membrane contacting system, *J. Membr. Sci.* 549 (2018) 75–83, doi:10.1016/j.memsci.2017.11.060.

[17] S. Nii, H. Takeuchi, K. Takahashi, Removal of CO_2 by gas absorption across a polymeric membrane, *J. Chem. Eng. Jpn.* 25 (1992) 67–72, doi:10.1252/jcej.25.67.

[18] P.S. Kumar, J.A. Hogendoorn, P.H.M. Feron, G.F. Versteeg, Approximate solution to predict the enhancement factor for the reactive absorption of a gas in a liquid flowing through a microporous membrane hollow fiber, *J. Membr. Sci.* 213 (2003) 231–245, doi:10.1016/S0376-7388(02)00531-8.

7.2 Uncatalyzed aza-Michael addition of amines to diethyl maleate

Krzysztof Kolankowski*,[1], Michał Wrzecionek[1], Paweł Ruśkowski[1]

1 Faculty of Chemistry, Warsaw University of Technology, Warsaw, Poland

Keywords: *aza-Michael addition*, *diethyl maleate*, *amines reactivity*, *green chemistry*, *poly(glycerol maleate)*.

Abstract

Actually valuable scaffolds building biomaterial can be poly(glycerol maleate) in which structure a double bond is present. It allows for many chain modifications, e.g., aza-Michael addition, considered as modern and innovative. To understand the reaction on the specious polymer better, introductory research is needed. The experiments aimed to choose the amine which will be used in further experiments optimizing the process of cross-linking poly(glycerol maleate) using amines. Triethylenetetramine (TETA), ethylenediamine, and piperazine were reacted with diethyl maleate. To confirm aza-Michael adduct formation ^{1}H NMR and FTIR spectra were analyzed. Based on ^{1}H NMR spectra, yields were calculated. Despite the fact aza-Michael addition has become evident only recently, it turns out to be useful.

Introduction

Michael addition defined by Kohler is the 1,4-addition of a double stabilized carbon nucleophile (Michael donor) to an α-β-unsaturated carbonyl compound (Michael acceptor) [1]. When the nucleophile involves nitrogen, usually from aliphatic/aromatic amines, amides, carbamates, azides, the reaction is named as an aza-Michael addition [2,3]. The aza-Michael reaction is considered an efficient and versatile method of creating new C – N bond, leading to an obtainment of β-amino carbonyl derivatives [2,4].

Aza-Michael addition characterizes high conversion degrees and mild experimental conditions [5,6]. Aza-Michael additions can be carried out catalyst and solvent-free [2,7]. Carrying out the reaction in room temperature, catalyst and solvent free variant is valuable from the green chemistry point of view [8]. It is important that aza-Michael addition minimizes usage of auxiliary agents like gases or purifying agents [9]. This reaction is also used in the synthesis of precursors of polymeric networks [10,11].

In the present article we compare amines reactivity due to their structures. It is found that dimethyl maleate is a very reactive and selective acceptor for the aza-Michael addition [2,12,13]. We consider the electrophilic properties of diethyl maleate the same. Triethylenetetramine is longer than ethylenediamine so we consider TETA more flexible. What is more, triethylenetetramine is not only primary amine like ethylenediamine but also secondary. Piperazine is inflexible, aromatic amine-containing only secondary amine groups. Secondary amines are more nucleophilic than primary amines [14]. It causes higher reactivity of secondary amines than primary amines [7,15,16]. Exceptional reactivity of secondary cyclic amines in the context of aza-Michael addition reaction is also known [17].

Confirmation of this information is important for further research in which we would like to cross-link poly(glycerol maleate). This polyester contains a maleic group in its structure and could be used in tissue engineering as a porous scaffold. In the literature it is known the usage of glycerol polyesters like poly(glycerol sebacate) or poly(glycerol succinate) to support the regeneration of myocardial tissue or tympanic membrane [18,19]. Cross-linking of poly(glycerol maleate) using amines addition would be a valuable method to receive biocompatible, biodegradable, and highly hydrophilic materials.

Materials and methods

Diethyl maleate (≥96%, Sigma Aldrich), triethylenetetramine (TETA) (≥95%, Merck), ethylenediamine (99%, Alfa Aesar), deuterated dimethyl sulfoxide (99.8%, VWR Chemicals) were used as received. Piperazine (99%, ACROS Organics) was dissolved in methanol (≥99%, Chempur).

IR spectra were obtained using a Bruker Alpha Platinum ATR Spectrometer (in ATR mode).

^{1}H NMR spectra were obtained using a Mercury-400BB spectrometer (400 MHz). Samples were dissolved in DMSO d-6 and measured as synthesized.

All reactions were carried out at room temperature in round-bottom 25 mL volume flasks. The ratio of diethyl maleate and amine was 1:2, 1:1, or 2:1. To magnetically stirred diethyl maleate amine was added with the use of a pipette. In the case of piperazine, the solution in methanol (3.06 g in 10 mL) was prepared 24 h before synthesis and stirred. Reactants were stirred for 24 h at 200 rpm. After 24 h FTIR and ^{1}H NMR spectra were collected. The Tab. 7.2.1 is presenting mass of used reactants and appearance of products.

Diethyl maleate:

^{1}H NMR (400 MHz, DMSO-d_6)

δ 6.44 (s, 1H), 4.15 (q, J = 7.1 Hz, 2H), 1.21 (t, J = 7.1 Hz, 3H).

FTIR (neat cm^{-1}): ν = 2986, 1730, 1641, 1447, 1164, 1028.

Diethyl 2-(triethylenetetramino)succinate:

^{1}H NMR (400 MHz, DMSO-d_6)

δ 4.16–4.03 (m, 1H), 4.08–3.98 (m, 2H), 3.60–3.48 (m, 1H), 3.51–3.37 (m, 4H), 3.36–3.16 (m, 1H), 3.01–2.90 (m, 1H), 2.88–2.75 (m, 1H), 2.62 (s, 1H), 2.78–2.41 (m, 6H), 2.39–2.21 (m, 0H), 2.25 (s, 3H), 1.24–1.11 (m, 5H), 1.11–0.99 (m, 4H).

FTIR (neat cm^{-1}): ν = 3304, 2967, 2820, 1728, 1637, 1447, 1178, 1046.

Diethyl 2-(ethylenediamino)succinate:

^{1}H NMR (400 MHz, DMSO-d_6)

δ 4.16–3.97 (m, 5H), 3.55–3.46 (m, 1H), 3.50–3.38 (m, 3H), 3.22–3.11 (m, 1H), 3.11–3.01 (m, 1H), 2.98–2.86 (m, 1H),

* Corresponding author, e-mail: *01123537@pw.edu.pl*

Table 7.2.1: Reaction conditions, amounts of reactants MWKK are the signatures of samples – see Fig. 7.2.2.

Signature		Used amine	Molar ratio diester:amine	Used mass diester	amine	Appearance
MWKK	2	triethylenetetramine	1:1	2.75	2.33	Resin
	9		2:1	2.77	1.18	Resin
	12		1:2	2.75	4.66	Liquid
	3	ethylenediamine	1:1	4.26	1.50	Liquid
	10		2:1	4.30	0.75	Liquid
	13		1:2	4.30	3.00	Resin
	4	piperazine	1:1	6.12	3.06	Wax
	11	(methanol solution)	2:1	3.10	0.78	Wax
	14		1:2	1.53	1.53	Liquid

2.80–2.65 (m, 2H), 2.59 (s, 1H), 2.68–2.51 (m, 2H), 2.51–2.41 (m, 2H), 1.24–1.10 (m, 9H), 1.10–0.99 (m, 4H).
FTIR (neat cm^{-1}): ν = 3292, 2933, 1727, 1654, 1447, 1177, 1046.

Diethyl 2-(piperazine)succinate:
^{1}H NMR (400 MHz, DMSO-d_6)
δ 4.20–4.08 (m, 1H), 4.12–4.04 (m, 1H), 4.08–3.99 (m, 2H), 3.65–3.49 (m, 1H), 3.17 (s, 4H), 2.75 (ddd, J = 15.9, 9.3, 4.2 Hz, 1H), 2.69–2.46 (m, 6H), 2.08 (s, 2H), 1.25–1.11 (m, 6H).
FTIR (neat cm^{-1}): ν = 3302, 2979, 2826, 1725, 1446, 1160, 1025.

Reaction yields calculations

To calculate reaction yields, the formula 7.2.1 was used:

$$\text{Reaction yield} = \frac{A}{\frac{B}{4}} \tag{7.2.1}$$

where:

- A is the integral of the signal generated by protons from succinic group, nearest the added amine (in the Fig. 7.2.4 without frames – 4.32–4.22 ppm)
- B is the integral of the signal generated by protons from diester's ethylene groups (in the Fig. 7.2.4 in frames – 4.22–4.14 ppm)
- Spectra were analyzed using MestReNova software (Mestrelab Research). All spectra were phase-adjusted and baseline-corrected.
- Signals were interpreted with the use of ChemDraw Professional 17.0 software and by comparison with pure reactants spectra.

Results and disscussion

To determine the conversion degree a series of experiments were conducted at room temperature. Diethyl maleate was reacted with triethylenetetramine, ethylenediamine, or piperazine (Fig. 7.2.1). Molar ratio was 1:2–2:1 (diester:amine). Flask warming and product (Fig. 7.2.2) viscosity increase were noticed.

^{1}H NMR spectra of products without any purification are presented in the Fig. 7.2.3 and Fig. 7.2.4. The yields were calculated based on the Fig. 7.2.4 (zoomed Fig. 7.2.3) using

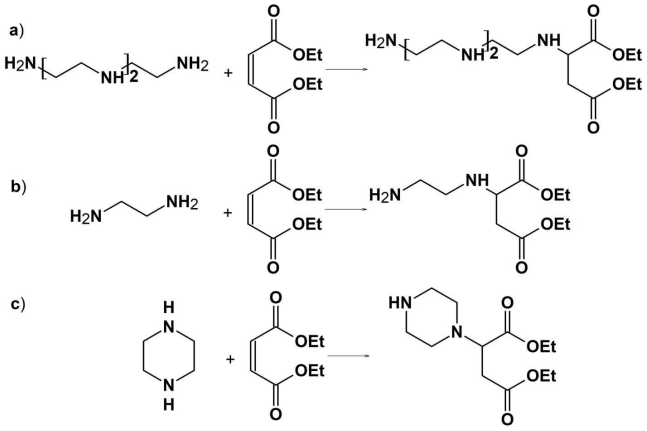

Figure 7.2.1: Aza-Michael addition to diethyl maleate scheme: a) TETA b) ethylenediamine c) piperazine.

Table 7.2.2: Reaction conditions and product appearance. MWKK are the signatures connected with Fig. 7.2.2 and Tab. 7.2.1.

Signature		Used amine	Molar ratio diester:amine	Yield
MWKK	2	triethylene-	1:1	43%
	9	tetramine	2:1	54%
	12		1:2	36%
	3	ethylene-	1:1	65%
	10	diamine	2:1	74%
	13		1:2	7%
	4	piperazine	1:1	79%
	11	(methanol	2:1	85%
	14	solution)	1:2	76%

Formula 7.2.1. Signals in frames (Fig. 7.2.4) are generated by protons from the diester's ethylene groups. Signals without frames (Fig. 7.2.4) are generated by succinic protons nearest the amine. FTIR spectra (Fig. 7.2.5) also confirmed obtaining the aza-Michael adduct.

^{1}H NMR spectra showed the double bond signal's disappearance (~6.58 ppm). This is evidence for aza-Michael's adduct formation.

In the Fig. 7.2.5 are single bands characteristic for secondary amine labeled as A (~3300 cm^{-1}) [20]. Bands

Figure 7.2.2: Obtained product's appearance (MWKK are the signatures from Tab. 7.2.1 and Tab. 7.2.2)

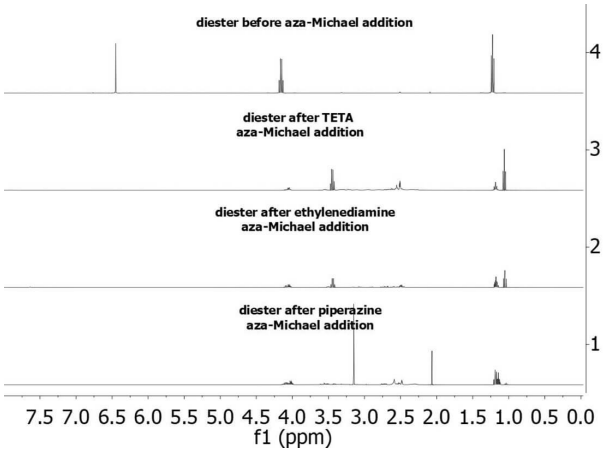

Figure 7.2.3: ^{1}H NMR spectra of:
1) Diethyl 2-(piperazine)succinate; 2) Diethyl 2-(ethylenediamino)succinate; 3) Diethyl 2-(triethylenetatramino)succinate 4) Diethyl maleate (molar ratio of reactants 1:1).

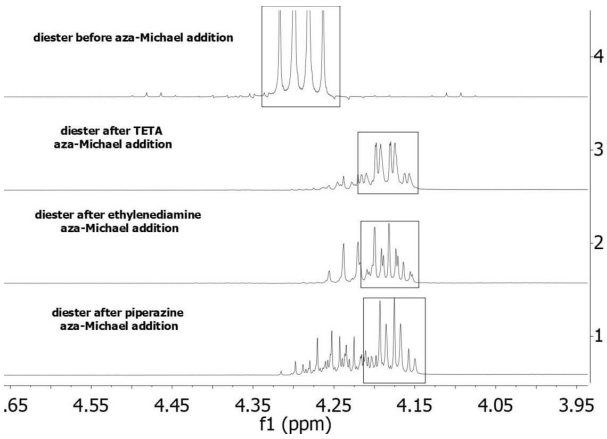

Figure 7.2.4: ^{1}H NMR spectra of reactants: yields calculating regions (molar ratio of reactants 1:1).

labeled E determine the C = C vibrations [20]. For the Diethyl 2-(piperazine)succinate the band intensity is the lowest. It proves that the yield calculated based on the ^{1}H NMR spectrum is the highest. Vibrations at 1725 cm^{-1} (D labeled) are typical for the C – O ester group. G and H bands are corresponding to the alkyl and alkoxy groups [20].

In summary, the analysis included in this article verified the rightness of amines usage to modify diethyl maleate. The highest yields were obtained when the molar ratio between diester and amine were 2:1. It is related to the number

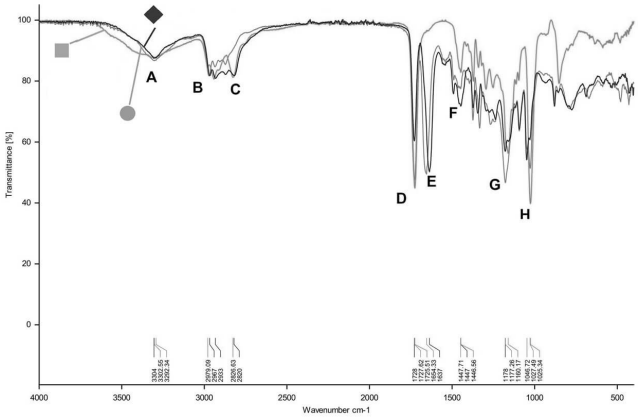

Figure 7.2.5: FTIR spectra: grey square – Diethyl 2-(piperazine) succinate; grey circle – Diethyl 2-(ethylenediamino)succinate; black diamond – Diethyl 2-(triethylenetatramino)succinate (molar ratio of reactants 1:1).

of amine groups in an amine structure. Diester molecule can react in aza-Michael addition with only one amine group. Therefore, to maximize the yield of reactions, molar deficiency of amine in reference to diester is required. Experiments also confirmed the highest reactivity of secondary, cyclic amine.

Conclusion

The results obtained in previous well-known publications have been confirmed. Despite the fact, that aza-Michael addition has become evident only recently, it turns out to be really useful [2]. Obtained results on smaller molecules lead to the conclusion that the poly(glycerol maleate) cross-linking process is available and worth experimenting on. Considering the containment of primary and secondary amine groups, triethylenetetramine is in our opinion the most intriguing. It could result in highly effective network formation by cross-clinking process on polymer structure. The fact that ethylenediamine contains only two primary amine groups leads us to believe that the cross-linking process wouldn't be as effective as with amine, containing more nitrogen atoms. Piperazine contains only two amine group and as a solid need dissolution which makes it inconvenient. Moreover, comparing LD50 values of used amines (orally for a rat, a mouse, and a rabbit) TETA is the least dangerous, so is the most valuable in tissue engineering [21–23]. Polyesters-based networks cross-linked by amines can be used for potential pharmaceutical applications such as carriers for sustained release of hydrophilic drugs, scaffolds, and biodegradable implants for controlled drug delivery [11].

Funding Sources

This research was financed under the "Diamond Grant" program (DI 2017 000347 (ID 395680)).

Acknowledgments

The authors would like to thank the Faculty of Chemistry of the Warsaw University of Technology for providing laboratory equipment.

References

[1] Krishna P.R., Sreeshailam A., Srinivas R., Recent advances and applications in asymmetric aza-Michael addition chemistry, *Tetrahedron*, 2009, 65, 9657–9672, doi:10.1016/j.tet.2009.08.021.

[2] Bosica G., Debono A.J., Uncatalyzed, green aza-Michael addition of amines to dimethyl maleate, *Tetrahedron*, 2014, 70, 6607–6612, doi:10.1016/j.tet.2014.06.124.

[3] Rathod P.B., Kumar K.S.A., Athawale A.A., Pandey A.K., Chattopadhyay S., Polymer-Shell-Encapsulated Magnetite Nanoparticles Bearing Hexamethylenetetramine for Catalysing Aza-Michael Addition Reactions, European *Journal of Organic Chemistry*, 2018, 2018, 5980–5987, doi:10.1002/ejoc.201801095.

[4] Rulev A.Y., Yenil N., Pesquet A., Oulyadi H., Maddaluno J., Tandem aza-Michael additions under high pressure: a shortcut to the azanorbornyl skeleton, *Tetrahedron*, 2006, 62, 5411–5416, doi:10.1016/j.tet.2006.03.070.

[5] Gunay U.S., Cetin M., Daglar O., Hizal G., et al., Ultrafast and efficient aza- and thiol-Michael reactions on a polyester scaffold with internal electron deficient triple bonds, *Polymer Chemistry*, 2018, 9, 3037–3054, doi:10.1039/c8py00485d.

[6] Wang J., Li P.F., Chan S.H., Chan A.S.C., Kwong F.Y., Catalyst-free aza-Michael addition of azole to β,γ-unsaturated-α-keto ester: An efficient access to C-N bond formation, *Tetrahedron Letters*, 2012, 53, 2887–2889, doi:10.1016/j.tetlet.2012.03.132.

[7] Genest A., Portinha D., Fleury E., Ganachaud F., The aza-Michael reaction as an alternative strategy to generate advanced silicon-based (macro)molecules and materials, *Progress in Polymer Science*, 2017, 72, 61–110, doi:10.1016/j.progpolymsci.2017.02.002.

[8] Anastas P., Eghbali N., Green Chemistry: Principles and Practice, *Chemical Society Reviews*, 2010, 39, 301–312, doi:10.1039/b918763b.

[9] Lewandowski T.A., Green Chemistry, vol. 2, Elsevier, 2014.

[10] Bláha M., Trhlíková O., Podešva J., Abbrent S., et al., Solvent-free, catalyst-free aza-Michael addition of cyclohexylamine to diethyl maleate: Reaction mechanism and kinetics, *Tetrahedron*, 2018, 74, 58–67, doi:10.1016/j.tet.2017.11.033.

[11] Alaneed R., Golitsyn Y., Hauenschild T., Pietzsch M., et al., Network formation by aza-Michael addition of primary amines to vinyl end groups of enzymatically synthesized poly(glycerol adipate), *Polymer International*, 2020, doi:10.1002/pi.6102.

[12] Ballini R., Bosica G., Palmieri A., Petrini M., Pierantozzi C., Conjugate addition of nitroalkanes to dimethyl maleate. Regioselective formation of both monoesters of 2-alkylsuccinic acids, *Tetrahedron*, 2003, 59, 7283–7289, doi:10.1016/S0040-4020(03)01175-X.

[13] Guarneri A., Cutifani V., Cespugli M., Pellis A., et al., Functionalization of Enzymatically Synthesized Rigid Poly(itaconate)s via Post-Polymerization Aza-Michael Addition of Primary Amines, *Advanced Synthesis and Catalysis*, 2019, 361, 2559–2573, doi:10.1002/adsc.201900055.

[14] Mather B.D., Viswanathan K., Miller K.M., Long T.E., Michael addition reactions in macromolecular design for emerging technologies, *Progress in Polymer Science (Oxford)*, 2006, 31, 487–531, doi:10.1016/j.progpolymsci.2006.03.001.

[15] Noordzij G.J., Wilsens C.H.R.M., Cascade aza-Michael Addition-Cyclizations; Toward Renewable and Multifunctional Carboxylic Acids for Melt-Polycondensation, *Frontiers in Chemistry*, 2019, 7, 1–14, doi:10.3389/fchem.2019.00729.

[16] Ecochard Y., Auvergne R., Boutevin B., Caillol S., Linseed Oil-Based Thermosets by Aza-Michael Polymerization, *European Journal of Lipid Science and Technology*, 2020, 122, doi:10.1002/ejlt.201900145.

[17] Hoffmann C., Stuparu M.C., Daugaard A., Khan A., Aza-Michael addition reaction: Post-polymerization modification and preparation of PEI/PEG-based polyester hydrogels from enzymatically synthesized reactive polymers, *Journal of Polymer Science*, Part A: Polymer Chemistry, 2015, 53, 745–749, doi:10.1002/pola.27498.

[18] Chen Q.Z., Bismarck A., Hansen U., Junaid S., et al., Characterisation of a soft elastomer poly(glycerol sebacate) designed to match the mechanical properties of myocardial tissue, *Biomaterials*, 2008, 29, 47–57, doi:10.1016/j.biomaterials.2007.09.010.

[19] Aydin H.M., Salimi K., Rzayev Z.M.O., Pişkin E., Microwave-assisted rapid synthesis of poly(glycerol-sebacate) elastomers, Biomaterials Science, 2013, 1, 503–509, doi:10.1039/c3bm00157a.

[20] Beauchamp P., Infrared Tables (short summary of common absorption frequencies), Course Notes, 2010, 2620, 19.

[21] Triethylenetetramine $C_6H_{18}N_4$ – PubChem n.d.

[22] Ethylenediamine – Registration Dossier – ECHA n.d.

[23] Nahler G., Nahler G., Committee for Veterinary Medicinal Products (CVMP), *Dictionary of Pharmaceutical Medicine*, 2009, 32–32, doi:10.1007/978-3-211-89836-9_245.

7.3 Improved nucleation and growth kinetics of molybdenum disulphide nanoparticles

Michał Wojtalik[1], Dominik Borkowski[1], Weronika Gołębiowska[1], Maria Jarząbek[1], Dominika Kasprzak[1], Łukasz Makowski[*,1]

1 Faculty of Chemical and Process Engineering, Warsaw University of Technology, Warsaw, Poland

Keywords: *molybdenum disulphide*, *nanoparticles*, *precipitation*, *kinetics*, *population balance*.

Abstract

Authors presented the results obtained using the new advanced model considering a more complex system of reactions. The first basic kinetics model was published by our team in 2020 and consisted of a set of population balance equations describing nucleation and growth rate of MoS_2 nanoparticles synthesised using wet chemical synthesis. The new model predicts that in the case of low HMA and CA concentration MoS_2 precipitation is the limiting factor to the process of nucleation and growth of molybdenum disulfide and sulfur composite particles. In the case of low CA concentration, the primary source of sulfuric ion for the reaction is the dissociation of AS. The presented model can be used to estimate particles sizes and population.

Introduction

In recent years more reports are appearing regarding molybdenum disulfide synthesis [1–4], modelling [5–7], and applications [8–17]. The most common use for MoS_2 is dry lubrication or as an additive for liquid lubricants [10]. The mining product has a low market value due to low purity and not reproducible properties. If adequately refined or synthesized to achieve the necessary morphology and size, it can be used as a catalyst or electrochemical capacitor and bring much profit. The catalytic properties of molybdenum disulfide are the subject of ongoing research and indicate auspicious catalytic properties for hydrogen desulfurisation, oxygen reduction reactions, methane conversion or hydrogen evolution reactions. Therefore this substance is vastly interesting. However, a sufficiently good model to predict its precipitation results has not been described so far, and further research is needed to establish this kinetics model.

Chemical wet synthesis of molybdenum disulfide has been described comprehensively by Deorsola, Russo and their team [4,5,7,8]. Still, no kinetics model was presented due to the complexity of the reaction and because it is generally hard to measure the progress of a very fast reaction. Molybdenum disulfide synthesis is similar to other metals sulfides, where the nucleation is very fast due to significant supersaturation. The solubility index of MoS_2 is as low as 10^{-43} [18], which strongly drags the reaction towards the products side. One of the methods of measuring the kinetics of metal sulfides precipitation was presented by Al-Tarazi [19], but it cannot be adapted directly to molybdenum disulfide wet chemical synthesis precipitation because the main limiting process was mass penetration of H_2S gas to a liquid phase which is not the case in considered reaction.

Reaction

The reaction involving HMA – Ammonium Heptamolybdate, AS – Ammonium Sulfide and CA – Citric Acid was described by authors in [3,6,20], and the reaction balance and indirect reactions are listed below:

$$(NH_4)_6Mo_7O_{24} + 21\,(NH_4)_2S \xrightarrow{H_3O^+} 7\,MoS_2\uparrow + 7\,S\downarrow + 24\,H_2O + 48\,NH_3\uparrow \quad \text{(A)}$$

$$(NH_4)_2S + 2\,C_6H_8O_7 \longrightarrow H_2S\uparrow + 2\,C_6H_7O_7NH_4 \quad \text{(B)}$$

$$(NH_4)_6Mo_7O_{24} \rightleftharpoons [Mo_7O_{24}]^{6-} + 6\,[NH_4]^+ \quad \text{(C)}$$

$$[Mo_7O_{24}]^{6-} + 4\,H_2O \rightleftharpoons 7\,[MoO_4]^{2-} + 8\,H^+ \quad \text{(D)}$$

$$(NH_4)_2S \rightleftharpoons [NH_4]HS + NH_3 \quad \text{(E)}$$

$$[NH_4]HS \rightleftharpoons H_2S + NH_3 \quad \text{(F)}$$

$$H^+ + NH_3 \rightleftharpoons [NH_4]^+ \quad \text{(G)}$$

$$H_2S \longrightarrow H^+ + HS^- \quad \text{(H)}$$

$$HS^- \longrightarrow H^+ + S^{2-} \quad \text{(I)}$$

$$[MoO_4]^{2-} + 3\,S^{2-} + 8\,H^+ \longrightarrow MoS_2\downarrow + S\downarrow + 4\,H_2O \quad \text{(J)}$$

The last reaction (J) described in [3,6] should rather be written as a set of two reactions:

$$[MoO_4]^{2-} + 8\,H^+ \longrightarrow Mo^{6+} + 4\,H_2O \quad \text{(K)}$$

$$Mo^{6+} + 3\,S^{2-} \longrightarrow MoS_2\downarrow + S\downarrow \quad \text{(L)}$$

and the reaction (L) is a redox reaction [6]:

$$Mo^{6+} + 2\,e^- \longrightarrow Mo^{4+} \quad \text{(M)}$$

$$S^{2-} \longrightarrow S\downarrow + 2\,e^- \quad \text{(N)}$$

The reaction product is an amorphous composite of MoS_2 and sulfur, as described in [3]. The authors claim that the complexes of molybdenum with citric acid are not involved in the reaction mechanism. The reaction can be performed using different reductive acids, such as hydrochloric acid, which do not produce molybdenum complexes.

* Corresponding author, e-mail: *lukasz.makowski.ichip@pw.edu.pl*

Experimental setup

Two experimental setups were used to obtain the product and determine the particle size distribution for kinetics modelling. In the first setup jet reactors were used to carry out the reaction, while the second one involved the use of semi-batch stirred tank reactors. The reaction was performed in impinging jet reactors with two different geometries: tangential (V-type) and coaxial (T-type). The geometries and dimensions of experimental rectors are shown in Fig. 7.3.1.

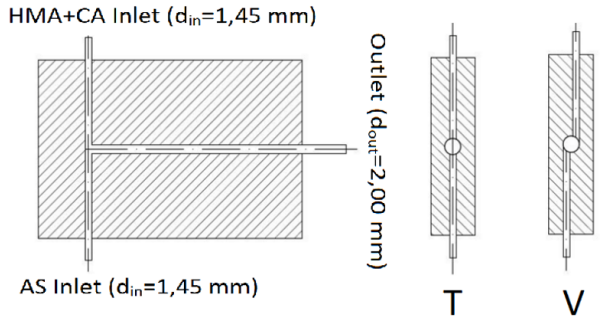

Figure 7.3.1: Geometries of impinging jet reactors.

The experimental setup for impinging jet reactors, which is shown in Fig. 7.3.2, included a thermostatic bath, syringe pump and H_2S detector. All substrates were pumped into the reactor by syringe pump with sets of 2 syringes (one for each substrate) of the same shape and capacity of 20 ml, to provide a constant and stable flow rate during the entire procedure. The reactor and the substrates were placed in a thermostatic bath at 25 °C before introducing into the syringes. The sample was collected after ten times the residence time to ensure that it is obtained during the process steady state.

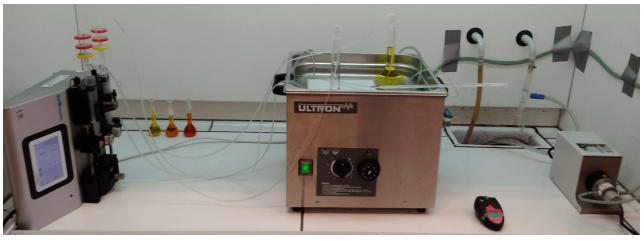

Figure 7.3.2: Experimental setup for impinging jet reactors.

The second experimental setup was a semi-batch system with a Rushton turbine. The geometry of the mixer and the reactor are shown in Fig. 7.3.3 and the setup is shown in Fig. 7.3.4.

The HMA with CA were dissolved in water and mixed at 90 °C for 30 minutes, then cooled down to experimental temperature. The molar ratios of Mo:CA:AS was 1:2:2 (with AS insufficiency). Ammonium sulfide solution was diluted with water depending on the concentration of Mo to achieve a given molar ratio as described in [3,6]. The concentrations of molybdenum vary from 0.2 mol/dm^3 to 1.6 mol/dm^3 and two symmetrical inlet flow rates were examined (20 ml/min and 50 ml/min).

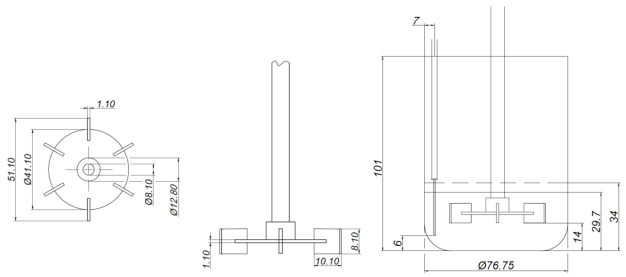

Figure 7.3.3: Dimensions of the Rushton turbine and the reactor

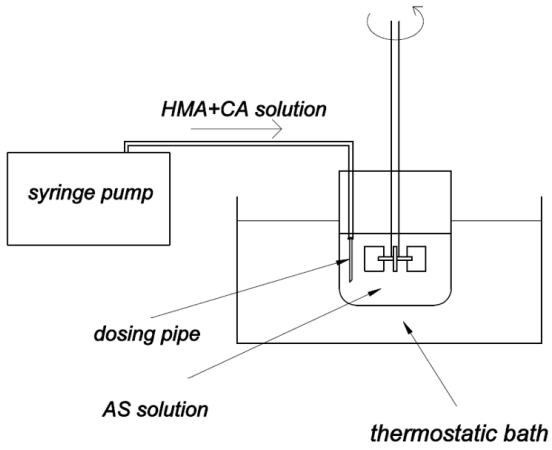

Figure 7.3.4: Semi-batch stirred tank reactor

In the semi-batch system, the reaction was performed as follows: first, ammonium sulfide solution in proper concentration was introduced into the reactor with the Rushton turbine, and the whole system was thermostated to 20 °C. HMA in 1.0 mol/dm^3 with CA solution at 50 ml/min flow rate were pumped into the reactor at the point given in Fig. 7.3.3 using a syringe pump. The AS concentration were change from 0.4 mol/dm^3 up to 1.6 mol/dm^3 and the mixing rate was 100, 200 and 300 rpm.

In the case of both systems, the HMA to CA mole ratio was 1:2 as described in [3]. The ratio of HMA to AS was set to 1:2, so the amount of AS was insufficient in terms of reaction balance. Each sample was measured directly after it was collected in case of impinging jet reactors. It was observed that primary particles distribution does not change if the measurement is delayed (even for hours), but the progressing aggregation and agglomeration of the particles reduces the amount of free primary particles in the solution, which limits the amount of information of its distribution. The size distributions were measured using particle size analyser LS 13 320, and only primary particles were taken into account (smaller than 550 nm) for the calculations. The distributions interpretation was detailed described in [3,6].

Results and modeling

The results indicate that homogenous and heterogeneous nucleation occurs. The basic kinetic model presented in [6] has five constants – two for homogenous nucleation, two for heterogeneous nucleation and linear growth rate constant. Therefore basic kinetics described the process only

Table 7.3.1: Advanced model equations.

$S = \sqrt[3]{\frac{7\,C_{\mathrm{HMA}}\left(1.068\times10^{-14}C_{\mathrm{AS}}\right)^2}{Ks}}$	Supersaturation (1.068×10^{-14} – product of the equilibrium constants of sulfide ion)	(1)
$R_{N_{\mathrm{MoS_2}}} = a'_{ho}\exp\left(\frac{-b'_{ho}}{\log^2(S)}\right) + a'_{he}\exp\left(\frac{-b'_{he}}{\log^2(S)}\right)$	Rate of formation from precipitation of MoS_2	(2)
$R_{N_S} = a_{he}C_{\mathrm{AS}}^{b_{he}} + a_{ho}C_{\mathrm{AS}}^{b_{ho}}$	Rate of formation from precipitation of S	(3)
$G_{\mathrm{MoS_2}} = k'_r S^{k_D}$	Linear growth rate coefficient from precipitation of MoS_2	(4)
$G_S = k_r C_{\mathrm{AS}}^2$	Linear growth rate coefficient from precipitation of S	(5)
$u_{\mathrm{MoS_2}} = \exp\left(\frac{-C_{\mathrm{HMA}}}{a}\right)$	Share function of MoS_2 precipitation kinetics in the model	(6)
$u_S = 1 - \exp\left(\frac{-C_{\mathrm{HMA}}}{a}\right)$	Share function of S precipitation kinetics in the model	(7)
$R_N = u_{\mathrm{MoS_2}}R_{N_{\mathrm{MoS_2}}} + u_S R_{N_S}$	The total rate of formation	(8)
$G = u_{\mathrm{MoS_2}}G_{\mathrm{MoS_2}} + u_S G_S$	The total linear growth rate coefficient	(9)
$R_M = \frac{\rho}{M}\frac{k_a Gm_2}{2}$	Substrate consumption rate	(10)
$\frac{d(VC_{\mathrm{HMA}})}{dt} = -\frac{1}{7}R_M$	HMA balance	(11)
$\frac{d(VC_{\mathrm{AS}})}{dt} = -3R_M$	AS balance	(12)
$\frac{dm_0}{dt} = R_N$	Zero moment balance	(13)
$\frac{dm_k}{dt} = k\,G\,m_{k-1}$	Higher moments balance (for $k = 1;2;3;4$)	(14)
$\frac{dV}{dt} = 0$	Volume change (zero for pipe reactor)	(15)

in terms of sulfur precipitation, which is limiting for the reaction (sulfur has to precipitate from the solution in order to transfer electrons to the molybdenum to reduce its oxidation state according to reaction (N) as described in REACTION section) [3,6]. The hypothesis is that to describe the precipitation of MoS_2 fully, it is necessary to add another set of equations. This precipitation is limiting the process in the case of low HMA and CA concentration. In the case of low CA concentration, the primary source of sulfuric ion for the reaction is the dissociation of AS represented by sets of four reactions: (E), (F), (H), (I).

The advanced kinetic model equations, given in Tab. 7.3.1, require 12 constants (Tab. 7.3.2), and they were determined by the procedure described in [6] – using a non-linear programming solver with multiple starting points. Similar procedure was also presented in [19,21].

The last constant (27) is the concentration of HMA at which the process limiting reaction switch (one of precipitations function begin to dominate over the others).

Results for the impinging jet reactor are shown in Fig. 7.3.5 and indicate that the mixing condition has a limited impact on precipitation. This is due to the exceptionally fast nucleation. The results for the semi-batch system are shown in Fig. 7.3.6 and they are presented as average

Table 7.3.2: Constants for the advanced kinetic model.

a_{he}	5.2527×10^{22}	–	(16)
a_{ho}	3.9774×10^{23}	–	(17)
b_{he}	1.8931	–	(18)
b_{ho}	6.5832	–	(19)
a'_{he}	3.0505×10^{15}	–	(20)
a'_{ho}	1.3197×10^{16}	–	(21)
b'_{he}	24.04	–	(22)
b'_{ho}	1.0418×10^{-11}	–	(23)
k_D	0.3533	–	(24)
k_r	0.010228	$\mathrm{m^5\,s^{-1}\,mol^{-2}}$	(25)
k'_r	3.2109×10^{-9}	$\mathrm{m^5\,s^{-1}\,mol^{-2}}$	(26)
a	0.033764	$\mathrm{mol\,m^{-3}}$	(27)

characteristic sizes from experiments performed with 100, 200 and 300 rpm. The impact of mixing in the semi-batch system on the process is negligible, and the standard deviation increase with the concentration due to the high tendency to aggregation and agglomeration in higher concentrations which limits the amount of information about the distribution of the primary particles in the system.

The values of moments and model predictions for impinging jet reactors are shown in Fig. 7.3.7. Experimental values

are the same as presented in [6] and were calculated in the same way. The fit for moment 3 is exact in every case because it is the reference value for other moments. The share functions values - equations (6) and (7) for the kinetic model are shown in Fig. 7.3.8 and it was not included in basic kinetics given in [6].

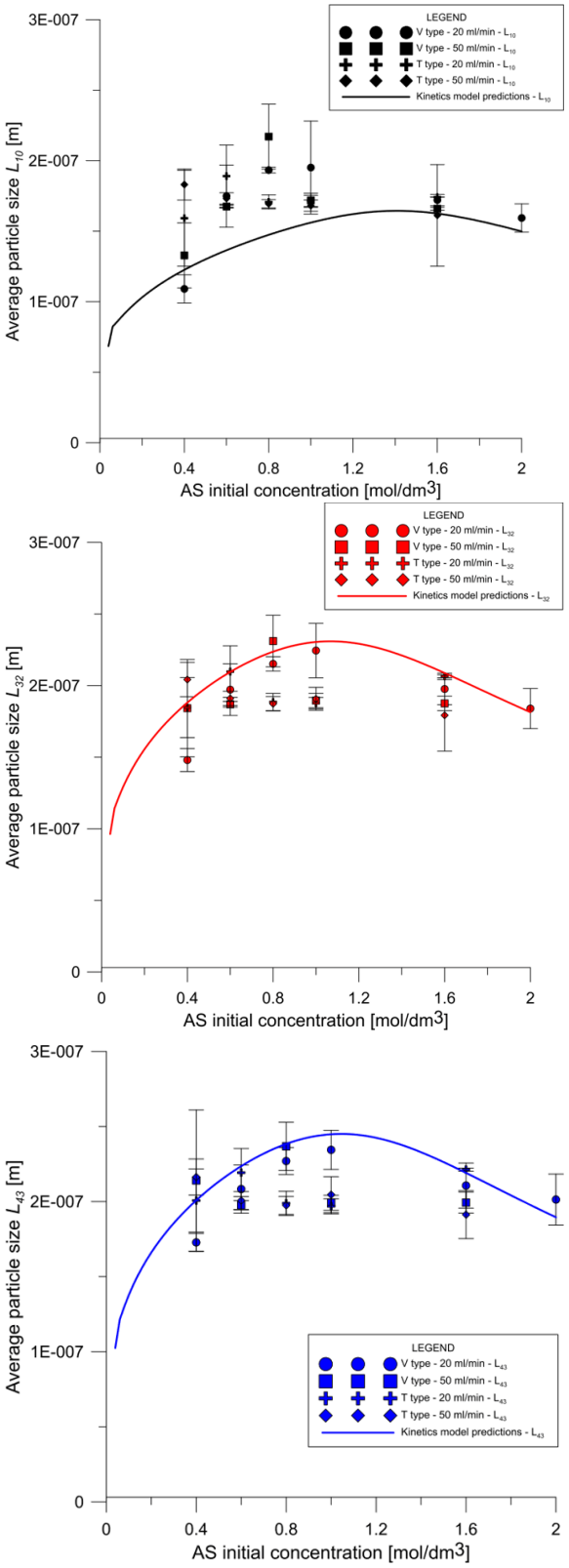

Figure 7.3.5: Results and kinetic model in ideal mixing for impinging jets

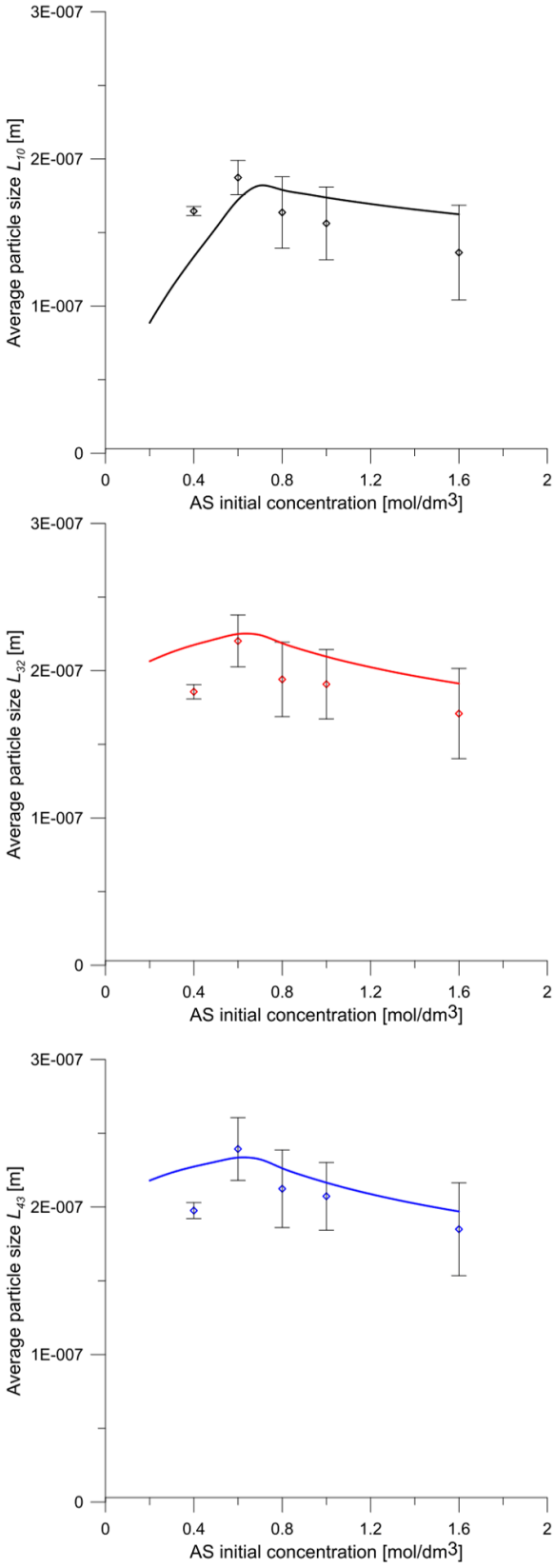

Figure 7.3.6: Results and kinetic model in ideal mixing for semi-batch system

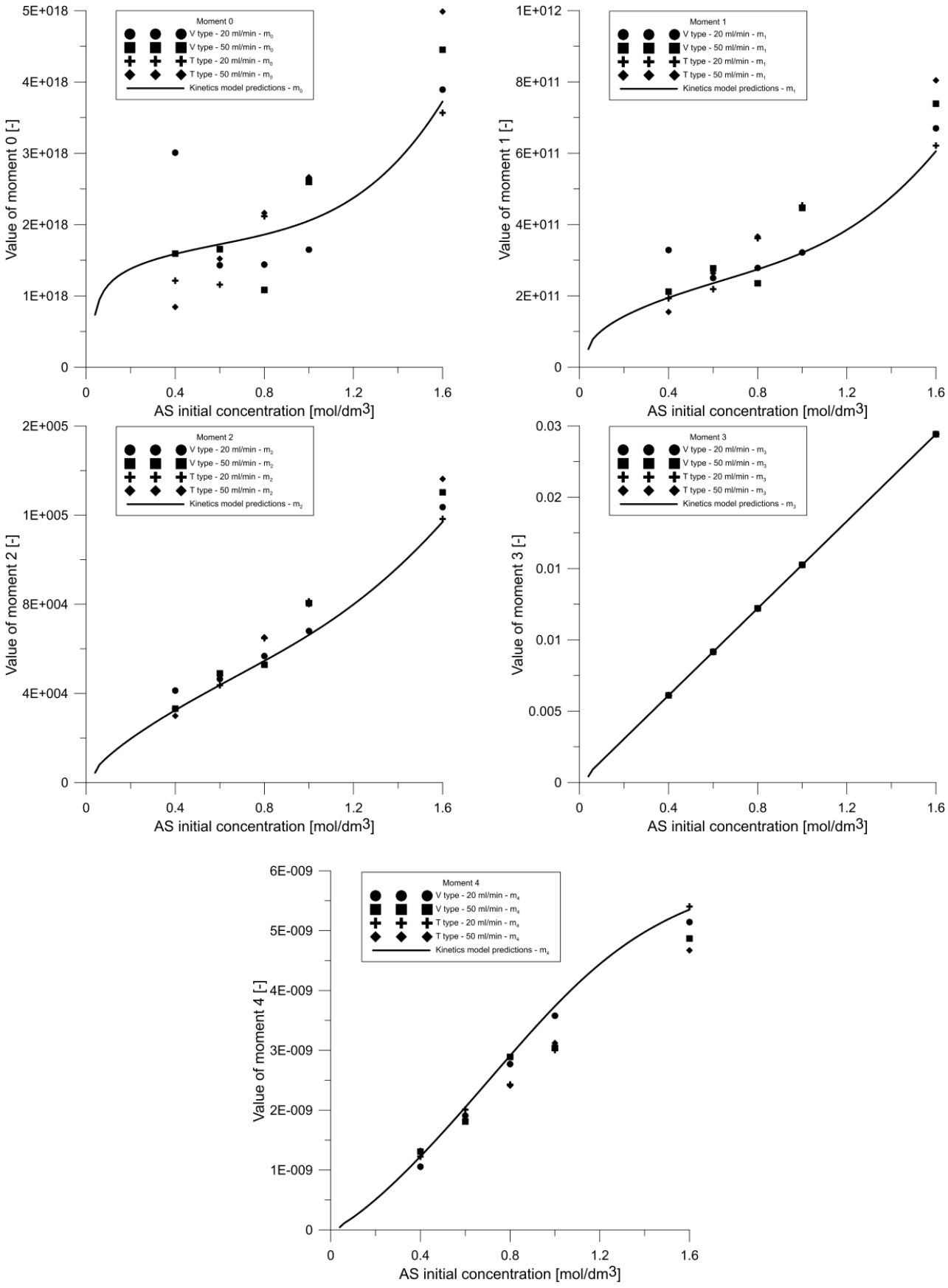

Figure 7.3.7: Values of moments and kinetic model in ideal mixing for impinging jet reactors

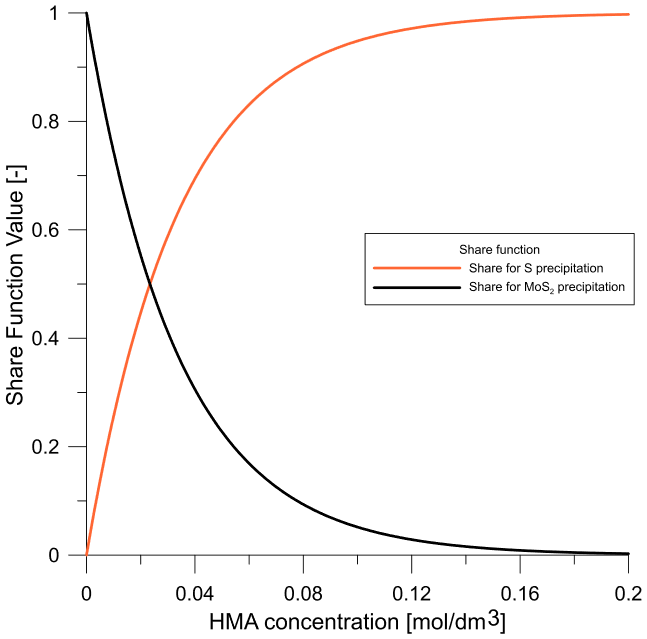

Figure 7.3.8: Share functions of the given model

Summary

The new model predictions are only slightly better than the basic kinetics model given in [6]. However, the model predicts the nucleation and growth at lower HMA concentrations better which is essential for modelling using the finite volumes method with CFD. This model is, therefore, better for such an application. Nevertheless, the nucleation is very fast for the molybdenum disulfide precipitation as for other metal sulfides, and therefore it will probably require an additional closure model for the reaction. The whole process probably takes place on the laminar-diffusion level, so the simple E – Engulfment or EDD – Engulfment-Deformation-Diffusion models [22] might not be sufficient to model the process [23,24]. Further studies are necessary to give a sufficient kinetics model for the nucleation and growth of MoS_2, its aggregation and agglomeration and to use the model in CFD modelling for predicting the process in different geometries.

Acknowledgments

This work was supported by the National Science Centre [Decision No. DEC-2017/27/B/ST8/01382].

NARODOWE CENTRUM NAUKI

Nomenclature

a_{ho}	Homogenous nucleation constant for sulfur, –
b_{he}	Heterogenous nucleation constant for sulfur, –
b_{ho}	Homogenous nucleation constant for sulfur, –
a_{he}	Heterogenous nucleation constant for MoS_2, –
a_{ho}	Homogenous nucleation constant for MoS_2, –
b_{he}	Heterogenous nucleation constant for MoS_2, –
b_{ho}	Homogenous nucleation constant for MoS_2, –
C_{AS}	Ammonium sulfide concentration, $mol\,m^{-3}$
C_{HMA}	Ammonium heptamolybdate concentration, $mol\,m^{-3}$
G_S	Sulfur growth rate, $m\,s^{-1}$
G_{MoS_2}	MoS_2 growth rate, $m\,s^{-1}$
k	Moment index, –
k_a	Surface shape factor for sphere, –
k_D	Exponent constant for MoS_2 growth rate, –
k_r	Linear growth rate constant for sulfur, $m^5\,s^{-1}\,mol^{-2}$
k_r'	Linear growth rate constant for MoS_2, $m^5\,s^{-1}\,mol^{-k_D}$
K_{sp}	Solubility index of MoS_2, $mol^3\,dm^{-3}$
M	Molar mass (average for amorphous particles of MoS_2 and sulfur), $kg\,mol^{-1}$
m_0	Moment 0, m^{-3}
m_1	Moment 1, $m\,m^{-3}$
m_2	Moment 2, $m^2\,m^{-3}$
m_3	Moment 3, $m^3\,m^{-3}$
m_4	Moment 4, $m^4\,m^{-3}$
R_M	Substrate consumption rate, $mol\,m^{-3}\,s^{-1}$
R_{N_S}	Nucleation rate for sulfur, s^{-1}
$R_{N_{MoS_2}}$	Nucleation rate for MoS_2, s^{-1}
t	Time, s
u_{MoS_2}	Share function for MoS_2, –
u_S	Share function for sulfur, –
V	Volume, m^3
$L_{10} = m_1/m_0$	Number-weighted average particle size, m
$L_{32} = m_3/m_2$	Surface-area-weighted average particle size, m
$L_{30} = m_3/m_0$	Particle size calculated from average particle volume, m
$L_{43} = m_4/m_3$	Volume-weighted average particle size, m

References

[1] D. Duphil, S. Bastide, C. Lévy-Clément, Chemical synthesis of molybdenum disulfide nanoparticles in an organic solution, *J. Mater. Chem.* 12 (2002) 2430–2432. doi:10.1039/b202162e.

[2] S.V.P. Vattikuti, C. Byon, Synthesis and Characterization of Molybdenum Disulfide Nanoflowers and Nanosheets: Nanotribology, *J. Nanomater.* 2015 (2015). doi:10.1155/2015/710462.

[3] M. Wojtalik, Z. Bojarska, Ł. Makowski, Experimental studies on the chemical wet synthesis for obtaining high-quality MoS_2 nanoparticles using impinging jet reactor, *J. Solid State Chem.* (2020). doi:10.1016/j.jssc.2020.121254.

[4] G. Santillo, F.A. Deorsola, S. Bensaid, N. Russo, D. Fino, MoS_2 nanoparticle precipitation in turbulent

micromixers, *Chem. Eng. J.* 207–208 (2012) 322–328. doi:10.1016/j.cej.2012.06.127.

[5] S. Bensaid, F.A. Deorsola, D.L. Marchisio, N. Russo, D. Fino, Flow field simulation and mixing efficiency assessment of the multi-inlet vortex mixer for molybdenum sulfide nanoparticle precipitation, *Chem. Eng. J.* 238 (2014) 66–77. doi:10.1016/j.cej.2013.09.065.

[6] M. Wojtalik, W. Orciuch, Ł. Makowski, Nucleation and growth kinetics of MoS2 nanoparticles obtained by chemical wet synthesis in a jet reactor, *Chem. Eng. Sci.* 225 (2020). doi:10.1016/j.ces.2020.115814.

[7] F.A. Deorsola, N. Russo, G.A. Blengini, D. Fino, Synthesis, characterization and environmental assessment of nanosized MoS_2 particles for lubricants applications, *Chem. Eng. J.* 195–196 (2012) 1–6. doi:10.1016/j.cej.2012.04.080.

[8] M.F. Sgroi, M. Asti, F. Gili, F.A. Deorsola, S. Bensaid, D. Fino, G. Kraft, I. Garcia, F. Dassenoy, Engine bench and road testing of an engine oil containing MoS_2 particles as nano-additive for friction reduction, *Tribol. Int.* 105 (2017) 317–325. doi:10.1016/j.triboint.2016.10.013.

[9] K. Bazaka, I. Levchenko, J. Lim Wei Mark, O. Baranov, C. Corbella, S. Xu, M. Keidar, MoS_2-based nanostructures: synthesis and applications in medicine, *J. Phys. D. Appl. Phys.* 52 (2019). doi:10.1088/1361-6463/ab03b3.

[10] E.R. Braithwaite, J. Haber, Studies in Inorganic Chemistry 19, Molybdenum: An Outline of its Chemistry and Uses, 1994. doi:10.1016/B978-0-444-88198-4.50012-7.

[11] Q. Ding, B. Song, P. Xu, S. Jin, Efficient Electrocatalytic and Photoelectrochemical Hydrogen Generation Using MoS_2 and Related Compounds, Chem. (2016). doi:10.1016/j.chempr.2016.10.007.

[12] J. Bonde, P.G. Moses, T.F. Jaramillo, J.K. Nørskov, I. Chorkendorff, Hydrogen evolution on nanoparticulate transition metal sulfides, *Faraday Discuss.* (2008). doi:10.1039/b803857k.

[13] L. Yang, P. Liu, J. Li, B. Xiang, Two-Dimensional Material Molybdenum Disulfides as Electrocatalysts for Hydrogen Evolution, *Catalysts.* (2017). doi:10.3390/catal7100285.

[14] Y. Li, H. Wang, L. Xie, Y. Liang, G. Hong, H. Dai, MoS_2 nanoparticles grown on graphene: An advanced catalyst for the hydrogen evolution reaction, *J. Am. Chem. Soc.* (2011). doi:10.1021/ja201269b.

[15] Z. He, W. Que, Molybdenum disulfide nanomaterials: Structures, properties, synthesis and recent progress on hydrogen evolution reaction, *Appl. Mater. Today.* (2016). doi:10.1016/j.apmt.2016.02.001.

[16] J.M. Soon, K.P. Loh, Electrochemical Double-Layer Capacitance of MoS_2 Nanowall Films, Electrochem. *Solid-State Lett.* (2007). doi:10.1149/1.2778851.

[17] Z. Bojarska, J. Kopytowski, M. Mazurkiewicz-Pawlicka, P. Bazarnik, S. Gierlotka, A. Rożeń, Ł. Makowski, Molybdenum disulfide-based hybrid materials as new types of oil additives with enhanced tribological and rheological properties, *Tribol. Int.* (2021). doi:10.1016/j.triboint.2021. 106999.

[18] D. Wang, R.C. Aller, S.A. Sañudo-Wilhelmy, Redox speciation and early diagenetic behavior of dissolved molybdenum in sulfidic muds, *Mar. Chem.* (2011). doi:10.1016/j.marchem.2011.03.002.

[19] M. Al-Tarazi, A.B.M. Heesink, G.F. Versteeg, New method for the determination of precipitation kinetics using a laminar jet reactor, *Chem. Eng. Sci.* 60 (2005) 805–814. doi:10.1016/j.ces.2004.09.043.

[20] M. Wojtalik, P. Przybyt, K. Zubańska, M. Żuchowska, Z. Bojarska, M. Arasimowicz-Andres, A. Rożeń, Ł. Makowski, Production of synthetic particles of MoS_2 using wet chemical synthesis, *Przem. Chem.* 98 (2019). doi:10.15199/62.2019.11.24.

[21] M. Al-Tarazi, A.B.M. Heesink, G.F. Versteeg, Precipitation of metal sulphides using gaseous hydrogen sulphide: Mathematical modelling, *Chem. Eng. Sci.* 59 (2004) 567–579. doi:10.1016/j.ces.2003.11.006.

[22] J. Baldyga, J.R. Bourne, Simplification of micromixing calculations. I. Derivation and application of new model, *Chem. Eng. J.* 42 (1989). doi:10.1016/0300-9467(89)85002-6.

[23] K. Wojtas, Ł. Makowski, W. Orciuch, Barium sulfate precipitation in jet reactors: Large eddy simulations, kinetics study and design considerations, *Chem. Eng. Res. Des.* (2020). doi:10.1016/j.cherd.2020.03.019.

[24] K. Wojtas, Ł. Makowski, W. Orciuch, J. Bałdyga, Comparison of Subgrid Closure Methods for Passive Scalar Variance at High Schmidt Number, *Chem. Eng. Technol.* (2015). doi:10.1002/ceat.201400646.

8 Abstracts: Analytical chemistry & Nanotechnology

8.1 Manipulation of optoelectronic properties of conjugated polymers by adding reduced graphene oxide or silver nanoparticles

Iulia Babutan[*,1,2], Raluca Tarcan[2], Lucian-Cristian Pop[1,2], Ioan Botiz[2]

1 Department of Chemistry, Faculty of Chemistry and Chemical Engineering, Babeș-Bolyai University, Cluj-Napoca, Romania
2 Institute of Interdisciplinary Research in Bio-Nano-Sciences, Babeș-Bolyai University, Cluj-Napoca, Romania

Keywords: *conjugated polymers*, *reduced graphene oxide*, *silver nanoparticles*, *N,N-dimethylformamide*, *explosives*.

Explosives are a problem for humanity, especially in war zones. Poly[2-methoxy-5-((2'-ethylhexyl)oxy)-1,4-phenylenvinylene] (MEH-PPV) is a highly luminescent conjugated polymer that exhibits rather high permeability towards analyte nitroaromatic molecules. Silver nanoparticles are often described as "silver", although they have a high percentage of silver oxide due to the high ratio of surface to silver atoms.

In this work we analyze the possibility to manipulate the absorption and photoluminescence properties of MEH-PPV thin films, obtained by spin-casting, either by mixing the MEH-PPV solutions in toluene with newly synthetized reduced graphene oxide (rGO) in *N,N*-dimethylformamide, or by drop-casting silver nanoparticles dispersions on top of as spin cast MEH-PPV films. The silver nanoparticles were obtained by the Creighton method, and rGO by introducing a dispersion of graphene oxide (GO) in DMF in a microwave synthesis reactor. While adding silver nanoparticles leads to photoluminescence quenching, thin hybrid films made of MEH-PPV and rGO exhibit significant photoluminescence enhancement. This enhancement is important when utilizing shorter MEH-PPV chains as compared to their much longer analogues, most probably due to more facile/efficient mixing and/or ordering of shorter polymer chains in presence of micrometer sized rGO flakes.

Our results show that there is a close connection between the interaction between polymer, solvent and colloid, as a result of making thin films of different thicknesses, which is reflected by photoluminescence quenching/enhancement by adding silver nanoparticles/rGO in DMF.

Acknowledgments

The authors acknowledge the financial support of the Romanian National Authority for Scientific Research and Innovation, CNCS – UEFISCDI, project no. PN-III-P2-2.1-PED-2019-3995.

[*] Corresponding author, e-mail: *iulia.babutan@ubbcluj.ro*, *babutan.iulia@yahoo.com*

8.2 Stable colloidal solution of ZnO quantum dots stabilized with selected organic ligands

Zygmunt Drużyński[*,1], Małgorzata Wolska-Pietkiewicz[1], Janusz Lewiński[1,2]

1 Faculty of Chemistry, Warsaw University of Technology, Warsaw, Poland
2 Institute of Physical Chemistry PAS, Warsaw, Poland

Keywords: *quantum dots*, *ZnO nanocrystals*, *amphoteric surfactants*, *colloidal solution*.

Nanometric structures made of ZnO core are the subject of particularly increased interest both at the level of basic and practical research. These materials are characterized by a unique set of properties and find application in many different fields, mainly due to the possibility of manipulation of their physicochemical properties through changes in the composition and structure of hybrid nanoobjects and the ability to functionalize their surfaces with biologically active molecules. One of the most promising areas of application for this type of material are biomedical applications. Charge on the surface of nanoparticles is one of the factors witch influences on colloidal stability (zeta potential) and cytotoxicity (by interaction with polarized cell membrane). Positively charged quantum dots in biological applications are interesting because they potentially enable the attachment of negatively charged proteins and nucleic acids to the surface through electrostatic interactions. Also, in light harvesting devices semiconductor as ZnO NCs might make electron transfer layer.

The aim of the presented work was to design and synthesize ZnO NCs stabilized with selected organic ligands which are amphoteric (zwitterionic) surfactants with quaternary nitrogen atom in the structure. Transformation of organozinc precursors were provided in controlled conditions. The rational selection of the ligand already at the precursor synthesis stage allows the design and construction of functional nanomaterials with new, interesting properties and surface features. Stable in wide range of solvents ZnO nanoparticles with very well passivated surface and core size within the so-called "Quantum size regime" (4–5 nm) were obtained and characterized.

Acknowledgements

This work was supported by National Science Centre, Poland – Grant OPUS 2017/25/B/ST5/02484, "Development of new pathways for CO_2 utilization: From a common waste to a valuable chemical feedstock".

[*] Corresponding author, e-mail: *zdruzynski@ch.pw.edu.pl*

8.3 Preparation of α-MoO_3 with different crystallographic plane ratios: study of the adsorption process using organic dyes

Claudiu Fodor[*,1], Endre-Zsolt Kedves[2,3], István Székely[2,3], Lucian-Cristian Pop[1], Lucian Baia[2,3]

1 Faculty of Chemistry and Chemical Engineering, Babeş-Bolyai University, Cluj-Napoca, Romania
2 Faculty of Physics, Babeş-Bolyai University, Cluj-Napoca, Romania
3 Institute for Interdisciplinary Research on Bio-Nano-Sciences, Cluj-Napoca, Romania

Keywords: *molybdenum trioxide*, *semiconductor*, *photocatalyst*, *adsorption*, *organic dyes*.

Molybdenum trioxide (MoO_3) is a semiconductor oxide widely used for its prominent catalytic, optical, and electrochemical properties. There are numerous studies regarding its photocatalytic properties, but its adsorption process is not sufficiently studied. Shape tailoring of semiconductors is used to enhance different properties depending on its application. Differently shaped MoO_3 can be obtained by various synthetic routes which could lead to the improvement of the above-mentioned properties.

In the present study, we successfully synthesized orthorhombic α-MoO_3 using ammonium molybdate tetrahydrate (AMT), cetrimonium bromide (CTAB), and hydrogen peroxide (H_2O_2). By calcination and recrystallization via hydrothermal method, the α-MoO_3 040 facet was successfully intensified, in parallel morphology change occurred – platelet-like crystals have formed. Raman spectra confirmed the XRD results and gave insight into the crystalline system Mo – O stoichiometry change. Moreover, zeta potential measurements were made to determine the oxide's surface charge.

It is known that α-MoO_3 slightly soluble in water, forming molybdic acid – declines the pH of the solution. Therefore, the pH drop rate was studied using differently structured α-MoO_3 crystals and the α-MoO_3 samples' adsorption properties were assessed. During adsorption processes, three similarly structured organic dyes were used, such as Eosin B, Eosin Y, and Rhodamine B. Our results disclose that the pH drop rate can be correlated with the adsorption rate, and both are determined by the pollutant and the crystal structure.

Acknowledgments

The authors are grateful for the financial support of the PN-III-P1-1.1-TE-2019-1318 project.

[*] Corresponding author, e-mail: *claudiu.fodor@stud.ubbcluj.ro*

8.4 Synthesis of copper (I) oxide nanoparticles and the possible uses in photocatalytic degradation

Andrei-Nicolae Giurgiu[*,1], Kata Saszet[2], Zsolt Pap[3], Lucian-Cristian Pop[1]

1 Faculty of Chemistry and Chemical Engineering, Babeş-Bolyai University, Cluj-Napoca, Romania
2 Centre of Nanostructured Materials and Bio-Nano Interfaces, Institute of Interdisciplinary Experimental Research in Bio-Nano-Science, Babeş-Bolyai University, Cluj-Napoca, Romania
3 Faculty of Physics, Babeş-Bolyai University, Cluj-Napoca, Romania

Keywords: *copper (I) oxide*, *hydrothermal synthesis*, *photocatalytic degradation*, *nanoparticles*, *materials science*.

The purpose of this study is to understand the proprieties and characteristics of cuprous oxide and the applicability in photocatalytic degradation.

In this work cuprous oxide was synthesized using a hydrothermal method. The nanoparticles were prepared using copper sulfate as the precursor and glucose monohydrate as oxidation agent. The adjusted synthesis parameter was the temperature of the hydrothermal method, the samples were prepared at a temperature of 50, 90 and 110 °C.

The prepared nanoparticles were studied by X-ray diffraction (XRD), Scanning electron microscopy (SEM) and Diffuse reflectance spectroscopy (DRS) in order to find out their crystal phase and composition, crystal structure, particle size, morphology and optical properties. The effect of the temperature of the synthesis on the nanoparticle properties was studied. Copper oxide nanoparticles were used in a photocatalytic degradation process of methylene blue and methyl orange, under UV-A irradiation for 2 hours. The concentration of methylene blue and methyl orange were determined using UV-Vis spectroscopy.

As a result of the good optic properties of cooper (I) oxide due to a small band gap, it has applicability in wastewater treatment by photodegradation of organic pollutants.

[*] Corresponding author, e-mail: *andrei.giurgiu@stud.ubbcluj.ro*, *giurgiu65@gmail.com*

8.5 Electro-synthesis of carbazole-based polymer layers for room temperature hydrogen gas sensing

Karolina Głosz[*,1], Agnieszka Stolarczyk[1], Tomasz Jarosz[1], Marcin Procek[2]

1 Department of Physical Chemistry and Technology of Polymers, Silesian University of Technology, Gliwice, Poland
2 Department of Optoelectronics, Silesian University of Technology, Gliwice, Poland

Keywords: *conjugated polymers*, *electrochemical polymerisation*, *hydrogen sensor*, *polycarbazole*.

Polycarbazole is a well-known conjugated polymer which has found application in organic photovoltaics, corrosion protection and gas sensing. In our study, we attempted to deposit polycarbazole on interdigitated Pt transducers form a solution, using electrochemical polymerisation.

In our work, at first we synthesised polycarbazole via cyclic voltammetry on interdigitated Pt electrodes. After that, we examined the obtained polymers layers in terms of their chemical structure (IR spectroscopy) and changes in their conductivity upon exposure to hydrogen gas, in order to investigate their potential as materials for chemoresistive hydrogen sensors.

The results of our investigations show that polycarbazole-based sensors are sensitive to hydrogen gas in the range of 1–4% at room temperature. Simultaneously, they have been fabricated using an inexpensive, cost-efficient and repeatable method, making for a promising sensing material.

Acknowledgements

This work was financed by National Science Centre of Poland via grant no. 2013/11/N/ST4/01849; 2016/23/B/ST5/03103.

[*] Corresponding author, e-mail: *karolina.glosz@polsl.pl*

8.6 Hydrogenolysis of furfural to pentadiols using a bifunctional Cu, Zn/Al_2O_3 heterogeneous catalyst

Marek Główka[*,1,2], Przemysław Boberski[1], Jan Wójcik[1], Tomasz Krawczyk[2]

1 Department of High Pressure, Łukasiewicz Network - Institute of Heavy Organic Chemistry, Kędzierzyn-Koźle, Poland
2 Department of Chemical Organic Technology and Petrochemistry , Silesian University of Technology, Gliwice, Poland

Keywords: *hydrogenolysis*, *furfural*, *pentadiols*, *heterogeneous catalyst*, *rewenable resources*.

Furfural is one of the most important raw materials of natural origin which is obtained during the hydrolysis of biomass. Due to the large scale of production, new applications are sought. One of the ways of its transformation is hydrogenolysis to 1,2-pentadiol and 1,5-pentadiol.

Pentadiols are valuable chemical compounds used in the production of polyesters and semi-finished products for the production plant protection products, as well as for the production paints and cosmetic. Currently, they are produced from crude oil by hydrolysis of 2-epoxypropan. From the point of view of sustainable chemistry, alternatives to the multi-step production of pentadiols should be found. One possibility is the direct hydrogenolysis of furfural to 1,2-pentadiol and 1,5-pentadiol using bifunctional metal catalyst.

The main aspect of the research was the preparation of the stationary catalyst used for obtaining 1,2-pentadiol and 1,5-pentadiol. $Cu,Zn/Al_2O_3$ was formed by extruder machine. Obtained catalyst was tested using thermoprogrammable methods (TPR-H_2, TPD-CO_2), surface analysis method (BET). The furfural hydrogenolysis process carried out in a trickle bed reactor and the obtained product ware analyzed by gas chromatography (GC-FID).

Acknowledgments

This work was supported by Ministry of Science and Higher Education in Poland as a part of the programme “Doktorat wdrożeniowy”.

[*] Corresponding author, e-mail: *Marek.Glowka@polsl.pl*

8.7 Highly sensitive voltammetric determination of anti-diabetic drug on renewable amalgam film electrode

Anna Górska*,1, Beata Paczosa-Bator[1], Robert Piech[1]

1 Faculty of Materials Science and Ceramics, AGH University of Science and Technology, Cracow, Poland

Keywords: *renewable amalgam film electrode*, *voltammetry*, *diabetes mellitus*, *sitagliptin*.

Diabetes mellitus is a metabolic disorder characterized by increased sugar level in blood. Two main types might be distinguished – type 1 (T1D) and type 2 (T2D). Statistics show that 90% of patients suffering from diabetes have T2D. One of the substances available on the market used in T2D therapy is sitagliptin. It belongs to the group of dipeptidyl peptidase 4 (DPP-4) inhibitors which are a new generation substances used as monotherapy or combined with metformin.

Sitagliptin might be determined using different analytical methods. Among them are spectrophotometry, electrophoresis, liquid chromatography (LC) as well as high-performance liquid chromatography (HPLC). Mentioned methods have advantages but they are also expensive, require toxic chemicals and sample preparation process is long and complicated. A good alternative are electrochemical methods, among them voltammetry, due to their low chemical consumption, possibility to reach low detection limits, simple process of sample preparation and small impact of interferences. Therefore in this work we propose highly sensitive voltammetric method for sitagliptin determination.

As working electrode renewable amalgam film electrode (Hg(Ag)FE) was used. Results obtained on mentioned electrode were compared with conventional mercury electrode used in similar applications. Instrumental parameters were optimized: sampling and waiting time, pulse amplitude, step potential. The type and concentration of supporting electrolyte as well as preconcentration potential and time were also investigated. Based on obtained results linear range and limit of detection were calculated and were as follow: 20 −140nM and 2.6 nM (1.3 ng ml^{-1}). Applicability of the method was confirmed by analysis of commercially available pharmaceutical products.

Acknowledgements

The publication is financed from the subsidy no. 16.16.160.557 of the Polish Ministry of Science and Education.

* Corresponding author, e-mail: *agorska@agh.edu.pl*

8.8 Application of renewable amalgam film electrode in the determination of organic substances

Anna Górska*,1, Beata Paczosa-Bator[1], Robert Piech[1]

1 Faculty of Materials Science and Ceramics, AGH University of Science and Technology, Cracow, Poland

Keywords: *renewable amalgam film electrode*, *voltammetry*, *electrochemical analysis*.

One of the most popular electrodes used in voltammetric measurements is hanging mercury drop electrode (HMDE). Mercury is a great electrode material due to its properties. It might be characterized by a smooth and clean surface and it is a liquid at room temperature. For a long time, mercury based electrodes were widely used for voltammetric determination of organic and inorganic substances.

In the recent years ecological aspects has become more important and researchers were trying to reduce mercury consumption. Therefore the renewable amalgam film electrode Hg(Ag)FE (constructed by B. Baś) became a good eco-friendly alternative for typical HMDE. The mercury consumption is negligibly small - approximately 10 µL for construction of one electrode which might perform at least hundreds measurements. The another advantage of Hg(Ag)FE is its relatively high surface area (in comparison with HMDE) what means that register signals are also higher.

In the work, examples of application of Hg(Ag)FE in determination of organic substances were presented, as well as comparison with results obtained using typical HMDE. Instrumental parameters, type and concentration of supporting electrolyte, preconcentration potential and time were optimized. For each analyte, parameters like linear range, limit of detection (LOD) and recoveries were determined.

The applicability of voltammetric method for organic substances determination was confirmed by analysis of products containing chosen analytes.

Acknowledgements

The publication is financed from the subsidy no. 16.16.160.557 of the Polish Ministry of Science and Education.

* Corresponding author, e-mail: *agorska@agh.edu.pl*

8.9 Electrodeposition of lead on graphite felt by using a flow-through reactor

Arminas Ilginis[*,1], Egidijus Griškonis[1]

1 Department of Physical and Inorganic Chemistry, Kaunas University of Technology, Kaunas, Lithuania

Keywords: *lead-acid battery*, *electrodeposition*, *graphite felt*, *flow-through reactor*.

Adaptation of lead-acid batteries (LAB) for requirements of electric vehicles has led to the introduction of graphite materials to the battery's electrode structure. One of the promising materials for the production of lightweight LAB electrodes is graphite felt (GF). However, the application of such three-dimensional material for this purpose poses new challenges.

In this study three different electrolytes were used for electrodeposition of Pb on GF substrate in a flow-through reactor (FTR) of a particular configuration under potentiostatic (2.5 V) conditions. Nitrate electrolyte consisted of 0.5 M $Pb(NO_3)_2$ and 0.1 M HNO_3, methanesulfonate of 0.5 M $(CH_3SO_3)_2Pb$ and 0.5 M CH_3SO_3H, acetate of 0.5 M $(CH_3COO)_2Pb$, 1.0 M CH_3COOH and 1.0 M CH_3COONH_4. Flow rate of electrolyte in FTR was kept constant at $100\,ml \cdot min^{-1}$. Electrodeposition was carried out for 60 minutes at 20 °C.

Electrodeposition of Pb on GF using acetate electrolyte demonstrated formation of large dendritic structures on the GF surface. Furthermore, gravimetric analysis showed that Coulombic efficiency of electrodeposited Pb was only 59.5%. A less dendritic Pb electrodeposit was obtained in nitrate electrolyte, however, it also exhibited low current efficiency (54.6%). The last, methanesulfonate based electrolyte, had both the best current efficiency (88.7%) and showed no dendritic and fine-grained Pb electrodeposit on the GF surface.

The usage of methanesulfonate electrolyte in flow-through reactor of a particular configuration proved to be the most promising. However, changing electrodeposition parameters (temperature, flow rate, voltage) could increase both current efficiency and improve quality of deposited material. Moreover, certain additives, such as lignin-sulfonate, could be used to enhance the structure and morphology of the electrodeposited Pb.

[*] Corresponding author, e-mail: *arminas.ilginis@ktu.lt*

8.10 Less is more: highly crystalline zinc oxide nanocrystals coated with short-chain ligands

Maria Jędrzejewska[*,1], Małgorzata Wolska-Pietkiewicz[1], Janusz Lewiński[1,2]

1 Faculty of Chemistry, Warsaw University of Technology, Warsaw, Poland
2 Institute of Physical Chemistry, Polish Academy of Sciences, Warsaw, Poland

Keywords: *zinc oxide*, *nanocrystals*, *organometallic approach*.

Semiconductor nanocrystals have been gaining tremendous attention over the past two decades. In an exceptional way they combine both the physicochemical peculiarity of molecules and optoelectronic properties of semiconductors. Zinc oxide nanocrystals (ZnO NCs) are now considered to be one of the most promising semiconductor metal oxides. The preparation of high-quality and isotropic ZnO NCs has been significantly advanced by our research group due to the introduction of one-pot self-supporting organometallic (OSSOM) procedure via the controlled exposition of an easy-to-prepare [EtZnX]-type precursor (where X-monoanionic organic ligand) solution to air, which leads to well-passivated, bio-safe colloidal ZnO NCs coated with X-type ligands.

However, the use of long-chain organic ligands can be particularly disadvantageous in the context of possible technological applications. For instance, the research on ZnO-based solar cells modules demonstrated that an atomic-scale control of the ZnO NC surface along with the reduced organic surface modifier content are critically important for the potential use of these NCs as electron transfer layer for solar cells and other particle-based light-emitting devices. Therefore, there is continuous interest to search for an efficient and well-reproducible synthetic strategies that exclude the use of an additional long-chain capping ligands to minimize energy barriers, enable efficient charge transfer and afford bio-safe and colloidal ZnO NCs with stable organic-inorganic interface.

For this reason we introduced short-chain neutral molecules – sulfoxides (i.e. ligands commonly used in coordination chemistry) as an effective and easily removable L-type stabilizing agents for the preparation of ZnO NCs with reduced organic layer, what makes them a great candidate for applications such as electron-transporting layer in photovoltaics. These results may pave the way for the further study on environmentally friendly, stable, highly efficient perovskite solar cells and more advanced energy harvesting devices.

[*] Corresponding author, e-mail: *maria.jedrzejewska.dokt@pw.edu.pl*

8.11 Molecularly imprinted polymer nanoparticles as the recognition unit of the electrochemical chemosensor for cilostazol

Jyoti[*,1], Carlo Gonzato[2], Frank Merlier[2], Karsten Haupt[2], Piyush Sindhu Sharma[1], Włodzimierz Kutner[1,3], Krzysztof Noworyta[1]

1 Institute of Physical Chemistry, Polish Academy of Sciences (IPC PAS), Warsaw, Poland
2 Génie Enzymatique et Cellulaire (GEC) – UMR-6022, Université de Technologie de Compiègne, Compiègne, France
3 Faculty of Mathematics and Natural Sciences. School of Sciences, Cardinal Stefan Wyszynski University, Warsaw, Poland

Keywords: *molecularly imprinted polymer*, *MIP*, *electrochemical sensor*, *cilostazol*, *differential pulse voltammetry*, *DPV*.

Cilostazol, 6-[4-(1-cyclohexyl-1H-tetrazol-5-yl)butoxy]-3,4 -dihydro-2(1H)-quinolinone, is an antiplatelet agent and a phosphodiesterase III inhibitor. It is used for the treatment of intermittent claudication (IC), a preliminary symptom of peripheral arterial disease (PAD). A fast, simple, and reliable method of this drug determination along with its principal active metabolites in body fluids is important from the personalized drug dosage point of view.

To selectively determine the cilostazol drug in biological matrices, molecularly imprinted polymer nanoparticles (nanoMIPs) were prepared by precipitation polymerization of the selected acrylate derivatives. Futher, characterization was done using the dynamic light scattering (DLS), SEM, AFM techniques.

Preliminary cilostazol binding tests were performed using high-performance liquid chromatography (HPLC). The nanoMIPs were immobilized on the electrode surface by engaging both covalent and non-covalent bonds. Finally, the differential pulse voltammetric (DPV) response to cilostazol of the fabricated electrochemical chemosensor was tested and found to be in linear dynamic concentration range of 134 nM to 2.58 μM.

Finally, an electrochemical chemosensor for selective detection and quantification of cilostazol using nanoMIPs as the recognition unit was successfully prepared.

Acknowledgements

The authors are grateful to E. Gilant, P. Rudzki, and A. Kutner of the Pharmaceutical Research Institute, Warsaw, Poland for synthesizing the cilostazol drug. The present work was financially supported by the Polish National Science Center through Grant No. 2015/19/B/ST4/03743.

* Corresponding author, e-mail: *jyoti@ichf.edu.pl*

8.12 Plasmonic nanoprobes transducing the length and flexibility of α,ω-alkanedicarboxylic acids into an optical readout

Mykola Kravets[*,1], Iwona Misztalewska-Turkowicz[2], Volodymyr Sashuk[1]

1 Institute of Physical Chemistry, Polish Academy of Sciences, Warsaw, Poland
2 Faculty of Chemistry, University of Bialystok, Białystok, Poland

Keywords: *anion recognition*, *nanoparticles*, *pillar[n]pyridinium*, *dicarboxylic acids*.

Dicarboxylic acids of the general formula HOOC–$(CH_2)_n$–COOH have wide use in our daily life. They are applicable in industry and many biochemical processes such as energy production and storage. However, increased amounts of these compounds may cause inflammation and more serious metabolic disorders. Accordingly, their detection and recognition are of high importance for environmental protection and public health. The discrimination of these acids is challenging because of their very similar physicochemical properties.

Here, we present an absolutely new method that recognizes the sequence of linear saturated carboxylic diacids by taking advantage of the difference in length and utilizing plasmon coupling. The interactions between these diacids and gold nanoparticles, the surface of which is covered by cationic pillar[n]pyridinium macrocycles, produce a multilevel response, including a color that can be watched with a naked eye. The color develops from purple to red and back to purple, gauging the length, flexibility as well as the odd-even character of the diacid chain.

To sum up, we presented handy nanoreceptors for the visual detection of linear fatty diacids. These receptors are simple aqueous ensembles of gold nanoparticles and pillar[n]pyridinium macrocycles. Cross-linking of these constructs with carboxylic diacids produce small interparticle gaps that allow plasmon coupling, and hence, the color change.

Acknowledgements

This work was supported by the National Science Centre of Poland (grant OPUS 18no. 2019/35/B/ST4/01758).

* Corresponding author, e-mail: *mkravets@ichf.edu.pl*

8.13 Synthesis and studies of donor-substituted bis(trifluoromethyl)biphenyl derivatives

Nerijus Kausas*[,1], Keruckiene Rasa[1], Grazulevicius Juozas Vidas[1]

1 Faculty of Chemical Technology, Kaunas University of Technology, Kaunas, Lithuania

Keywords: *carbazole*, *phenothiazine*, *room temperature phosphorescence*.

Organic luminescent materials have attracted increasing attention for their potential applications in the fields of organic light emitting diodes (OLEDs) and sensors. Employment of materials exhibiting thermally activated delayed fluorescence (TADF) in the active layers of OLEDs has been stated to be very efficient. TADF materials can achieve 100% of use of excitons through reverse intersystem crossing because of their low energy gap between the lowest singlet excited state S1 and triplet excited state T1. The strategy to achieve such characteristics is to employ both donor and acceptor moieties in a single molecular structure. In addition to OLED applications, TADF emitters due to the long lifetime of fluorescence (RTP) are promising candidates for time resolved imaging and sensing of different analyte, such as oxygen.

In this work, bis(trifluoromethyl)biphenyl-based emitters with various donor moieties, such as carbazole, dimethylacridan, phenothiazine are presented.
Bis(trifluoromethyl)biphenyl acceptor and various donor fragments were chosen for the synthesis of novel electroactive compounds exhibiting thermally activated delayed emission and room temperature phosphorescence phenomena. A two-step synthetic route was chosen to obtain the target compounds. Thermal, photophysical, electrochemical, and photoelectrical properties of the compounds were analyzed. The compounds were synthesized as amorphous substances with glass transition temperatures ranging from 152 to 255℃ 5% weight loss temperature of the compounds exceeded 390 ℃. Synthesized compounds were found to be electrochemically stable. Analysis of properties of the compounds provide promising results for possible fabrication of novel OLEDs.

* Corresponding author, e-mail: *nerijus.kusas@ktu.edu*

8.14 Hydrous vs anhydrous ruthenium dioxide as solid contact layer in ion-selective electrodes

Nikola Lenar*[,1], Beata Paczosa-Bator[1], Robert Piech[1]

1 Faculty of Materials Science and Ceramics, AGH University of Science and Technology, Cracow, Poland

Keywords: *solid-contact*, *ISEs*, *ruthenium dioxide*, *hydrous ruthenium dioxide*.

One of the current trends in potentiometric research is finding new materials for solid-contact layers in ion-selective electrodes (ISEs). This work presents the use of ruthenium dioxide as mediation layer in potassium selective electrodes.

Ruthenium dioxide (RuO_2) characterized as transition metal dioxide with a rutile structure is of both scientific and technological importance, what results from its unique properties. Ruthenium dioxide exhibits a combination of unique characteristics such as high thermal and chemical stability, low resistivity, and remarkable redox properties what was taken advantage of when designing the ISE. Ruthenium dioxide occurs in two morphologically varied structures: anhydrous and hydrous form, both of them were studied in the scope of this work and applied as mediation layers in ion selective electrodes.

The differences between the electrochemical properties of those two materials underlie in their diverse structure and hydration properties. One of the main differences is the occurrence of structural water in $RuO_2 \cdot x\,HS_2O$ which creates large inner surface available for ion transport what was shown to be a favorable feature in the context of designing potentiometric sensors. Both materials were examined with SEM microscope, X-ray diffractometer and contact angle microscope and the results revealed that hydrous form can be characterized as porous structure with smaller crystallites size and more hydrophobic properties contrary to the anhydrous form. Potentiometric and electrochemical tests carried on designed $GCD/RuO_2/K^+$ – ISM and $GCD/RuO_2 \cdot x\,H_2O/K^+$ – ISM electrodes proved that the loose porous microstructure with chemically bounded water, that is characteristic for the hydrous form, ensures high electrical capacitance of electrodes (up to 1.2 mF) with consequently more stable potential (with the potential drift of 0.0015 mV/h) and faster response (of a few seconds).

* Corresponding author, e-mail: *nlenar@agh.edu.pl*

8.15 The new hybrid material as mediation layer in potassium-selective potentiometric sensors

Nikola Lenar*[,1], Beata Paczosa-Bator[1], Robert Piech[1]

1 Faculty of Materials Science and Ceramics, AGH University of Science and Technology, Cracow, Poland

Keywords: *ruthenium dioxide*, *POT*, *hybrid material*, *solid-contact*, *potassium selective electrodes*.

Potassium belongs to the group of the most important macroelements, necessary for the proper development and functioning of living organisms. In human organisms and environment potassium regulates water management and participate in enzymatic processes. Ion-selective electrodes due to their fast, reliable response, low cost - in comparison with other methods and small size - enabling their mobility are widely used for potassium determination.

Potentiometric sensors also known as ion-selective electrodes (ISEs) usually consist of two layers: the mediation layer, which simplifies the ion-to-electron exchange processes between the electronic conductor and the membrane, and ion-selective membrane itself, which is responsible for the selective recognition of analyzed ion (in this case potassium ion).

This work presents the novel and universal approach to designing potentiometric sensors with PVC membrane by implementing the conducting polymer - nanoparticles of ceramic dioxide composite material as mediation layer. Properties of ruthenium dioxide RuO_2 and poly(3-octylthiophene-2,5-diyl) (POT) were combined into one mediation layer in K+-selective electrodes what resulted in their great performance parameters.

The layers' microstructure, wettability and electrical parameters were studied using various methods. RuO_2 particles turned out to enhance polymer's electrical and hydrophobic properties and allowed to obtain superhydrophobic layer of high electrical capacity which is favorable for solid contact. The SEM and TEM scans revealed the nanosized particles of RuO_2 contributing to the large surface area and the wettability test exposed the contact angle of 149°. Electrical capacitance obtained for the RuO_2-POT composite material was as high as 1.17 mF and allowed to obtain stable potentiometric response of electrodes, while the superhydrophobic properties of the layer resulted in their great performance during the water-layer test.

* Corresponding author, e-mail: *nlenar@agh.edu.pl*

8.16 Surface modification of working electrodes through the cold plasma depostion of thin layers for voltammetric applications

Justyna Lipinska*[,1], Maria Madej[2], Bogusław Baś[1], Jacek Tyczkowski[3]

1 Department of Analytical Chemistry, AGH University of Science and Technology, Cracow, Poland
2 Department of Analytical Chemistry, Jagiellonian University in Kraków, Cracow, Poland
3 Depratment of Molecular Engineering, Lodz University of Technology, Lodz, Poland

Keywords: *voltammetry*, *surface modifications*, *cold plasma deposition*, *working electrodes*.

Nowadays, analytical methods are increasingly used in fields such as medicine, industry, agriculture and environmental protection. A very important group is constituted by electrochemical methods which allow speciation determination of trace amounts of analytes in the presence of interferents. However, these methods require appropriate tools, i.e. electrochemical sensors that allow the determination of the chosen electroanalytical method. Electrochemical sensors convert the effect of electrochemical interaction between the analyte and the receptor into an electrical signal that is the basis for system calibration.

Current research is focused on the search for new, physically and chemically stable electrode materials or their volumetric or surface modification. In the group of basic electrode materials most commonly used are metals, solid and liquid amalgam, carbon materials (graphite, glassy carbon, diamond doped with boron), ceramics and more often polymers modified with nanomaterials.

This work includes a literature review of the design solutions of working electrodes used for voltammetric determinations, as well as the optimization of the conditions for obtaining and the application of thin layers by the plasma enhanced chemical vapor deposition (PECVD) method on carbon and metallic substrates. Our research is focused on the deposition of layers of acrylonitrile on various substrates: graphite, glassy carbon, gold and microstructure examination of the obtained layers. The final stage of work was the use of discs coated with a thin layer of acrylonitrile to make working electrodes for the voltammetric determinations.

Acknowledgements

JL and MM have been partly supported by the EU Project POWR.03.02.00-00-I004/16

* Corresponding author, e-mail: *justyna.lipinska@agh.edu.pl*

8.17 Optimization of condition for cold plasma deposition of thin layers for electrochemical applications

Justyna Lipińska[*,1], Maria Madej[2], Bogusław Baś[1], Jacek Tyczkowski[3]

1 Department of Analytical Chemistry, AGH University of Science and Technology, Cracow, Poland
2 Department of Analytical Chemistry, Jagiellonian University in Kraków, Cracow, Poland
3 Depratment of Molecular Engineering, Lodz University of Technology, Lodz, Poland

Keywords: *cold plasma deposition*, *thin layers*, *electrochemical applications*, *surface modification*.

Currently, research is focused on the search for new, physically and chemically stable materials as well as volume or surface modification. One of the methods used for surface modification is the application of thin layers from inorganic and organic compounds. The plasma enhanced chemical vapor deposition (PECVD) is a method that allows material modification and also deposition of thin layers.

This work concerns optimization of cold plasma deposition parameters and to achieve the best electrical conductivity while maintaining the high mechanical strength of the formed layers.

Preliminary tests were focused on optimizing the layering parameters such as the deposition time, discharge power, pressure of monomer and the flow of argon. The obtained samples were subjected to thermal treatment after which they were covered with a layer of aluminum. The thickness of the obtained layers was determined on the basis of interference microscopy measurements. As a result of the experiments, layers with a thickness of 20 nm to 600 nm were obtained.

The conductivity of the deposited layers was also determined and values from $0.03\,\mathrm{S}\cdot\mathrm{m}^{-1}$ to $150\,\mathrm{S}\cdot\mathrm{m}^{-1}$ were obtained.

Acknowledgements

JL and MM have been partly supported by the EU Project POWR.03.02.00-00-I004/16

* Corresponding author, e-mail: *justyna.lipinska@agh.edu.pl*

8.18 Study of nanocomposites based on PA6/selenium compounds

Henrieta Markevičiūtė[*,1], Valentina Krylova[1]

1 Department of Physical and Inorganic Chemistry, Kaunas University of Technology, Kaunas, Lithuania

Keywords: *nanocomposites*, *metal selenides*, *atomic force microscopy*.

In recent years, nanotechnology and the potential of forming nanocomposites by incorporation of nanosized particles in biopolymer matrices have drawn increased attention. So far, the most studied matrices for the nanocomposite synthesis are various artificial and natural polyamides. The application of high-molecular compounds as matrix for the synthesis of selenium compounds-containing nanocomposites is of particular interest. The present work aims to characterize the surface morphology of PA6/selenium compounds-containing nanocomposites.

Nanocomposites were obtained applying different chemical synthesis methods: the synthesis of layers of selenium on PA6 film via chemical bath deposition method using H_2SeO_3 and Na_2SO_3 at 20 ℃ for 24 h, the PA6/Cd-Se by successive ionic layer adsorption and reaction from PA6/Se using $Cd(CH_3COO)_2$ at 80 ℃ for 3 h and the PA6/Ag-Cd-Se by cation-cation exchange method from PA6/Cd-Se using $AgNO_3$ at 20 ℃ for 10 min. The bulk chemical composition was determined using atomic absorption spectroscopy (AAS). Atomic force microscopy (AFM) was used to characterize surface morphology. The main morphology parameters were as follows: Z_{mean}: average height, R_a: arithmetic average surface roughness, R_q: root-mean-square surface roughness, and R_t: peak-to-valley roughness.

When PA6/Se samples were exposed in an aqueous medium containing Cd^{2+} cations, insoluble nanoparticles of CdSe deposited in situ on PA6/Se template and produced the PA6/Cd-Se nanocomposite. The Z_{mean} and R_a of PA6/Cd-Se composite significantly decreased in comparison with those of the PA6/Se. After the PA6/Cd-Se composite exposure in an aqueous $AgNO_3$ solution, the surface of the obtained composite showed the presence of nano-sized particles, assumed to be of Ag_2Se. As a result, the quantitative parameters of the surfaces decreased. Furthermore, R_t of the PA6/Cd-Se and PA6/Ag-Cd-Se composite surface like no undergoes. It should be noted, that the RMS of deposited films decreased with the formation of the CdSe and Ag_2Se nanoparticles as compared to deposited amorphous Se films on PA6 surface.

* Corresponding author, e-mail: *henrieta.markeviciute@ktu.edu*

8.19 Investigation of the influence of gold nanoparticle stabilizer on metrological parameters of potentiometric sensors

Barbara Niemiec*,[1], Nikola Lenar[1], Robert Piech[1], Beata Paczosa-Bator[1]

1 Faculty of Materials Science and Ceramics, AGH University of Science and Technology, Cracow, Poland

Keywords: *all-solid-state electrode*, *gold nanoparticles*, *potassium selective electrode*, *organic stabilizers*.

The elimination of an internal solution from the design of ion-selective electrodes initiated a lot of work on all-solid-state electrodes. Unfortunately, the first proposition of this electrode type called coated-disc electrode, turned out to be an insufficient solution mainly due to the lack of potential stability. This disadvantage was eliminated by the use of a mediation layer between a substrate electrode and an ion-selective membrane, which initiated the development of solid-contact electrodes. Since then, new materials have been proposed for the mediation layer to obtain electrodes with the best analytical parameters, including nanomaterials.

This paper presents a proposal of all-solid-state electrodes using gold nanoparticles as a mediation layer. The layers were stabilized with various stabilizers: poly(vinyl pyrrolidone) PVP, cetyltrime-thylammonium bromide CTAB and thanine TA. The aim of use of stabilizers was to limit the agglomeration of nanoparticles in order to obtain layers with the highest possible surface expansion, which affects the electric charge capacity of the layer and the stability of the potential.

The work compares the characteristics of the tested electrodes with the parameters of the coated-disc electrode. The applied layers allowed to improve the parameters of the obtained electrodes. The proposed electrodes were characterized by good sensitivity (close to the theoretical value). In particular, the electrodes with the CTAB stabilized layer were characterized by good stability and reproducibility of the normal potential and an increased electric charge capacity.

* Corresponding author, e-mail: *bniemiec@agh.edu.pl*

8.20 Synthesis and applications of $AgInS_2$ QDs-modified Bi_2WO_6

Patrycja Parnicka*,[1], Patrycja Wilczewska[1], Adriana Zaleska-Medynska[1]

1 Department of Environmental Technology, University of Gdansk, Gdansk, Poland

Keywords: *photocatalysis*, *bismuth tungstate*, *$AgInS_2$ quantum dots*, *hydrogen evolution*.

One of the central global socio-economic challenges of the next decades is the sustainable supply of energy. Heterogeneous photocatalysis systems, which includes dispersed particulate photocatalysts in aqueous electrolytes appear to be very promising for generate hydrogen from water under the exposure of photonic radiation.

Bismuth tungstate as one of the simplest Aurivillius oxides with a narrow band gap of ~2.5 – 2.9 eV has got wide attention due to its potential for photocatalytic applications. However, the inherent disadvantages such as a fast recombination of photogenerated electron-hole pairs and slow charge carrier transfer leads to low photocatalytic efficiency. In recent years, there has been considerable interest in the modification of Bi_2WO_6 using quantum dots, resulting in improved photocatalytic efficiencies that are attributed to inter-particle electron transfer in composite samples. Thus, this work focuses on environmentally friendly visible-light-driven photocatalyst which is silver indium disulfide. $AgInS_2$ has a narrow direct band gap of ~1.5 – 1.8 eV and an excellent absorption coefficient of $\sim 10^5$ cm^{-1}.

Herein, the $AgInS_2/Bi_2WO_6$ system was prepared via a multistep route, i.e. the hot-injection method was used to synthesize the quantum dots (QDs), while hydrothermal precipitation was employed to prepare Bi_2WO_6, and the two materials were coupled together via low-temperature annealing. The photocatalysts were characterized by diffuse reflectance spectroscopy (DRS), scanning electron microscopy (SEM), transmission electron microscopy (TEM), powder X-ray diffraction (pXRD), X-ray photoelectron spectroscopy (XPS), and photoluminescence spectroscopy (PL). The photocatalytic behaviors of $AgInS_2$ QD-modified Bi_2WO_6 nanoflowers were evaluated by hydrogen production under UV–Vis light irradiation.

Acknowledgments

This work was supported by Polish National Science Center, under the grant titled: "Mechanism of quantum dots excitation in photocatalytic reaction", contract no.: 2016/23/B/ST8/03336.

* Corresponding author, e-mail: *patrycja.parnicka@phdstud.ug.edu.pl*

8.21 Lanthanide-organic frameworks-modified TiO_2 photocatalysts with enhanced photocatalytic activity

Patrycja Parnicka*,[1], Patrycja Wilczewska[1], Adriana Zaleska-Medynska[1]

1 Department of Environmental Technology, University of Gdansk, Gdansk, Poland

Keywords: *photocatalyst*, *titanium dioxide*, *lanthanide-organic frameworks*.

Semiconductor-based heterogeneous photocatalysis is promising technology for water purification without using consumables and generating harmful by-products. Lanthanide metal ions have become current interests owning to possible up-conversion luminescence effect (converting long-wavelength radiation into shorter wavelength through multiphoton processes). Lanthanide-organic frameworks (LnOF), which are synthesized by assembling lanthanide ions with organic linkers, have attracted great interest. In particular, LnOF have become current interests in gas storage, catalysis, as well as sensing, owing to their high porosities and regularity, simultaneously tunable pore structures. Moreover, LnOF have been found to be ideal materials for enhancement charge carrier separation.

Therefore, we report a simple strategy for the synthesis of TiO_2 modified with LnOF structure via hydrothermal method. We have used naphthalate-2,6-dicarboxylic acid as bridging ligand in which carboxylate groups are connected to lanthanide ions (Nd^{3+}, Er^{3+}, Ho^{3+}, Tm^{3+}). The photocatalysts were characterized by diffuse reflectance spectroscopy, powder X-ray diffraction, fourier-transform infrared spectroscopy, scanning electron microscopy, and photoluminescence analyses. The photocatalytic properties of the obtained samples were investigated by employing the photodegradation of phenol in the aqueous phase as a model pollutant under visible ($\lambda > 420$ nm) light irradiation. To clarify the possible mechanism of Ln(ndc)/TiO_2 hybrid photocatalysts excitation under visible light, the action spectra measurements were investigated for selected samples. For this purpose, the effect of irradiation wavelength on the apparent quantum efficiency have been studied employing by using photodegradation of phenol.

Acknowledgments

This research was supported by National Science Center (grant titled: "Novel REOF@TiO2 nanomaterials with potential applications in photocatalytic processes"; contract No.: 2017/27/N/ST5/00738).

* Corresponding author, e-mail: *patrycja.parnicka@phdstud.ug.edu.pl*

8.22 Voltammetric determination of folic acid

Radosław Porada*,[1], Katarzyna Fendrych[1], Bogusław Baś[1]

1 Department of Analytical Chemistry, AGH University of Science and Technology, Cracow, Poland

Keywords: *folic acid*, *electroanalysis*, *vitamin B_9*, *voltammetry*.

Folic acid (FA), also known as vitamin B_9, is a coenzyme participating in multiple human metabolic pathways, therefore it is crucial for DNA replication, synthesis of methionine, the formation of red blood cells, and prevention of anemia. Moreover, its significance for the proper growth of the fetus and avoiding its congenital malformation cannot be omitted. As stated by The European Food International Council, the recommended dose of FA equals 0.2 mg daily for adults and 0.4 mg for pregnant women. When overdosed, FA can mask the deficiency of vitamin B_{12} and thus prevents the proper diagnosis of the related diseases. Due to the multiplicity of available sources, FA concentration within them has to be known to avoid its hipo- and hypervitaminosis.

This work presents the voltammetric determination of FA with the usage of the novel, environmentally-friendly Screen-Printed Carbon Electrode (SPCE) covered with the composite layer containing graphite and natural zeolite exchanged with Mn^{2+} cations. All the corresponding measurements were conducted by means of Differential Pulse Voltammetry in the three-electrode cell. Derivative UV-Vis spectroscopy was used as the reference method. For the study of the reaction mechanism, Cyclic Voltammetry was employed.

Based on the obtained dependencies, the reduction of FA was identified as two electrons-two protons process resulting in the formation of 7,8-dihydrofolic acid. Thanks to the careful optimization of experimental conditions, the proposed method of FA determination possesses the limit of quantification of 2.9 nmol L^{-1}. The conducted interference study indicated that inorganic cations, surface-active species, and other vitamins do not cause the disappearance or disturbance of the analytical signal. The recoveries obtained for the FA determination in dietary supplements and pharmaceuticals ranged from 96.5 to 112.6 % and were consistent for the used analytical methods, thus confirming the reliability of the developed protocol.

Acknowledgments

RP has been greatly supported by the EU Project POWR.03.02.00-00-I004/16.

* Corresponding author, e-mail: *rporada@agh.edu.pl*

8.23 The microelectrode effect

Radosław Porada[*,1], Katarzyna Jedlińska[1], Justyna Lipińska[1], Bogusław Baś[1]

1 Department of Analytical Chemistry, AGH University of Science and Technology, Cracow, Poland

Keywords: *microelectrode*, *spherical diffusion*, *voltammetry*, *impedance*.

Microelectrodes are defined as the electrodes whose dimensions are less than 25 µm. This geometry allows for an enhanced mass-transport, steady-state current, and higher current densities in comparison to commonly used macroelectrodes. Moreover, the microelectrode dimension is comparable to or lesser than the length of the diffusion layer. Since the currents flowing through microelectrodes are small, the ohmic drop becomes negligible even in highly resistive media, e.g. organic solvents. The faradaic current is proportional to the electrode radius (r_e), while the capacitive current is proportional to r_e^2, meaning that with the decrease of the electrode dimension, the signal-to-noise ratio can be improved.

This work aimed to find the distinguishing marks for different electrode constructions. For that purpose, disc Glassy Carbon Electrode, Silver Annular Band Electrode, Gold Microelectrode, and bi-Band Silver Microelectrode were investigated by means of cyclic voltammetry and electrochemical impedance spectroscopy using hexaaminaruthenium(III) chloride as a redox indicator. Based on that, the important figures of merit, including the anodic-to-cathodic peak ratio, peak separation, charge-transfer resistance, differential capacitance of the double layer, were calculated.

For classical macroelectrodes, a peak-shaped cyclic voltammogram was obtained with peak current increasing with the square root of the scan rate. The impedance spectrum was composed mainly of a straight line corresponding to the diffusion of the depolarizer. In case of the microelectrode, the cyclic voltammogram has a sigmoidal shape with superimposed oxidation and reduction curves. At the same time, only the charge-transfer semicircle is observed in the Nyquist plot.

Concluding, the steady-state is noted for electrodes with convergent diffusion. To maximize this effect, the electrode area closed to its edges has to be increased, either by narrowing the lateral dimension or reducing the electrode radius.

Acknowledgments

RP and JL have been greatly supported by the EU Project POWR.03.02.00-00-I004/16.

* Corresponding author, e-mail: *rporada@agh.edu.pl*

8.24 Preparation of polycaprolactone nanoparticles via nanoprecipitation method and evaluation of their properties

Ewa Rybak[*,1], Tomasz Ciach[1]

1 Faculty of Chemical and Process Engineering, Warsaw University of Technology, Warsaw, Poland

Keywords: *polymeric nanoparticles*, *nanoprecipitation*, *polycaprolactone*, *drug-carriers*.

In the field of pharmaceutical research, nanoprecipitation has been used as an alternative for common drug-carrier formulations. In this method, the nanoparticles (NPs) are formed by precipitation from dissolved polymer mixture after exposure to a polymer non-solvent. The use of polymeric nanoparticles as drug nanocarriers is a promising strategy for anticancer targeted therapy. The formulated particles' size significantly impacts drug loading, distribution in vivo, diffusion into the tumor, and cell uptake. Thus, it is essential for the successful progression of a drug delivery system.

The presented work concerns formulation of polymeric nanoparticles via polymer nanoprecipitation in a non-solvent (water) environment. A syringe pump was used to dose the organic phase into the aqueous phase. Different concentrations of polymer (polycaprolactone) and surfactant (Pluronic® F-127) were evaluated. The impact of studied parameters on the size and polydispersity of obtained nanoparticles were analyzed by Dynamic Light Scattering (DLS). Moreover, the cytotoxicity of the produced NPs was investigated by the in vitro cell culture of the human cervical tumor HeLa cells.

Preliminary results confirm that nanoparticles formed in the presence of surfactants are characterized by better stability in the water phase as well as after the lyophilization process, which was confirmed by DLS measurements. The increasing polymer concentration in the organic phase resulted in decreasing particle size depending on the concentration of surfactant.

* Corresponding author, e-mail: *Ewa.Rybak.dokt@pw.edu.pl*

8.25 Investigations on nucleic acids extraction from biological samples with modified magnetic nanoparticles

Anna Szymczyk[*,1], Robert Ziółkowski[1], Marcin Drozd[1,2], Elżbieta Malinowska[1,2]

1 Faculty of Chemistry, Warsaw University of Technology, Warsaw, Poland
2 Centre for Advanced Materials and Technologies, Warsaw University of Technology, Warsaw, Poland

Keywords: *iron (II,III) oxide*, *modified magnetic nanoparticles*, *nucleic acids extraction*, *graphene*, *polymers*, *gold*.

Fast, reliable and cost efficient molecular diagnostic tests which could be performed outside laboratories mostly are still only in the research phase. However, in the point of view of even recent SARS-CoV-2 spread and COVID-19 pandemic, wide availability of such tests would significantly contribute to the reduction of the infected persons number and the same to its ending. However, to perform the diagnostic based on detection of nucleic acids, it is indispensable to develop efficient methods for their extraction and purification. This step is first and crucial in the whole procedure, as inhibitors offend present in the biological samples could hamper the next steps, polymerase chain reaction dedicated to nucleic acid sequence amplification and its subsequent detection. To date, to obtain high purity nucleic acids for diagnostic procedure the appropriate benchtop equipment (e.g. centrifuges) and labor intensive procedure is needed. These can be replaced by appropriately prepared magnetic nanoparticles (MN) which exhibit high affinity towards nucleic acids. The same the whole extraction and purification procedure could be shortened only to adsorption of the DNA or RNA at the MN surface, its magnetic separation, washing and finally nucleic acids desorption back to appropriate buffer.

In our investigations Fe_3O_4 magnetic nanoparticles prepared by co-precipitation and controlled oxidation of iron(II) precursor were used as magnetic cores. Both types were coated with versatile surface modifiers e.g. polyethyleneimine, gold and silica shell or graphene oxide also additionally modified with carboxylic or thiolate-groups. All obtained nanoparticles were purified by means of a magnet. These, which characterized long-term stability in the solution and showed a very good magnetism, were selected for future analysis. Then they were characterized with zeta potential, UV-Vis absorption and size distribution profile. The initial experiments dedicated to evaluation of DNA adsorption efficiency were performed.

Acknowledgments

This work was supported by IDUB project "Against COVID-19" and Warsaw University of Technology.

[*] Corresponding author, e-mail: *anna.szymczyk.dokt@pw.edu.pl*

8.26 A giant Faraday effect in a semiconductive polymer doped with magnetic nanoparticles

Aleksandra Wosztyl[*,1,2], Karolina Łempicka[1], Sara Piotrowska[1], Katarzyna Pietrusińska[1], Aleksandra Pietranik[1], Paweł W. Majewski[2], Barbara Piętka[1], Jacek Szczytko[1]

1 Division of Solid State Physics, Institute of Experimental Physics, Faculty of Physics, University of Warsaw, Warsaw, Poland
2 Faculty of Chemistry, University of Warsaw, Warsaw, Poland

Keywords: *a giant Faraday effect*, *semiconductive polymer*, *P3HT*, *nanoparticles*.

The giant Faraday effect is a magneto-optical phenomenon, which appears as the rotation of the polarization plane of light passing through a medium in an external magnetic field. In materials that do not contain magnetic ions detection of Faraday rotation requires either very strong magnetic fields or a long optical path to observe the effect. To enhance Verdet constant – the parameter describing the proportion between the angle of rotation and magnetic field – material can be doped with magnetic ions. This solution can be found in various types of glasses.

One of the potential alternatives of transparent materials is organic polymers which pose potential properties such as flexibility, low sensitivity to temperature changes, saturating in much larger magnetic fields, and ease of manufacture. The most problematic aspect of these approaches is relatively small values of Verdet constant in regions far from optical resonances.

The goal of this project is to obtain hybrid organic-inorganic materials which exhibit higher values of Verdet constant. Accord to the results, semiconductive polymer poly-3-hexylthiophene (P3HT) doped with iron (III) oxide nanoparticles turns out to be a promising candidate. Hybrid materials have been characterized by UV-Vis spectroscopy. The Faraday effect was measured with a magnetic coil (0.4 T) for different wavelengths (450 nm, 543 nm, 594 nm, 604 nm, 612 nm, 633 nm, 640 nm).

It was observed that iron oxide-doped samples with a wavelength greater than 594 nm reveal higher values of the Verdet constant.

Acknowledgments

This work was supported by the NCN OPUS [grant numbers: 2013/11/B/ST3/04193].

[*] Corresponding author, e-mail: *a.wosztyl@student.uw.edu.pl*

8.27 Deep learning in interpretation of voltammetric data

Szymon Wójcik*,[1], Filip Ciepiela[1], Małgorzata Jakubowska[1]

1 Department of Analytical Chemistry, Faculty of Materials Science and Ceramics, AGH University of Science and Technology, Cracow, Poland

Keywords: *q-DIrE*, *DNN*, *DPV*, *PLS*.

Deep learning with the use of multilayer neural networks is a modern strategy for modeling and interpretation of large data sets, supported by efficient software tools. This computational strategy finds application in various fields of science and technology, it will be shown in this work that this approach can find solutions to many problems when the data source is a voltammetric signal. Examples include the evaluation of food origin and the study of undesirable food additives and advanced signal processing.

Food adulteration is now a very serious global problem. Producers wanting to achieve higher profits, try to reduce production costs by using various undesirable or forbidden food additives. Apple juice is the second most consumed fruit juice and due to its position in the consumption ranking, it is often adulterated.

In this work glucose-fructose syrup (GFS, CAS: 8029-43-4) was chosen as a substance imitating adulteration. Differential Pulse Adsorptive Stripping Voltammetry (DP-AdSV) with a iridium electrode was used to test 17 apple juices of Polish production as well as prepared in a laboratory with GFS additions (up to 50% of the juice volume). The calculations were performed in Python 3.8 with Keras 2.3 and TensorFlow 2.0 backend. Deep neural network models were tested using the Google Colab platform.

Methods of the linear multivariate calibration models and deep neural networks were used for the chemometric analysis of various syrup additives. The most optimal calibration model, using the recurrent multi-layer neural networks with LSTM layer, the value of the root mean squared error of prediction (RMSEP) was 1.9 - 2.1% of the GFS addition with the correlation (R^2PRED) above 0.98. The obtained result is three times better compared to linear models. The use of the deep machine learning approach allowed for the development of a universal procedure for testing the syrup content in apple juices.

Acknowledgements

This work was supported by the subvention from the Ministry of Science and Higher Education No.16.16.160.557 in 2020.

* Corresponding author, e-mail: *szwojcik@agh.edu.pl*

8.28 Quadruple disk metallic electrodes for voltammetric profiling of local food

Szymon Wójcik*,[1], Bogusław Baś[1], Małgorzata Jakubowska[1]

1 Department of Analytical Chemistry, Faculty of Materials Science and Ceramics, AGH University of Science and Technology, Cracow, Poland

Keywords: *disk metallic electrodes*, *fruit juices*, *natural wine*, *honey*, *PCA*.

The undertaken task demonstrates that there is a possibility of various types of local food profiling using voltammetric methods and chemometric algorithms. In the study, three different quadruple disk metallic electrodes were selected for the tests: q-DIrE (iridium), q-DPtE (platinum) and q-DIrPtE (iridium- platinum). All the electrodes used are of a similar construction. Two metal wires (iridium or platinum) were mounted in a silver rod. Whole structure is secured with an epoxy resin. In the case of single-metal electrodes, both wires are made of the same metal. In the case of a mixed electrode, one of the wires used is iridium and the other is platinum.

The electrode tests were carried out on three groups of food samples: natural red and rose wines, fruit juices and honeys, obtained from the local producers. The voltammetric profiles of these samples were recorded using DPV technique in 0.1M KCl or 0.1M KNO_3 as supporting electrolytes. Interpretation of the results in each of the studied groups was carried out using Matlab 2014b with the PLS Toolbox. The principal component analysis (PCA) has demonstrated the ability to discriminate between local food samples of the different origin.

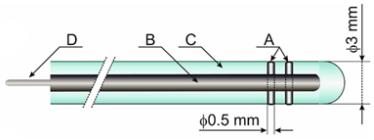

Figure 8.28.1: Construction of the voltammetric sensor, the quadruple disk metallic electrode: (A) metallic wires, (B) silver rod, (C) epoxy resin, and (D) electric contact pin.

Acknowledgements

This work was supported by the subvention from the Ministry of Science and Higher Education No.16.16.160.557 in 2020.

* Corresponding author, e-mail: *szwojcik@agh.edu.pl*

8.29 Synthesis of graphene oxide nanoparticles obtained by pyrolysis of citric acid

Piotr Wyrębiak[*,1], Aleksandra Poniatowska[1], Tomasz Ciach[1]

1 Faculty of Chemical and Process Engineering, Warsaw University of Technology, Warsaw, Poland

Keywords: *citric acid*, *graphene oxide*, *carbon quantum dots*, *fluorescence*, *cytotoxicity*.

Carbon dots (CDs), which are the newly discovered fluorescent nanomaterials, have become popular in the last decade due to their unique optical properties, good biocompatibility, low toxicity, high stability in water, and ease of synthesis. One of the types of CDs are graphene oxide nanoparticles (GONPs). GONPs have a non-zero bandwidth as opposed to graphene. With good fluorescent properties, GONPs can have much potential use in various fields.

The aim of the research was to synthesize graphene oxide from citric acid with nitrogen atoms incorporated in the structure of GO and to study its effect on the viability of cells cultured in vitro. The sources of nitrogen were urea, ammonia, ethanolamine, Tris(2-amino-2-(hydroxymethyl)propane-1,3-diol). Homogeneous, mixed solutions were pyrolyzed in 200 °Cand various time variants: 1h, 1h 40 min, 2h 30 min. The analysis of the physicochemical properties of the graphene oxides was investigated by Fourier transform infrared spectroscopy (FTIR), dynamic light scattering technique (particle size distribution), and fluorescence measurement. The acid-base characteristics was also examined. Because of the potential use in medicine, a commonly known short cytotoxicity test MTT was used for this purpose. The mouse fibroblasts cell line L929 was incubated at 37 °C for 24h with solutions of modified graphene oxide at a concentration of 1 mg/ml and 0.5 mg/ml.

Particle size analysis showed that the obtained particles are characterized by a wide distribution of diameter, especially GO after synthesis with ammonia and urea. The highest relative fluorescence was obtained for graphene oxide with nitrogen groups derived from Tris. The viability for cells incubated with this material was over 70%, so it is supposed, that it has no negative influence on the viability of cells. On the contrary, GO obtained with the addition of urea and ammonia turned out to be toxic to cells (viability below 40%). The research shows also differences between graphene oxide-based materials with nitrogen depending on nitrogen sources and its properties are strongly dependent on the synthesis conditions and confirmed that graphene oxide can be a promising material in medical applications, for example, cancer diagnostics or anticancer therapy.

[*] Corresponding author, e-mail: *wyrebiakpiotr@gmail.com*

9 Abstracts: Mathematical modeling, simulations & optimization

9.1 Development and optimization of a synthesis procedure of poly(glycerol citrate)

Aleksandra Bandzerewicz*,[1], Michał Wrzecionek[1], Agnieszka Gadomska-Gajadhur[1]

1 Faculty of Chemistry, Warsaw University of Technology, Warsaw, Poland

Keywords: *glycerol based polyesters*, *poly(glycerol citrate)*, *polycondensation*, *biomaterial*, *tissue engineering*.

A variety of polymers have been evaluated and acknowledged as new biomaterials for scaffolds development, many of them are polyesters. Following the success of poly(glycerol sebacate), it is deemed reasonable to continue search for new biomaterials among glycerol based polyesters, hence the idea to obtain poly(glycerol citrate). Both monomers – glycerol and citric acid – are non-toxic and known for their human body occurrence. Besides, they are low-priced and available in large quantities, as citric acid is the main organic acid manufactured nowadays and glycerol is a by-product of biodiesel production. Therefore, poly(glycerol citrate) has real potential for its biomedical application and is interesting from an economic perspective.

The purpose of this work is to obtain poly(glycerol citrate) by carrying out non-solvent catalyst-free polycondensation of glycerol and citric acid. Preliminary results defining the relationship between reaction time and conversion of carboxyl groups of citric acid were acquired, allowing for the more comprehensive study of the impact of synthesis parameters on the product based on methods of design of experiments. Several experiments under different conditions were carried out.

FTIR and NMR spectroscopy were used to confirm the polyester structure of the products of the synthesis. Products were characterized by their acid number, ester number, and conversion degree. A central composite design was used to create a mathematical model of the polycondensation. Therefore, it is possible to choose optimal synthesis parameters to obtain poly(glycerol citrate) of the desired features.

Acknowledgements

This scientific research was financed from the National Science Centre as a research project "Miniatura 3" (2019/03/X/ST5/01208) titled: "Preparation and testing of the properties of cell scaffolds from poly(glycerol citrate)".

* Corresponding author, e-mail: *aleksandra.bandzerewicz.stud@pw.edu.pl*

9.2 Analysis of the maintenance cost for heterogeneous systems subject to a periodic inspection policy

Lucía Bautista*,[1], Inma T. Castro [2]

1 Department of Computers and Communications Technology, Universidad de Extremadura, Cáceres, Spain
2 Department of Mathematics, Universidad de Extremadura, Cáceres, Spain

Keywords: *preventive maintenance*, *gamma process*, *periodic inspection*, *optimization*, *stochastic modelling*.

Maintenance of heterogeneous systems composed of several components that require different maintenance strategies is a key challenge nowadays. Techniques like preventive maintenance, corrective maintenance or condition-based maintenance are usually employed in the literature. In this work, a complex system with monitored and non-monitored components is analyzed. Monitored components are subject to a continuous deterioration, following a homogeneous gamma process, while non-monitored components are subject to sudden failures, whose appearance time follow an exponential distribution.

A failure of a monitored component occurs when its deterioration level reaches the so-called corrective threshold. A preventive threshold, lower than the corrective one, is also set to avoid a complete failure of the system. Periodic inspections are performed to check the state of the system. In addition, repair times are viewed as opportunities for preventive maintenance of the rest of monitored components if necessary.

Assuming a sequence of costs for the different maintenance tasks, the expected cost rate of this system is analytically obtained. The maintenance strategy is optimized through the search of the preventive thresholds and time between inspections that minimize the expected cost rate. To deal with this, meta-heuristic algorithms, such as Genetic Algorithm, and traditional Monte Carlo simulation are used to compute the costs.

Acknowledgements

This work was supported by Junta de Extremadura, Spain (Project GR18108) and European Union (European Regional Development Funds.

* Corresponding author, e-mail: *luciabb@unex.es*

9.3 Computation of closed form solutions to the stochastic Green function in electromagnetism

Lucía Bautista[*,1], Inma T. Castro [2], Luis Landesa[1]

1 Department of Computers and Communications Technology, Universidad de Extremadura, Cáceres, Spain
2 Department of Mathematics, Universidad de Extremadura, Cáceres, Spain

Keywords: *Green function*, *closed cavities*, *wave propagation*, *Cauchy distribution*.

Deterministic computation of electromagnetic fields inside closed cavities is ineffective because small changes in the problem or the boundary conditions produce very large changes in the electric and magnetic fields. Monte-Carlo simulation could provide a statistical behaviour of the electromagnetic fields inside those cavities, but it is computationally expensive.

Based on the assumption that the eigenvalues of the electromagnetic problem follow a uniform distribution, the deterministic Green function can be expressed as a sum of random variables following a heavy-tailed distribution, that is, variables whose tails decrease more slowly than the tails of an exponential distribution. These variables have neither mean nor variance defined, but we can obtain the parameters of their corresponding stable distributions using the Generalized Central Limit Theorem for stable distributions and, from this, adjust a suitable probability distribution for the stochastic case.

In this work, we proof that the stochastic Green functions have closed form solutions based on Cauchy distribution. Additionally, these solutions are proportional to the well-known Green function in free space. Some numerical examples comparing the empirical cumulative distribution function and the predicted Cauchy distribution function are also given.

Acknowledgements

This work was supported by the Extremadura Government by projects DEEP-EM (Ref IB18073) and GR18055 and by the Spanish Government and FEDER by projects TEC2017-85736-C2-1-R and MTM2015-63978-P.

* Corresponding author, e-mail: *luciabb@unex.es*

9.4 Modeling and simulation of CO_2 capture using MEA in hollow fiber membrane contactors

Alexandru-Constantin Bozonc[*,1], Ana-Maria Cormos[1]

1 Department of Chemical Engineering, Faculty of Chemistry and Chemical Engineering, Babes-Bolyai University, Cluj-Napoca, Romania

Keywords: *mathematical modeling*, *CO_2 capture process*, *hollow fiber membrane contactors*.

Global warming and climate change produced by CO_2 emissions is an important issue today. Carbon capture represents a promising option of reducing CO_2 emissions and allows the continuation of fossil fuels usage for at least a short to medium period of time. The most common process for removal of CO_2 from flue gases is the absorption into a solvent using conventional gas–liquid contactor such as packed bed absorber. This conventional chemical absorption processes for CO_2 capture suffers many drawbacks such as flooding, foaming, entraining, channeling, high capital and operating costs. In order to solve the operational problems related to the usage of conventional gas–liquid contactors, a new promising and effective CO_2 capture technology, the gas-liquid membrane contactor, was developed. The membrane contactor consists of three sections: tube side, membrane, and shell side. The gas mixture flows through the shell side, while the solvent flows through the tube side in a countercurrent arrangement.

In this work, a mathematical model is developed in order to evaluate the CO_2 capture process into hollow fiber membrane contactors. The developed model constitutes in equations that describe the complex nature of the process, referring not only to the mass transfer between the gas and the liquid phase, but also to the hydrodynamics and kinetics of absorption of CO_2. An important part of the developed model is the calculation procedure of the mass transfer coefficients.

To analyze the performance of the system, the mathematical model was implemented in Matlab/Simulink. The simulation results indicate that hollow fiber membrane contactors have better efficiency to remove CO_2 from flue gases in comparison with packed bed contactors. Comparing the simulation results with the experimental data presented in literature we obtained similar mass transfer coefficients. On this basis, the developed model would be used to evaluate CO_2 capture process in hollow fiber membrane contactors for wide domain of operating conditions in order to predict with accuracy the process parameters (liquid and gaseous flows, composition of the streams, mass transfer area, mass transfer coefficient, pressure drop etc).

* Corresponding author, e-mail: *alexandrubozonc0@gmail.com*

9.5 Analysis of gas network storage capacity for hydrogen

Marta Ciuksza*,1

1 Faculty of Chemical Technology and Engineering, West Pomeranian University of Technology, Szczecin, Poland

Keywords: *natural gas*, *alternative gas fuels*, *gas network*, *storage of gas fuels*, *hydrogen*.

Currently, there are many fuels used in the world, one of them is natural gas, consisting of a mixture of various gases, but the basic flammable component is methane. Besides methane, there are also small amounts of hydrocarbons and other pollutants. Natural gas is one of the cleanest, safest and most convenient energy sources and is used for example as a raw energy material. The heat from the combustion of natural gas is equal to 34–46 MJ/m^3, while the minimum heat combustion value of gas transmitted through the gas network in Poland is 34 MJ/m^3. This allows it to be added to alternative fuels with a lower heat combustion value than natural gas, such as hydrogen, which is obtained when there is a surplus of energy production from renewables.

This paper analyses the storage capacity of a part of the low pressure gas network located in Szczecin for 2018. The distribution of overpressure, streams and velocities of natural gas were generated via the GASNET program.

Analysis were carried out for six different air temperature ranges. The lowest overpressure needed to supply the network at selected gas intakes from the nodes for each air temperature range was chosen. The distributions of overpressure, velocity and natural gas streams as well as mixtures of natural gas and hydrogen in the gas network were examined. This work showed that an increase in air temperature and type of gas fuel causes a reduction in the volume of gas streams taken from the gas network, and a drop in the overpressure needed to supply the gas network. The storage capacity of a specific area of the Szczecin gas network for hydrogen was estimated on the basis of the difference in a mixture of natural gas streams with hydrogen and natural gas over a period of one year.

* Corresponding author, e-mail: *marta.ciuksza@zut.edu.pl*

9.6 Modelling of deagglomeration process using dissolvers – application of population balance

Radosław Krzosa*,1, Łukasz Makowski 1, Wojciech Orciuch1, Radosław Adamek2

1 Faculty of Chemical and Process Engineering, Warsaw University of Technology, Warsaw, Poland
2 ICHEMAD - Profarb, Gliwice, Poland

Keywords: *mixing*, *impeller*, *dispersion*, *population balance*, *CFD*.

Solid particles suspensions are often used in coating and paint making industries. To obtain desirable properties of the product, particles must have strictly specified size distribution that has influence on product properties, such as mixture viscosity, suspension stability, coating appearance, surface roughness, etc. Therefore, solid component must be prepared to reach specified properties. Deagglomeration of solid particles takes place usually in dissolvers or grinding mills and sometimes ultrasonication methods are used.

The deagglomeration process can be divided into three stages. The first step is wetting the powder to create a suspension. The second step is breaking up agglomerates to obtain specific particle size distribution. In the last stage product suspension is stabilized by surfactants to prevent reagglomeration. The second stage mechanism depends on powder material and three main breakage mechanisms could be considered: shattering, rupture and erosion.

Experimental particle size distributions allow to identify the mechanism that dominates and population balance methods allow predicting influence process conditions on particle size change in the deagglomeration process. To properly describe the process using population balance equations, it is crucial to identify mechanism of breakage and other powder properties.

In this work, periodic processes, carried out in dissolvers were investigated. Computational fluid dynamics simulations were applied to predict flow fields, turbulence and shear stress in process. Direct quadrature method of moments (DQMOM) was applied to solve population balance equations and investigate particle size distribution change during the process. These values allow to describe the efficiency of the process and predict properties of the product.

Acknowledgements

This work was supported by ICHEMAD - Profarb sp. z o. o. ICHEMAD - Profarb sp. z o. o. has implemented a project entitled: "Development of utility models for the construction of a set of energy-saving devices for the chemical industry, in particular for the production of paints and varnishes" under Measure 1.1.1 of the Intelligent Development Operational Program 2014-2020 co-financed by the European Regional Development Fund.

* Corresponding author, e-mail: *radoslaw.krzosa.dokt@pw.edu.pl*

9.7 Dynamic modelling of hydrogen production by biogas steam reforming process

Alessandra-Diana Selejan[*,1], Ana-Maria Cormos[1]

1 Department of Chemical Engineering, Faculty of Chemistry and Chemical Engineering, Babes-Bolyai University, Cluj-Napoca, Romania

Keywords: *dynamic mathematical modeling*, *hydrogen production*, *biogas steam reforming process*, *CO_2 neutral source*.

Hydrogen is nowadays considered the energy vector of the future, thanks to its high energy density, the high availability and the low environmental impact in the use as a fuel. Among the possible sources of hydrogen, water and natural gas are the most interesting ones. The high energy consumption makes the electrolysis usable only to obtain high purity hydrogen for special application. Natural gas is the primary source in hydrogen production, throughout a reforming process in which it is converted to syngas and then into hydrogen. Natural gas comes is a conventional fossil fuels, whose replacement are needed in near future, which makes the biogas the one of most favorable renewable energy and CO_2 neutral sources, which can be a preferable choice for H_2 production.

In this work, a dynamic 1D heterogeneous model for catalytic hydrogen production by biogas steam reforming process is developed. The model consists of partial differential equations which describes both mass and energy conservation in the given system. The biogas steam methane reforming process is catalytic and generally endothermic. It consists of 2 parallel reactions in which CH_4 reacts with water vapors in different stoichiometric ratios giving CO or CO_2 and H_2, and a successive reaction in which CO reacts with water vapors giving CO_2 and H_2. In the current work is used the kinetic model developed by Xu and Froment for nickel-alumina catalysts, based on Langmuir-Hinshelwood approach.

The partial differential equations have been converted into total differential equations, by spatial discretization and implemented in Matlab/Simulink for process simulation. Base on simulation results the profiles for mass, temperature and concentration of the reactants and products were obtained. The developed model has been validated with available industrial data presented in literature.

The model is used to study the effects of step and ramp flow/temperature inputs disturbances in the methane conversion. The dynamic behavior study of the steam methane reforming process reflects that plant performance (methane conversion) is increased for 100 °C higher feed temperature, as the reaction is endothermic.

* Corresponding author, e-mail: *alessandra.selejan@gmail.com*

9.8 CFD study of monolithic structures with enhanced transport properties

Katarzyna Sindera[*,1], Marzena Iwaniszyn[1], Anna Gancarczyk[1], Mateusz Korpyś[1], Andrzej Kołodziej[1]

1 Institute of Chemical Engineering, Polish Academy of Sciences, Gliwice, Poland

Keywords: *short-channel structures*, *computational fluid dynamics*, *turbulence models*, *heat transport*.

Rapid industrial and civilisational development have increased the amount of dangerous substances emitted to the atmosphere (NO_x, SO_x, PM2.5, PM10). Heterogeneous catalytic processes enable the effective elimination of toxic emissions. Such processes have been developed rapidly in recent decades, but they still need to be improved.

Computational Fluid Dynamics (CFD) software is a powerful tool for simulating real processes. It enables the impact of catalyst carrier geometry on transport properties to be assessed numerically (and therefore much faster than experimentally). The usefulness and legitimacy of CFD has been proven in many works focusing on classic and short-channel monoliths. The method consists of a pre-processing (preparation of geometry and mesh for simulation), simulation and post-processing (processing of results). Simulations were carried out with the use of different turbulence models as: laminar, k-ε (renormalization-group RNG, realizable, standard) and k-ω (shear stress transport SST).

The beneficial transport properties of short-channel (few mm long) hexagonal cross-section monoliths have been numerically proven (in comparison to classic, long monolith). Influence of chosen turbulence model was confirmed. k-ω SST model led to reduction of heat transfer coefficients values, in contrast to k-ε standard model.

Acknowledgments

This work was supported by the Polish National Science Centre (Project No. 2016/21/B/ST8/00496).

* Corresponding author, e-mail: *katarzyna.sindera@iich.gliwice.pl*

9.9 CFD simulation of drag force in porous packing for rotating packed beds

Justyna Wojtasik-Malinowska[*,1], Maciej Jaskulski[1], Marcin Piątkowski[1]

1 Faculty of Process and Environmental Engineering, Department of Environmental Engineering, Lodz University of Technology, Lodz, Poland

Keywords: *rotating packed bed*, *RPB*, *hydrodynamics*, *CFD*, *pressure drop*.

Rotating packed bed (RPB) technology is designed for intensifying industrial processes, e.g. distillation, absorption, etc. The RPB's are the type of HiGee equipment that occurs in the mass transfer process in high-gravity conditions. The centrifugal force induced by the rotation of the packing increase the capacity and to enhances mass transfer between phases, through what overcoming the limiting parameter found in packed columns – which is the gravity force. Very important issue in RPB is understanding the fluid dynamic inside a rotating packing. This issue is complex because of the annular shape of the rotor and presents of centrifugal force which is changing together with radius.

In this study, a CFD (Computational Fluid Dynamics) simulation is proposed as a tool for the study of gas phase flow inside porous packing, which was difficult to determine in an experimental way. To describe this issue, the three-dimensional numerical model for two fluid models: k-ε and RNG k-ε for predicting the dry pressure drop is presented. Obtained simulation results were compared with experimental results.

The experimental dry pressure drop for porous packing was investigated for rotational speed in the range from 150 rpm to 1500 rpm and compared to the results from the numerical model. The comparison of experimental and simulation results indicate very good consistency within the whole range of rotor speed of interest.

The CFD modeling is recognized as a good tool which leading to better understanding of gas phase behavior inside a RPB, filling the gap in fundamental knowledge on hydrodynamics of rotating packing. What is more the CFD can be used to predict the hydrodynamics for new types of packing and shape validation in order to lower pressure drop and better fluid pattern inside the packing.

* Corresponding author, e-mail: *justyna.wojtasik-malinowska@dokt.p.lodz.pl*

9.10 Predicting N-methyldiethanolamine (MDEA) concentration using analytical techniques

Justyna Wojtasik-Malinowska[*,1], Dawid Zawadzki[1], Maciej Jaskulski[1], Marcin Piątkowski[1], Andrzej Górak[1,2]

1 Faculty of Process and Environmental Engineering, Department of Environmental Engineering, Lodz University of Technology, Lodz, Poland
2 Faculty of Biochemical and Chemical Engineering, Laboratory of Fluid Separation, TU Dortmund University, Dortmund, Germany

Keywords: *MDEA*, *concentration*, *ATR-FTIR*.

Determination of amine solution is very important in industry. Mainly used analytical methods require expensive equipment and experience in data analysis. One of the most common method using to determine amine concentration is Fourier transform infrared spectroscopy (FTIR) combined with partial least-square regression (PLSR), which allow a qualitative and quantitative analysis of components. In this study, approach allows predicting N-methyldiethanolamine (MDEA) amine concentration using "simple" and "quick" analytical techniques is investigated.

In this work, four different methods: refractometry, density, conductometry and pH metrics were presented as simple methods for determining the concentration of MDEA amine in water solutions. For independent verification of MDEA concentration, the infrared (IR) spectra were measured using attenuated total reflectance (ATR) FTIR spectroscopy combined with partial least-square regression (PLSR). The tests were carried out for all mentioned methods in 13 concentration from 2.5 wt.% to 80 wt.% MDEA in water.

The refractometry and density measurements were found as the most precise and accurate among the "simple" techniques investigated in this study. Both give high repeatability of obtained results what is represented by standard deviation $<10^{-3}$ and can be successfully used to either separately or mutually using correlations presented in this study.

The ATR-FTIR spectroscopy supported by PLSR model is recognized as an appropriate method to confirm the amine concentration due to repeatability of the measured value and linear correlation between the absorbance and MDEA concentration. The combination of simple analytic methods can be successfully applied for the determination of MDEA concentration in aqueous solutions.

* Corresponding author, e-mail: *justyna.wojtasik-malinowska@dokt.p.lodz.pl*

9.11 Synthesis of poly(glycerol succinate) with simplex optimization

Michał Wrzecionek*,[1], Aleksandra Bandzerewicz[1], Agnieszka Gadomska-Gajadhur[1]

1 Faculty of Chemistry, Warsaw University of Technology, Warsaw, Poland

Keywords: *poly(glycerol succinate)*, *polycondensation*, *optimization*, *simplex*.

Glycerol and succinic acid are favorable for building polyester chains because they naturally occur in the organism. Glycerol is necessary for the proper functioning of the organism, it builds fats and phospholipids chains. It's metabolized in glycolysis or gluconeogenesis processes. Succinic acid is one of the key products of the Krebs cycle, which is a fast metabolic pathway. Moreover, the US Department of Energy published in 2008 a list of twelve block chemicals which may be produced from sugars and other renewable raw materials by biological or chemical transformations and transformed into valuable biological materials or chemicals. Both glycerol and succinic acid or anhydrirde were included in this list. Because of that, poly(glycerol succinate) – PGSu – could be very valuable material in the future.

In this work, two steps polycondensation of glycerol and succinic anhydride is presented. The first step was a classic polycondensation without receiving water to obtain prepolymer. Water was receiving in the second step by using reduced pressure. The second step of this reaction was optimized by simplex for obtaining poly(glycerol succinate) with possible high molecular weight.

PGSu was characterized by FTIR spectroscopy, NMR spectroscopy, degree of esterification was determined, and also via Carothers equations molecular weight was calculated for each experiment.

The new synthesis route was developed and optimized. Temperature and time influence on molecular weight and esterification degree of obtained polyester is presented. The mathematical model for this process is proposed. It is possible to obtain poly(glycerol succinate) with 6.7 kDa molecular weight.

Acknowledgements

This scientific research was financed from the budgetary funds on science projected for 2018–2022 as a research project under the "Diamond Grant" program (DI 2017 000347 (ID 395680)).

* Corresponding author, e-mail: *6824@pw.edu.pl*

9.12 Computer-aided modeling and experimental studies of 3D printed internals customized for CO_2 absorption in rotating absorbers

Dawid Zawadzki*,[1], Maciej Jaskulski[1], Andrzej Górak[1,2]

1 Faculty of Process and Environmental Engineering, Lodz University of Technology, Lodz, Poland
2 Department of Biochemical and Chemical Engineering, Laboratory of Fluid Separations, TU Dortmund University, Dortmund, Germany

Keywords: *CFD*, *rotating packed bed*, *absorption*, *optimization*.

One of the most frequently performed unit operations in the chemical industry is the absorption of gases in liquids. Nowadays, generally conducted absorption installations are the packed bed columns. In recent years, Rotating Packed Bed (RPB) technology has gained great interest, it addresses size reduction and high separation efficiency by applying a centrifugal force. Gravity force was replaced by 10-100 times greater centrifugal force and improve the performance of the mass transfer process, which results in savings in operational and investment costs.

Designing and verification of new packing in rotating absorbers take a long time and costs due to limited fundamental knowledge of how RPB unit works in the literature. The purpose of the project is to create computer-aided rapid prototyping of tailor-made internals which accelerate the designing process.

In this study, eleven types of packing were designed in 3D modeling software. Next, computational fluid dynamics (CFD) software was used to simulate fluid flow in internals and to determine velocity distribution and dry pressure drop, which was the first criterion for assessing the quality of packings. Results from the simulations were validated by comparison with the experimental data. This procedure allowed to select the most promising geometries for which a multiphase absorption CFD simulation will be performed.

Acknowledgements

Project co-financed by the National Science Center Poland, within the "OPUS 17" (agreement number UMO-2019/33/B/ST8/00886.

* Corresponding author, e-mail: *dawid.zawadzki@dokt.p.lodz.pl*

10 Abstracts: Bioengineering, biotechnology, biomedical engineering

10.1 Adhesion properties of plant-based perfume microcapsules for laundry applications

Daniele Baiocco[1], Zhibing Zhang[*,1], Jon A. Preece[2]

1 School of Chemical Engineering, University of Birmingham, Birmingham, United Kingdom
2 School of Chemistry, University of Birmingham, Birmingham, United Kingdom

Keywords: *microcapsules*, *coacervation*, *adhesion*, *flow chamber*.

There is a growing need to effectively deliver perfume molecules to fabric surfaces throughout laundry processes in order to release pleasant scents to clothes, and enhance the usage experiences of consumers. Perfume microcapsules (PMCs) fabricated with formaldehyde have long played a significant role in laundry industry. However, regulations against cancer-causing materials have been recently enforced urging for hazard-free formulation replacements. The purpose of this study firstly includes the development of a robust microencapsulation process to entrap perfume oils (hexyl salicylate and limonene) within plant-based shells (gum Arabic and fungal chitosan) via complex coacervation, and secondly to mimic the adhesion of such microcapsules to fabric surface in real washing by using a flow chamber technique equipped with smooth polyethylene terephthalate (PET) film as model.

A flow chamber paired with a bright-field microscope was employed to understand the interactions of microcapsules with the PET film, and thus their retention at increasing flow rate/shear stress. Since laundry products can have different pH values, the effect of the environmental pH was also investigated. Image analysis was automatically performed using ad-hoc codes generated via Matlab®/ImageJ.

At highly acidic pHs ($\leq$ 5.0), the retention of PMC was found to be ~85% and ~60% at low ($\leq$ 50 mPa) and high shear stress (1 Pa), respectively. However, at nearly neutral pHs the retention was much worse. This phenomenon is probably due to the nature of the biopolymeric shell of microcapsules, which is pH-sensitive. Overall, a flow chamber technique can be used as a powerful microfluidic platform to quantify the retention properties of PMCs for laundry applications at different environmental pH conditions.

Acknowledgements

This work was supported by EPSRC, UK (Grant number EP/L015133/1).

[*] Corresponding author, e-mail: *Z.Zhang@bham.ac.uk*

10.2 Determination of mixing time in a disposable bioreactor supported with wave-induced agitation

Mateusz Bartczak[*,1], Aleksandra Raczkowska[1], Kamil Wierzchowski[1], Maciej Pilarek[1]

1 Faculty of Chemical and Process Engineering, Warsaw University of Technology, Warsaw, Poland

Keywords: *mixing time*, *single-use bioreactor*, *wave-type agitation*, *operation parameters*, *design of experiments (DoE)*.

Bioreactors equipped with disposable (i.e. single-use) culture bags are alternatives to equipment supported with steel- or glass-made culture vessels. Wave-type agitated bioreactors are the most popular group of disposable bioreactors. Such non-typical kind of agitation is induced by oscillatory rocking movements of the whole single-use vessel. The wave-type agitation is widely recognized as a low shear stress process, and it is particularly recommended for bioprocessing of fragile types of biomass, i.e. animal or plant cells/organs, which can be easily destroyed by typical spinning stirrers applied for mechanical mixing of culture systems.

The aim of the study was to recognize the influence of operational parameters defining the wave-type agitation intensity on values of mixing time (τ) reached in *ReadyToProcess* WAVE™ 25 bioreactor. The impact of four operational parameters has been investigated: (i) angle (2–12°) and (ii) frequency of oscillations (2–40 rpm), (iii) rocking motion (30–90%), and (iv) volume of the aqueous phase (0.2–1.0 dm^3) inside the vessel. The design of experiments (DoE) methodology has been applied for distinguishing operating parameters as relevant or irrelevant ones. The two experimental methods have been applied for independent validation of τ values reached in the studied system: the standard decolorization method and the sensor method of pH level monitoring during neutralization reaction.

The results unequivocally exhibited predominance of the sensor vs. decolorization method in the case of accurate and repeatable determination of τ. The angle and the frequency of oscillations, and the volume of the aqueous phase impacted significantly on τ, with the highest influence of the frequency of oscillations. The impact of the rocking motion parameter was statistically irrelevant.

[*] Corresponding author, e-mail: *Mateusz.Bartczak.dokt@pw.edu.pl*

10.3 Biodegradable slow-released fertilizer

Przemysław Boberski[*,1], Kamila Torchała[1], Jan Wójcik[1], Marek Główka[1], Nikodem Kuźnik[2]

1 Łukasiewicz Research Network – Institute of Heavy Organic Chemistry "Blachownia", Kędzierzyn-Koźle, Poland
2 Chemical Department, Silesian University of Technology, Gliwice, Poland

Keywords: *natural polymers*, *biodegradable polymers*, *controlled release fertilizer*, *slow release fertilizer*.

The reduction of microplastics in the soil is a significant challenge for our generation. Currently, the technology of coated fertilizers is accessible, however, the materials used for this purpose do not show the ability to biodegrade. After use, huge amounts of microplastics get into the soil and groundwater, where they are deposited.

The aim of this work is to show how the Controled Release Fertilizer (CRF) is prepared from natural raw materials. A double coated fertilizer was obtained as the final product. The core of prepared fertilizer was a multi-nutrient granular fertilizer such as NPK. The substances used as a coating material were natural modified polymers – derivates of cellulose and polymerized plant oil e.g. linseed or hemp.

Following the standard PN-EN 13266:2003, it was studied how nutrients were released from the fertilizer. The biodegradability of coated fertilizer was assessed according to the standard ISO 21263.

Results showed that the fertilizer complies with the standard set for coated fertilizers, in terms of the amount of nutrients released over time. In relation to the studies on potential biodegradability, the results about 10% per month, which was promising and suggested that the entire fertilizer will biodegrade after approximately one year.

The content presented in the poster is protected under patent applications number P434355 and P434356, and the work was done as a part of research in the "Doktorat wdrożeniowy" financed by Ministry of Science and Higher Education.

Acknowledgments

This work was supported by Ministry of Science and Higher Education.

[*] Corresponding author, e-mail: *przemyslaw.boberski@icso.lukasiewicz.gov.pl*

10.4 The continuous production and real-time monitoring of galactooligosaccharides

Teng Cao[*,1], Balázs Erdős[1], Marietta Fodor[2], Zoltán Kovács[3], Zoltán Kovács[1]

1 Department of Food Engineering, Szent István University, Budapest, Hungary
2 Department of Applied Chemistry, Szent István University, Budapest, Hungary
3 Department of Physics and Control, Szent István University, Budapest, Hungary

Keywords: *galactooligosaccharides*, *enzyme membrane reactor*, *stirred tank reactor*, *fourier transform near infrared spectrometry*, *PLSR*.

Galactooligosaccharides (GOS) are recognized as one of the most important prebiotics. Currently, GOS are commercially produced from lactose through transglycosylation by β-galactosidase in a batch fashion. The usage of conventional stirred-tank reactors (STR) require further processing steps to inactivate and to remove the enzymes from the final products. Moreover, the detection of GOS composition is performed with the time-consuming and expensive offline liquid chromatography in the industrial practice.

The objective of our work was twofold. First, to investigate the applicability of a continuous enzyme membrane reactor (EMR) in manufacturing GOS and to compare that of STR. Second, to establish a rapid and efficient method for the direct monitoring of the GOS formation.

Our results indicated that although STR showed a slightly better performance in term of GOS yield, it had a considerably lower productivity than EMR. Besides, a stable degree of conversion in the EMR was observed over the long term (120 h) investigations. The concentration of individual saccharides fractions was analyzed by HPLC as a reference method. A rapid method based on FT-NIR spectrometry coupled by partial least squares regression (PLSR) modeling was developed and proved to be a promising tool for the direct monitoring of GOS production.

Acknowledgements

This research was supported by the New National Excellence Program of the Ministry of Human Capacities and by the European Union and co-financed by the European Social Fund (grant agreement no. EFOP-3.6.3-VEKOP-16-2017-00005), the Food Science Doctoral School of Szent István University, and the Stipendium Hungaricum Scholarship by Tempus Public Foundation.

[*] Corresponding author, e-mail: *catherinecaot@gmail.com*

10.5 Long-term degradation of bioactive glass-modified composites loaded of polyphenolic compounds extracted from *Salvia officinalis L.*

Kamila Chęcińska[*,1], Michał Dziadek[1,2], Kinga Dziadek[3], Barbara Zagrajczuk[2], Aneta Kopeć[3], Katarzyna Cholewa-Kowalska[1]

1 Department of Glass Technology and Amorphous Coatings, AGH University of Science and Technology, Cracow, Poland
2 Faculty of Chemistry, Jagiellonian University, Cracow, Poland
3 Department of Human Nutrition, University of Agriculture in Krakow, Cracow, Poland

Keywords: *biomaterials for drug delivery*, *bioactive glass*, *polyphenols*.

The search for a new generation of biomaterials for bone regeneration results from the growing demands of bone tissue engineering (BTE). Challenges include preventing periimplantitis, tumor growth and antibiotic resistant infections. Thus, to change the properties (e.g. degradation process) and biological activity of BTE composites, active compounds are used, e.g. of plant origin, such as polyphenols (PPh).

Polymeric materials (PCL, PLGA) and bioactive glass (BG)-modified composites loaded with PPh compounds extracted from *Salvia officinalis L.* (1 and 4.5 wt.%) were prepared in form of films. Sol-gel-derived BG particles (d_{50} = 2 µm) with the composition of (mol%) 40 SiO_2–54 CaO–6 P_2O_5 were used as a modifying phase (30 wt.%). During long-term (up to 6 months) incubation in PBS, thermal and mechanical properties, microstructure, surface chemical composition, pH and mass changes were monitored.

The addition of PPh to PCL (PCL/PPh) and PCL-BG biocomposites (PCL-BG/PPh) slows down their degradation in PBS, among others, due to the formation of a calcium phosphate (CaP) layer. It is manifested in mass increase and confirmed by SEM/EDX analysis. During incubation the degree of crystallinity of PCL/PPh and PCL-BG/PPh increases. It correlates with the enhancement of mechanical properties, including Young's modulus. Albeit, the same addition of PPh enhances the degradation of the PLGA-based biomaterial (PLGA/PPh) and BG-modified PLGA (PLGA-BG/PPh), which is expressed by a decrease in the pH of the incubation media. The degradation process of PLGA/PPh and PLGA-BG/PPh is most intense in the initial period of incubation.

Acknowledgements

This work was supported by the National Science Centre, Poland Grant no. 2017/27/B/ST8/00195 (KCK).

* Corresponding author, e-mail: *checinska@agh.edu.pl*

10.6 Antibacterial and neuroprotective conducting polymers for biomedical applications

Dominika Czerwińska-Główka[*,1], Magdalena Skonieczna[2,3], Katarzyna Krukiewicz[1], Wioletta Przystaś[2], Ewa Zabłocka-Godlewska[2], Sebastian Student[3], Beata Cwalina[2], Mieczysław Łapkowski[1]

1 Department of Physical Chemistry and Technology of Polymers, Silesian University of Technology, Gliwice, Poland
2 Department of Environmental Biotechnology, Silesian University of Technology, Gliwice, Poland
3 Department of Automation, Electronics and Computer Science, Silesian University of Technology, Gliwice, Poland

Keywords: *conducting polymer*, *poly(3,4-ethylenedioxypyrrole)*, *tetracycline*, *bacterial biofilm*, *neural interfaces*.

Conducting polymers combine electrical activity with biocompatibility, which gives them an innovative nature. This connection significantly increases the range of potential applications of polymers. Due to the known immobilization method, one of the idea might be to create unique neuroprotective coating with antibacterial properties.

In this work, the electroactive matrix based on poly(3,4-ethylenedioxypyrrole) (PEDOP) with immobilized drug (tetracycline) was obtained via electropolymerization process. The matrices have been extensively studied by electrochemical methods, UV-Vis spectroscopy, IR spectroscopy and SEM microscopy. The antimicrobial properties were assessed with *E. coli* strain by SEM microscopy observation and LIVE/DEAD assay. Simultaneously, the obtained layers were evaluated with the use of a model rat neuroblastoma B35 cell line. The cytotoxicity of the tested matrices were assessed (MTT test) based on the metabolic activity of the cells. The cytometer were used to assess cell cycles and apoptosis.

The obtained results provide a solution to challenges associated with implantable neural electrodes through the development of a conducting polymer coating possessing high conductivity and biocompatibility towards neural tissue.

Acknowledgments

This work was supported by National Science Centre in Poland in the framework of SONATA program (2016/23/D/ST5/01306).

* Corresponding author, e-mail: *Dominika.Czerwinska-Glowka@polsl.pl*

10.7 Natural polysaccharides as a potential viscosity modifier of nebulization drugs: preliminary studies on sodium hyaluronate

Katarzyna Dobrowolska[*,1], Tomasz R. Sosnowski[1]

1 Faculty of Chemical and Process Engineering, Warsaw University of Technology, Warsaw, Poland

Keywords: *viscosity modifier*, *atomization*, *potential drug excipient*, *aerosol properties*, *sodium hyaluronate*.

Sodium hyaluronate (HANa) is a well-known natural polysaccharide valued in the bioengineering field for its biocompatible, moisturizing and rheological properties. Due to these properties, it can be also considered as a viscosity modifier excipient of nebulization drugs. As a result of atomization process in an inhaler, nebulization drugs are converted to aerosol, that is delivered to the respiratory tract. The efficiency of the therapy depends on aerosol quality which determines drug deposition in the lungs. Aerosol properties may be improved either due to changes of inhaler construction or by modification of the physicochemical properties of the drug formulation.

The aim of this work is to investigate the potential application of natural polysaccharides as a viscosity modifier in the medicine formulation. This study presents the preliminary data regarding the rheological characteristics of biopolymer solutions and the properties of aerosol generated in a medical jet nebulizer. Flow curves and viscosity analysis of solutions were obtained from oscillatory rheometer. The quality of the emitted mists was evaluated by measuring droplet size distribution and output rate, using laser diffraction and gravimetric method, respectively.

The results shows that the presence of HANa in aqueous samples, especially at concentrations higher than 0.1%, visibly modifies their viscosity, whereas the addition of sodium chloride plays the specific role in this process. By combined measurements of rheological properties and the performance of the selected jet nebulizer (aerosolization rate, aerosol characteristics) it was possible to obtain a deeper understanding of atomization process itself and its usefulness in a better drug targeting during inhalation.

Acknowledgements

This work was supported by National Science Centre project No. 2019/33/N/ST8/01181.

[*] Corresponding author, e-mail: *Katarzyna.Dobrowolska.dokt@pw.edu.pl*

10.8 Effect of liquid properties and aerosol dilution conditions on the final droplet size of aerosol delivered from nebulizers

Katarzyna Dobrowolska[*,1], Małgorzata Matyśkiewicz[1], Tomasz R. Sosnowski[1]

1 Faculty of Chemical and Process Engineering, Warsaw University of Technology, Warsaw, Poland

Keywords: *nebulization*, *droplet size distribution*, *atomization conditions*, *therapeutic aerosol*.

Nebulizers are medical devices, which disperse pharmaceutical liquids to fine droplets for inhalation (aerosol therapy). Such droplets with diameter below 5 µm can penetrate to the lowest parts of human lungs and deposit on the surface of lungs. Deposition areas and hence the efficiency of aerosol therapy are strongly influenced by many factors, i.e.: geometry of the respiratory system, individual respiratory parameters and the properties of aerosol which are related to the physicochemical properties of the liquid drug. Optimization of these parameters and better understanding of their impact on droplet size distribution in the aerosol cloud can improve the effectiveness of the therapy.

The aim of this study was to investigate the influence of: (i) physicochemical properties (i.e., surface tension, viscosity and conductivity) of selected reference liquids, and (ii) properties and amount of external air which dilutes the aerosol during inhalation from nebulizers (i.e. air temperature and humidity) on the characteristics of the aerosol (droplet size distribution and mass output). Aerosol parameters were measured, among others, by laser diffraction with the simultaneous monitoring the external conditions of air admixed to the clouds emitted from jet (Pari Boy) and mesh (Intec Twister) nebulizers.

The results show that the surface tension and viscosity of atomized liquid change the droplet size distribution of aerosol. The principle of operation of a given nebulizer (jet or mesh) also strongly influence the characteristics of aerosol. The effect of diluting was noted.

To conclude, the variation in aerosol parameters measured in this study being the result of liquid properties and different conditions of aerosol dilution, show the importance of tested factors on predicted drug deposition in the lungs. Therefore, these factors should be taken into account in the optimization of drug nebulization process for inhalation therapy.

Acknowledgements

The work was supported by National Science Centre (grant no. 2018/29/B/ST8/00273).

[*] Corresponding author, e-mail: *Katarzyna.Dobrowolska.dokt@pw.edu.pl*

10.9 In-Silico Design of High Affinity Recombinant Antibodies

Mohammed AH Farouq[*,1]

1 Department of Chemical and Process Engineering, University of Strathclyde, Glasgow, Scotland

Keywords: *bioinformatics*, *chemistry*, *biology*, *engineering*, *nanomaterials*.

Nanoparticles with size 1 to 100 nm have large surface to volume ratio, allowing efficient adsorption of drugs, proteins and a variety of other chemical compounds. Consequently, functionalised nanoparticles have various potential applications including imaging and therapeutics. A variety of nanoparticles have been studied, including inorganic materials, bio-polymers and liposomes. Monoclonal antibody (mAb) therapy uses highly specific antibodies to bind to cells or proteins, to stimulate the immune system to destroy or neutralise those components that may be involved in disease progression. This immunotherapy can be optimised using mutated antibody structures to achieve optimal binding to certain cells or proteins, stimulating the immune system to destroy the pathogenic cells. These ideas will be used as a basis to achieve high binding specificity of an antibody structure to a target structure and use this as part of new technology.

The aims are to study the adsorption of Staphylococcal Protein A (SpA) onto inorganic nanomaterials and therefore develop a computational workflow to study these binding interactions. This will develop the initial understanding of protein interactions on inorganic surfaces Au and silica. After this, select candidate antibody structures will be studied for interactions and I will explore immobilisation on nanofilms, or design of a new biosensor/drug delivery technology. The designs will be developed and tested experimentally to find the best performing structures, and these will be evaluated, with the aim to develop new therapy.

Acknowledgments

Paul A Mulheran, Valerie A Ferro, Archie-West HPC, University of Strathclyde. This work was supported by: BBSRC, IBioIC.

[*] Corresponding author, e-mail: *haider.farouq@strath.ac.uk*

10.10 Theoretical model of blood rheology including hemolysis

Krystian Jędrzejczak[*,1], Łukasz Makowski[1], Wojciech Orciuch[1]

1 Faculty of Chemical and Process Engineering, Warsaw University of Technology,Warsaw, Poland

Keywords: *blood rheology*, *hemolysis*, *atherosclerosis*, *CFD*, *DQMOM*.

Mathematical modeling of blood flow in the in vivo environment is a complex issue due to the non-newtonian rheology of blood and the occurrence of hemolysis. As part of this work, a simulation in the ANSYS Fluent software was performed for a model blood vessel with atherosclerotic changes. The blood rheological model based on the work of Buyevich-Kapbsov and the population balance of red cell agglomerates size coupled with hemolysis model was used to create a two-parameter model taking into account the change of the size of blood agglomerates and blood hemolysis in a transient flow.

The population balance was solved using the Direct Quadrature Methods of Moments (DQMOM), that takes into account the agglomeration of red blood cells and their breakage under the shear and turbulent stresses and also hemolysis of red cells. The effective volume fraction changed due to the variable shape factor depending on the size of the agglomerate. Local size distribution of agglomerates direct influences blood rheology and flow.

The theoretical model was implemented in Computational Fluid Dynamics (CFD) code and the simulation was carried out in a conventional blood vessel with cholesterol deposits with the pulsative flow reflecting the typical heart rate.

The rheological parameters of blood and the percentage of blood hemolysis were discussed in comparison with the experimental data of hemolysis depending on the shear rate in the in vitro environment.

Acknowledgements

This study was funded by the BIOTECHMED-1 project of the Warsaw University of Technology under the program Excellence Initiative: Research University (ID-UB).

[*] Corresponding author, e-mail: *Krystian.Jedrzejczak.dokt@pw.edu.pl*

10.11 The influence of the size of yeast cells on the course of the ultrasonic disintegration process

Anna Kacprowicz*,[1], Agnieszka Trawińska[1], Marek Solecki[1]

1 Faculty of Process Engineering and Environmental Protection, Lodz University of Technology, Lodz, Poland

Keywords: *microorganisms*, *disintegration process*, *ultrasound*, *kinetics*.

There are many compounds inside the cells of microorganisms that are used in the food and pharmaceutical industries, as well as in environmental protection. In order to extract them, usually it is necessary to destroy the cellular structure in the process of mechanical disintegration. One of the most commonly used mechanical methods is ultrasonic disintegration. Its mechanism is complex and has not been fully understood, therefore research is being conducted to better understand the nature of the phenomena of this process.

The purpose of the research was to check the influence of the size and shape of yeast cells on the course of the ultrasonic disintegration process. The research material used was baker's yeast *Saccharomyces cerevisiae* manufactured by Lesaffre Polska S.A. Experiments were performed for the concentration of 0.05 g d.w./cm^3. The Verba Cell Ultra Sonic Processor (VCX-500) was used until disintegration. The device was equipped with a spherical-shaped working chamber with a capacity of 100 cm^3. The course of the disintegration process was determined on the basis of the analysis of microscopic images. The number of living cells and their parameters were examined using the Thoma neu chamber under the Olympus BX51 microscope. It was equipped with a CCD digital camera. The ANALYSIS 5 software was used for the performed measurements.

The cell set was divided into size fractions and the kinetics of the ultrasonic cell disruption process was described for them. The results of cell disruption were compared depending on their minimum and mean diameter.

On the basis of the obtained results, the following conclusions can be made: (i) the linear first-order differential equation describes very well the disruption of yeast cells considered as one homogeneous set; (ii) large differences in the size of microorganisms (D min: 1.90–10.94 μm and D average: 2.41–11.89 μm justify dividing the whole set into size classes and considering the process of cell disruption in them; (iii) the first-order linear differential equation also describes very well the course of cell disruption in size classes; (iv) the process rate constant for the largest cell size class is about ten times the rate constant for the smallest cell size class; (v) the mathematical model describes the cell disruption kinetics more preferably for the independent variable Dmean than for Dmin.

* Corresponding author, e-mail: *anna.kacprowicz@dokt.p.lodz.pl*

10.12 Optimization of poly(glycerol maleate) cross-linking process with the use of amines addition

Krzysztof Kolankowski*,[1], Anna Kołakowska[1], Paweł Ruśkowski[1]

1 Faculty of Chemistry, Warsaw University of Technology, Warsaw, Poland

Keywords: *biomaterials*, *glycerol polyesters*, *poly(glycerol maleate)*, *aza-Michael addition*, *cross-linking*.

Recently intensive development of tissue engineering is noticeable. It has caused a considerable rise in scientist's interest in biomaterials, which build scaffolds. Due to that incredibly useful are biocompatible, biodegradable polyesters. Due to a similar structure to well-known poly(glycerol sebacate), poly(glycerol maleate) (PGMal) can be such material. Moreover, PGMal is an α,β-unsaturated polyester, which allows for many chain modifications. One of them is cross-linking by reaction with amines. This modification we consider as modern and innovative.

The experiments aimed to optimize the process of cross-linking poly(glycerol maleate) using amines. Firstly, the usage of triethylenetetramine (TETA), ethylenediamine and piperazine were tested. From them TETA was selected for further experiments. Due to the polymer's high viscosity, it was decided to carry out the optimization in the solvent variant in the presence of tetrahydrofuran. A central, compositional, two-component plan was used to optimize the process. The optimizing value was the degree of conversion, which was calculated basing on 1H NMR spectrum. Its maximization was sought. Obtained products were also characterized using FTIR spectroscopy.

High conversion rates were obtained during this research. The aza-Michael addition turns out to be a valuable reaction for modifying and cross-linking unsaturated polyesters. The amount of amine for modification and cross-linking were both determined via the mathematical model.

* Corresponding author, e-mail: *01123537@pw.edu.pl*

10.13 Synthesis and analysis of polycatecholamines coatings for applications in biotechnology

Daniel Kopeć*,1, Kamil Kopeć[1], Tomasz Ciach[1]

1 Faculty of Chemical and Process Engineering, Warsaw University of Technology, Warsaw, Poland

Keywords: *polycatecholamines*, *coatings*, *polydopamine*.

Polydopamine is a biomimetic polymer which can create a stable coating on virtually any material and attracts interest as a multifunctional biocoating for many biomedical applications. It is known that polydopamine makes the coated surface biocompatible, hydrophilic and can be a base for the covalent attachment of many chemical compounds.

The coatings synthesized by the Fenton reaction from tyrosine, phenylalanine and phenylethylamine were compared with polydopamine coatings prepared by oxidation of dopamine with air oxygen or periodate. The mass, thickness, water contact angle and UV-VIS spectrum of the produced coatings were analyzed.

Our research showed that coatings made of polydopamine and its derivatives show similar UV-VIS spectrum. The Atomic Force Microscopy showed that the thickness of the prepared coatings increases with the synthesis time. We obtained the layers of thickness of 20–100 nm for coating based on polydopamine oxidized with sodium periodate, 5–17 nm for polydopamine oxidized with atmospheric oxygen, 5–24 nm for polytyrosine and 5–8 nm for polyphenylethylamine and polyphenylalanine. A significant reduction in the water contact angle value for all tested coatings was observed. The obtained results suggest that the coatings made of polydopamine derivatives can be successfully applied in Biotechnology.

Acknowledgements

This work was supported by The National Centre for Research and Development in the frame of 2nd joint Polish-South African research projects (contract number: PL-RPA2/05/UROCOAT/2019).

* Corresponding author, e-mail: *daniel.kopec.stud@pw.edu.pl*

10.14 Composite chitosan-human bone granulates for bone tissue regeneration

Piotr Kowalczyk*,1, Rafał Podgórski[1], Michał Wojasiński[1], Grzegorz Gut[2], Witold Bojar[3], Tomasz Ciach[1]

1 Faculty of Chemical and Process Engineering, Warsaw University of Technology, Warsaw, Poland
2 Department of Transplantology, Medical University of Warsaw, Warsaw, Poland
3 Dental Clinic Witold Bojar, Warsaw, Poland

Keywords: *bone regeneration*, *chitosan*, *cellular scaffolds* .

Regeneration of lost bone is necessary after fractures and resections, most often caused by cancer, when diseased tissue is removed. Human bone is ideal for replacing lost tissue, however the procedure of autografting is highly morbid and risks complications. A large focus of tissue engineering is placed on materials which can emulate the human bone – polymers, ceramics, composites of those, both: natural and synthetic origin.

The primary objective of these materials is to support the growth of cells, blood vessels, and new, regenerated bone tissue. We have developed a granulate composed of β-tricalcium phosphate, pulverized human bone and biopolymer – chitosan, a highly potent compound applied in tissue engineering, regenerative medicine and biotechnology. For repair of bone losses, granulation allows easy application and formation of an interconnected porous structure.

The granulate was obtained with gelation of chitosan in alkaline pH, dissolved in acetic acid beforehand and added to the coagulation bath with an encapsulator. Additives (10% β-TCP or 5% β-TCP and 5% human bone) were suspended in the dissolved polymer and formed together as a composite material. The obtained granulates were freeze-dried and sterilized with an autoclave. Granulates were contacted with L929 cells and proven non-cytotoxic via XTT assay. MG63 cells were seeded on the surface of prepared materials, and within 2 weeks, they have entirely colonized the surface of composite materials, opposed to pure chitosan. Alkaline phosphatase activity after 2 weeks was increased in the composites with human bone compared to these with β-TCP only.

A chitosan/β-TCP/human bone composite material with better osteoinductive properties than chitosan/β-TCP composite was prepared and described. The prepared granules are also suitable for autoclave sterilization, which is a very convenient alternative to other methods of implant sterilization (gamma rays, ethylene oxide, or ethanol soaking).

* Corresponding author, e-mail: *piotr.kowalczyk.dokt@pw.edu.pl*

10.15 Pre- and probiotics as raw materials for cosmetic products

Anna Łętocha*[,1], Elżbieta Sikora[1]

1 Faculty of Chemical Engineering and Technology, Cracow University of Technology, Cracow, Poland

Keywords: *skin microbiome*, *probiotics*, *prebiotics*, *cosmetic ingredients*.

Human skin is a complex ecosystem, colonized by wide variety of bacteria, fungi and viruses known as the skin microbiome or *Stratum microbium* (SM). Skin microbiome plays crucial roles in the skin health, among others it protects skin against pathogenic microbes. Any disruption in the SM can cause an inflammation, irritation, skin dryness or some dermatitis, e.g. atopic dermatitis.

Recently, the influence of different factors, such as using of cleansing and daily skin care products, on the skin microbiome balance are discussed. The necessity to use SM-friendly raw materials or addition to the cosmetics formulations pre- or/and probiotic ingredients is emphasized and become the subject of scientific research.

The problem is especially important in the current situation, in the era of Coronavirus, where the requirement of cleansing and disinfecting hands is one of the elements of the sanitary regime, and the products used effectively cleanse the skin, removing from its surface, apart from pathogenic microorganisms, also components of the skin microbiome.

Pre- and probiotic substances have been successfully used for years as ingredients in dietary supplements. According to the generally accepted definition established by FAO/WHO "probiotics are live microorganisms which when administered in adequate amounts confer a health benefit on the host". In the case of cosmetics, these terms are used more widely. In order to use live bacteria in cosmetic products, preservatives should be omitted, what is very difficult from the products safety point of view and the requirements for cosmetic formulations (Regulation No. 1223/2009). As an effect, in the case of beauty care products, inactivated microbes or their metabolic byproducts are used most often than living microbes. Generally, probiotic cosmetic ingredients are divided into: fermentation products, cell lysates and raw materials obtained after tyndalization.

In the work, the current state of knowledge on the skin microbiome and pre-/probiotic raw materials used in cosmetic formulations is presented.

* Corresponding author, e-mail: *anna.letocha@doktorant.pk.edu.pl*

10.16 Fibrous scaffolds from biodegradable polymers for nerve and muscle tissue regeneration

Łopianiak Iwona*[,1], Beata Butruk-Raszeja[1], Michał Wojasiński[1], Tomasz Ciach[1]

1 Faculty of Chemical and Process Engineering, Warsaw University of Technology, Warsaw, Poland

Keywords: *aligned fibers*, *solution blow spinning*, *biodegradable polymers*, *scaffolds functionalization*, *polydopamine*.

Obtaining an ideal scaffold has been a long-term challenge for researchers. The main problem is the differentiation of individual cells and tissues, which makes it impossible to create a universal scaffold. This work aimed to develop fibrous scaffolds from biodegradable polymers for nerve and muscle tissue regeneration.

We produced nano- (~500 nm) and microfibrous (1–2 μm) scaffolds from three medical grade biodegradable polymers (PLLA, PLGA, PCL) by solution blow spinning technique. What is more, we produced random and aligned fibers materials for every type of polymer and fiber diameter. Next, we coated fibers with polydopamine and functionalized with peptide. Fiber diameter, pore size, material porosity, and fiber arrangement were investigated based on SEM images of produced and modified materials. We compared modified and unmodified material's mechanical properties using Instron 3345 equipment. Spectroscopic analysis and wettability measurement before and after modifications were also conducted.

The change of collector speed rate allows obtaining homogeneous oriented (aligned) fibers in solution blow spinning process. Materials with homogenous oriented fibers have sustain lower mechanical load than materials with non-aligned (random) fibers. Coating fibers with polydopamine increased their hydrophilic and mechanical properties. Spectroscopic analysis confirmed the successful attachment of the peptide on the material's surface.

Produced scaffolds with aligned fibers are biodegradable, biocompatible, and hydrophilic. Successful materials functionalization with polydopamine and peptide will help to grow well organized and elongated cells in further research.

Acknowledgments

This work was supported by the National Centre for Research and Development in the frame of Project "Scaffolds for Guided Neural and Muscle Tissue Regeneration – GuideTiReg" PL-TW/VI/4/2019.

* Corresponding author, e-mail: *iwona.lopianiak.dokt@pw.edu.pl*

10.17 Silicon/Indigoid-dye hybrid heterojunction near infrared photodetector operating at room temperature

Karolina Miszczyszyn[*,1,2], Wojciech Domagała[1], Mieczysław Łapkowski[1], Michał Dłubek[2]

1 Department of Physical Chemistry and Technology of Polymers, Silesian University of Technology, Gliwice, Poland
2 FIBRAIN Sp. z o.o., Zaczernie, Poland

Keywords: *photodetector*, *organic electronics*, *indigoid*, *indigo dyes*, *infrared spectroscopy*.

Near infrared photodetectors are widely utilized in many applications, including optical fiber telecommunication, imaging and quality control systems. Nowadays, commercially available detectors are based on relatively expensive and environmentally unfriendly inorganic materials (group III-V compounds). An interesting alternative could be hybrid devices made of silicon enhanced with a thin layer of novel organic semiconductors.

In this work, a prototype silicon/organic heterojunction infrared photodetector operating at room temperature is presented. The photodetector was manufactured by depositing a thin layer of organic material on the p-Si substrate in the hot-wall epitaxy process, followed by evaporating aluminium electrodes on top of the layer. As organic materials, custom synthesized indigo dye derivatives were used.

The devices were subjected to 1.55 μm wavelength laser illumination, and their current – voltage characteristics measured. The results show that the Al/p-Si/Indigoid-dye/Al heterostructure demonstrates rectifying behaviour and photovoltaic effect at room temperature.

Acknowledgements

This work was carried out in the framework of the first edition of the "Doktorat Wdrożeniowy" programme ran by the Ministry of Science and Higher Education, Poland.

[*] Corresponding author, e-mail: *Karolina.Miszczyszyn@polsl.pl*

10.18 Electrospun polyaniline and polyethylene oxide nanofibre sensor for detection of biogenic amines in meat products

Ingrida Pauliukaitytė[*,1], Lauryna Dabašinskaitė[1], Edvinas Krugly[1], Dainius Martuzevičius[1]

1 Faculty of Chemical Technology, Kaunas University of Technology, Kaunas, Lithuania

Keywords: *biogenic amines*, *polyaniline*, *sensor*, *nanofibers*, *electrospinning*.

The formation of biogenic amines in the meat products are one of the first signs of food spoilage. This may happen because of improper product storage conditions, microbiological contamination during the packaging, or simply due to the natural maturation. Biogenic amines not only reduce the organoleptic properties of products but also are harmful to human health because of their toxicity. The quality of meat may be assessed using sophisticated techniques, but faster and cheaper ways to detect spoiled food products are important for the efficient shelf-life control.

We have developed a Polyaniline and Polyethylene oxide nanofiber sensor, which is sensitive to biogenic amines (such as Cadaverine, Spermine, Putrescine, Spermidine) resulting from the decarboxylation of specific free amino acids. In the polyaniline-polyethylene oxide sensor matrix, polyaniline works as a sensing material and reacts with Cadaverine, resulting in a color changing reaction visible to the naked eye. The sensor matrix has been developed using electrospinning technique. The experimental variables related to materials (types of polymers and their concentration, as well as solvent ratio) and electrical process (tip-to-collector distance and voltage, as well as duration of spinning to achieve stable and solid sensor that could be applied and tested on food) were researched. The obtained matrix has been characterized for its morphology (Scanning Electron Microscopy analysis) and reactivity to pure Cadaverine vapour.

The simplicity of the Polyaniline-Cadaverine reaction is a key of a cheaper and faster way to detect formation of biogenic amines and prevent possible poisoning with the spoiled meat products, by installing directly in the packaging of the meat products.

[*] Corresponding author, e-mail: *ingrida.pauliukaityte@ktu.edu*

10.19 Characteristic of polymeric biomaterials formed at the human body temperature

Katarzyna Pieklarz*,1, Zofia Modrzejewska[1], Michał Tylman[2]

1 Department of Environmental Engineering, Faculty of Process and Environmental Engineering, Lodz University of Technology, Lodz, Poland
2 PGE GiEK S.A., Bełchatów, Poland

Keywords: *biopolymers*, *biomaterials*, *chitosan*, *hydrogel*, *tissue engineering*.

Currently, polymeric biomaterials are an integral part of the solutions used in modern medicine. They ensure the restoration of the functions of damaged tissues or organs and facilitate the process of convalescence in people after injuries and diseases. The numerous literature reports indicate that systems based on biopolymers, mainly chitosan, are of particular importance. This compound is a polysaccharide resulting from the alkaline deacetylation of chitin, carried out with the use of hydrated alkali, mainly NaOH. In chemical terms, the polymer has three types of reactive functional groups: an amino group, and primary and secondary hydrogen groups, respectively in the C-2, C-3, and C-6 position.

This paper presents a study on chitosan hydrogels formed at the human body temperature, developed for potential application in biomedical engineering. The experiments were carried out for two types of biomaterials: chitosan chloride gels and chitosan lactate gels.

Structural properties of the obtained systems have been studied by FTIR spectra. The crystallinity of hydrogels structure was determined by X-ray diffraction analysis (XRD) and polarizing microscopy.

The FTIR spectra of gels exhibited a characteristic band at 3600–3100 cm^{-1} (–OH group), band at 2950 –2850 cm^{-1} (stretching vibrations in the aliphatic groups ($-CH_2$ and $-CH_3$), 1660 and 1600 (C=O stretching in the primary amide) and 1520 cm^{-1} ($-NH_2$ bending in the secondary amide). Both XRD method and polarizing microscopy demonstrated that the chitosan lactate gels are practically amorphous, while the chloride gels contain crystalline phases.

In conclusion, these results present a simple method to produce thermosensitive chitosan hydrogels which can be an interesting material as a drug carrier and as a material for scaffolds in biomedical engineering.

* Corresponding author, e-mail: *katarzyna.pieklarz@edu.p.lodz.pl*

10.20 Production and properties of micro-porous polymer-ceramic scaffolds for 3D printing bone implants

Rafał Podgórski*,1, Michał Wojasiński[1], Tomasz Ciach[1]

1 Faculty of Chemical and Process Engineering, Warsaw University of Technology, Warsaw, Poland

Keywords: *3D printing*, *bone implants*, *micro-porosity*, *cytotoxicity*.

Osteoarthritis, osteoporosis and bone damage are some of the most disruptive diseases to afflict human mobility. The most common approach is the implantation of artificial, metal, or ceramic implants or bone from another donor. The better option would be to use biodegradable materials, which can use the organism's natural regeneration forces to heal damaged tissue. 3D printing techniques can deliver such materials tailored to each patient. In this work, we present a method of producing polymer or polymer-ceramic filament for obtaining 3D printed scaffolds with micro-porous structure.

To obtaining a polymer-ceramic filament production method, polycaprolactone polymer (PCL), β-tricalcium phosphate (β-TCP) were chosen as model materials, and polyethylene glycol (PEG) was selected as a porous-making agent. PCL was dissolved in dichloromethane and mixed with β-TCP and PEG. Solutions of polymers and ceramic were poured on the flat glass bed and dried at 40 °C The obtained polymer-ceramic foils were melted at 100°C in a stainless-steel container, pressed through a nozzle, and cooled into filaments with 2.85 mm diameter. Filaments were used to 3D print simple scaffolds in ZMorph VX commercial 3D printer. Produced scaffolds were washed in distilled water for removing PEG, and obtained micro-porous structures were evaluated by scanning electron microscopy (SEM) and in vitro culture with MG63 human cell line.

The presented method gave flexible and resilient filaments containing PCL, β-TCP, and PEG, useful in commercial 3D printers and can be used to print 3D objects. SEM images of printed scaffolds show microporous polymer structure with evenly deployed ceramic particles on a surface. Furthermore, materials obtained in this way have good printing precision and show low cytotoxicity. These results open up a path for fast and cheap production of micro-porous 3D printed implants.

* Corresponding author, e-mail: *rafal.podgorski.dokt@pw.edu.pl*

10.21 Silicon/Indigoid-dye hybrid heterojunction near infrared photodetector operating at room temperature

Szonja P. Pósa[1,2], Gyula Dargó[1], Szilárd Tóth[2], Lilla Hámori[2], Péter Huszthy[1], József Kupai[*,1]

1 Department of Organic Chemistry and Technology, Budapest University of Technology and Economics, Budapest, Hungary
2 Institute of Enzymology, Research Centre for Natural Sciences, Budapest, Hungary

Keywords: *cytotoxicity*, *multidrug resistance*, *P-glycoprotein*, *organocatalyst*, *cinchona alkaloids*.

The success of chemotherapy in the treatment of progressive, advanced stage cancers is often set back by one of the most common mechanisms of resistance, namely multidrug resistance (MDR). The mechanism of multidrug resistance is often related to the increased expression of drug efflux pump proteins located in the cell membrane. P-glycoprotein (ABCB1, MDR1, Pgp) is a key member of the ABC family transporters, as this pump is primarily associated with drug resistance during chemotherapy.

The primary focus of our research was on cinchona alkaloid derivatives, a powerful class of organocatalysts, whose bioactivity was characterized in an in vitro co-culture model involving a parental and a multidrug-resistant human uterine sarcoma cell line. In addition to characterizing the cytotoxicity of the tested compounds and the selectivity of the antiproliferative effect on tumor cells, the aim of our scientific work was also to determine the attack strategy that could potentially be exploited to combat MDR when it comes to speaking about organocatalysts. To this end, we used a fluorescent protein-based cytotoxicity assay designed for the study of the given chemical function (Pgp inhibition, Pgp bypass, MDR selectivity). Our results may contribute to setting a new trend in the use of organocatalysts while providing the pharmaceutical industry with deeper information on the bioactivity and toxicity of the families of compounds used for catalytic reactions. The best IC50 values we measured with a cinchona-thiourea derivative containing ethyl substituent at position 3 of quinuclidine moiety was 1.22 µM for MES-mCh, and 1.30µM for Dx5-eGFP cell lines.

Acknowledgements

This work was supported by the János Bolyai Research Scholarship of the 128473), and the ÚNKP-20-5-BME-322 New National Excellence Program of the Ministry of Human Capacities.

[*] Corresponding author, e-mail: *jkupai@mail.bme.hu*

10.22 Osteogenic potential of the gel -derived bioactive glasses doped with zinc, strontium and cerium on NHOst cells

Szymon Salagierski[*,1], Barbara Zagrajczuk[1], Michał Dziadek [1,2], Elżbieta Menaszek[3], Katarzyna Cholewa-Kowalska[1]

1 Faculty of Materials Science and Ceramics, AGH University of Science and Technology, Cracow, Poland
2 Faculty of Chemistry, Jagiellonian University, Cracow, Poland
3 Faculty of Pharmacy, Jagiellonian University, Cracow, Poland

Keywords: *bioglass*, *osteoinductive properties*, *in vitro*.

Bioactive glasses is a group of ceramic materials used for the bone tissue regeneration. Their composition can be easily modified to obtain specific properties. The aim of this study was synthesis of bioglasses modified with zinc, strontium and cerium and evaluation of their osteogenic potential in vitro.

Various glasses from two systems – A2 (40% SiO_2, 54% CaO, 6% P_2O_5, % mol) and S2 (80% SiO_2, 16% CaO, 4% P_2O_5, % mol) modified with Zn, Sr and Ce in concentrations up to 15% mol were obtained by the sol-gel method. Initial cellular response in vitro was assessed using the fibroblasts Hs680 to select most promising modifiers concentrations. In vitro osteogenic potential of the obtained materials was carried out on the human osteoblast cells (NHOst). For the NHOst cells the following characteristics have been evaluated: proliferation, metabolic activity, alkaline phosphatase (ALP) activity, osteocalcin and osteopontin proteins concentration and mineralization.

The proliferation study indicated that NHOst cells have proliferated preferably on the materials containing bioglasses doped with Sr and Zn. The evaluation of the ALP activity showed that the highest levels were obtained by materials based on zinc-bioglasses, while the highest mineralization level was detected for materials with Sr-doped bioglasses. Moreover, strontium addition positively influenced the production of both osteocalcin and osteopontin by NHOst cells, while zinc increased production of osteocalcin.

Based on the obtained results of this research and the conclusions drawn from them it was found that zinc and strontium exert the most favorable effect among the analyzed modifiers on NHOst cells.

Acknowledgements

This work was supported by the National Science Centre Poland Grant no. 2017/25/N/ST8/01593, 2019/32/T/ST5/00453 and 2017/27/B/ST8/00195.

[*] Corresponding author, e-mail: *ssalagierski@gmail.com*

10.23 Studies on properties of CsA-LG monolayers on water subphase

Klaudia Szafran[*,1], Małgorzata Jurak[1], Santiago Martin[2], Agnieszka Ewa Wiącek[1], Agata Ładniak[1], Kacper Przykaza[1]

1 Faculty of Chemistry, Department of Interfacial Phenomena, Maria Curie-Skłodowska University, Lublin, Poland
2 Instituto de Nanociencia y Materiales de Aragón (INMA), CSIC-Universidad de Zaragoza, and Departamento de Química Física, Facultad de Ciencias, Universidad de Zaragoza, Zaragoza, Spain

Keywords: *Langmuir monolayer*, *lauryl gallate*, *cyclosporine A*.

To obtain high-quality films deposited onto solid support it is extremely important to study the miscibility and morphology of monolayers at the air/water interface. In our research cyclosporine A (CsA) and lauryl gallate (LG) were applied. CsA is strong immunosuppressant widely used in medicine, including prevention of transplant/implant rejection. But it causes many side-effects, which are associated with reactive oxygen species, to lipid peroxidation-damage of cell membrane integrity. To reduce these undesirable effects the antioxidant-LG was used. LG is the most active derivative of gallic acid and can protect phospholipids from peroxidation.

Surface pressure-area per molecule (π-A) isotherms were obtained by means of Langmuir technique. Proper volume of solutions was spread onto water subphase and after solvent evaporation the monolayer was symmetrically compressed. At the same time the surface potential (SP) was measured by vibrating plate method. In addition, morphology of monolayers was examined by Brewster angle microscopy (BAM). In addition, the stability of monolayers was obtained as changes of the surface pressure in time.

Research proved that we obtained stable monolayers. They were miscible, and there was no phase separation-BAM images did not show any domains. SP exhibited that during compression the molecules orientation was changed. These studies showed that monolayers can be deposited onto solid support to obtain more biocompatible implant surface.

Acknowledgement

Małgorzata Jurak acknowledges the National Science Centre in Poland for partial funding the studies in the framework of the project "Comprehensive physicochemical studies of multi-component films: phospholipid-immuno -suppressant-antioxidant on liquid or solid support", no. 2019/03/X/ST4/01470.

* Corresponding author, e-mail: *klaudia.wozniak@poczta.umcs.lublin.pl*

10.24 Studying the Langmuir-Blodgett monolayers deposited onto solid support

Klaudia Szafran[*,1], Małgorzata Jurak[1], Santiago Martin[2], Agnieszka Ewa Wiącek[1], Agata Ładniak[1], Kacper Przykaza[1]

1 Faculty of Chemistry, Department of Interfacial Phenomena, Maria Curie-Skłodowska University, Lublin, Poland
2 Instituto de Nanociencia y Materiales de Aragón (INMA), CSIC-Universidad de Zaragoza, and Departamento de Química Física, Facultad de Ciencias, Universidad de Zaragoza, Zaragoza, Spain

Keywords: *Langmuir-Blodgett monolayer*, *cyclic voltammetry*, *quartz crystal microbalance*.

Integration of implants with the tissue depends on the immune response of the organism, which is mainly determined by the degree of biocompatibility of the material with cells. One of the ways to improve biocompatibility is to modify the implant surface with a biocompatible living tissue layer of the desired physicochemical properties. In this aspect, there is a need for the preparation and characterization of multicomponent Langmuir films. The quartz crystal microbalance (QCM) method estimate the mass of the deposited film, while cyclic voltammetry (CV) determines the homogeneity of layers and the presence of holes and defects. These methods allow to design the highest quality layer that can be deposited onto solid support.

To modify the properties of a solid surface, the Langmuir monolayers of biologically active substances were deposited. Firstly, the best miscible films of well-defined ratios were chosen. Then, qualities of the obtained Langmuir-Blodgett (LB) films were analysed using various techniques.

To estimate the mass of deposited films and support coverage, the quartz QCM was used. QCM measurements showed that for all compounds we obtained monolayers. Experimental mass was smaller than the theoretical one, which evidenced that all compounds deposited onto QCM substrate did not form strictly packed LB films and their molecules were inclined. This can be related to defects in the monolayers. To confirm this, CV was used. CV data showed that in the middle of solid support the LB films were more packed than those in the ends of the plates. The more compact was the monolayer, the smaller number of defects was obtained.

* Corresponding author, e-mail: *klaudia.wozniak@poczta.umcs.lublin.pl*

10.25 Influence of selected inhalation drugs on dynamic physicochemical properties of a pulmonary surfactant model

Justyna Szczepańska[1], Katarzyna Dobrowolska[*,1], Tomasz R. Sosnowski[1]

1 Faculty of Chemical and Process Engineering, Warsaw University of Technology, Warsaw, Poland

Keywords: *pulmonary surfactant*, *dynamic surface tension*, *surface rheology*, *air-liquid interface*, *inhalation drugs*.

Pulmonary surfactant (PS) is a thin lipoprotein complex covering the whole alveolar surface. One of its main features is the ability to reduce surface tension at the air-liquid interface during the breathing cycle. Pulmonary surfactant works as a natural barrier impeding the particle penetration deeper into the human body, what is crucial in the terms of different kinds of molecules deposition in the lower respiratory tract. Physicochemical properties of the pulmonary surfactant are involved in the elimination of deposited particles (e.g. dust particles, but also inhaled therapeutic aerosols). Thus, it is necessary to investigate whether inhaled aerosols, including drugs, have any negative impact on both structure and physicochemical properties of PS, including its ability to adsorb at the air-liquid interface inside the alveoli.

The aim of this work was to investigate the impact of three different inhalation anti-asthmatic drugs at various concentrations on the pulmonary surfactant model under dynamic conditions simulating the breathing cycle, and then to analyze these results in terms of surfactant physiology. The measurements were conducted with a pendant drop technique using a profile analysis tensiometer PAT-1M. This method enabled studying the surface tension both at constant interfacial area and also during breathing-like surface oscillations for tracking the changes in the surface rheological properties. Additionally, surface tension hysteresis for all the samples was determined. Comparison of this hysteresis allowed to detect disturbances in the interfacial dynamics, which might help to identify abnormalities in the functioning of PS.

The changes of the interfacial properties such as the surface tension and the dilatational rheological parameters of the gas-liquid interface (dilatational elasticity and viscosity) were detected and this enabled drawing certain conclusions regarding the influence of different inhaled therapeutics on the dynamic surface properties of the PS. These interactions largely depend on the type of drug, the inhaled dose (i.e. final concentration in the system), as well as on the whole composition of the inhaled therapeutic formulation that may contain additional surfactants.

Acknowledgments

This work was supported by the National Science Centre, project No. 2019/33/N/ST8/01181.

[*] Corresponding author, e-mail: *katarzyna.dobrowolska.dokt@pw.edu.pl*

10.26 The antioxidant potential of multifunctional bioactive glasses doped with cerium, strontium and zinc

Barbara Zagrajczuk[*,1], Szymon Salagierski[1], Michał Dziadek[1,2], Kinga Dziadek[3], Patrycja Janowska[1], Elżbieta Menaszek[4], Katarzyna Cholewa-Kowalska[1]

1 Faculty of Materials Science and Ceramics, AGH University of Science and Technology, Cracow, Poland
2 Faculty of Chemistry, Jagiellonian University, Cracow, Poland
3 Faculty of Food Technology, University of Agriculture in Cracow, Cracow, Poland
4 Faculty of Pharmacy, Jagiellonian University, Cracow, Poland

Keywords: *bioactive glasses*, *antioxidant biomaterials*, *cell cultures*.

Recently, the antioxidant potential has become one of the most desirable features of the biomaterials. Aim of the presented study was to characterize how incorporation of cerium, strontium and zinc affect antioxidant potential of bioactive glasses in vitro and relate it with their material determinants such as solubility and structural characteristic.

The sol-gel derived ternary SiO_2 - CaO – P_2O_5 system glasses with two various CaO/SiO_2 ratios (A2 and S2 glasses) were doped with CeO_2, SrO and ZnO up to 15% mol. Bioglass powders were dedicated to detailed structural characteristics, and to solubility study, through powders incubation in UHQ-water. Antioxidant properties of glasses were tested in two ways: by determining their Radical Scavenging Capacity in ABTS test and by assessing their impact on the macrophages cell culture (RAW 264.7 cell line).

Due to the ABTS test A2 type glasses indicated higher antioxidant activity in comparison with S2 ones. Moreover, addition of strontium and cerium amplified antioxidant activity of studied glasses at most. In the cell culture studies doping bioglasses with strontium and zinc improved proliferation and metabolic activity, while doping them with strontium and cerium helped to reduce ROS (reactive oxygen species) number.

Not only doping with cerium may improve antioxidant performance of the gel-derived bioactive glasses, similar or even better effect may be obtained by incorporation of strontium.

Acknowledgements

This work was supported by the National Science Centre Poland Grants no. 2017/25/N/ST8/01593, 2019/32/T/ST5/00453 (BZ) and 2017/27/B/ST8/00195 (KCK).

[*] Corresponding author, e-mail: *b.zagrajczuk@gmail.com*

11 Abstracts: Apparatus, separation processes & Environmental protection, alternative energy sources

11.1 MoS_2/CNMs hybrid nanostructures for photo-electrocatalytic applications

Zuzanna Bojarska*[,1], Marta Mazurkiewicz-Pawlicka[1], Łukasz Makowski[1]

1 Faculty of Chemical and Process Engineering, Warsaw University of Technology, Warsaw, Poland

Keywords: *molybdenum disulphide*, *carbon nanomaterials*, *micromixers*, *photocatalysts*, *tribological properties*.

Designing and manufacturing new nanostructures with improved properties using modern techniques is a tempting prospect for nanotechnology. Molybdenum disulphide (MoS_2) is a widely used 2D nanomaterial. MoS_2 found various applications such as a dry lubricant, in catalysis, hydrogen storage, and others. MoS_2 can be an excellent candidate for being combined with carbon nanomaterials (CNMs) to obtain new hybrid nanostructures with outstanding properties including higher photo- and electrocatalytic activity.

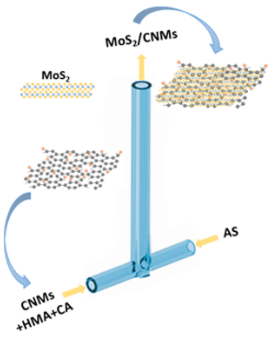

The aim of the conducted research was the preparation of hybrid nanostructures formed from MoS_2 and CNMs such as graphene oxide, reduced graphene oxide, and carbon nanotubes. The nanostructures were synthesized in a continuous flow reactor. Physicochemical analysis of obtained materials was carried out, using various analytical techniques: FTIR spectroscopy, thermo-gravimetric analysis, X-ray diffraction, Raman spectroscopy, and scanning electron microscopy. Furthermore, the obtained materials were analysed in a photo-electrochemical system for further application in catalysis.

Synthesis of hybrid nanocomposites MoS_2/CNMs in the continuous flow reactor is a proper method allowing to easily obtain product with desired properties. The conducted research has shown that the addition of CNMs to MoS_2 promote the charge transport of MoS_2, due to their high electrical conductivity and large surface area.

Acknowledgments

This work was supported by the National Science Centre (No. 2017/27/B/ST8/01382) and the Excellence Initiative – Research University (No. 1820/11/Z01/POB5/2020).

* Corresponding author, e-mail: *zuzanna.bojarska.dokt@pw.edu.pl*

11.2 Research of rapeseed oil qualitative characteristics with IR spectroscopy

Roman Chyzhovych*[,1], Oleksandr Ivashchuk[1], Semen Khomyak[2], Yevhen Semenyshyn[1], Tetiana Kuzminchuk[1], Anna Hlukhaniuk[1], Roman Zherebetskyi[3]

1 Department of Chemical Engineering, Lviv Polytechnic National University, Lviv, Ukraine
2 Department of Technology of Biologically Active Substances, Pharmacy and Biotechnology, Lviv Polytechnic National University, Lviv, Ukraine
3 Department of Organic Products Technology, Lviv Polytechnic National University, Lviv, Ukraine

Keywords: *extraction*, *rapeseed oil*, *qualitative composition*, *IR spectroscopy*.

Previous studies of rapeseed oil samples obtained by extraction, refractometry and UV-Vis spectroscopy showed some differences in the results, depending on the sample obtaining method (the degree of the raw material grinding – fractions of 0.2 mm, 0.5 mm, 1.0 mm and a mixture of crushed seeds). With this in mind, the extracted oil was analyzed with IR spectroscopy to confirm and clarify the previous conclusions.

The study was done on the IR spectrophotometer SPECORD M80 (Carl Zeiss Jena) in thin films. For each sample of rapeseed oil, a spectrum in the range from 400 to 4000 cm^{-1} was obtained. Integration time: 1 second; slit width: 12, wave number accuracy: 0.2 cm^{-1}, photometric accuracy: ± 0.2% T.

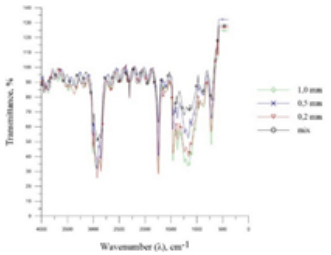

The results of studies of oil samples on the IR spectrometer are presented as the dependence of the transmittance on the wavenumber.

The obtained IR spectra showed the presence of alkyl residues of triglycerides – the main components of vegetable oils, as evidenced by peaks with the wave numbers close to 2900 cm^{-1}. The main differences in absorption are present mainly for the groups $-C=O$ (1700 cm^{-1}) and $-C-O$ (1200 cm^{-1}).

* Corresponding author, e-mail: *roman.chyzhovych.mnxt.2020@lpnu.ua*

11.3 Comparison of physical and chemical activation of tyre pyrolysis char

Tomasz Kotkowski[*,1], Robert Cherbański[1], Eugeniusz Molga[1]

1 Faculty of Chemical and Process Engineering, Warsaw University of Technology, Warsaw, Poland

Keywords: *end-of-life tyres,pyrolysis,physical activation,chemical activation.*

Nowadays, the growth of the amount of end-of-life tyres (ELTs) is observed because of perpetual development of motorization. ELTs cannot be reused on vehicles anymore. Moreover, the storage of them on landfills is banned in Europe. One of the possible methods of the ELT recycling is pyrolysis, which gives the following products: gas, oil, char and steel.

The char activation develops its porous structure. It is necessary to receive high – quality adsorbent.

In this work, the physical and chemical activations of the char were carried out. Then, the samples were characterized and the results compared.

For physical activation, a thermobalance TG 209 F1 Libra (Netzsch, Germany), equipped with a micro furnace and a precise ultra-microbalance, was used. On the basis of the experimental results, the optimal conditions (temperature and time) for this activation were found. Then, this process was carried out in an electric, horizontal laboratory furnace (Czylok, type PRW 55/1200M, Poland) to scale up the process. Also, the chemical activation of char with KOH as an activating agent was carried out in the same laboratory furnace.

The physically and chemically activated chars, non-activated char and activated carbon (reference material) were characterized using nitrogen adsorption at 77K. The isotherms were determined by using the 3Flex Surface Characterization Analyzer (Micromeritics, USA). On the basis of the isotherms the BET surface area and pore size distribution were calculated. In sum, the porous structure of the physically and chemically activated chars were compared.

The results indicate that the BET surface area is higher for the chemically activated char. The largest BET surface area for physically activated char equals 256 m^2/g while for chemically activated char it equals 669 m^2/g. The samples are mostly microporous.

* Corresponding author, e-mail: *tomasz.kotkowski@pw.edu.pl*

11.4 Investigating flow and power input of viscoelastic fluids in a stirred tank

Alexander Maywurm[*,1], Markus Kolano[1], Matthias Kraume[1]

1 Chair of Chemical & Process Engineering, Technical University Berlin, Berlin, Germany

Keywords: *mixing*, *stirred tank*, *rheology*, *viscoelasticity*.

Stirring processes involving viscoelastic fluids are present in food industry, polymer industry and biotechnology, e.g. in xanthan fermentation, polystyrol production or fermentation of substrate in biogas processes. The DFG funded project "Mixing of fluids with viscoelastic flow behavior in stirred tanks" aims to find basic principles that relate complex rheological properties to mixing characteristics.

Shear thinning aqueous polymer solutions, glucose syrup based Boger fluids and wormlike micellar solutions serve as transparent viscoelastic model fluids. Their characterization is conducted with an Anton Paar MCR 302 rotational rheometer and an Anton Paar DMA density meter. The fluid's flow in a flat-bottom 20 L stirred tank at low Reynolds numbers is examined with phase triggered 2D3C Particle Image Velocimetry (equipment by Lavision GmbH) using fluorescent particles (microParticles GmbH) to obtain a spatially resolved three-dimensional flow field. Power input at different stirring speeds is obtained via torque measurements (DR-2112, Lorenz Messtechnik GmbH). The data is complemented with down-scale experiments in a 1 L stirred tank recording the power input with a HAAKE Viscotester VT550.

In terms of secondary flow, three different flow regimes are identified: elasticity dominated, transition flow, and inertia dominated. Other qualitative phenomena are presented and discussed as well as quantitative results. Finally, different approaches of dimensional analysis are applied to connect the complex rheological properties of viscoelastic fluids to their mixing characteristics.

Acknowledgements

Funded by the Deutsche Forschungsgemeinschaft (DFG – German Research Foundation). We thank Mohamed El-Khatib, Kübra Kabakci and Joshua Soyke for their assistance with the experiments.

* Corresponding author, e-mail: *alexander.maywurm@tu-berlin.de*

11.5 About Solid Recovered Fuel: chemical characteristics and role in waste management system

Inna Pitak[*,1], Gintaras Denafas[1,2], Rita Kriukiene[1]

1 Laboratory of Materials Research and Testing, Lithuanian Energy Institute, Kaunas, Lithuania
2 Department of Environmental Technology, Kaunas University of Technology, Kaunas, Lithuania

Keywords: *SRF*, *characteristics*, *separation*, *system*, *economy*.

Solid Recovered Fuel (SRF) is a fuel produced from non-hazardous waste in accordance with EU standards for SRF, especially EN15359. It may be produced from the advanced processing of combustible fractions of non-hazardous materials recovered from municipal solid waste (MSW), commercial and industrial waste (C and IW) and construction and demolition waste (CDW), such as paper, cardboard, wood, textiles and plastics.

Processing takes place in mechanical-only or mechanical-biological treatment (MBT) plants. SRF is therefore quality assured fuel, and should not be confused with the term "refuse-derived fuel" (RDF).

RDF is generated through the separation of waste, often with the mere aim of obtaining a fraction of the Waste to energy plant. Production of SRF is complementary to recycling. SRF production, as it does not stand on its own, will never compete with recycling.

A main advantage of SRF is that it provides for flexible use of the calorific value in waste. SRF is stored and shipped as fluff or pellets. It is used in those places where there is an actual need for fuel and where there is an actual demand for heat. SRF is used in combustion processes that are designed to generate heat and/or power. The efficiency of such processes is high.

Data on the current production and use of SRF are difficult to obtain. The concept of standardization is not yet well applied during the practice.

In this study the chemical characteristic of SRF obtained from RDF are presented: volatile matter, moisture, ash content and fixed carbon. We cannot put an "equal sign" between SRF and RDF because it has different meanings by chemical characteristics.

[*] Corresponding author, e-mail: *Inna.Pitak@lei.lt*

11.6 Ecological study of a mineral carbon capture and conversion process

Wanawam Pragot[*,1], Maria-Ara Carballo-Meilan[1], Waheed Afzal[1]

1 Chemical & Materials Engineering, School of Engineering, University of Aberdeen, Aberdeen, UK

Keywords: *carbon capture and utilisation (CCU)*, *mineral carbonation*, *life cycle analysis (LCA)*,*NaOH*, *precipitated calcium carbonate (PCC)*.

The rise in carbon dioxide emissions is creating environmental problems of unprecedented magnitude and impact. Current total global emissions of CO_2 from the fossil chemical use and industrial chemical processes are 38 GT CO_2-eq per year with growth rate of 2.7 % during past decade. Due to COVID-19 pandemic and its impact, a temporary decrease in the global emissions is expected. Carbon capture and utilization (CCU) strategies can aid a potential mitigation option for the reduction of greenhouse gas emissions.

This study presents a mineral CCU process that employed flue gas and an alkaline solution to develop an integrated absorption-based carbon removal and conversion process and then used an ion exchange reaction by using available brines to produce a useful form of precipitated calcium carbonate (PCC). Furthermore, this study compared the environmental impact of proposed mineral carbonation process with other three mineral CCU processes reported in the literatures; mineral carbonation processes from; 1) fly ash from power plants, 2) mineral wollastonite rock ($CaCO_3$), and 3) steel slag using life cycle assessment (LCA) provided in ISO 14044. The LCA was investigated using gate to gate (G-G) system boundary and 1 kg of $CaCO_3$ product as functional unit for comparison.

Results indicate that the PCC carbon capture technology using four different materials has a positive environmental impact. NaOH-based process has the lowest land use and water depletion impacts but it has the second largest global warming potential (GWP) within four options studied here due to NaOH solvent identified as the process hot-spot. The fly ash-based PCC has the highest environmental impact due to the process waste (direct emission), raw materials used and the energy consumption. The $CaSiO_3$ and steel slag-based PCC have comparable low toxicity impact as low chemical consumption and the waste generation in the process capture system. The overall environmental impact of carbon capture into PCC indicated that while mineral CCU presents long-term carbon sequestration potential and scalable markets but all of the processes studied here are far from being carbon negative.

Acknowledgements

This work was financial supported by The Royal Embassy of Thailand.

[*] Corresponding author, e-mail: *r02wp17@abdn.ac.uk*

11.7 CFD analysis of mass transport mechanism in porous SOFC electrode

Monika Sikora[*,1], Marcin Błesznowski[2,3], Wojciech Orciuch[1], Łukasz Makowski[1]

1 Faculty of Chemical and Process Engineering, Warsaw University of Technology, Warsaw, Poland
2 Institute of Power Engineering – Research Institute, Warsaw, Poland
3 Center for Hydrogen Technologies (CTH2), Institute of Power Engineering, Warsaw, Poland

Keywords: *SOFC*, *mass transport*, *CFD*, *modelling*, *Knudsen diffusion*.

As Mahatma Gandhi used to say, constant development is the law of life. Constant development and population growth increase the demand for energy. Finite fossil fuels resources and deteriorating quality of air is the strong motivation to modernize the energy sector which should base on environmentally and energy efficient technologies. Noteworthy are Solid Oxide Cells (SOC), which distinguish high electrical efficiency in Solid Oxide Fuel Cell mode (over 58%), high rate of fuel conversion in the electrochemical reaction and near-zero greenhouse gases emissions.

Nowadays, SOFC technology is in pre-commerce phase where a lot of effort is put to increase the generated power and extend the lifetime. This work concerns computational fluid dynamics (CFD) modelling of diffusion transport mechanism in porous anode in order to examine limiting factors of mass transport throughout porous media at high temperature conditions. Various mathematical models of diffusive mass transport were investigated. Finally, Dusty Gas Model was taken into consideration and implemented in Fluent solver. This work presents the numerical analysis validated by laboratory tests. Experiments were performed using SOFC's electrodes which were produced in the Institute of Power Engineering in Poland.

Obtained results indicate that the most appropriate mathematical model of gas diffusion in porous media at high temperature and in the regime of significant concentration gradients of the gaseous components is Dusty Gas Model. Experiments and simulations results demonstrate satisfactory compliance. The maximum relative error of the computational method does not exceed 15%. The numerical analysis reveals the risk of uneven use of catalyst surface due to the rapid loss of hydrogen kinetic energy and further displacement of hydrogen with steam - the product of electrochemical reaction. It was proven that consideration of Knudsen diffusion coefficients emphasises the difference between diffusion rates of hydrogen and steam throughout the porous electrode. It is worth noting that slower steam diffusion to the flow channel in the worst scenario may lead to its adsorption on porous surface and blockage of reaction sites.

Acknowledgements

This work was financially supported by the National Science Centre, Poland, Grant No. 2016/23/N/ST8/01580.

* Corresponding author, e-mail: *monika.jalowiecka.stud@pw.edu.pl*

11.8 Computational Fluid Dynamics modeling of a direct fuel cell with a novel channel design

Monika Sikora[*,1], Zuzanna Bojarska[1], Artur Małolepszy[1], Łukasz Makowski[1]

1 Faculty of Chemical and Process Engineering, Warsaw University of Technology, Warsaw, Poland

Keywords: *CFD*, *modelling*, *DFAFC*, *PEMFC*.

Fuel cells are electrochemical devices used for converting high-energy materials such as hydrogen, methanol, or formic acid into usable power. All fuel cells are based on the spatial separation of oxidation and reduction reactions. The proper fuel cell operation depends on the selection of appropriate process parameters, such as temperature, pressure, flow rate of reagents, and the renewal of the interface of the catalyst. An important, but often overlooked parameter is the selection of proper hydrodynamic conditions in the system. This is particularly important due to the prevailing laminar flow regime, which significantly slows down the mass transfer. For this reason, it becomes necessary to modify the channel geometry used in fuel cells to equalize the reagent concentrations.

The main objective of this study is i) to determine the impact of geometry and process parameters of fuel cell operation with PEMFC proton polymer electrolyte using CFD computational fluid mechanics, and ii) to propose innovative channel geometric solutions. In order to perform model calculations, ANSYS Fluent Software was used.

A number of calculations were done for a range of inlet velocities, and various reagents concentrations. The tests also include verification of the results obtained in a prototype direct formic acid fuel cell (DFAFC). The obtained results have shown that the best-operating conditions of the DFAFC are: the formic acid concentration of 3 M and fuel flow of 1 ml/min. Furthermore, the new proposed geometry of the channel allows increasing the efficiency of electricity production.

Acknowledgements

This work was supported by the Excellence Initiative – Research University, ENERGYTECH-1 (Energy Conversion and Storage) [1820/29/Z01/POB7/2020].

* Corresponding author, e-mail: *monika.jalowiecka.stud@pw.edu.pl*

11.9 MOF-Al_2O_3 composites for catalytic applications

Alexandru Sonica[*,1], Oana Grad[2], Alex Turza[2], Sebastian Porav[2], Maria Mihet[*,2]

1 Faculty of Chemistry and Chemical Engineering, Babes-Bolyai University, Cluj-Napoca, Romania
2 National Institute for R&D of Isotopic and Molecular Technologies – INCDTIM, Cluj-Napoca, Romania

Keywords: *MOF-alumina composites*, *impregnation*, *thermal stability*, *selectivity*.

Metal-organic frameworks (MOFs), a class of compounds resulted from the connection by moderate coordination bonds of inorganic secondary building units (metal ions or clusters) with organic linkers, are highly versatile compounds due to their exceptionally high surface area, tunable porous structure, or structural diversity. The unique physical and chemical properties of MOFs make them suitable for various applications, such as adsorption, storage and separation of gases, catalysis, etc. Catalytic applications of MOFs are especially interesting due to the diversity of catalytic functionalities which can be introduced in precise locations of the MOF. However, due to their large porosity and low density, the mechanical and thermal stability of MOFs is quite low, so that their use as heterogeneous catalysts is quite troublesome. Thus, shaping of MOFs is highly desirable in order to take advantage of their unique properties in catalysis.

The aim of this work is to report the immobilization of MOFs on alumina pellets in order to obtain MOF-Al_2O_3 composites with enhanced thermal and mechanical properties, and preserving the special catalytic properties of the MOF. MIL-101 and MIL-53 are two MOF structures which can be obtained starting from the same equimolar mixture of terephtalic acid and $CrCl_3$ in water, using different temperatures and water contents. Immobilization of these two MOFs was pursued following two strategies: (a) crystallization of MIL-101/MIL-53 directly on the Al_2O_3 pellets immersed in the reaction mixture, or (b) formation of MIL-101/MIL-53 on previously impregnated Al_2O_3 pellets with the necessary amount of $CrCl_3$. The influence of reaction temperature, water content, or reactants ratio was investigated in order to obtain either MIL-101-Al_2O_3, or MIL-53-Al_2O_3 composites, which were characterized by powder X-ray diffraction, specific surface area determination, thermogravimetric analysis and electron microscopy.

Acknowledgments

This work was supported by a grant of the Romanian Ministry of Education and Research, CNCS-UEFISCDI, project number PN-III-P1-1.1-TE-2019-1447, within PNCDI III.

[*] Corresponding author, e-mail: *alexandru.sonica@stud.ubbcluj.ro*
[*] Corresponding author, e-mail: *maria.mihet@itim-cj.ro*

11.10 The comparison of the performance of nanofiltration and reverse osmosis in reducing the salinity of M'rirt water (Morocco)

Noureddine Zouhri[*,1], Mestapha Tahaikt[1], Mahacine El Amrani[1], Mohamed Taky[1], Mahmoud Hafsi[2], Azzedine Elmidaoui[1]

1 Laboratory of Separation Processes, Department of Chemistry, Faculty of Sciences, Ibn Tofail University, Kenitra, Morocco
2 International Institute for Water and Sanitation, National office of Electricity and Potable water (ONEE-IEA), Rabat, Morocco

Keywords: *sodium reverse osmosis*, *nanofiltration*, *desalination*, *Spiegler-Kedem model*.

M'rirt is a small Moroccan mountain town. The drinking water of M'rirt comes from Oum Errabia river, with a salinity of 2140 µs/cm conforming to Moroccan standards but the sodium content exceeds Moroccan standards and also those of the World Organization for Health (WHO).

Diseases associated with sodium deficiency in humans are very rare. However, sodium excess can cause acute health problems and long-term effects. Acute effects and death have been reported in the event of an accidental overdose of sodium chloride. Acute effects may include dryness of the mucous membranes, a violent inflammatory reaction and ulceration of the gastrointestinal tract.

In order to reduce sodium concentration and improve the quality of the drinking water for the population, the National Office for Water and Electricity (ONEE) and Ibn Tofail University have collaborated to study and compare the performance of nanofiltration and reverse osmosis in reducing the salinity of M'rirt water.

Demineralization rates of 34 %, 62 %, 92 %, 98 % and 98.5 % and rejection rates of sodium ion of 16 %, 17 %, 81 %, 98 % and 99 % were achieved respectively for the NF270, TR60, NF90, TM710 and BW30LE membranes.

On the other hand, Spiegler-Kedem model was applied to determine the constants of the model, namely the reflection coefficient and the coefficient of permeability for all the membranes. A good agreement between the experimental release rates and the model release rates was obtained. In addition, the Hermia model was applied to identify the fouling mechanisms for the five membranes tested. Cake-like fouling was found.

Acknowledgments

This work was supported by ONEE Co. (Morocco) and TIA Co. (France). The authors express their thanks for this support.

[*] Corresponding author, e-mail: *noureddinezouhri1981@gmail.com*

11.11 Generation of sulfuric acid and sodium hydroxide from the sodium sulphate salt by electro-electrodialysis (EED)

Noureddine Zouhri[*,1], Said Ait Habzize[1], Mahacine El Amrani[1], Mohamed Taky[1], Azzedine Elmidaoui[1]

1 Separation Process Laboratory, Department of Chemistry, Faculty of Science, Ibn Tofail University, Kenitra, Morocco

Keywords: *electro-electrodialysis*, *sodium sulphate*, *sulfuric acid*, *sodium hydroxide*.

The electro-electrodialysis process (EED) is used to generate H_2SO_4 and NaOH from sulphate sodium salt Na_2SO_4. The key phenomenon limiting the current efficiency of this process is the proton leakage through the anion selective membrane was not observed.

The electro-electrodialysis was carried out with a three-compartment cell with two platinum-coated titanium electrodes separated by three compartments. The couple membrane used in this work is AFN and CMX. The experiments were carried out for four current densities 8.33 mA cm^{-2}, 11.11 mA cm^{-2}, 13.88 mA cm^{-2} and 27.77 mA cm^{-2}.

For each current density, a voltage variation of cell and concentrations of H_2SO_4 and NaOH in the two compartments with the current density was used. The concentration of H_2SO_4 and NaOH increases with current density and with time, but higher for NaOH. The current efficiency increases with the current applied to the cell.

The request for the electro-electrodialysis operation power was calculated in terms of the electrical energy consumed to produce H_2SO_4 and NaOH for 6 hours of electro-electrodialysis and it was found floating with the current applied and concentration sodium sulphate used and the concentration of H_2SO_4 and NaOH products, but is comparable for both initial concentrations of sodium sulfate.

Acknowledgments

This work was supported by TIA Co. (France). The authors express their thanks for this support.

[*] Corresponding author, e-mail: *noureddinezouhri1981@gmail.com*

12 Abstracts: Material Engineering

12.1 Aerobic biodegradation of xenobiotics: degradation profiles of selected analgesic drugs in wastewater

Bishnu Bhattarai[*,1]

1 School of Engineering, University of Aberdeen, Aberdeen, United Kingdom

Keywords: *biological process*, *biodegradation*, *wastewater treatment*.

Several industries including pharmaceutical and agricultural, often produce waste containing xenobiotics. Analgesics and nonsteroidal anti-inflammatory drugs (NSAIDs) are an emerging group of xenobiotics and have been noticed in various environmental conditions, including wastewater. Furthermore, household and service applications like personal care compounds, steroid hormones and fluorinated detergents are further contributors of xenobiotic pollution. They may be removed from different effluents using various physical/chemical processes (for example activated carbon adsorption, catalytic oxidation and incineration). For the removal of organic xenobiotics from wastewater, their biodegradation and removal during aerobic digestion is an exciting area of the research with a little work done in the past. The potential advantages of the biodegradation process are: its ability to convert xenobiotic compounds into nontoxic products such as carbon dioxide and new biomass, and it is relatively low in cost. Many xenobiotics have been found to be biodegradable as sole carbon and energy in pure culture.

The general aim of this is to investigate the process conditions that favour the biodegradation of xenobiotics with open mixed cultures in the aerobic biodigester. The preliminary results shown in this work include batch experiments with xenobiotics at different concentration and different biomass concentration along with the biodegradation profiles in terms of time, dissolved oxygen and COD. Similar studied are undergoing in a sequencing batch reactor (SBR). Further work includes the impact of micronutrients on the process. We also study batch experiments with and without co-substrate (example yeast extract and peptone) and with and without previous biomass acclimation. This research investigates the effects of parameters in a continuous process (such as, substrate concentration, sludge retention time, acclimation of the microorganisms and medium composition) on the biodegradation of paracetamol.

Acknowledgements

This work was supported by Dr Waheed Afzal and Dr Davide Dionisi.

[*] Corresponding author, e-mail: *r01bb18@abdn.ac.uk*

12.2 Microstructure of the combined nano/microscale fibers for medical application

Ewa Dzierzkowska[*,1], Przemysław Żmuda[2], Anna Ścisłowska-Czarnecka[3], Kamil Kornaus[4], Ewa Stodolak-Zych[1]

1 Department of Biomaterials and Composites, AGH University of Science and Technology, Cracow, Poland
2 Department of Biocybernetics and Biomedical Engineering, AGH University of Science and Technology, Cracow, Poland
3 Department of Cosmetology, Academy of Physical Education, Cracow, Poland
4 Department of Ceramics and Refractories, AGH University of Science and Technology, Cracow, Poland

Keywords: *electrospinning*, *meltblown*, *tissue engineering*, *skin regeneration*, *polylactic acid*.

Scaffold for skin regeneration should possess both nanometric architecture and optimal porosity. Nanoscale architecture reflect the structure of the natural extracellular matrix and the optimal porosity enhance cell infiltration into the material. This condition could be fulfilled by combination of microfibers and nanofibers supplied by electrospinning and meltblown technique.

We present the preparation of polylactic acid (PLA, 3251D, Nature Works) fibers obtained with electrospinning and meltblown technique. Prior electrospinning, spinning solution was prepared by dissolving PLA in dichloromethane (DCM, Avantor) and dimethylformamide (DMF, Avantor). Morphology was characterized used the scanning electron microscope (NOVA NANO SEM 200). Physicochemical properties of the surface: wettability, surface energy was tested using a goniometer (DSA 25 Kruss). The porosity of the manufactured membranes was determined by gravimetric method and mercury perimetry (PoreMaster 60, Quantachrome). Furthermore, the cross-section microstructure of combined scaffold was observed using hematoxylin and eosin staining methods.

Nano/microfiber combined scaffold was successfully produced using two manufacturing methods. No additional bonding was necessary. The materials provide a larger pore diameter while providing multiple sites for cell attachment and proliferation.

Acknowledgments

This study was funding for subsidy of AGH University of Science and Technology, Faculty of Materials Science and Ceramics.

[*] Corresponding author, e-mail: *dzierzkowska@agh.edu.pl*

12.3 Structural features of P_2O_5–Fe_2O_3–FeO–CaO glasses

Paweł Goj*,1,Paweł Stoch[1], Małgorzata Ciecińska[1]

1 Faculty of Materials Science and Ceramics, AGH University of Science and Technology, Cracow, Poland

Keywords: *Raman spectroscopy*, *FT-IR spectroscopy*, *molecular dynamics*, *structural studies*.

The glasses which contain mainly P_2O_5, SiO_2, CaO and Na_2O are called bio-glasses witch create chemical bonds witch tissues. This glass can be used as bone implants. The Ca^{2+}, PO_4^{3-} ions coming from glass provide nucleation centres for the crystallization of hydroxy-carbonate apatite (HCAp) layer on a surface of material. The surface of HCAp layer bound to proteins and mucopolysaccharides contained within tissues. Therefore, glasses from P_2O_5–Fe_2O_3–CaO system can be used as bone implants. Also, P_2O_5–Fe_2O_3–CaO glasses are non-toxic, bio-chemically and biomechanically compatible. The phosphate glasses with a high content of Fe_2O_3 (about 30 mol. %) have good chemical resistance. Therefore, can be used in immobilization low-level radioactive waste (LLW) incineration ash of high content of CaO and heavy metals. Unfortunately, there is no complete description of the structure of these glasses in the literature.

The glasses of composition (100-x)(30 Fe_2O_3–70 P_2O_5)-xCaO mol. % where x=10, 20, .., 40 were the subject of the studies. The structural properties have been determined using experimental methods like FTIR, Raman spectroscopy. The experimental results were compared to molecular dynamics theoretical investigation.

Increasing content of CaO causes an increase of Fe(II)/Fe_{tot} ratio and depolymerization of iron phosphate glass network. The P-O-Fe(III) and P-O-Fe(II) linkages in glass network are more resistant to Ca^{2+} than P-O-P. Ca^{2+} accumulates mainly in voids around phosphorus creates $[PO_3]$–O^- Ca^{2+} ^-O–$[PO_3]$ connections. The quantity of non-bridging oxygens increases with increasing content of CaO. It suggests that Ca^{2+}–O^{2-}–Ca^{2+} bounds and large voids where Ca_2^{+} can be accumulated are possible at high content of CaO. This explains the high structure capacity of these glasses on CaO (in standard preparation method up to 40 mol. % of CaO).

Acknowledgements

This work was supported in part by PL-Grid Infrastructure and National Science Centre Poland (grant number 2017/27/B/ST8/01477). PG has been partly supported by the EU Project POWR.03.02.00-00-I004/16

* Corresponding author, e-mail: *pgoj@agh.edu.pl*

12.4 Structural and thermal properties of strontium iron-phosphate glasses

Paweł Goj*,1, Paweł Stoch[1], Małgorzata Ciecińska[1]

1 Faculty of Materials Science and Ceramics, AGH University of Science and Technology, Cracow, Poland

Keywords: *Raman spectroscopy*, *FT-IR spectroscopy*, *DSC analysis*, *structural studies*.

Iron phosphate glasses because of excellent chemical durability and lower transformation temperature than silicate can be considered as a matrix for vitrification of radioactive wastes. Also, these glasses have melting temperature 100-200K lower than borosilicate. This leads to a reduction of processing temperature, which is important to avoid excess radionuclide volatilisation. One of the main fission short-lived product is ^{90}Sr. It is source of β-radiation. The effect of strontium on thermal properties is quite important for technological reasons.

The subject of studies was (100-x)(30 Fe_2O_3–70 P_2O_5)–*x* SrO mol.% glasses, where x = 10, 20, ..., 50. The thermal properties have been identified using DSC analysis. The composition of glasses was checked using the XRF and amorphous character using XRD technique. Structural investigations have also been carried out using Raman and FT-IR spectroscopy.

From the DSC curves were determined glass transformation (Tg) and crystallization (Tc) temperatures. Additionally, heat capacity accompanying the glass transformation (ΔCp) was evaluated. The glass transformation decreases with increase in the content of SrO up to 30 mol. % and then increase. This suggests structure rebuilding for 30 mol. % content of SrO. Spectroscopic studies showed that as the SrO content increases, the number of Q^2 structural units decreases and the number of Q^1 and Q^0 units increases.

Acknowledgements

This work was supported by National Science Centre Poland (grant number 2017/27/B/ST8/01477). PG has been partly supported by the EU Project POWR.03.02.00-00-I004/16.

* Corresponding author, e-mail: *pgoj@agh.edu.pl*

12.5 Structural and textural properties of Cu-doped bioactive glasses

Kinga Halastra[*,1], Barbara Zagrajczuk[1], John Griffin[2], Valerie Seymour[2], Mark E. Smith[2], Rafał Baran[3], Magdalena Zarzecka-Napierała[1], Katarzyna Cholewa-Kowalska[1], Michał Dziadek[1,4]

1 AGH University of Science and Technology, Cracow, Poland
2 Lancaster University, Lancaster, United Kingdom
3 European Synchrotron Radiation Facility, Grenoble, France
4 Jagiellonian University, Cracow, Poland

Keywords: *bioactive glass*, *therapeutic ions*, *angiogenesis*, *antibacterial activity*.

Bioactive glasses (BGs) are one of the most attractive biomaterials for bone tissue engineering which can be used as effective carriers for therapeutic ions. Among them, copper (Cu) has drawn great attention as it shows high antibacterial and angiogenic activities. Understanding the dissolution behavior of biologically active ions (Si, Ca, P, Cu) from BGs structure is the key to control their biological properties. In order to be able to model and predict the behavior of bioactive glasses it is important to identify their structural and textural properties and factors affecting them.

The Cu-doped BGs from the basic SiO_2–CaO–P_2O_5 system were produced using melt-quenching and sol-gel techniques. CuO was substituted for CaO in the amounts of 1-5 mol%. S2 and A2 groups of glasses, with the CaO/SiO_2 molar ratio varied between 0.20 and 1.35 were obtained. Glasses were analyzed using ^{29}Si and ^{31}P MAS-NMR (magic angle spinning-nuclear magnetic resonance), XPS (X-ray photoelectron spectroscopy) and XANES (X-ray absorption near edge structure), and BET (Brunauer-Emmett-Teller nitrogen adsorption/desorption) methods. The materials were incubated in simulated body fluid (SBF) and deionized water (DW) for 14 days. ICP-OES (inductively coupled plasma optical emission spectrometry) technique was used to evaluate changes in the concentration of the ions in incubation media.

The results clearly indicated that both synthesis route and CaO/SiO_2 ratio strongly affected structure of base glasses, including i.a. the type and/or the relative contributions of Q^n(Si) and Q^n(P) structural units, and thus network connectivity. The introduction of Cu ions into the structure of glasses leads to further changes. XPS and XANES spectroscopies showed different valance state and/or oxygen coordination number of Cu in glasses. The base and modified glasses showed significantly different specific surface areas. Significantly, both variables used were crucial factors affecting the solubility of ions (Si, Ca, P, Cu) from the glasses during incubation in SBF and DW.

Acknowledgements

This work was supported by the National Science Centre, Poland Grant no. 2019/32/C/ST5/00386 (MD).

* Corresponding author, e-mail: *halastra@student.agh.edu.pl*

12.6 Synthesis, optimization and characterization of iron oxide nanoparticles obtained by co-precipitation method

Simona Halmagyi[*,1], Lucian C. Pop[1,3], Kata Saszet[2,3]

1 Faculty of Chemistry and Chemical Engineering, Babeș-Bolyai University, Cluj-Napoca, Romania
2 Faculty of Physics, Babeș-Bolyai University, Cluj-Napoca, Romania
3 Institute of Interdisciplinary Research in Bio-Nano Sciences, Babeș-Bolyai University, Cluj-Napoca, Romania

Keywords: *iron oxide nanoparticles*, *co-precipitation method*, *heterogeneous photocatalysis*, *magnetism*, *synthesis optimization*.

Iron oxide nanoparticles, magnetite (Fe_3O_4), maghemite (γ–Fe_2O_3) and hematite (α-Fe_2O_3) synthesis is possible via co-precipitation method. This is a facile and convenient approach because of the high yield, the low cost, the simplicity of the method which allows few glassware and lab equipment to be used and it's easily reproducible.

However, the method presented above has its own limitations. The obtained particles are highly dependent on the reaction parameters (temperature, pH, ionic strength, and others). The size, the crystal structure, the morphology, the optical properties, the magnetism and the composition of the nanoparticles were characterized using XRD (X-ray diffraction), SEM (scanning electron microscopy), DRS (diffuse reflectance spectroscopy) and Raman spectroscopy.

Magnetite and maghemite have ferromagnetic proprieties which provide them with high importance in nanotechnology by using them as magnetic support for recyclable photocatalysts. For this reason their physical properties along with the proportion in which they are obtained are necessary to be well controlled during the synthesis. The pH and the temperature influence the oxidation process of the precursors into magnetite, maghemite and hematite. Hence, the reaction parameters were adjusted for the optimization of the process.

Acknowledgments

This work was supported by the PN-III-P1-1.1-TE-2019-1318 project.

* Corresponding author, e-mail: *msimona.halmagyi@stud.ubbcluj.ro*

12.7 Photoluminescence properties of carbon nanoparticles synthesized by laser ablation in water and aqueous solutions of amine-based reagents

Agata Kaczmarek[*,1], Jacek Hoffman[1], Adrian Okołowicz[2], Artur Małolepszy[2]

1 Department of Experimental Mechanics, Institute of Fundamental Technological Research, Polish Academy of Sciences, Warsaw, Poland
2 Faculty of Chemical and Process Engineering, Warsaw University of Technology, Warsaw, Poland

Keywords: *pulsed laser ablation in liquids*, *carbon nanoparticles*, *optical properties*.

The comparison between two synthesis routes for obtaining carbon nanoparticles (CNPs) in water and in aqueous solutions of amine-based reagents is presented. The influence of synthesis approach and parameters on structural and luminescent properties of CNPs is discussed.

Each of the synthesis routes was a two-step process. In the first approach, the graphite target submerged in water was ablated using moderate fluence of a laser beam. Next, a certain amount of aqueous reagent solution was added to the suspension of carbon particles. Such a mixture was then exposed to a much stronger laser beam in order to reduce the size of particles. In contrast to the first approach, during another synthesis route the graphite target was immersed in aqueous reagent solution and exposed to laser irradiation. The obtained suspension of carbon nanoparticles was further irradiated without the presence of graphite target.

Luminescence and absorbance studies revealed interesting properties of obtained colloids. Suspension of particles produced in pure water after first step is yellowish and has some absorbance in whole spectrum rising as the wavelength decreases. After second step it is colourless and fully transparent in visible light and has high absorbance in UV with distinct maximum about 285 nm. The addition of the reagent at the second step of the synthesis leads to location of absorbance maximum at about 285 nm. However, using amine-based solution from the beginning causes high absorbance in the whole spectrum without any distinctive maximum. It may indicate the simultaneous creation of different carbon structures and fluorescent molecules during laser ablation process.

Acknowledgements

The research was financed by National Center for Research Development, project LIDER/33/0117/L-9/17/NCBR/2018.

* Corresponding author, e-mail: *akaczmar@ippt.pan.pl*

12.8 Corrosion resistance of spinels with different $MgO:Al_2O_3$ molar ratio in contact with steel slag

Jakub Ramult[*,1], Karina Warmuz[1], Ryszard Prorok[1], Dominika Madej[1]

1 Faculty of Materials Science and Ceramics, Department of Ceramics and Refractories, AGH University of Science and Technology, Cracow, Poland

Keywords: *refractories*, *corrosion*, *spinel*, *steel slag*, *microstructure*.

The steel industry requires continuous improvement of castables quality. Spinel has a significant influence on the properties of castables. The main phenomena causing degradation of the refractory material is slag corrosion. It results from the difference of chemical substances between slag and refractory material. The stoichiometric spinel $MgAl_2O_4$ is the only stable compound in the MgO-Al_2O_3 system that melts congruently at 2105 °C. It has excellent corrosion resistance as well as a high melting point. Among other things, these properties mean that it is used in used castables, for example in the metallurgical industry for lining thermal devices or steel ladles. Spinel tends to replace both aluminum and magnesium cations with other cations of similar size, while maintaining electrochemical balance. Spinel undergoes structural changes in contact with slag. For example, chromium ions can replace aluminum ions in the spinel structure, while iron ions can replace both aluminum and magnesium ions in the spinel structure. Crystalline lattice vacancies may arise. The low-melting phases formed in contact with the slag also have a negative impact.

The aim of the study was to determine the effect of MgO content in the spinel on the corrosion resistance of the tested spinels. The study was carried out with the use of industrial slag, on three samples differing in spinel stoichiometry: MgO-rich spinel, stoichiometric spinel and Al_2O_3-rich spinel. The corrosion resistance was verified on the basis of tests using the contact method. Using the SEM-EDS technique, the microstructure of the tested samples after corrosion was determined. Based on the pictures of the sample cross-sections and calculations made in the MATLAB calculation program, the corrosion coefficient IC was determined. An XRD analysis of the tested samples was also performed. Spinel rich in MgO is characterized by higher sinterability and is strongly resistant to basic slags.

Acknowledgements

This study was founded by The National Centre for Research and Development within the framework of LIDER VIII project No.LIDER/5/0034/L8/16/NCBR/2017.

* Corresponding author, e-mail: *jramult@agh.edu.pl*

12.9 A determination of difference in hydration kinetics of binary mixtures with the MgO:Al_2O_3 micro- or nano-powders

Karina Warmuz*,[1], Jakub Ramult[1], Ryszard Prorok[1], Dominika Madej[1]

1 Faculty of Materials Science and Ceramics, Department of Ceramics and Refractories, AGH University of Science and Technology, Cracow, Poland

Keywords: *nanostructured materials*, *long term investigation*, *hydrotalcite*, *cement-free binder*, *refractories*.

Mg-Al layered double hydroxides (LDH's) are commonly known anionic clay which is a promising hydraulic binder component for refractory ceramics materials. The Mg-Al hydrotalcite $Mg_6Al_2CO_3(OH)_{16} \cdot 4H_2O$ is a product of the reaction of reactive Al_2O_3 and MgO nano or micro- powders with excess water. Additionally can be obtained synthesized using various methods like: mechanochemical synthesis, sol-gel synthesis and hydrothermal precipitation. The structure of these materials is similar to brucite $Mg(OH)_2$ and consist of positively charged brucite-like layers $[Mg_{1-x}Al_x(OH)_2]^{x+}$ with disordered opposite charged interlayers $[CO_{x/2}{}^2 \cdot nH_2O]^{x+}$. Is commonly known that some Mg^{2+} and Al^{3+} ions can dissolve in gibbsite or boehmite and brucite respectively. Due to this fact LDH's can have a wide range of stoichiometry.

The recent findings from the literature reveal that the kinetic and mechanism of the hydration is influenced by the degree of homogenization, specific surface area development, degree of packing, type and size of grains of MgO and Al_2O_3 in initial powders. In order to conduct research, three mixtures were composed of: nano-MgO and nano-Al_2O_3, nano-MgO and micro-Al_2O_3, micro-MgO and nano-Al_2O_3 powders with the MgO:Al_2O_3 molar ratio of 1:1 have been prepared. Both initial MgO and Al_2O_3 powders and blended pastes were subjected to thermal stability, phase composition and structure determination. The following research techniques: DSC-TG-EGA, XRD and FT-IR were adopted for this purpose.

The aim of this work was to determine the difference in the hydration products between the blended pastes which contain several forms of magnesia and alumina. We compared results obtained using micro- or nano- powders of Al2O3 and MgO and the research revealed significant difference in the hydration process depending on nano- or micro-powders used.

Acknowledgements

This study was founded by The National Centre for Research and Development within the framework of LIDER VIII project No.LIDER/5/0034/L8/16/NCBR/2017.

* Corresponding author, e-mail: *ktyrala@agh.edu.pl*

12.10 Engineering bismuth based semiconductors properties for enhancement photocatalytic degradation of anticancer drugs

Patrycja Wilczewska*,[1], Patrycja Parnicka[1], Aleksandra Bielicka-Giełdoń[1], Ewa Maria Siedlecka[1]

1 Department of Environmental Technology, University of Gdansk, Gdansk, Poland

Keywords: *photocatalysis*, *bismuth oxybromides*, *anticancer drugs*, *morphology*.

Bismuth-based semiconductors are an unique and promising group of recently developed advanced photocatalytic materials. They have been widely applied in several areas including the generation of H_2 by splitting water, decomposition of organic and inorganic pollutants in both wastewater and polluted air such as CO_2 or NO_x, and organic synthesis through harvesting the energy of light. The electronic structure of bismuth-based semiconductors possess a suitable band gap for visible-light response making them a promising candidate when compared to other metal oxide semiconductors. Bismuth-based compounds can be prepared by various methods such as solid-state reactions, and hydrothermal and solvothermal methods. Samples prepared by different methods exhibit various morphologies and properties, including variable band gap energies.

Aim of presented research were to engineering bismuth based semiconductors $Bi_aO_bBr_c$ properties for highly efficient removal pharmaceuticals (anticancer drugs) from water phase. 5-fluorouracil (5-FU) and imatinib (IMA) were as model contaminants. Morphology and surfaces properties were controlled by various parameters of synthesis (solvents, additives, reaction time and temperature). Prepared photocatalysts characterized in details.

Solvents used in the synthesis were crucial for formation nanoparticles and their photocatalytic activity. Most active samples were prepared in glycerol and degradation efficiency of 5-FU and IMA was enhance for both drugs without metal/nonmetal doping or surface modifications (quantum dots, carbon nanotubes, etc.).

Acknowledgments

This work was supported by National Science Center (grant: MINIATURA 1 DEC-2017/01X/ST5/01136).

* Corresponding author, e-mail: *patrycja.wilczewska@phdstud.ug.edu.pl*

12.11 Visible light-driven selective oxidation of benzyl alcohol to benzaldehyde by bismuth based photocatalysts

Patrycja Wilczewska[*,1], Patrycja Parnicka[1], Aleksandra Bielicka-Giełdoń[1], Artur Giełdoń[2], Ewa Maria Siedlecka[1]

1 Department of Environmental Technology, University of Gdansk, Gdansk, Poland
2 Department of Theoretical Chemistry, University of Gdansk, Gdansk, Poland

Keywords: *photocatalysis*, *selective oxidation*, *benzyl alcohol*, *bismuth*.

Benzaldehyde (BAD) is widely used in fragrance, confectionary and pharmacy industries and is also an important organic reaction intermediate. The traditional synthesis of BAD through oxidation of liquid toluene or hydrolysis of benzyl chloride forms the co-product bromobenzene but involves toxic or corrosive reagents such as chromate, hypochlorite, peroxy acids and other chemicals. Therefore, it is necessary and beneficial to develop a green, highly selective, and environmentally friendly approach to produce BAD under moderate conditions.

The aim of this research is to efficiently obtain benzaldehyde using the heterogeneous photocatalysis under visible light and to evaluate the utilization of bismuth based photocatalysts in presented photoconversion reaction.

Photocatalytic activity was evaluated as selective oxidation of benzyl alcohol into benzaldehyde in presence of various bismuth based photocatalysts (BiOBr, $Bi_4O_5Br_2$, $BiOCl_{0.5}Br_{0.5}$ and $Bi/Bi_4O_5Br_2$). Photocatalytic oxidation tests was performed for 6 hours. In experiments 30 mg ($1\,g\,L^{-1}$) of photocatalyst was dispersed into 30 ml of $0.5\,mmol\,L^{-1}$ benzyl alcohol acetonitrile solution under blue light emitting diode LED irradiation as a light source. Additionally, influence of photocatalysts doses and concentration of benzyl alcohol on photoconversion were examined. BiOBr was demonstrated the highest photocatalytic activity. Bismuth oxyhalides were able to oxidized BA into corresponding aldehyde. Furthermore, optimal condition of conversion benzyl alcohol were $1\,g\,L^{-1}$ concentration of photocatalyst and $1.5\,mmol\,L^{-1}$ BA.

[*] Corresponding author, e-mail: *patrycja.wilczewska@phdstud.ug.edu.pl*

13 Abstracts: Kinetics, thermodynamics

13.1 Vegan microcapsules to encapsulate peppermint oil

Daniele Baiocco[1], Zhibing Zhang[*,1], Jon A. Preece[2]

1 School of Chemical Engineering, University of Birmingham, Birmingham, United Kingdom
2 School of Chemistry, University of Birmingham, Birmingham, United Kingdom

Keywords: *food-grade*, *microcapsules*, *coacervation*, *micromanipulation*.

Fast-growing food industry has long included many appealing essential oils in food products to meet consumers' need. Among all, the demand for peppermint oil (PO) has recently surged due to its multiple end-use applications and health beneficial properties. Notwithstanding, PO is extremely volatile, and has often been encapsulated for a longer shelf-life. To date, animal-derived ingredients have been extensively employed but there is a growing demand from consumers for solely plant-based ingredients. The present research aims to develop PO-entrapping microcapsules fabricated via complex coacervation using gum Arabic (GA) and fungal chitosan (fCh) as shell precursors.

The encapsulation efficiency (EE) for the oil, and its leakage profile for the microcapsules in several hydroalcoholic environments were quantified by UV-Vis spectroscopy. The morphology of PO-entrapping microcapsules was investigated via bright-field/fluorescent-sensing and scanning/transmission electron microscopy, and the mechanical properties of the shell were characterised using a micromanipulation technique.

Spherical core-shell microcapsules (EE ~ 40%) exhibiting a heterogeneous surface with smooth, dent- and ripple-rich areas were obtained. Moreover, the shell permeability of PO in different hydroalcoholic environments was determined to be 10^{-6}–10^{-5} m s^{-1}.These results suggest that vegan fCh-GA microcapsules with a core of PO can be fabricated, with a potential for more sustainable and friendly end-use applications in food products, such as lozenges and chewing gum. Details of the findings will be presented.

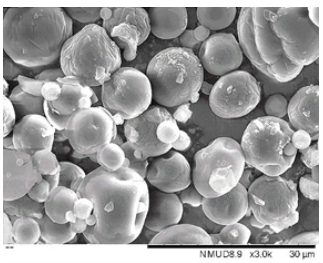

Figure 13.1.1: Vegan PO-entrapping microcapsules with heterogeneous surface properties.

Acknowledgements

This work was supported by EPSRC, UK (Grant number EP/L015133/1).

* Corresponding author, e-mail: *Z.Zhang@bham.ac.uk*

13.2 Activity and kinetics tests of Cu/Zn/Zr-based catalysts for methanol synthesis from CO_2 and H_2

Łukasz Hamryszak[*,1], Mirosław Grzesik[1], Maria Madej-Lachowska[2]

1 Institute of Chemical Engineering of the Polish Academy of Sciences, Gliwice, Poland
2 Opole University of Technology, Opole, Poland

Keywords: *CO_2 hydrogenation*, *methanol synthesis*, *Cu/Zn/Zr-based catalyst*, *chemical kinetic*.

Climate change, caused to a large degree by rising carbon dioxide concentrations in the atmosphere and the depletion of fossil fuels, is becoming a major challenge for modern society. The continuous increase in CO_2 emissions is due to the rapid growth of the global economy. Catalytic CO_2 conversion to methanol is a promising and ecological way to solve the problem of excess anthropogenic CO_2 and reduce the use of fossil fuels. Methanol is an important chemical compound with a wide range of applications in many industries. Moreover, it is one of the liquid "energy carriers" that can be converted by decomposition or steam reforming to hydrogen, for example for fuel cells.

The catalyst used in the production of methanol should be highly efficient, selective towards the formation of methanol, resistant to sintering, sulfur and water poisoning. Zinc-copper catalysts used in industrial methanol production from synthesis gas are not suitable for the synthesis of methanol from CO_2-rich gas. Therefore, it still seems necessary to search for more active (higher MeOH yield and selectivity) and more durable catalysts, ensuring stable operation in the process of hydrogenation of carbon dioxide to methanol.

The Cu/Zn/Zr precursor have been modified by small amounts of Ce, Cr, Ga or their mixtures. The catalysts were obtained by complexing with citric acid and studied by synthesis of methanol with H_2 and CO_2 in a tube reactor with a fixed bed at 443 −513K at a pressure of 8 MPa. The MeOH yield, selectivity and CO_2 conversion were measured.

Cu/Zn/Zr/Ga catalyst with the highest (200 g/(kgh)) MeOH yield and selectivity to methanol (70%) was selected for kinetic tests.

Kinetic investigations included the influence of process parameters like: temperature, pressure, GHSV and the concentration of reagents on the process rate.

* Corresponding author, e-mail: *lukasz.hamryszak@interia.pl*

13.3 Organocatalytic synthesis of disubstituted amino acids' intermediates

Dóra Richter[1], Zsuzsanna Fehér[1], Sándor Nagy[1], Zsolt Rapi[1], Péter Huszthy[1], József Kupai[*,1]

1 Department of Organic Chemistry and Technology, Faculty of Chemical Technology and Biotechnology, Budapest University of Technology and Economics, Budapest, Hungary

Keywords: *organocatalysis*, *cinchona alkaloids*, *phase transfer catalyst*, *amino acids*, *enantioselective reaction.*

NThe class of enantiopure α,α-disubstituted α-amino acids has gained considerable attention in the past decades since some of them have interesting properties as antibiotics.

During my work, the goal was to synthesize a new type of chiral phase transfer organocatalyst, which can catalyze reactions leading to such amino acid intermediates. As phase transfer units, I used crown ethers, while the parts responsible for chiral induction were cinchona derivatives and glucose (Figure). The activity of the catalysts was examined in asymmetric alkylations of a benzylated malonate derivative, obtaining an allylated product with up to 98% yield. The intermediates gained in these reactions can be converted to amino acids through a selective hydrolysis followed by a multistep reaction.

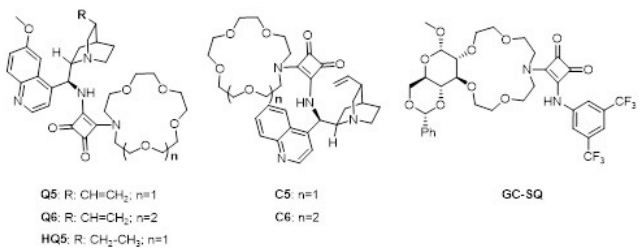

Figure 13.3.1: New, squaramide-based phase transfer organocatalysts.

Acknowledgements

This work was supported by Richter Talentum Excellence PhD Scholarship, the János Bolyai Research Scholarship of the Hungarian Academy of Sciences, Hungarian Scientific Research Fund (OTKA K 128473), and the ÚNKP-20-5-BME-322 New National Excellence Program of the Ministry of Human Capacities.

* Corresponding author, e-mail: *jkupai@mail.bme.hu*

13.4 Simple and advanced nucleation and growth kinetics of MoS_2

Michał Wojtalik[1], Łukasz Makowski[*,1]

1 Faculty of Chemical and Process Engineering, Warsaw University of Technology, Warsaw, Poland

Keywords: *molybdenum disulphide*, *nanoparticles*, *precipitation*, *jet reactor*.

Molybdenum disulphide nanoparticles (MoS_2) synthesis were examined in terms of the precipitation kinetics. The authors describe the simple and advance kinetic model of molybdenum disulphide nucleation and growth in the complex wet chemical synthesis using ammonium heptamolybdate and ammonium sulphide in a vortex jet reactor.

Molybdenum disulphide (MoS_2) is one of the transition metal dichalcogenides (TMDs), and it is considered to be a valuable 2D-nanomaterial for a wide range of industrial applications. One of promising application is the use of MoS_2 in several catalytic reactions, such as hydrogen evolution reaction (HER), hydrodesulfurization, oxygen reduction reactions (ORR), and methane conversion. This could be essential in future environmental projects involves sustainable sources of energy.

Synthesis of molybdenum disulphide nanoparticles was carried out in the turbulent mixer with tangential geometry. Ammonium molybdate tetrahydrate $(NH_4)_6Mo_7O_{24} \cdot 4\,H_2O$ (HMA), citric acid $C_6H_8O_7$ (CA), and ammonium sulphide $(NH_4)_2S$ (AS) were used as substrates of the reaction. Firstly, ammonium molybdate tetrahydrate and citric acid were dissolved at 90 °C and mixed for at least 30 minutes. To keep expected stoichiometric molar ratio of Mo:$(NH_4)_2S$, 20 wt.% solution of ammonium sulphide (AS) were properly diluted. In order to measure particles diameter, Beckman&Coulter LS 13 320 device has been employed, which uses DLS – dynamic light scattering and LD – laser diffraction to improve possible measurement range.

The reaction mechanism in witch sulfuric ion dissociation is a limiting process has been partially confirmed by experiments with excess and insufficient amount of HMA. Parity plots for moments and characteristic sizes shows clearly the accuracy of the model. Therefore proposed kinetics model for the nucleation and growth is assumed to be sufficient empirical model of the process and can be used in basic engineering application to predict the final PSD of MoS_2.

Acknowledgments

This work was supported by the National Science Centre [No.2017/27/B/ST8/01382].

* Corresponding author, e-mail: *lukasz.makowski.ichip@pw.edu.pl*

14 Abstracts: Other

14.1 Emulsions as vehicles for the controlled release of astaxanthin in topical application

Michał Dymek*[,1], Elżbieta Sikora [1]

1 Faculty of Chemical Engineering and Technology, Cracow University of Technology, Cracow, Poland

Keywords: *astaxanthin*, *release kinetics*, *skin delivery systems*, *cosmetic emulsions*, *antioxidant activity*.

The key point of modern cosmetics is their efficiency, which is influenced by few factors such as properties of the active substance applied or the nature of the cosmetic formulation. Astaxanthin (AST) is a carotenoid obtained, most often, from the *Haematococcus pluvialis* microalgae. It is one of the strongest natural antioxidants, lowering transepidermal water loss and protecting against the harmful effects of UV radiation.

In the work, the antioxidant activity of AST derived from the supercritical CO_2 extract of the microalgae was investigated using ABTS radical scavenging capacity assay. Moreover, the influence of the base formulation on the AST release was studied. Three O/W AST loaded emulsions, differing in droplet size of the internal phase (12.7μm (E_1), 3.8μm (E_2), 3.2μm (E_3)) and a nanoemulsion (0.13μm, NE) were prepared. Stability and rheological properties of the obtained formulations were determined. The AST release studies were carried out in thermostated (32°C) diffusion chambers, during 24h, using Spectra/Por dialysis membranes. The mixture of phosphate buffer (pH=7.4) and Tween 20 (0.5%) was used as the acceptor solution.

The results of antioxidant tests confirmed very strong activity of AST. Stable, non-Newtonian emulsion systems were obtained. It has been shown that the emulsion internal phase droplet size did not significantly affect the AST release. The amount of released astaxanthin was respectively: 13.60% (E_1), 11.42% (E_2), 9.45%(E_3), 9.71% (NE) and 7.68%, in the case of the caprylic/capric triglycerides (O_1).

The kinetics studies, supported by calculations for four popular mathematical models, showed that the process of AST release from the O/W emulsions is limited by diffusion through the vehicles, which is probably directly related to the viscosity of the carriers. For the emulsions, the best match was achieved for the Higuchi model, while for NE it was Korsmeyer-Peppas model. The results indicate controlled release of the actives, which is desirable from a cosmetic point of view, since it allows maintaining a constant concentration of the active ingredient in the skin.

* Corresponding author, e-mail: *michal.dymek@doktorant.pk.edu.pl*

14.2 Depolymerization of poly(ethylene terephthalate) with recyclable organocatalysts

Johanna Kiss[1], Zsuzsanna Fehér[1], Diana Daicu[1], Péter Kisszékelyi[1], Sándor Nagy[1], Levente Kárpáti[2], Péter Huszthy[1], József Kupai*[,1]

1 Department of Organic Chemistry and Technology, Budapest University of Technology and Economics, Budapest, Hungary
2 Downstream Hungary, Polyolefin R&D, MOL Nyrt., Budapest, Hungary

Keywords: *depolymerization of PET*, *chemical recycling*, *glycolysis*, *organocatalysis*, *recyclable catalyst*.

As our planet is facing climate change problems, the recycling of plastic materials has a crucial role in reducing environmental pollution. During our work, we investigated the glycolytic depolymerization of poly(ethylene terephthalate) (PET), using ethylene glycol as reagent and solvent. Our aim was to optimize the glycolysis of PET, then recycle the silica gel supported catalyst.

We applied different organocatalysts supported on silica gel as catalysts. The reactions (see Figure) were carried out in sealed vials, under inert atmosphere (Ar), at a range of temperatures between 170 to 190 °C. The stability of the supported organocatalysts was determined by TG-DSC analysis.

After conducting the optimization, we found a method resulting in almost quantitative production (90%) of BHET, which is a readily appropriate starting material for preparing PET. We also managed to recycle the catalyst, achieving almost as high production of BHET.

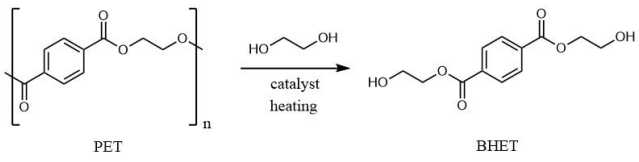

Figure 14.2.1: Depolymerization of PET by glycolysis.

Acknowledgements

This work was supported by Richter Talentum Excellence PhD Scholarship, the János Bolyai Research Scholarship of the Hungarian Academy of Sciences, Hungarian Scientific Research Fund (OTKA K 128473), and the ÚNKP-20-5-BME-322 New National Excellence Program of the Ministry of Human Capacities.

* Corresponding author, e-mail: *jkupai@mail.bme.hu*

14.3 Synthesis of inulin acetate for potential use as a surfactant or an emulsifier

Anna Kołakowska*[,1], Krzysztof Kolankowski[1], Paweł Ruśkowski[1]

1 Faculty of Chemistry, Warsaw University of Technology, Warsaw, Poland

Keywords: *inulin*, *inulin acetate*, *inulin ester*.

The physical and chemical properties of inulin and inulin acetate are described, many of which are unusual due to inulin's structure. The possible ester applications are considered as an emulsifier. Due to that inulin acetate could be useful in the food, pharmaceutical, paint industries. It can be used in cosmetics as an innovative emulgator of plant origin, potentially more eco-friendly than the ones used nowadays. It can also be a surfactant e.g. in a laundry or dishwashing detergents.

In this work the inulin acetate synthesis pathways were studied. The syntheses were carried out with acetic anhydride as the acylating agent with use of different catalysts (4-dimethylaminopyridine (DMAP) and sodium acetate). Also the influence of solvents (pyridine and dimethylformamide (DMF)), temperature and reaction time were tested. The purifying of post-reaction mixtures were performed differently for each reaction due to used chemicals. In order to confirm the presence of the desired compound FTIR spectra analyses were performed.

In both cases, using DMAP and sodium acetate, syntheses result in inulin acetate, though with low yields: 37% and 28%, respectively. The obtained ester was a yellow, viscous substance. The purification process yields well-purified inulin acetate. However, it could be improved due to slight solvent contamination.

* Corresponding author, e-mail: *01123540@pw.edu.pl*

14.4 Cinchona organocatalysts modified with a lipophilic moiety

Balázs Molnár[1], Gyula Dargó[1], Péter Kisszékelyi[1], Zsuzsanna Fehér[1], Péter Huszthy[1], József Kupai*[,1]

1 Department of Organic Chemistry and Technology, Faculty of Chemical Technology and Biotechnology, Budapest University of Technology and Economics, Budapest, Hungary

Keywords: *organocatalysis*, *catalyst recovery*, *hydrophobization*, *cinchona alkaloids*, *squaramide*.

Nowadays, the recovery of organocatalysts is a crucial issue considering both environmental and economic aspects. An effective and yet simple solution to meet this challenge is to change the solubility of the reaction components. To reach this aim, lipophilic side chain can be incorporated into the organocatalyst. This causes a considerable difference in the polarity, which allows the catalyst to be separated from the reaction mixture by filtration after changing the solvent.

Our aim was to develop a new synthetic method for the incorporation of a lipophilic moiety into the catalysts. At first, we prepared a carboxylic acid derivative containing three octadecyl groups. This lipophilic unit was then linked to a cinchona squaramide organocatalyst, which had led to excellent enantioselectivity (99% ee) in *Michael* reactions. In the amide formation, we examined two pathways: 1) through an acyl chloride intermediate and 2) using coupling agents as well. We applied the gained lipophilic catalyst (see Figure) in asymmetric *Michael* addition reaction resulting 96% yield. The recovery of the catalyst can be solved by utilizing its hydrophobic character.

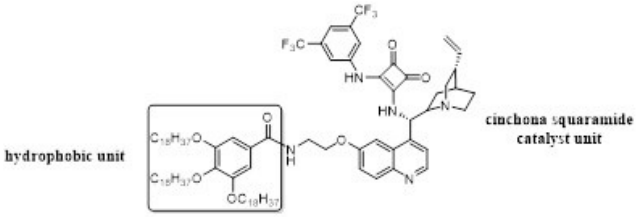

Figure 14.4.1: The synthesized and applied lipophilic cinchona squaramide organocatalyst.

Acknowledgements

This work was supported by the Hungarian Scientific Research Fund (OTKA K128473), the New National Excellence Program of the Ministry of Innovation and Technology (ÚNKP-20-1-I-BME-240, ÚNKP-20-5-BME-322) and the Bolyai János Research Fund.

* Corresponding author, e-mail: *jkupai@mail.bme.hu*

14.5 Application of elemental sulfur in multicomponent reactions

András Gy. Németh[*,1], Renáta Szabó[1], György Orsy[2], Bence Marlok[1],István M. Mándity[2], György M. Keserű[1], Péter Ábrányi-Balogh[*,1]

1 Medicinal Chemistry Research Group, Research Centre for Natural Sciences (RCNS), Budapest, Hungary
2 Artificial Transporters Research Group, RCNS, Budapest, Hungary

Keywords: *elemental sulfur*, *multicomponent reaction*, *continuous flow*, *isothiocyanates*, *water*.

The application of the naturally occurring, easy to handle elemental sulfur in multicomponent reactions (MCRs) enables the practical and atom efficient synthesis of complex structures containing sulfur, even in one technological step. The substitution of hazardous, toxic reagents with the environmentally benign sulfur, and the in situ generation and application of sensitive intermediates offers safe and efficient alternatives to existing synthetic procedures.

The reaction conditions of the developed MCRs were optimized followed by the investigation of their scope and limitations.

Our work covers the evaluation of efficient methods for the catalyst-free synthesis of isothiocyanates from isocyanides and elemental sulfur and their application in MCRs to synthesize thiocarbamates, thioureas and thiazol derivatives. In addition, the introduction of the aqueous solution of polysulfide anions enabled the use of sulfur under continuous flow (CF) conditions for the synthesis of thioureas. Moreover, we have developed a new, one-pot three-step reaction for the synthesis of thioethers starting from electron deficient olefins.

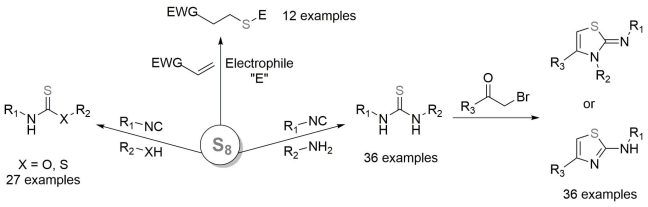

Figure 14.5.1: Multicomponent reactions based on elemental sulfur.

Acknowledgements

The authors appreciate the contribution of Krisztina Németh and Pál Szabó for the HRMS measurements and Attila Domján for NMR measurements. This work was supported by the PD124598 grant of the National Office of Science, Innovation and Technology (NKFIH).

* Corresponding author, e-mail: *nemeth.andras.gyorgy@ttk.hu*
* Corresponding author, e-mail: *abranyi-balogh.peter@ttk.hu*

14.6 Comparison of wettability of human skin and its equivalents by aqueous solutions of chosen surfactants

Edyta Rekiel[*,1], Joanna Krawczyk[1], Anna Zdziennicka[1]

1 Department of Interfacial Phenomena, Institute of Chemical Sciences, Faculty of Chemistry, Maria Curie-Skłodowska University in Lublin, Lublin, Poland

Keywords: *skin*, *polymeric materials*, *wettability*.

Skin can be called 'the largest tissue' of the human body, sometimes even 'the largest organ' as it has many different, very important properties. It is the first barrier allowing the basic sensing of organism, providing protection against environmental influences and solar radiation. Skin regulates body temperature and maintains general homeostasis, it is also a source of information about heat, cold and pain. It is the main producer of vitamin D and folate which play important role in providing proper bone structures. Moreover, the surface properties of the human skin (especially wettability) enable cosmetics, creams and ointments adsorption. Both adsorption and wetting processes are crucial for skin ecosystem, protecting natural lipid barrier and its proper hydration.

Most of cosmetics are based on water, which has high surface tension (72.8 mN/m). This reason alone might be an obstacle to obtain good wettability of a given formulation. To get over this natural barrier, many other substances are added i.a. surface active agents called surfactants. Surfactants influence skin surface wettability as well as cosmetic ingredients sorption (adsorption and absorption). Therefore, thorough study and investigation concerning skin wettability is needed. In many of these, the researchers use PTFE (polytetrafluoroethylene) and PMMA (poly(methyl methacrylate)) polymers as substitutes for human skin. In this study, measurements of contact angle of anionic (SDDS), cationic (CTAB), and non-ionic (TX-100) aqueous solutions of surfactant on the skin surface were performed. The obtained values of contact angle were next compared with these of PTFE and PMMA.

As follows, the wettability of skin depends on the concentration and the type of surfactant. However, the complete spreading does not occur. It was also possible to determine the critical surface tension of the human skin wetting based on the measurements of the contact angle of aqueous solutions of studied surfactants and the values of their surface tension. The obtained values are very close to the surface tension or critical surface tension of PTFE wetting; although, these values are lower even than Lifshitz-van der Waals component of surface free energy of skin or PMMA. This fact shows the human skin belongs to low hydrophobic surfaces.

* Corresponding author, e-mail: *edyta.rekiel@poczta.umcs.lublin.pl*

14.7 Adsorption of chosen surfactants at the liquid-gas interface

Edyta Rekiel[*,1], Anna Zdziennicka[1]

1 Department of Interfacial Phenomena, Institute of Chemical Sciences, Faculty of Chemistry, Maria Curie-Skłodowska University in Lublin, Lublin, Poland

Keywords: *adsorption*, *surfactants*, *biosurfactants*.

Surfactants are surface active substances, well known for their ability to lower naturally occurring surface tension. They have characteristic amphiphilic structure as they consist of hydrophobic 'tail' and hydrophilic 'head' and it allows surfactants to orient themselves properly at the interface. Surfactants are widely used in the various industry branches, among others: cosmetics, pharmaceutics and food processing.

Surfactants can adsorb at different types of interfaces. Due to this fact, they significantly influence wettability, the reduction of surface tension, detergency, dispersion, solubilization and emulsification of various systems. To measure adsorption of surfactants, Gibbs free energy of adsorption (ΔG_{ads}) can be used. There are a few methods of measuring Gibbs free energy of adsorption, but the most popular ones are Langmuir equation modified by Boer, and method proposed by Rosen and Aronson as well as Gamboa and Olea. Moreover, ΔGads can inform about spontaneous (or not) character of the process.

As the purpose of this study, Gibbs free energy of adsorption for anionic SDS (sodium dodecyl sulfate), cationic CTAB (cetyltrimethylammonium bromide) and nonioinic TX-100 (triton X-100) were analysed and compared with Gibbs free energy of adsorption for rhamnolipid and surfactin, natural biosurfactants produced by bacteria. It was concluded that adsorption of rhamnolipid is the highest in comparison to other surfactants. Moreover, ionic SDDS displayed the biggest tendency to adsorption at liquid-gas interface in comparison to cationic CTAB and nonionic TX-100.

* Corresponding author, e-mail: *edyta.rekiel@poczta.umcs.lublin.pl*

Index of authors

Cover design
Monika Klimek, klimek.monika2000@gmail.com

Book layout design, EYEC LaTeX package
Mateusz Bartczak, bartczak.mateusz@protonmail.com

Paper review team
Piotr Cendrowski – Leader
Zuzanna Bojarska
Nina Borzęcka
Katarzyna Dobrowolska

Typesetting team
Maria Ziąbska – Coordinator
Mateusz Bartczak
Grzegorz Bernacki
Monika Binkiewicz
Nikodem Dąbrowski
Magdalena Majchrzyk
Olga Przybył

Typeset using Libertinus font family, distributed
under SIL Open Font License 1.1

Krystel

Printed and bound in Poland by PHU Krystel
Generała Władysława Andersa 13, 00-159 Warsaw
tel. +48 22 831 76 57, www.krystel.com.pl

9TH EYEC

SPECIAL GUESTS

· Prof. Jörg Vienken
· Prof. Bernhard Seyfang
· Prof. Andrzej Stankiewicz
· Zoltán Kovács, PhD
· Michał Wojasiński, PhD

SCIENTIFIC COMMISSION

· Prof. Łukasz Madej
· Magda Barecka, PhD
· József Kupai, PhD
· Maria Kurańska, PhD
· Agata Przekora-Kuśmierz, PhD
· Lena Ruzik, PhD

112	59	42	15
participants	plenary presentations	poster presentations	articles

ISBN: 978-83-936575-9-9